Thesis for the Degree of Licentiate of Engineering

Electrocatalyst materials for low-temperature hydrogen fuel cells

Gerard Montserrat Sisó

CHALMERS

Department of Physics

CHALMERS UNIVERSITY OF TECHNOLOGY

Gothenburg, Sweden 2021

Electrocatalyst materials for low-temperature hydrogen fuel cells

GERARD MONTSERRAT SISÓ

Department of Physics

Chalmers University of Technology

SE-412 96 Gothenburg

Sweden

Telephone +46 (0)31-772 1000

Printed at Chalmers Reproservice

Göteborg, Sweden 2021

Electrocatalyst materials for low-temperature hydrogen fuel cells

Gerard Montserrat Sisó
Department of Physics, Division of Chemical Physics
Chalmers University of Technology

ABSTRACT

Fuel cells have emerged as one alternative to satisfy the need of energy systems with net-zero emissions. Although fuel cells date back to the 1800s, it is only during the last decades that their research has boosted to ease their commercialization. This growing interest in fuel cells implementation goes hand in hand with the decrease in green H_2 production cost, which makes fuel cells a cornerstone in the promising energy system based on hydrogen with water as the only by-product. For this, it is crucial that the transport sector shifts towards effective, inexpensive and carbon-free fuel alternatives which is possible with hydrogen owing to its high energy density. A broad implementation of fuel cells is, however, impeded by the high cost of fuel cell systems, which is in turn greatly attributed to the Pt-based catalyst layer currently used in low-temperature hydrogen fuel cells. As Pt is a scarce resource and an expensive material, development of new efficient, stable and inexpensive electrocatalysts is essential for large-scale fuel cells implementation. Although many strategies have been explored to reduce the amount of Pt without compromising the power output and lifetime, electrocatalyst development is currently hindered by the lack of mechanistic understanding. In order to gain a better understanding of the mechanisms behind the electrochemical reactions in proton exchange membrane fuel cells (PEMFC) and anion exchange membrane fuel cells (AEMFC), this thesis delves into both the fabrication and the characterization of electrocatalysts. A versatile platform was built to study model system catalysts with the aim to test electrocatalytic materials and establish reliable comparisons. In this way, the performance of model system catalysts can be rationalized in terms of geometric structure and electronic structure. Pt-rare earth metals thin-film alloys were studied with respect to their activity towards the oxygen reduction reaction (ORR) in PEMFCs. Similarly, NiAg nanoparticles in different morphologies were studied for the ORR in alkaline conditions for AEMFCs. Hydrogen oxidation reaction (HOR) and ORR activity of PdNi annealed thin films were investigated to pinpoint the mechanism behind the increased activity for the alloy in both reactions. This provides insights to the fundamental principles that lead to a good catalyst efficiency and effectiveness. The presented work takes a step in tailoring new electrocatalytic materials that could eventually outperform Pt in both activity and stability while reducing the total cost.

List of Appended Papers

This thesis is based on the work presented in the following papers:

Paper I

Enhanced oxygen reduction activity with rare earth metal alloy catalysts in proton exchange membrane fuel cells

B. Eriksson, G. Montserrat-Sisó, R. Brown, T. Skála, R. W. Lindström, G. Lindbergh, B. Wickman, C. Lagergren

Electrochimica Acta (In revision)

Paper II

γ-Radiation Induced Engineering of Interfaces in Bimetallic Ag-Ni Nanocomposites for Oxygen Reduction in Alkaline Media

Y. Yang, G. Montserrat-Sisó, B. Wickman, P. Nikolaychuk, I. Soroka

ACS Applied Nano Materials (Submitted)

Paper III

PdNi Thin Films for Hydrogen Oxidation Reaction and Oxygen Reduction Reaction in Alkaline Media

G. Montserrat-Sisó and B. Wickman

In Manuscript

Related papers not included in this thesis

Paper IV

Hydrogen Evolution Reaction for Vacancy-Ordered i-MXenes and the Impact of Proton Absorption into the Vacancies

H. Lind, B. Wickman, J. Halim, G. Montserrat-Sisó, A. Hellman, J. Rosen

Advanced Sustainable Systems **5**, 2000158 (2021)

Paper V

Tuning morphology, composition and oxygen reduction reaction (ORR) catalytic performance of manganese oxide particles fabricated by γ-radiation induced synthesis

Z. Li, Y. Yang, A. Relefors, X. Kong, G. Montserrat-Sisó, B. Wickman, Y. Kiros, I. L. Soroka

Journal of Colloid and Interface Science **583**, 71-79 (2021)

Table of Contents

1. Introduction

The Industrial Revolution is a turning point in the history of mankind, which transformed economies based on agriculture and handicrafts into large-scale industry-based economies. Modern civilization has seen thenceforth a tremendous and fast-growing industrialization that, accompanied by growth in human population, has raised the energy demand to unprecedented levels. As society develops and energy consumption grows, concerns for future energy supply and sustainability issues emphasize the need for shifting away from fossil fuels. Combustion of this finite resource is strongly contributing to emissions of anthropogenic greenhouse gases (GHG), which represent an imminent threat to public health and the environment [1]. This, together with the depletion of viable fossil fuel reserves, evidences the necessity of rapid improvements in energy efficiency and the adoption of low-carbon energy alternatives, as well as policies that implement the alternatives effectively.

As a result of the European Green Deal, the European Union (EU) aims to be an economy with net-zero greenhouse gas emissions by 2050 [2]. At the same time, the European Commission estimates that a continuation of the current trends would result in only a 40% reduction in GHG emissions by the same year [3]. This implies that renewable energy sources need to be expeditiously implemented in Europe if the clean energy goals should be met by 2050. Nevertheless, there are uncertainties and constrains involved in a shift towards renewable energies, such as high equipment cost or spatial and temporal mismatch between availability and demand. The problem with the equipment cost may be mitigated by an increase in production volumes together with the simultaneous increase of fossil fuel prices, which will make green fuels competitive. On the other hand, the availability problem may be solved by converting excess energy that cannot be utilized immediately to energy carriers that can be stored, transported and converted to useful forms of energy.

An energy carrier that satisfies the requirements is hydrogen, the most abundant chemical substance in the universe and third most abundant element in the Earth's crust [4]. Hydrogen represents a promising energy carrier thanks to its potential to be used as a power supply for almost all devices using fuel-based energy. Moreover, it also presents the advantage of long-term energy storage, long distance transport, high energy density and light weight [5]. However, there are still challenges such as hydrogen storage, cost

of production and infrastructure that have to be overcome. Besides the mentioned problems with hydrogen as an energy carrier, challenges also arise in the production of hydrogen. Currently, around 95% of hydrogen is produced from fossil fuels (grey hydrogen) [6], which gives rise to significant amounts of CO_2. Net-zero emissions hydrogen production can also be carried out by splitting natural gas with an additional CO_2 capture process (blue hydrogen), although it only provides a short-term solution [7]. Thus, in the long-term, carbon-neutral hydrogen sources must be considered to make hydrogen a clean energy alternative.

Water is one of the most abundant and inexhaustible raw materials in Earth and can be used for H_2 production through water-splitting processes, of which electrolysis is the most effective. Water electrolysis is a commercially available electrochemical technology that can produce hydrogen from electricity with oxygen as the only by-product, making this hydrogen the cleanest energy carrier that could be used provided that the electricity is produced in a sustainable way (green hydrogen) [8]. Hydrogen obtained from water electrolysis presents the advantage of high purity after removal of oxygen impurities, which is a critical feature in several applications [9]. More importantly, the integration of large-scale water electrolysis into the power grid can mitigate the discordance between clean energy availability and demand by immediately converting renewable electricity into hydrogen that can be stored and used on-demand [10]. However, power-to-power electricity storage based on hydrogen requires an efficient energy conversion -both from electricity to hydrogen and vice versa- in order to make the storage of renewable energy profitable.

Hydrogen produced via water electrolysis is one of the potential applications of the fundamental electrochemical mechanism through which energy carriers can be produced. However, electrochemical methods involving hydrogen are not limited to green hydrogen production. Numerous electrochemical devices are used for storage of energy carriers, such as batteries [11] and supercapacitors [12]. However, other electrochemical devices such as fuel cells are commonly used to make use of the high-purity hydrogen as a fuel produced from an electrolyzer. In fact, hydrogen fuel cells operate like an electrolyzer in reverse: they combine hydrogen and oxygen to produce electricity and water (Fig. 1.1). Although they are often compared to batteries because both convert energy produced by a chemical reaction into usable electric power, fuel cells have the additional feature of producing electricity as long as fuel, hydrogen in this case, is supplied. Thus, fuel cells present the advantage over batteries in that they do not run down or need recharging, which many applications take advantage of. More importantly, fuel cells use a renewable energy source and they do not release any harmful substances, which make them highly sustainable power generators.

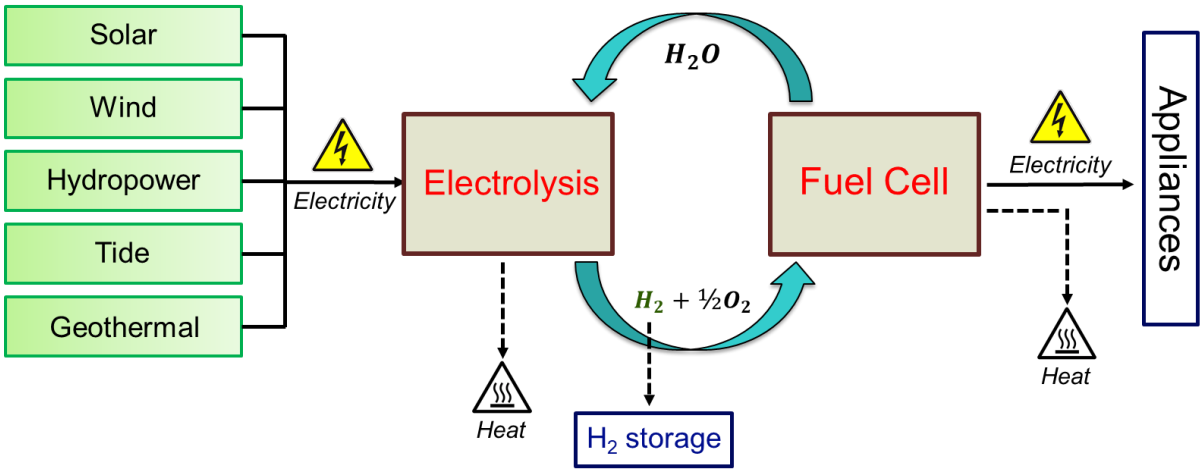

Figure 1.1 Schematic illustration of the production of green hydrogen and its use in carbon-free power generation.

There are many types of fuel cells considered for a wide range of applications, from small portable devices to large-scale stationary power generation systems. They all consist of an anode, a cathode and an electrolyte that allows the transport of charge carriers, i.e. ions, from the anode to the cathode. At the same time, an electron flow produced by a chemical reaction occurring inside the fuel cell travels from the anode to the cathode through an external circuit, which generates an electric current. The different fuel cell types have intrinsic differences in their operating conditions, components and fuel. They are often classified by the type of electrolyte they use, which dictates their operating temperature range. This temperature, as well as the useful life of the fuel cell, commands the properties of the other materials used in the cell components. The underlying theme of this thesis is based on low-temperature hydrogen fuel cells, which are the most viable option for vehicles, portable devices and small stationary power.

Proton exchange membrane fuel cells (PEMFCs), which operate at low temperatures, form the most widely studied category of fuel cells. The PEMFC was invented during the 1960s and since then has been considered a promising candidate as a power source due to its low operating temperature and high power density. However, it has not been until the last two decades that the PEMFC has reached commercialization [13]. In fact, today there are commercially available systems that use PEMFC technology within transport, as well as stationary and portable power generation. Examples of vehicles that use fuel cells as a source of power (FCV), are Toyota Mirai, Honda Clarity and Hyundai Nexo, as well as busses fleets [14]. Similarly, PEMFCs are also currently used for small-scale power demands (<10 kW) in for example domestic applications [15]. However, the world-wide commercialization of PEMFC has not come yet owing to two major technical barriers: durability and cost. Durability issues arise from the degradation that fuel cell components, such as the membrane electrode assembly (MEA), suffer during long-term operation. For transportation powered with direct hydrogen fuel cell systems, the U.S.

Department of Energy (DOE) has set a target of 8,000 hours of durability in automotive load cycles with a 65% peak energy efficiency by 2025 [16]. For state-of-the-art PEM fuel cells, however, lifetime decreases with decreasing platinum group metal (PGM) loading in the catalyst layer, which accounts for approximately 40% of the total fuel cell cost at high volume production. The high cost of the catalyst layer arises from the scarcity of Pt, which is commonly used as electrocatalyst [17]. Thus, both the lifetime and cost issues that hinder the large-scale commercialization of PEMFCs are related to the metal that catalyzes the fuel cell electrochemical reactions. Moreover, the DOE has also established a cost target of 30 $/kW with a total PGM content of ≤ 0.10 g_{PGM}/kW at high volume production by 2025 [16,18]. Several strategies have been adopted with the aim to decrease the cost of the catalyst layer and, thus, facilitate the wide-spread implementation of PEMFCs, including better Pt utilization through material optimization or alloying with less expensive metals [19–21]. Nonetheless, state-of-the-art PEM systems are still far from the ultimate desired cost and durability set by the DOE and other alternatives started gaining prominence.

The anion exchange membrane fuel cell (AEMFC) has recently gained increased attention in the fuel cell research community motivated by the intrinsic advantages over their acidic analog, including more facile cathode kinetics, minimized corrosion problems and a wider range of materials stable in the fuel cell environment [22]. The most prominent merit of AEMFCs is the possibility to use non-noble metal electrocatalysts thanks to milder alkaline conditions, which opens up new possibilities of finding less expensive catalyst materials without compromising the power density of the fuel cell. Thus, during the last decade, much fuel cell research has focused on finding efficient inexpensive catalytic materials that could potentially bring the AEMFC technology to the frontline of the low-temperature fuel cell market [23]. Although there are a number of major issues that still remain to be resolved for the AEMFC technology, such as MEA poor performance [24], their successful application can already be foreseen with continuous industrial and policy support.

To summarize, there are currently numerous issues that impede the global implementation of carbon-free technologies with net-zero GHG emissions for energy utilization. However, during the last decades, the awareness of the need for green energy sources and sustainable energy utilization to palliate the sequels of human activities has grown hand in hand with the development of devices that could (and can) make it happen. The successful implementation of the already existing technologies demonstrates the feasibility of such technologies and, together with competent policies, provides the impetus needed to shift towards a development completely independent from fossil fuels. In this way, the eventual deployment of efficient and profitable electrolysis and fuel cell

systems will certainly lead to a turning point as revolutionary for modern civilization as the Industrial Revolution.

1.1 Scope of this thesis

The overall aim of this thesis is to contribute to the development of low-temperature fuel cell systems and thus accomplish a sustainable and resource-efficient energy supply without the net emissions of GHG. By providing a better understanding of the mechanisms through which the electrochemical reactions occur in fuel cells, new inexpensive and efficient catalysts can be tailored. In this way, the cost and durability barriers that hinder the wide-spread commercialization of low-temperature fuel cells can be overcome, thereby facilitating the implementation of a sustainable fossil-free energy system.

In this thesis, physical vapor deposition methods such as thermal deposition and sputtering are used to fabricate thin-film catalysts for both PEMFCs and AEMFCs. The electrocatalytic materials have been used to study electrode reactions, namely hydrogen oxidation (anode) and oxygen reduction (cathode). A major part of this work has been focused on increasing the understanding of the reaction mechanisms in both alkaline and acidic media, providing key knowledge for the unclear mechanism of the former. Another part of this work has been dedicated to the fabrication of thin-film model electrodes that have been evaluated in a fuel cell system with the aim to study the thin-film catalysts under realistic fuel cell conditions. This model system has been used to isolate the catalyst contribution and provide a reliable comparison between catalyst materials and thus bridge the gaps in fuel cell catalysis research. Catalyst fabrication and electrochemical measurements in liquid half-cell have been conducted at Chalmers, as well as physical characterization by spectroscopic (X-ray Photoelectron Spectroscopy [XPS] and energy-dispersive X-ray spectroscopy [EDX]) and microscopic techniques (SEM), which paper III was based on. Collaborations with the Applied Electrochemistry Department at the Royal Institute of Technology (KTH) in Stockholm resulted in measurements of thin-films catalysts fabricated at Chalmers in model systems (Membrane Electrode Assembly), whose physical characterization was also carried out at Chalmers (paper I). Another collaboration with the Applied Physical Chemistry Department at KTH allowed the electrochemical characterization of nanoparticles-based catalysts produced via radiation synthesis which, together with X-ray diffraction (XRD) and XPS measurements, resulted in paper II.

2. Electrochemistry

The *Journal of Natural Philosophy, Chemistry and the Arts*, which was the first monthly independent scientific journal, had one of the earliest references to electrochemistry back in 1829. It was defined as 'one of the connecting branches between remote divisions of the Philosophy of Nature' [25]. Thus, although electrochemistry is often labelled as a discipline within Physical Chemistry, the truth is that it is not solely physics nor chemistry, but actually encompasses a vast range of science from biology to material science. In fact, the birth of electrochemistry was marked by a discovery in the field of biology back in the 18th century.

In 1786, the Italian anatomist Luigi Galvani discovered that the leg muscles of a dead frog twitched when struck by an electrical spark, which he termed as 'animal electricity'. Shortly after, another Italian scientist Alessandro Volta refuted Galvani's finding by proposing that electricity was generated because of two dissimilar metals in contact with each other through a moist conductor. He further proved his hypothesis by reproducing Galvani's system with pairs of zinc and silver disks connected by brine-soaked cardboard, which generated electricity. This became the first example of a practical battery, the so-called 'Voltaic pile'. During the same time, English researchers Nicholson and Carlisle used Volta's configuration to separate water into its constituent elements by passing electricity through it, which is now known as 'electrolysis'. They published their findings in 1800 in the *Journal of Natural Philosophy, Chemistry and the Arts*, where Nicholson was the editor. Using the same concept, Humphrey Davy used the electricity generated by the pile to separate different compounds into their constituents and realized that the electricity produced depended on the occurrence of chemical reactions. In this way, he discovered several new elements such as potassium, sodium, calcium and magnesium. Davy's student and successor, Michael Faraday, pursued the relationship between electricity and magnetism and invented the electric motor and the dynamo. He also predicted the relationship between the applied current and the amount of chemical product generated through a process that he named "electrolysis". His two laws of electrolysis were published in 1834 and nowadays are still fundamental to industrial electrolytic production of chemicals [25,26].

The laws of electrolysis established by Faraday back in 1834 set the bases of the modern definition of electrochemistry: 'a branch of chemistry concerned with the relations between chemical and electrical phenomena, especially with reactions occurring at the

point of contact of an electrical conductor and a conducting liquid' [27]. Thus, electrochemistry can be defined as the study of interfaces, where interactions between phases containing electrons (electrode) and phases containing ions (electrolyte) take place. The chemical processes that occur between these phases involve an electron transfer to or from an ion changing its oxidation state, either through the application of an external voltage (electrolytic cell) or through the release of chemical energy in a spontaneous reaction (galvanic cell). These electron transfer reactions are known as 'redox', which stands for reduction-oxidation, being *reduction* the gain of electrons (i.e. decrease of the oxidation state) and *oxidation* the loss of electrons (i.e. increase in the oxidation state) of an atom. Similar to acid-base reactions, these processes occur simultaneously and cannot occur independently of one another. Hence, both reduction and oxidation processes are considered "half-reactions" and redox constitutes the "whole reaction".

Redox reactions are driven by the difference between the energy states of their reactants and products which, in the case of electron transfer reactions, corresponds to the difference in electrochemical potential. Once the potential difference is balanced out, the reaction is considered to be in thermodynamic equilibrium and there is no net flux of electrons. Thus, as in any other chemical reaction, the rate of redox reactions is governed by the principles of thermodynamics.

2.1 Thermodynamics: Equilibrium and Nernst Equation

Electrochemistry obeys all the same laws of nature as the rest of science, including thermodynamics. Thermodynamic equilibrium is of special interest for electrochemical reactions in both galvanic and electrolytic cells, which require the non-equilibrium of the redox reaction to produce electrical and chemical energy respectively. Hence, as there is no current when the reaction is at equilibrium, determination of electrochemical equilibrium is crucial for the study of electron transfer reactions [28].

Considering the following redox reaction with n electrons transferred:

$$Ox + n\,e^- \rightleftharpoons Red$$

standard thermodynamics dictate that the actual Gibbs free energy (ΔG) of a reaction is related to the free energy change under standard conditions (ΔG^o) by:

$$\Delta G = \Delta H - T\Delta S = \Delta G^o + RTlnQ_r \tag{2.1}$$

where Q_r is the reaction quotient, R the gas constant and T absolute temperature.

For an electrochemcial system, the maximum possible voltage of the cell is at zero current, which is used to calculate the maximum possible electrical energy that could be obtained from a chemical reaction ($W_{electrical}$). Thus, since ΔG is the maximum amount of work that can be extracted from a system, it can be expressed as:

$$W_{max} = W_{electrical} = \Delta G = -nFE_{cell} \tag{2.2}$$

being F the Faraday constant (96485 C/mol). ΔG is also related to the cell potential (E) under general conditions (standard or not). Similarly, ΔG^o and E^o are related by the same relation. Hence, combining Eq. 2.1 and Eq. 2.2 gives:

$$-nFE_{cell} = -nFE^o_{cell} + RTlnQ_r \tag{2.3}$$

by dividing by the amount of charge transferred (i.e. $-nF$) leads to the Nernst equation for a redox reaction:

$$E_{cell} = E^o_{cell} - \frac{RT}{nF} lnQ_r \tag{2.4}$$

which relates the reduction potential of an electrochemical reaction to the standard electrode potential.

The Nernst equation states that the E_{cell} depends on the relative amount of products and reactants (i.e. Q_r). As the redox reaction proceeds, reactants are consumed and product concentration increases. The potential of the cell gradually decreases until the reaction is at equilibrium, at which $\Delta G = 0$ and $Q_r = K_{eq}$, so $E_{cell} = 0$. As shown in Eq. 2.2, positive cell potential gives a negative ΔG, indicating spontaneous electrochemical reaction. Thus, a positive cell potential is needed for the generation of electric current, which is the basis of batteries and fuel cells. Conversely, a positive ΔG indicates a non-spontaneous reaction ($E_{cell} < 0$) and thus electric current should be applied for the redox to occur, which is the principle of electrolytic cells [28,29].

Moreover, since the cell potential corresponds to the difference between cathode (reduction) and anode (oxidation) potentials:

$$E_{cell} = E_{red} - E_{ox} \tag{2.5}$$

the Nernst equation can also be used for the study of a half-cell reaction with:

$$E_{red} = E^o_{red} - \frac{RT}{nF} ln \frac{a_{red}}{a_{ox}} \tag{2.6}$$

Essentially, the Nernst equation relates the reduction potential of a half or full cell reaction to the concentrations of the chemical species being reduced or oxidized, i.e. the

position of the redox reaction equilibrium. However, the Nernst equation does not explain how fast the system reaches equilibrium and, since reactions are prevented from reaching equilibrium by their kinetic limitations, the study of the reaction kinetics at the electrode surface is of crucial importance for electrochemical reactions.

2.2 Electrode Kinetics and Overpotential

The kinetics of electrode reactions can be treated in a completely analogous way to solution-phase reactions, but with the added dimension of electric potential.

Again, considering the following reversible one-step redox reaction:

$$Ox + n\,e^- \underset{k_{ox}}{\overset{k_{red}}{\rightleftharpoons}} Red \tag{2.7}$$

the dependence of the reaction rate constants on temperature can be described by the Eyring-Polanyi equation, an Arrhenius-like equation that follows the transition state theory [30]:

$$k_{red} = Ae^{\frac{-\Delta G^{\ddagger}_{red}}{RT}}; k_{ox} = Ae^{\frac{-\Delta G^{\ddagger}_{ox}}{RT}} \tag{2.8}$$

Where A is the pre-exponential factor and $\Delta G^{\ddagger}$ the Gibbs free energy of activation, which corresponds to the energy of the transition state (TS), as depicted in Fig. 2.1.

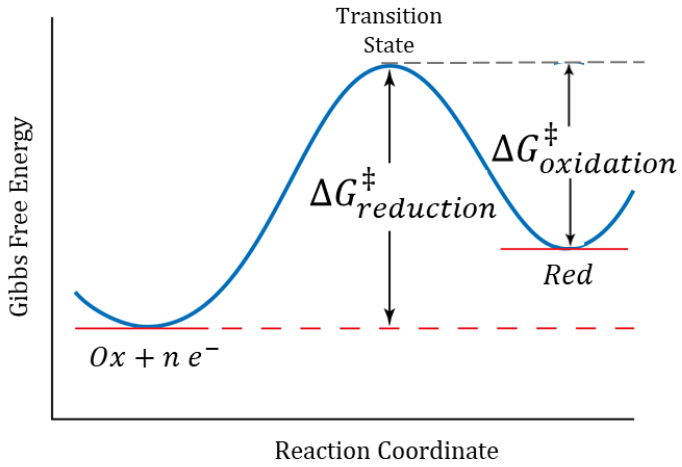

Figure 2.1 Gibbs free energy curve for a redox reaction. $\Delta G^{\ddagger}_{ox}$ represents the minimum amount of energy required to transform *Ox* into *Red* (i.e. reduction) and $\Delta G^{\ddagger}_{red}$ for oxidation. The value of $\Delta G^{\ddagger}$ is equivalent to the difference in potential energy between the initial state and the transition state.

The forward and backward reaction rates (r_{red} and r_{ox}) can be taken as the expressions for first-order chemical reactions. However, reaction rates for redox reactions must bring

in a measurable voltage, which is when the Faraday's law of electrolysis comes in (i.e. the current is directly related to the rate of the reaction):

$$r_{red} = k_{ox}c_{Red} = \frac{j_{red}}{nF} \;\; ; \;\; r_{ox} = k_{ox}c_{Red} = \frac{j_{ox}}{nF} \tag{2.9}$$

Where j_{red} and j_{ox} are the reduction and oxidation current densities respectively. Henceforth, we will be referring to *current* as a faradaic current, i.e. current generated by any chemical reaction involving an electron transfer. The net rate of the redox reaction (r) and net current density (j) can be written as:

$$r = r_{ox} - r_{red} = k_{ox}c_{Red} - k_{ox}c_{Red} = \frac{j_{ox} - j_{red}}{nF} = \frac{j}{nF} \tag{2.10}$$

Although both reactions take place at both electrodes, if r>0 then the oxidation reaction dominates and, if r<0, then reduction commands the net rate. In electrochemistry, an additional electrode potential relative to the equilibrium potential, i.e. beyond the thermodynamic requirement, is needed to drive reactions at a certain rate. The magnitude of the deviation of the potential (E) from the equilibrium value ($E_{eq.}$) is known as *overpotential*:

$$\eta = E - E_{eq.} \tag{2.11}$$

If the electrode is polarized to a greater potential than at equilibrium, η is positive and oxidation occurs. If instead the electrode is polarized to a smaller potential than at equilibrium, then η is negative and reduction takes place. Thus, application of an E greater than $E_{eq.}$, so that η>0, reduces the activation barrier of the oxidation ($\Delta G_{ox}^{\ddagger}$) by $(1-\alpha)F(E - E_{eq.})$ and that for the reduction increases by $\alpha F(E - E_{eq.})$. α represents how far the transition state is found along the reaction coordinate. Since the current density depends on the Gibbs free energy of the TS, α determines the dependence of the current density on overpotential. Hence, the value of α is between 0 and 1, being α=0.5 when the TS lies at the same distance from *Ox* and *Red* and, thus, j_{ox} and j_{red} have the same absolute value at the same overpotential. The origin of these factors is, however, beyond the scope of this thesis [29].

Under the application of an overpotential, the Gibbs free energies of activation for cathodic (reduction) and anodic (oxidation) reactions thus become:

$$\Delta G_c^{\ddagger} = \Delta G_{0,c}^{\ddagger} - \alpha F\big(E - E_{eq.}\big) \tag{2.12a}$$

$$\Delta G_a^{\ddagger} = \Delta G_{0,a}^{\ddagger} - (1-\alpha)F(E - E_{eq.}) \tag{2.12b}$$

bringing these expressions into the reduction and oxidation rate constants (Eq. 2.8) leads to:

$$k_{red} = Ae^{(-\frac{\Delta G^{\ddagger}_{0,c}}{RT})}e^{[-\frac{\alpha F}{RT}(E-E_{eq.})]} \tag{2.13a}$$

$$k_{ox} = Ae^{(-\frac{\Delta G^{\ddagger}_{0,a}}{RT})}e^{[\frac{(1-\alpha)F}{RT}(E-E_{eq.})]} \tag{2.13b}$$

where $\Delta G^{\ddagger}_{0,c}$ and $\Delta G^{\ddagger}_{0,a}$ are the activation Gibbs free energies of the TS when the reaction is at equilibrium (i.e. no overpotential). Since at equilibrium the net current is 0 (η=0 and $E = E_{eq.}$) and both oxidation and reduction rate constants have the same value, Eq 2.13a and 2.13b can be written as:

$$k_{red} = Ae^{(-\frac{\Delta G^{\ddagger}_{0,c}}{RT})} = k_0 \tag{2.14a}$$

$$k_{ox} = Ae^{(-\frac{\Delta G^{\ddagger}_{0,a}}{RT})} = k_0 \tag{2.14b}$$

where the constant k_0 is the standard rate constant, which brings all the non-electrochemical terms together.

Accordingly, if we merge Eq. 2.10. 2.11 and 2.13, we can now write an equation relating the electrode potential (E) to the observed current density (j) as:

$$j = j_{ox} - j_{red} = nF[c_{red}k_{ox} - c_{ox}k_{red}] = nFk_0[c_{red}e^{\left(\frac{(1-\alpha)F\eta}{RT}\right)} - c_{ox}e^{\left(-\frac{\alpha F\eta}{RT}\right)}] \tag{2.15}$$

Even though $j = 0$ at the equilibrium potential, the oxidation and reduction current densities are not. The oxidation and reduction current densities just add together to yield 0 since they are equal in magnitude. The value of the oxidation (and reduction) current density is called the exchange current density (j_0), which is the current at zero overpotential and, from Eq. 2.15, it can be written in terms of either reduction or oxidation as:

$$j_0 = j_{ox} = j_{red} = nFk_0c_{red}e^{\left(\frac{(1-\alpha)F\eta}{RT}\right)} = nFk_0c_{ox}e^{\left(-\frac{\alpha F\eta}{RT}\right)} \tag{2.16}$$

As a pre-exponential factor, the j_0 greatly determines the overall kinetics, with large values of j_0 indicating that high current densities are already reached at small overpotentials and thus fast electrode kinetics. Inserting Eq. 2.16 into Eq. 2.15 leads to the Butler-Volmer reaction for $n = 1$ reactions:

$$j = j_{ox} - j_{red} = j_0[e^{\left(\frac{(1-\alpha)F\eta}{RT}\right)} - e^{\left(-\frac{\alpha F\eta}{RT}\right)}] \tag{2.17}$$

which show that anodic and cathodic current densities will increase or decrease exponentially with overpotential and the slope will depend on α.There are two limiting cases in the Butler-Volmer equation (Fig. 2.2a):

A) The low overpotential region ($|\eta|$ < ca. 10 mV):

At such small values of η, the exponents in Eq. 2.17 are small enough to allow for the expansion of both exponential terms according to $e^x \approx 1+x$ for very small x. We can thus linearize the exponential terms to obtain:

$$j = j_{ox} - j_{red} = j_0 \left[1 + \frac{(1-\alpha)F\eta}{RT} - \left(1 - \frac{\alpha F\eta}{RT}\right)\right] = j_0 \frac{F\eta}{RT} = \eta R_{ct} \qquad (2.18)$$

where $R_{ct} = j_0 F/RT$, the charge-transfer resistance. Hence, in this region, a linear current-voltage dependence in the form of Ohm's law is found, which can be used to determine the exchange current density.

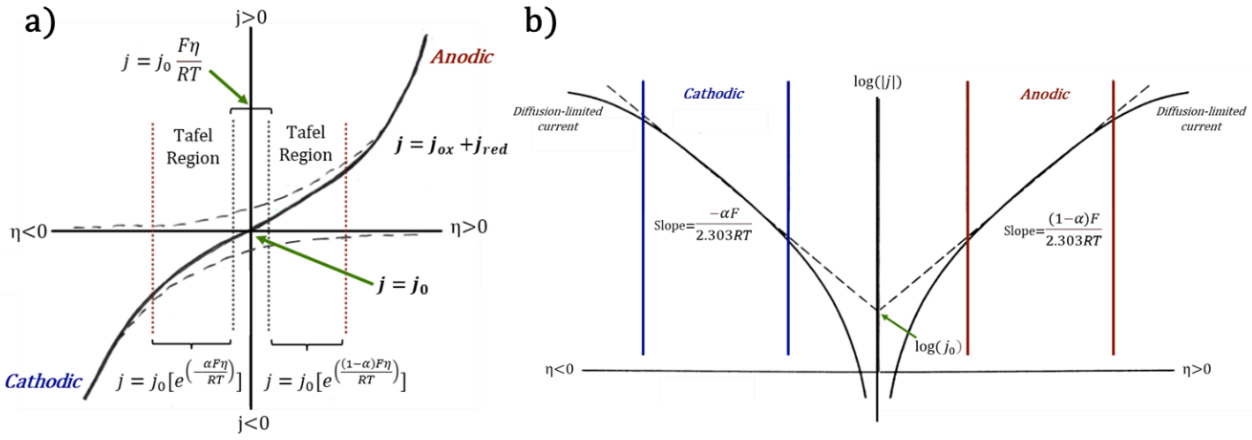

Figure 2.2 (a) Current-overpotential curve for a system with one electron transfer (n=1) and α=0.5 with the two regions for the limiting cases of the Butler-Volmer equation and **(b)** Tafel plots for anodic and cathodic branches for the same system. Adapted from [29].

B) The high overpotential region ($|\eta|$ > ca. 100 mV):

For large values of $|\eta|$, one of the partial current densities dominates so that the opposite reaction in Eq. 2.17 becomes small enough to be considered negligible. The two possibilities are:

B.1) Cathodic currents dominate:

Then $\eta \ll 0$ and thus: $j \approx j_{red}$ and $j_{ox} \approx 0$, leading to: $j = j_0[e^{\left(-\frac{\alpha F\eta}{RT}\right)}]$ (2.19a)

B.2) Anodic currents dominate:

Then $\eta \gg 0$ and thus: $j \approx j_{ox}$ and $j_{red} \approx 0$, becoming: $$j = j_0 \left[e^{\left(\frac{(1-\alpha)F\eta}{RT}\right)} \right] \quad (2.19b)$$

Taking logarithms to the base 10 in Eq. 2.19a and 2.19b, we can write:

$$\log(j) = \log(j_0) - \frac{\alpha F \eta}{2.303RT} \quad (2.20a)$$

$$\log(j) = \log(j_0) + \frac{(1-\alpha)F\eta}{2.303RT} \quad (2.20b)$$

for cathodic and anodic currents respectively. If we want to express Eq. 2.20a and 2.20b in terms of overpotential then, at for instance high cathodic currents, it becomes:

$$(cathodic) \qquad \eta = \left(\frac{2.303RT}{\alpha F}\right)\log(j_0) - \left(\frac{2.303RT}{\alpha F}\right)\log(|j|) \quad (2.21a)$$

$$(anodic) \qquad \eta = \left(\frac{2.303RT}{(1-\alpha)F}\right)\log(j_0) - \left(\frac{2.303RT}{(1-\alpha)F}\right)\log(|j|) \quad (2.21b)$$

These equations can also be written in the form of:

$$\eta = A + B\log(|j|) \quad (2.22)$$

which is known as the Tafel equation, which also gives name to the Tafel region (Fig. 2.2a), This equation expresses how the current varies exponentially with overpotential. By plotting $\log(|j|)$ vs. η, we can extract the α from the slope of the plot and the value of j_0 from the intercept with the ordinate (Fig. 2.2b).

As shown in Fig. 2.2b, the current-overpotential plots deviate sharply from linear behavior as η approaches zero. The deviation from linear behavior arises because the back reactions cannot be considered negligible and thus the reaction cannot longer be treated as irreversible. On the other hand, at high values of η, the net current density reaches a limiting value because the reaction rates become limited by diffusion of reactants to the electrode. Hence, transport of reactants to the electrode surface where the charge transfer takes place is of crucial importance for heterogeneous electron transfer reactions [28–30].

2.3 The Electrochemical Double Layer

The charge transfer processes that give rise to the current are governed by the properties of the interface formed by a charged electrode surface immersed in an electrolyte, which influences the electrochemical response of the electrolyte/electrode system. Aqueous

electrochemical interfaces differ from other interfaces in that they are governed by potential-dependent interactions between water molecules and species found in the so-called *electrical double layer* (EDL) [31]. Two types of physicochemical interactions control the structure of the double layer in aqueous electrolytes: interactions between adsorbates and the electrode, which are chemical in nature (chemisorption and electron transfer), and electrostatic metal-ion forces that attract ions in the vicinity of the electrode but do not involve metal-adsorbate bonding. The first layer, governed by chemical interactions, is a two-dimensional surface with a non-zero electric charge (either positive or negative depending on the applied potential) and it is known as the *Helmholtz layer*. The second layer, which arises from long-range Coulombic forces, is made of free solvated ions whose movement is driven by electrostatic attractions and is called the *diffuse layer*. These two regions at the electrode/electrolyte interface form the double layer (Fig. 2.3, top) [32,33].

Since the conception of the EDL in the 19th century, many researchers have refined the model developed by Helmholtz in order to describe the fundamentals of the EDL. However, nowadays the Goüy-Chapman-Stern model (GCS) is the most commonly used model to explain simplistically the structures involved in the EDL [34]. In this model, the EDL is divided into the same two layers explained above, but they incorporated the electric potential response as a function of distance from the electrode surface: a first layer formed by ions of opposite charge to those on the electrode in which the potential drop is linear, and a second layer of solvated ions after which the potential decreases exponentially (Fig. 2.3, bottom) [29].

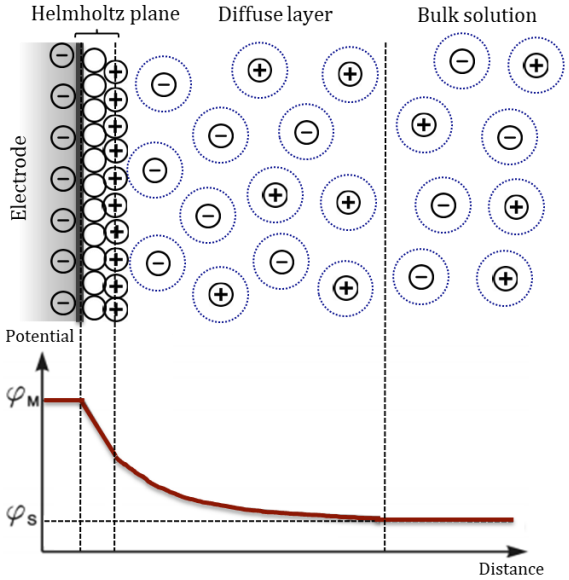

Figure 2.3 Schematic illustration of the structure (top) and potential distribution (bottom) of the electrical double layer according to the Goüy-Chapman-Stern model. ϕ_M and ϕ_S represent the metal and solution electric potentials respectively [33].

Although the EDL is always composed of two layers, the charge of the ions in the vicinity of the electrode surface depends on the electrode potential. If a potential is applied across an electrolyte (i.e. between two electrodes), the ions in the electrolyte migrate along the electric field, resulting in the polarization of the electrolyte and the build-up of the EDL at each electrode. If the potential is reversed, the electrodes will switch over their charge and ions will migrate towards the opposite electrode. However, at short timescales the ions do not have time to move from one electrode to the other and the electrolyte acts like a dielectric material with a uniform potential drop over the electrolyte. With a continuous change of the electrode potentials, the EDLs build-up along the interface and the potential drop becomes more pronounced within the EDL. At longer timescales, if a constant changing potential is applied long enough to establish a steady state condition, the potential drop will become completely concentrated at the EDLs, where the electric field is very high [28,33]. Thus, the double layer behaves as a conventional capacitor, in which the stored electrical charge is linearly dependent on voltage. The electrical double layer capacitance is given by:

$$C = \frac{\partial Q}{\partial E} \tag{2.23}$$

where Q is the charge stored (C), E the potential applied (V) and capacitance is usually measured in μF/cm^2. Applying a potential difference in an electrode/electrolyte system results in charge accumulation within the electrical double layer, which gives rise to non-Faradaic (capacitive) currents [28].

2.4 Transport

As explained in the previous sections, the faradaic current generated is a direct measure of the rate of the electrochemical reaction taking place at the electrode surface, which depends on the applied potential. Furthermore, the current itself is dependent upon two rates [35]:

(i) the rate at which electrons transfer occurs across the interface between the electrode and the solution, known as *charge transfer* rate.
(ii) the rate at which reactants are provided from the bulk solution to the electrode and products removed from the electrode, known as *mass transport* rate.

As in any other chemical reaction influenced by its kinetics, the slowest of these rates will determine the rate of the overall reaction. Thus, both mass transport and charge transfer rates will dictate the concentrations of the reactants (O) and products (R) at the electrode surface, which at the same time are dictated by them (Fig. 2.3).

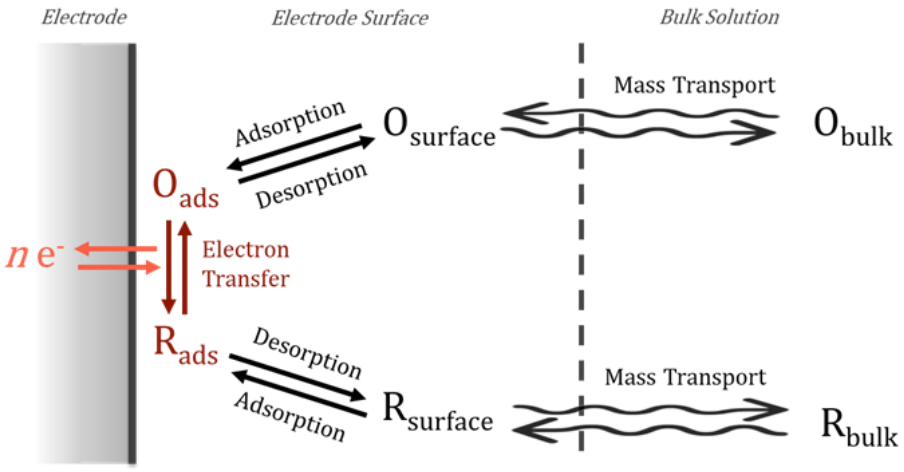

Figure 2.3 Schematic illustration of the different steps during an electrochemical reaction as a function of the distance from the electrode surface.

Charge Transfer

Although the term *charge transfer* is used in electrochemistry to refer to electron transfer processes at the electrode, in galvanic cells this term is often used to denote both the flux of electrons within the electrode and the flux of ions in the electrolyte. This rate is governed by the applied potential across the electrodes, as evidenced by the proportionality between potential and current derived in the preceding section.

In electrochemical systems, such as fuel cells, the voltage responsible for the charge transfer represents a loss which obeys Ohm's law (i.e. Ohmic loss): $V = iR$. This Ohmic loss depends on both the current that flows through the electrode and the resistance of the conducting media (e.g. electrolyte for ions). Hence, the total voltage loss in an electrochemcial system is the summation of all Ohmic resistances, including electrodes and electrolyte resistance. However, for the majority of systems, the ionic conductivity in the electrolyte is generally the major contributor to the Ohmic resistance. The overall Ohmic resistance can be mitigated by: i) using electrolytes with high ionic conductivity, ii) using highly conductive electrodes, and iii) reducing the distance between electrodes [30,35,36].

Mass Transport

Since the generation of current needs the constant addition of reactants and constant removal of products, the transport of these from the bulk solution to the electrode surface is essential for any electron transfer reaction. There are three basic mechanisms of mass transport:

a) *Diffusion*: random movement of molecules driven by the concentration gradient between a region of high concentration of molecules and a region with low

concentration. The rate of diffusion therefore depends on the concentration gradient and on the diffusion coefficient, which has the dimension of the media where diffusion takes place.

b) *Migration*: movement of charged particles (e.g. protons) in response to an electric field. It depends on the applied potential and is proportional to the charge of the ions, their diffusion coefficient and the ion concentration.

c) *Convection*: forced movement of the species in solution by an external mechanical force, e.g. stirring.

Although the utilization of the Butler-Volmer equation (Eq. 2.17) in electrochemistry is broad, it assumes that the concentrations at the electrode surface are the same as that of the bulk solution. In this way, by assuming that the charge transfer is much faster than mass transport, current can be expressed only in terms of potential. However, concentrations of reactants and products can be incorporated in the Butler-Volmer equation and thus obtain current as a function of both the bulk and surface concentrations, which in turn depend on the potential as well. Hence, mass transport effects may also be taken into account in the extended Butler-Volmer reaction [28,35]:

$$j = j_0[\frac{c_O(0,t)}{c_O^*}e^{\left(\frac{(1-\alpha)F\eta}{RT}\right)} - \frac{c_R(0,t)}{c_R^*}e^{\left(-\frac{\alpha F\eta}{RT}\right)}] \tag{2.24}$$

where c_O^* and c_R^* are the bulk concentrations of the species to be oxidized and to be reduced respectively and $c(0,t)$ is the time-dependent concentration at a distance 0 from the electrode surface. In this form, the Butler-Volmer equation expresses the concentration dependence of the current, which becomes entirely dependent on mass transport when the electron transfer rate is very fast (i.e. O and R are being converted at a faster rate than their mass transport rate to the electrode). This current is known as the *limiting current density* (j_L) and relates to the concentration of O/R by:

$$c(0,t) = c^*\frac{j_L - j}{j_L} \tag{2.25}$$

Eq. 2.22 can now be written as a function of the limiting current:

$$j = j_0[(1 - \frac{j}{j_{ox,L}})e^{\left(\frac{(1-\alpha)F\eta}{RT}\right)} - (1 - \frac{j}{j_{red,L}})e^{\left(-\frac{\alpha F\eta}{RT}\right)}] \tag{2.26}$$

where $j_{ox,L}$ and $j_{red,L}$ correspond to the anodic and cathodic limiting current densities.

2.5 Electrochemical Methods

There are many experimental designs and methods to study electrical and chemical transport properties by means of potential, current or charge. These are often classified into either *static* methods, in which there is no current flowing between electrodes, and *dynamic* methods, in which current passes and concentrations change as a result of a redox reaction at the solution-electrode interface. Dynamic methods can be further subdivided into: i) measuring potential while controlling current or ii) measuring current under potential control. As this thesis delves into the study of electrochemical reactions taking place at fuel cell electrodes, only dynamic methods with potential control will be considered [29,35].

Most dynamic electrochemical techniques in which current is measured are carried out using a potentiostat to control the voltage difference between electrodes in an electrochemical cell, in which the controlled variable is the cell potential and the measured variable is the cell current. This cell typically contains three electrodes:

i) *Working electrode* (WE), in which the reaction to be studied is occurring.

ii) *Reference electrode* (RE), through which no current flows and whose potential remains constant. Since no current flows through it, it is used to measure the electrode potential.

iii) *Counter electrode* (CE), which completes the electric circuit and through which current is allowed to flow. It is usually an inert conductor like platinum or graphite.

By measuring the resulting current when applying a varying potential between the working and reference electrode, the reduction potential of an analyte and its electrochemical reactivity can be revealed. Thus, in this section, electrochemical techniques used for the study of mechanistic, kinetic and structural properties of electrodes will be discussed.

Cyclic Voltammetry

In voltammetry, a time-dependent potential is applied linearly to the WE (changing its potential relative to the stable potential of the RE) and the current that flows between the WE and CE is measured. In cyclic voltammetry (CV), after the limit potential is reached, the WE potential is ramped in the opposite direction to return to the initial potential, repeating this cycle as many times as needed. By convention, negative currents obtained in the region where potential is scanned negatively (i.e. towards negative potentials) are known as *cathodic* currents (reduction) and, positive currents generated by scanning positively are known as *anodic* currents (oxidation) The current measured

between WE and CE is then plotted versus the applied potential at the WE to give a cyclic voltammogram. The CV parameters that are under the control of the experimenter are: i) the lower and upper potential limits (E_1 and E_2 in Fig. 2.3) and the direction of the initial scan, ii) the potential scan rate (ν), i.e. the rate of potential change over time and iii) number of cycles.

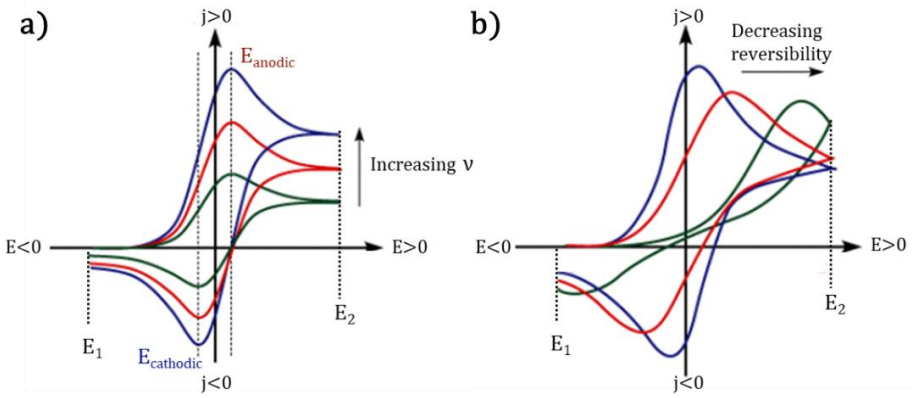

Figure 2.3 Typical cyclic voltammetry for (a) a reversible and (b) a kinetically slow redox reaction couple.

CV provides a rather fast qualitative interpretation of a redox reaction without need for any calculations. However, in order to gain the knowledge needed for the correct interpretation of the electrochemical process, the following parameters should be properly monitored:

a) Number of peaks in the forward and reverse scans, with each peak corresponding to current generation through an electron transfer process (i.e. faradaic current).

b) The shape of the peaks, which, among other experimental factors, depend on whether convection is included in mass transport or not. In the absence of external stirring, the current will pass through a maximum and will thereafter decrease as the concentration of analyte on the electrode surface is depleted. Conversely, in the case of a continuous supply of reactants to the electrode by convection, the current will increase as a response of the applied potential until it reaches a limiting current, thereby showing a current plateau.

c) Peak potentials, which indicate the potential at which the reaction occurs. In the case of a reversible redox reaction, the cathodic and anodic peak positions are similar (Fig. 2.3a). If instead the redox is not reversible, the cathodic and anodic peaks are found at different potentials (Fig. 2.3b).

d) Peak current densities, which are proportional to the charge being transferred during an electrochemical process.

e) Difference between cycles, since different behavior through cycling between E_1 and E_2 relates to the nature of the electron transfer reaction, e.g. formation of a monolayer.

Cyclic voltammograms are presented in a form that allows the rapid qualitative interpretation of a current-generating process. Thus, the insights gained from a CV may immediately be used in the design of the next experiment, for instance, a polarization curve [28,30,35].

Polarization Curves

Although polarization curves can be plotted in numerous ways, the most common representation follows the same principle as the cyclic voltammetry: current vs. applied potential. Since by changing the overpotential, the free energy barrier of a given electron transfer reaction is either lowered or raised, they are often obtained by recording the current density as a function of the overpotential. They are determined after the open-circuit electrode potential, i.e. potential at which there is no current, has reached a steady-state value. Then, by recording the current generated when a potential that differs from the equilibrium potential is applied, a polarization curve is obtained [29,37].

Electrochemical Impedance Spectroscopy

Like resistance, impedance is a measure of the ability of an alternating current circuit to resist the flow of electrical current. In electrochemical impedance spectroscopy (EIS), the impedance of the circuit of the electrochemical cell is measured by applying an AC potential and measuring the current through the cell. Although there are many interpretations of EIS data, a common analysis is carried out by interpreting the Nyquist plot, which plots the real and imaginary parts of the impedance. The uncompensated resistance (i.e. solution resistance, R_u) of the cell can be found from the Nyquist plot at the high frequency intercept and the charge transfer resistance (R_{ct} in Eq. 2.18) can be obtained from the difference between the high frequency intercept and low frequency intercept [29,30].

3. Catalysis

By the end of the 18th and the beginning of the 19th centuries, experimental data across the globe relative to the modification of chemical reactions by the presence of small amounts of foreign substances was enough to indicate a common, but then unknown, theme [38]. The explanation of this phenomena was first proposed by Jöns Jakob Berzelius in 1835, who established the relation between the otherwise disparate studies [39]. He described those reactions in a frame outside the theory of chemical affinity and termed the process as *catalysis*, a term derived from Greek meaning down (*kata*) and loosen (*lyein*) [40]. These early experimental observations were the genesis of what we know now as the field of catalysis, which endorses many of the chemical processes conducted by modern civilization [41]. In fact, approximately 35% of world's GDP relies on catalysts [42]. Examples of these applications are commonplace in everyday life, from catalytic converters in the exhaust of vehicles to mitigate pollution, to catalysts in ammonia synthesis for fertilizer production to increase global food production [43,44].

Nowadays we have a somewhat clearer understanding of how a catalytic process works, which the IPUAC describes as: '*A substance that increases the rate of a reaction without modifying the overall standard Gibbs energy change in the reaction; the process is called catalysis'* [45]. In this way, any material which accelerates a chemical reaction without being consumed in the process is called a *catalyst* and, correspondingly, the process of converting substrate molecules to products using a catalyst is called *catalysis*. There are two key roles that catalysts play in chemical reactions: enhancing the reaction rate and increasing selectivity towards desired products. An enhanced reaction rate makes slow reactions more economically viable and improved selectivity reduces the energy required to separate a desired product from the reaction mixture. Thus, catalysis research is of crucial importance to improve the sustainability of chemical industries.

Depending on the phase at which a catalytic process occurs, catalysis is often subdivided in two groups: homogeneous and heterogeneous catalysis. Homogeneous catalysis entails those catalytic processes in which the catalyst and the reactants are dispersed in the same phase (usually gaseous or liquid). In heterogeneous catalysis, instead, the reaction components are at least in two phases. The present work is focused on heterogeneous catalysis, in particular reactions taking place at the solid-liquid interface.

3.1 Heterogeneous Catalysis

The vast majority of materials that we encounter in our day-to-day lives have been produced, at least partially, using catalytic processes. Most of the largest processes for industrial applications are based on heterogenous catalysis, which include crude oil cracking, methane steam reforming, ammonia synthesis, sulfuric acid production, polymerizations and water-gas shift reaction [46]. In fact, catalytic reactions are used in around 90% of the processes in chemical industry, most of which take place on heterogeneous catalysts [47]. These catalysts are not only used to increase the effectiveness of an industrial process, they also contribute to the environmental protection by lowering the energy needed to drive the chemical reactions, as well as reducing waste products that are harmful for the environment. Three-way catalysts are a very good example of the latter, which are used to remove NO, CO and hydrocarbons from the exhaust of combustion engine vehicles [46,48].

It is well known that the underlying mechanism behind the enhancement of a certain chemical reaction relies on its intermediate states. More precisely, catalysts increase the reaction rate by lowering the activation energy of a reaction (E_a). This is achieved by providing alternative routes to overcome to the potential energy barrier between reactants and products, which are energetically more favorable compared to the uncatalyzed reaction (Fig. 3.1). The preferred route involves the formation of lower energy transition states, which result in a decrease of the overall activation energy [47].

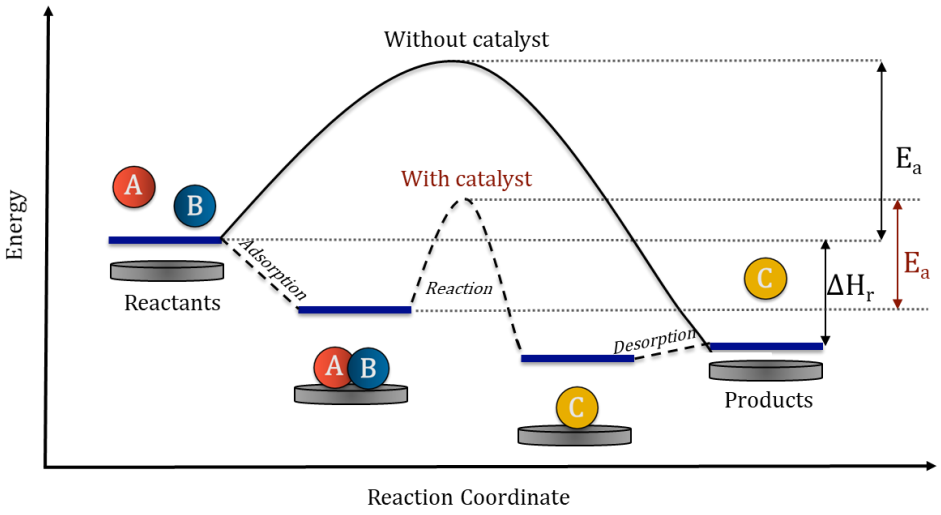

Figure 3.1 Energy diagram of an exothermic reaction of reactants A and B to produce C in the presence and absence of an heterogeneous catalyst, which changes the energy landscape by adding more favorable reaction pathways and thus lowering the activation energy (E_a).

Considering that most reactions in heterogeneous catalysis are between gaseous reactants on a solid surface, the catalyzed reaction can be broken down into four elementary steps:

adsorption of reactants on the catalyst, the diffusion of adsorbed species along the surface, the surface reaction and the desorption of the products back into the gas phase [47,49]. How fast each elementary step can proceed is determined by the activation energy.

The dependence of the reaction rate with the adsorption/desorption of reactants and products is given by the *Sabatier's principle*. This principle states that, if the interaction between catalyst and reactants is too weak, then the activation of the reactant would be the rate-determining step. On the contrary, a too strong interaction will make the adsorbed species unable to desorb from the catalyst surface, blocking the active sites and thus stopping other reactants from being adsorbed. In this case, the rate-determining step would be the regeneration of the catalyst surface [47,50]. This principle can be shown graphically by plotting the overall reaction rate against the adsorption energy, which leads to a triangle-shaped plot known as the Volcano plot (Fig. 3.2). The Volcano curve describes the relation between the interaction reactant-catalytic surface and the catalytic activity of a catalyst for a given reaction. A reaction catalyzed by those catalyst laying on the left part of the curve (strong adsorption) will be limited by the product desorption and those placed at the right (weak adsorption) will be limited by the adsorption of reactants. Thus, an ideal catalyst would be located at the top of the Volcano plot.

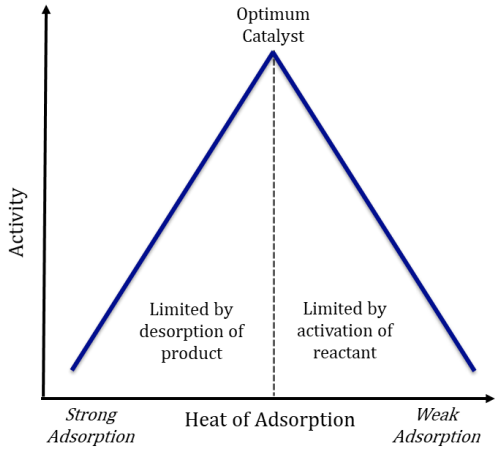

Figure 3.2 Typical Volcano plot representing the Sabatier principle [50].

The majority of heterogeneous catalysts are metals or metal oxides dispersed on an inert support that enhances the effectiveness and minimizes their cost. However, as some metals used in catalysis such as platinum are scarce, alloying is regarded as a good strategy for tailoring new inexpensive catalyst that could potentially improve the activity, selectivity and stability of the current scarce metals used in catalysis.

Alloying of different metals and metal oxides induces a change in the intrinsic catalytic properties of a material by two electronic effects: ligand and strain effects. The *ligand effect* is caused by the atomic vicinity of two dissimilar atoms that induces an electronic modification of the alloy components, resulting in a change of the binding energies of reactants and intermediates and thus a change in the catalytic activity [51,52]. On the other hand, the *strain effect* originates from the alteration of a metal lattice when metals with different atomic radii are alloyed together. The incorporation of a metal with a different radius results in either a compressed structure (compressive strain) or an expanded structure (tensile strain) [53,54]. In either case, a modification of the lattice structure results in a change of the electronic structure, whose extend and nature will be given by the difference in atomic radii between the alloy components. Although electronic effects have been demonstrated to be advantageous on tunning the binding energy of catalyst materials, it is usually very difficult to deconvolute the interplay between strain and ligand effects.

A useful model to predict trends in reactivity among alloys is the d-band model, which correlates the interaction strength of adsorbate-metal surface with the average energy of the d-electrons, that is, the d-band center [55]. This model is a convenient tool to describe the bond formation at a metal surface, which can be used to predict the origin of catalytic trends for transition metals in heterogeneous catalysis [56]. A transition metal surface has a continuum of energy levels with electrons filling the states from the lowest energy level until the highest occupied electronic level formed by the valence states of the surface atoms, i.e. the Fermi level. When adsorption on the metal surface takes place, the electronic states of the transition metal interact with the adsorbate energy levels, which can be divided into two interactions: the interactions with the s-band of the metal, and the d-band interaction. This gives rise to the formation of separate bonding and anti-bonding states, with the strength of the bonding depending on the electronic filling and the orbital overlap. Filled antibonding states will results in a weak bond and vice versa. At the same time, the splitting of the bonding and anti-bonding states depends on the energy of the d-band center (ϵ_d) relative to the energy of the adsorbed species (ϵ_a). The closer the d-band center is to the adsorbates energy, the larger is the splitting (Fig. 3.3). However, since the strength of the metal-adsorbate bond also depends on the overlap between the orbitals, it will also depend on the metal structure [55,57]. Based on this so-called d-band model, the d-band center of the metal can be used to predict changes in adsorption strength upon, for example, alloying, and thus the adsorption strength can be adjusted.

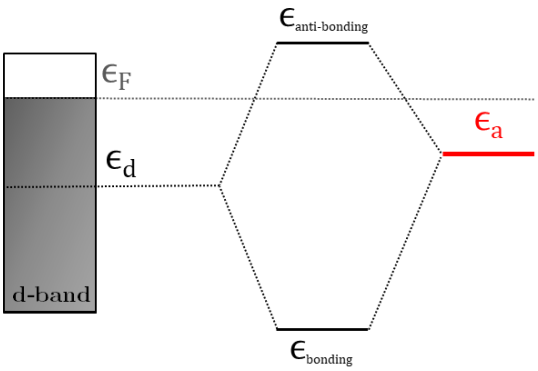

Figure 3.3 Schematic model regarding the whole d-band located at its center and interacting with an adsorbate, together with the resulting bonding and anti-bonding states.

3.2 Electrocatalysis

In electrochemistry the reactants are adsorbed at the surface of the electrode where the electrochemical reaction occurs. Electrocatalysis can be seen as the heterogeneous catalysis of electrochemical reactions, which occur at the electrode–electrolyte interface and where the electrode plays both the role of electron donor/acceptor and of catalyst. The activation energy in electrochemical processes is related to the potential, at which the reaction takes place. Thus, electrocatalysts usually enhance the reaction rate by changing the potential at which oxidation and reduction are observed. Moreover, since electrochemical reactions occur when electrons are passed from one chemical species to another, the potential at which those reactions occur highly depend on the favorable interactions at the electrode surface.

As many other catalysts, the development of electrocatalysts is based on the optimization of three key factors that determine their performance [58]:

i) *Activity*, which is evaluated by how much current density is generated at a given potential, as described in Eq. 2.22.
ii) *Selectivity*, which is evaluated by comparing the response of the electrocatalyst to a desired analyte with the response to others.
iii) *Stability*, which is assessed qualitatively by their ability to withstand potentials at which reactions occur, as well as fast potential changes.

The three figures of merit mentioned above, together with cost and abundance, are the most important parameters taken into account when searching for a better electrocatalyst. The electrocatalyst research involves finding better materials that could potentially improve the efficiency of the main processes that they are used for, such as water splitting [59], fuel cells [60] and electrochemical carbon dioxide reduction [61].

4. Hydrogen Fuel Cells

Modern society will face severe challenges if our lifestyle does not shift away from the use of fossil fuels to meet the ever-growing energy demand. There is no doubt that GHG emissions are responsible for several serious environmental issues, which manifests the need for harness carbon-free renewable energy sources. Many alternatives have been proposed to take over the highly efficient conventional combustion engines, but only a few represent a stable, cost-effective and efficient candidates for energy generation. Among all those alternatives, fuel cells have emerged as a promising competitor to combustion engines because of their high operating efficiency, environmental-friendly operation and the range of fuels that they can use. Thus, fuel cells are energy converters that could potentially provide a highly efficient energy generation, either at the point of use or on a large scale. However, an energy system based on renewable energy sources must have a storage to match generation and consumer demand. Hence, combination of water electrolysis, H_2 storage and fuel cells could provide a solution to this issue.

Fuel cells electrochemically convert the chemical energy stored in fuels (e.g. H_2) directly to useful electricity. As opposed to combustion engines, fuel cells convert chemical energy directly into electrical energy without the need of mechanical work generation. Moreover, electricity is produced as long as fuels and oxidants, that are stored externally to the cell, are supplied, which is their main difference with batteries. Besides the advantages stated above, fuel cells also present the following assets over other power generation systems [15,62–64]:

- High energy density and high operating energy efficiency, which can attain over 60%.
- Scalable production to a range of sizes.
- Environmental-friendly due to absence of GHG emissions (in case of using green hydrogen as a fuel). If green hydrogen is used as a fuel and oxygen as an oxidant, emissions are only water.
- Ease of hydrogen refueling - almost immediate recharge capability.
- Quality of power generated does not degrade over time.
- Manageability: lighter, compact and no moving parts, which makes them very suitable long operating periods.
- More silent energy production.

Nevertheless, fuel cells currently present technical limitations that are yet to be overcome [15,64,65]:

- Safety and cost issues related to hydrogen storage.
- Most of used hydrogen still comes from fossil fuels (grey hydrogen)
- Lack of infrastructure to support hydrogen distribution, impeding the wide availability of hydrogen.
- Most of currently available fuel cell technology still in a prototype stage.
- Expensive fuel cell production (primarily attributed to the cost of the catalyst layer and its application), which should be reduced to 35 $/kW for automotive applications by 2025 [16].
- Reliability and durability of fuel cell systems still far from 2025 target (8000 h durability in automotive load cycles) [16].
- Specific power density and peak energy efficiency still need improvement if DOE target is meant to be met (900 W/Kg power density and 65 % efficiency) [16].

In this chapter, an introduction to fuel cell technology is given and a glimpse of their history is provided. The basic thermodynamic principles under which fuel cells operate are also explained and the different types of fuel cells are briefly described. Parameters influencing fuel cell performance are then discussed, followed by a description and comparison of the two main low-temperature hydrogen fuel cells: PEMFCs and AEMFCs. Lastly, the current status of the electrocatalysts used in these two types of fuel cells is presented, as well as the state-of-the-art of this technology.

4.1 History

It is no surprise that fuel cell history comes hand in hand with the history of electrochemistry explained in Section 2.1. After the discovery of electrolysis in 1800 and the postulation of Faraday's laws of electrochemistry in 1834, Sir William Grove took the idea of electrolysis in reverse back in 1838 [66]. He discovered that, by placing two platinum electrodes with one end immersed in a beaker with sulfuric acid and each of the other ends sealed in glass tubes containing H_2 and O_2, a constant current flowing between the two electrodes was observed [67]. Over time, Grove noticed that the reaction was consuming both gases as the current flowed. A few years later, he created what he called a "gaseous battery" by combining 26 pairs of tubes in a series circuit, which made him earn the title of "father of the fuel cell". Ironically, this discovery took place at roughly the same time as the first combustion engines were developed [67,68].

During the upcoming years, several insights on the theoretical understanding of how fuel cells operate were provided by several scientists, including Friedrich Ostwald. However, it took over one hundred years after Grove's discovery before fuel cells were used in applications. Beginning in the late 1930s, F.T Bacon made great advances in alkaline hydrogen fuel cells, which ended up being used for the Britain's Royal Navy submarines during World War II [69]. Although they were very costly, they quickly attracted attention and Bacon's fuel cell was licensed to provide on-board power for the Apollo spacecraft in the mid-1960s. Improvements in fuel cells efficiency and cost were made in dribs and drabs until the 1990s, when environmental concerns regarding the use of fossil fuels for power generation started emerging [68,69]. This growing awareness of environmental and sustainable issues with the usage of a finite and polluting source of energy is what catalyzed the development of hydrogen fuel cell technologies, which has continued to grow until the time being.

4.2 Principle and Thermodynamics

In a low-temperature hydrogen fuel cell, hydrogen is electrochemically oxidized at the anode electrode, which generates electrons. These electrons flow through an external circuit to the cathode electrode, where oxygen is supplied, usually through air, and reduced to eventually form water as a waste product [37]. The overall reaction for a hydrogen fuel cell is:

$$H_2 + \frac{1}{2}O_2 \longrightarrow H_2O \tag{4.1}$$

As the enthalpy of water is lower than the combined enthalpy of the reactants, the reaction is exothermic, thereby producing heat as the only by-product (besides water).

Electrons produced in the anodic electrode are forced to pass through a circuit where they are used to perform electrical work before they are used to reduce oxygen at the cathode. Electricity is therefore generated directly from the electrochemical reaction. However, the two half-cell reactions must be physically separated and electrons must be forced to get through the external circuit to produce an electric current. The spatial separation is achieved by using an electrolyte, whose nature will dictate the operating temperature of the fuel cell. The particularity of the electrolyte is that it allows the conduction of ions but not electrons, which prevents the redox reaction to take place without electrons flowing. The nature of the ions being conducted through the electrolyte (H^+ or OH^-) will depend on the media in which the half-cell reactions take place (i.e. alkaline or acid), which in turn are also governed by the media in which they occur. Thus, the mechanisms of the anode and cathode reactions will be determined by the pH

of the electrolyte [70]. These half-cell reactions are known as hydrogen oxidation reaction (HOR) and oxygen reduction reaction (ORR) respectively. The features of these reactions in acid and alkaline media will be extensively discussed in the upcoming sections of this chapter.

The electrical energy generated from the overall fuel cell reaction depends on the chemical energy of the same reaction. According to thermodynamics, the maximum amount of chemical energy of any system that can be converted into energy (electricity in this case) is given by the change in Gibbs free energy (ΔG):

$$\Delta G = \Delta H - T\Delta S \tag{4.2}$$

Thus, the balance between the enthalpy of the reaction (ΔH) and the minimum heat necessary for entropy production ($T\Delta S$) will determine if the reaction can take place spontaneously ($\Delta G < 0$), if it is in equilibrium ($\Delta G = 0$) or if another driving force is needed ($\Delta G > 0$). Since the fuel cell energy conversion implies the energy generation without the need of any external work, fuel cells -together with batteries- will only involve spontaneous reactions.

From a thermodynamic point of view, it could be mentioned that if all the chemical energy released from a reaction is converted into electrical energy, the efficiency would be 100 %. Nonetheless, not all the chemical energy is used to generate current. The maximum thermodynamic efficiency is therefore used as a theoretical reference point for comparing efficiencies. This parameter is defined as the ratio between the maximum energy available and the total energy of the reactants. Thus, for ideal processes:

$$\eta_{FC} = \frac{\Delta G^o}{\Delta H^o} \tag{4.3}$$

For the hydrogen-oxygen fuel cell, the enthalpy change of the overall process is -2.86 $\cdot 10^5$ J/mole of H_2O formed, which leads to a maximum thermodynamic efficiency of 83% [71]. This efficiency is obviously never reached in practice, so the real energy efficiency must be used instead.

The effectiveness of the fuel cell in converting chemical into electrical energy is reflected by the cell voltage:

$$\Delta E = \Delta E_{cell} - \eta_a - \eta_c - iR \tag{4.4}$$

where η_a and η_c are the anodic and cathodic overpotentials and the final term corresponds to the iR drop through the cell. ΔE_{cell} is the difference in equilibrium potentials of the anode and cathode reactions, as described in Eq. 2.2. As the

overpotentials and iR drop must be regarded as inefficiencies lowering the fraction of energy effectively converted, the electrochemical fuel cell efficiency can be written as:

$$\epsilon_{FC} = \frac{maximum\ power\ obtained}{maximum\ power\ possible} = \frac{\Delta E}{\Delta E_{cell}} \tag{4.5}$$

4.3 Fuel Cell Components

In this section, the basic components of a single fuel cell will be explained. For the operation of hydrogen fuel cells, basic components are needed to facilitate the following:

- Fuel and oxidant feeding to the anode and cathode, respectively.
- Electrical charge flow through an external circuit.
- Prevent direct mixing of hydrogen and oxygen.
- Dissipation of heat released during operation.
- Water removal from the cell to ensure an efficient performance.

In order to successfully carry out the operations stated above, the basic components of hydrogen low-temperature fuel cells are: electrolyte, gas diffusion layer, catalyst layer and bipolar plates (Fig. 4.1) [37].

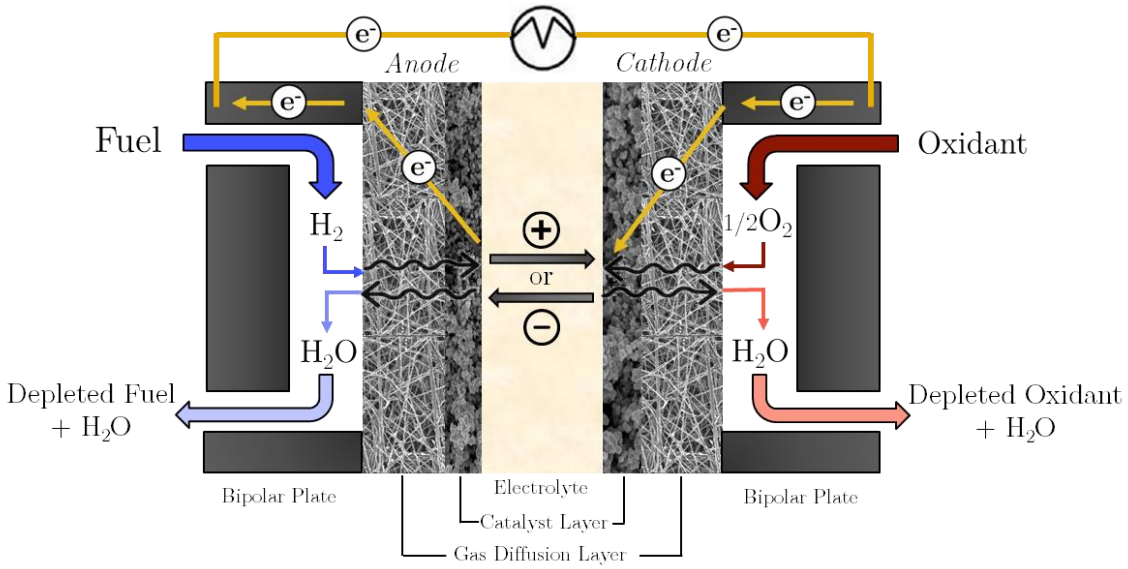

Figure 4.1 Schematic illustration of a single low-temperature hydrogen fuel cell.

In a typical fuel cell, oxidant (often oxygen from air) and fuel (e.g. hydrogen) are fed continuously to the cathode and anode, respectively. Electrochemical reactions take place at the electrodes to produce an electric current through an external circuit. Thus, on the contrary to batteries, fuel cells produce power as long as fuels are supplied. Among all the areas in a fuel cell where a process occurs, the tiny area at which the actual redox

takes place is most likely the most crucial part. This portion of the cell is found where the electrolyte, the electrode and the catalyst sites meet and thus the starting point of all the energy conversion processes. It is named the Three Phase Boundary (TPB) and it must fulfill the following conditions: i) be exposed to the reactant, ii) be in electrical contact with the electrode, iii) be in ionic contact with the electrolyte, and iv) must contain enough catalyst exposed for the reaction to proceed at the desired rate.

The Electrolyte

For all types of fuel cells, the electrolyte constitutes an indispensable component. In fact, the type of electrolyte used determines the name given to a certain fuel cell. The electrolyte not only transports reactants to the electrode but also conducts ionic charge between the electrodes and thus maintain the electroneutrality of the system. Moreover, it also provides a physical barrier to prevent the fuel and oxidant from directly reacting with each other. The desired properties of the electrolyte are therefore: i) high specific ionic conductivity, ii) high electronic resistivity and iii) low reactant permeability [37,70].

There are mainly two types of electrolytes based on their phase: liquid and solid electrolyte. For the low-temperature hydrogen fuel cells considered in this thesis, only polymer membrane electrolytes will be taken into account. These membranes are semipermeable, generally made from ionomers and they are designed to conduct either protons (acid media) or hydroxides (alkaline media) when they are hydrated. Thus, polymeric membranes should be both mechanically and chemically resistant, as well as possess a high water intake [70].

The Gas Diffusion Layer (GDL)

Besides reactants and the ionic conducting medium, a surface for the electrochemical reaction to take place is of crucial importance for the correct operation of the fuel cell. The role of the gas diffusion layer (GDL) will therefore be determined by its specific area, which is, in fact, the number of pores engineered. The GDL plays an essential role inside a fuel cell, namely:

- Even distribution of hydrogen and oxidant to the catalyst layer.
- Proper conduction of electric current
- Effective removal of products generated in the redox reaction.
- Efficient water removal to avoid water flooding.

In order to fulfill the requirements above, a GDL must possess the following features: i) high electronic, ionic and heat conductivity; ii) high corrosion resistance and iii) porous material to ensure proper mass transport. For the latter, carbon cloth or paper are

usually chosen as a GDL material, which are also sulphonated to provide hydrophobicity for the correct water removal [37,70].

The Catalyst Layer

The catalyst provides active sites which serve as a platform for the correct occurrence of the two half-cell reactions. The electrocatalysts must provide a high catalytic activity and stability under fuel cell conditions in order to maintain a high reaction rate and thus the desired power output. For this, the requirements that the catalyst layer should fulfill are:

- Large surface area to ensure proper contact in the TPB.
- Proper dispersion to maximize exposed active sites.
- Suitable porosity to ensure proper mass transport.
- Tolerant towards impurities that could potentially poison the catalyst.
- Support with a large area and high electric conductivity.
- High corrosion resistance.

For low-temperature fuel cells, only a few relatively rare and expensive materials provide sufficient electrocatalytic activity, and so such catalysts are deposited in small quantities and properly dispersed to maximize the catalyst utilization. For fuel cells using a polymeric membrane as electrolyte, an ionomer is often added to the catalyst layer to guarantee the ionic transport of reactants and products at the TPB [37,70].

Bipolar Plates (BPs)

In order to achieve a higher voltage and power, individual fuel cells are assembled in series forming a fuel cell stack. Bipolar plates (BPs) are a key component in fuel cell stacks because they connect the single fuel cells. They conduct electrical current from cell to cell and provide a uniform distribution of hydrogen and oxygen throughout the fuel cell. Moreover, they contribute to the cooling of the cell by removing the heat generated and prevent leakage of gases and coolant. In order to properly conduct current through the assembly, BPs are usually made of high electrically conductive material, e.g., graphite or stainless steel [37,72].

4.4 Types of Fuel Cells

Fuel cells are applicable in the entire spectrum of energy demand. Their applications are determined by the type of electrolyte they use for ion conduction, which in turn determines the electrochemical reactions, the catalyst type, operating temperature and the fuel used. Most often, their classification is mainly based on the nature of the electrolyte they use and subsequently their typical operating temperature. This temperature, as well as the useful life of the fuel cell, commands the properties of the other materials used in the cell components. The operating temperature also plays an important role in dictating the degree of fuel processing required. In low-temperature fuel cells, for instance, all the fuel must be converted to hydrogen previously to entering the fuel cell. The most common types of fuel cells, their operational strategy, typical applications and their main advantages and limitations are listed in Table 3.1 [37,60,73].

The different types of fuel cells are not exclusive to each other but serve as a complement that broadens their range of applications, which mainly depend on the operating temperature. High-temperature fuel cells, for instance, can achieve high reaction rates without expensive catalysts due to the high temperature at which the reactions take place, as well as being less sensitive to poisoning. Furthermore, natural gas is internally reformed, which can be used directly within the fuel cell without the need for a separate unit. The molten carbonate fuel cell (MCFC) and the solid oxide fuel cell (SOFC) belong to this category and they are mainly considered for stationary power units owing to their waste heat that can be combined with the produced electricity in a combined heat and power (CHP) system. Nevertheless, the high operating temperature implies the use of ceramic materials, which can be difficult to handle and expensive to manufacture. These systems, moreover, require long startup times, which hinders their applications in vehicles [37,74].

The phosphoric acid fuel cell (PAFC) and the alkaline fuel cell (AFC) operate at medium temperatures and demonstrated excellent thermal and electrochemical stability compared with other fuel cell systems. There are two main commercial uses for PAFC and AFC: small-scale onsite power generation and distributed power using reformed natural gas. However, they both use a liquid electrolyte, which makes manufacturing and handling more difficult [37,75,76].

Table 3.1 Key parameters of the main types of fuel cells [37,60,73].

Fuel Cell Type[¥]	**PEMFC**	**AFC**	**PAFC**	**MCFC**	**SOFC**
Electrolyte	Hydrated Polymeric Membrane	$KOH_{(aq)}$	$H_3PO_{4(aq)}$ in SiC	Molten Carbonate in $LiAlO_2$	Ceramic (Perovskites)
Fuel	H_2+H_2O	H_2+H_2O	H_2	H_2+H_2O +CO+CO_2	H_2+H_2O +CO+CO_2
Charge Carrier	$\uparrow H^+$	$\downarrow OH^-$	$\uparrow H^+$	$\downarrow CO_3^{2-}$	$\downarrow O^{2-}$
Oxidant	O_2+H_2O	O_2	O_2+H_2O	CO_2+O_2	O_2
Catalyst	Platinum	Platinum	Platinum	Nickel and Nickel Oxide	Perovskite
Operating T°	40-100 °C	60-220 °C	150-220 °C	650-800 °C	600-1000 °C
Power Range[§]	<1-100 kW	1-100 kW	5-400 kW	300 kW–3 MW	1 kW–2 MW
Primary Contaminant	CO, S and NH_3	CO, CO_2 and S	CO and S	S	S
Primary Cell Components	Carbon-based	Carbon-based	Graphite-based	Stainless-based	Ceramic
Advantages	High power density, quick start-up and low T°	High performance and low-cost components	High CHP efficiency, low-cost and reliable	High efficiency, flexibility of fuels and catalysts and solid electrolyte	High efficiency, fuel flexibility, variety of catalysts and solid electrolyte
Limitations	Expensive catalysts, sensitive to fuel impurities and water management	Sensitive to CO_2, electrolyte management and expensive catalysts	Corrosive electrolyte, expensive catalysts, long start-up times	Expensive materials, corrosion, low power density, degradation and long start-up	Expensive materials, corrosion, long start-up and degradation
Applications	Small-scale back-up power, portab electric devices and transport	Electrical equipment, transportation and stationary	Spacecrafts, military	Stationary	Stationary and heavy-duty transportation

[¥]Only hydrogen fuel cells considered.

[§]Data from US department of Energy – March 2021 (http://www.hydrogenandfuelcells.energy.gov).

Lastly, low-temperature fuel cells are remarkably stable and cover a large power range, which include subtypes such as the proton exchange membrane fuel cells (PEMFCs), direct methanol fuel cells (DMFCs), or direct formic acid fuel cells (DFAFCs). PEMFC form the most widely used category of fuel cells, whose main characteristic is the use of a solid polymer membrane as electrolyte. The low temperatures at which PEMFC typically operate (60 to 80 °C) makes them excellent candidates for short start-up applications [77]. This, together with their high-power densities, makes PEMFC the best candidate for small-scale backup power, portable electric devices and automotive applications [37,65,78].

As already explained, there are numerous types of fuel cells that operate under different conditions, which make them suitable for a vast range of applications. However, as previously noted, this chapter will deal only with low-temperature technologies using hydrogen as fuel.

4.5 Fuel Cell Performance

Among other factors, the performance of a hydrogen fuel cell is closely dependent on the capability of hydrogen and oxygen to react at the TPB of their respective electrodes, which in turn is dependent on the morphology, area and structure of the electrode. More importantly, the rate of the half-cell reactions depends on the catalyst used to catalyze the anodic and cathodic reactions. Furthermore, in order to ensure the proper adsorption of reactants on the catalyst active sites, both the electrode and the electrolyte must first provide adequate gas and ionic diffusion respectively.

A commonly used method to measure the fuel cell performance is the current-voltage (I-V) curve or polarization curve, which is usually plotted with current density, i.e. current normalized by the geometric surface area of the electrode, vs. voltage. In this subsection, the polarization curve of the ORR at the cathode of a PEMFC (which uses a Pt catalyst) will be considered for practical reasons (Fig. 4.2). The theoretical open circuit voltage (OCV) of the fuel cell is a function of the Gibbs free energy of the overall reaction. However, the actual OCV is lower than the theoretically predicted value even when no current is drawn due to irreversible voltage loss, which arise from secondary reactions at the cathode [79,80]:

- Reversible O adsorption at the Pt surface:

$$Pt + H_2O \longleftrightarrow PtO + 2H^+ + 2e^- \qquad E^\circ=0.88 \text{ V vs. RHE} \qquad (4.6)$$

- Fuel crossover: H_2 permeates across the membrane from the anode to the cathode, where it can be directly oxidized by O_2, i.e. *in situ* electron transfer. This undesirable reaction also generates peroxide radicals, which degrades the membrane and thus reduces the TPB in the catalyst layer.

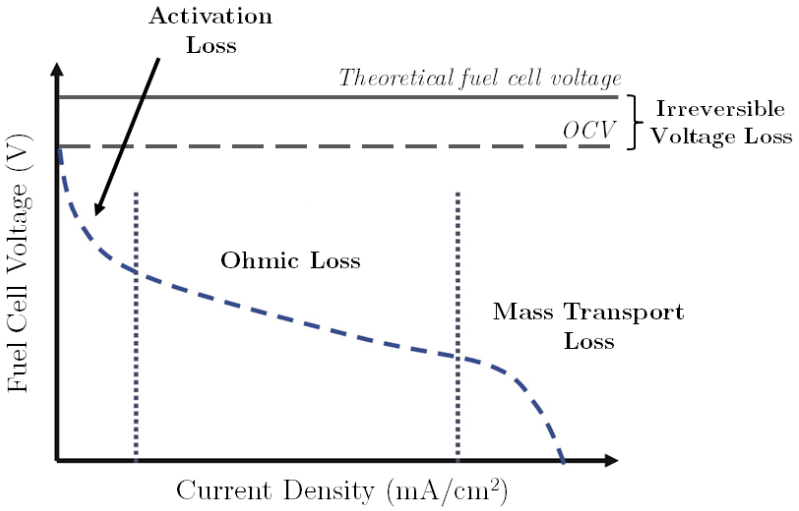

Figure 4.2 Typical fuel cell I-V curve.

Similar to cyclic voltammetry, a qualitive interpretation of an I-V curve requires analysis of the shape of the curve. The total power that can be delivered by the cell is limited by the current generated, which in turn depends on the voltage of the cell. Different fuel cell designs operate at different voltages, but the higher the voltage at a given current density the better. Voltage decreases as the current increases due different losses, which occur at different stages:

I) Activation Loss

Activation overpotential arises from the additional energy required to drive the half-cell reaction compared to the thermodynamically expected value. As explained in Section 2.3, the existence of overpotential implies that less energy is recovered from what is predicted thermodynamically. Thus, activation losses (η_{act}) are associated with the ORR kinetics taking place at the cathode. Even for the same reaction, the value of η_{act} is specific to the design of the ell and operating conditions [37].

II) Ohmic Loss

The linear voltage drop in Fig. 4.2 is related to Ohmic loses (η_{ohmic}), which are caused by the resistance to the electrons flow through the cell components and interconnections, as well as the ion resistance in the electrolyte. The typical fuel cell operating voltage lays in this region [37].

III) Mass Transport Loss

The prompt decay in voltage at high current densities is related to mass transport phenomena ($\eta_{mass\ transport}$), which fails to transport reactant species from the bulk solution to the electrode surface fast enough to keep the electron transfer at a certain rate [37].

Thus, the actual fuel cell voltage will be determined by the contribution of all the voltage losses explained above to the equilibrium potential, i.e. the thermodynamically predicted voltage (E^o):

$$V = E^o - \eta_{act} - \eta_{ohmic} - \eta_{mass\ transport} \tag{4.7}$$

In order to make a reliable comparison among different electrodes, the current in a polarization curve is usually normalized. There are three ways to normalize current: i) geometric current density (A/cm_{geo}^2), which is obtained by using the geometrical area of the electrode; ii) specific current density ($A/cm^2_{catalyst}$), which is normalized by the electrochemical surface area (ECSA) of the catalyst, i.e. area exposed to reactants; and iii) mass activity ($A/mg_{catalyst}$), which gives information about the utilization of the catalyst .

4.6 Electrocatalysts for Low-Temperature Hydrogen Fuel Cells

Platinum and its alloys are currently used as catalyst for most of the commonly used low-temperature fuel cells because its remarkable activity and stability for both electrode reactions. However, Pt demand is growing as the populations of developing countries gain wealth and move towards the desired net-zero GHG emissions mobility, which depletes its reservoirs and thus contributes to the increase of its cost [81,82]. In this thesis, Pt will be used as an example of electrocatalyst characterization to illustrate the methods followed for the qualitative and quantitative analysis of catalytic materials for low-temperature hydrogen fuel cells.

As described in Section 2.6, cyclic voltammetry is one of the simplest and most revealing electrochemical methods for electrocatalysts analysis. Thus, insights of the electrochemical behavior of a certain catalytic material can be obtained by looking at the shape and position of the features exhibited in a CV. A typical CV for a Pt electrode in acid media is shown in Fig. 4.3, which shows different types of responses to the applied potential sweep. Each region in the CV reveals different electrochemical surface processes

that give rise to faradaic and non-faradaic currents, both in the cathodic region (I and VII) and in the anodic region (II-VI):

I) Underpotential Deposited Hydrogen (H_{UPD}) region at 0-0.4 V, which is dominated by the adsorption of atomic H on Pt right before the equilibrium potential for hydrogen reduction (i.e. hydrogen evolution) at 0 V vs. RHE. The adsorption process involves one electron transfer:

$$Pt + e^- + H^+ \longrightarrow Pt - H \tag{4.8}$$

The peaks at 0.25 and 0.1 V correspond to hydrogen adsorption on Pt (100) and on Pt (110) respectively [83].

II) Also H_{UPD}, but dominated by H desorption during anodic scans:

$$Pt - H \longrightarrow Pt + e^- + H^+ \tag{4.9}$$

III) Double layer region, where only capacitive (non-faradaic) currents arising from a changing potential are seen.

IV) Onset of Pt surface oxidation, which starts with the formation of an adsorbate layer of O-containing species from either OH^- or O^{2-} adsorption, although the former is more commonly accepted [84]:

$$Pt + H_2O \longrightarrow Pt - OH + e^- + H^+ \tag{4.10}$$

V) Formation of a surface oxide layer:

$$Pt - OH \longrightarrow Pt - O + e^- + H^+ \tag{4.11}$$

VI) Growing of the surface oxide to finally form the bulk oxide.

VII) Pt oxide reduction to metallic Pt:

$$Pt - O + 2e^- + 2H^+ \longrightarrow Pt + H_2O \tag{4.12}$$

The exact potential range of the processes mentioned above depend on several experimental parameters, including temperature and scan rate. Moreover, these processes depend also on the catalysts nature and surface morphology. If Pt is alloyed with other elements, new peaks may appear due to either changes in the surface binding energy or reactions in the alloying material [85].

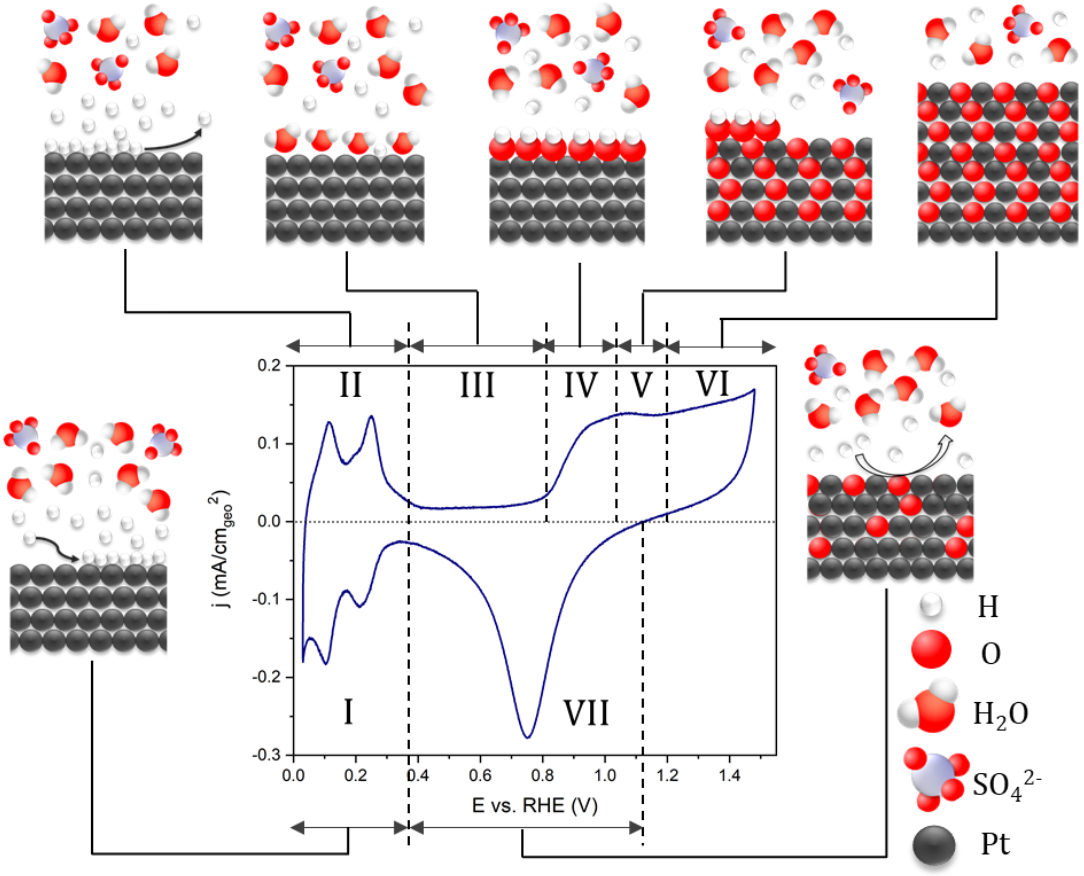

Figure 4.3 Typical cyclic voltammogram of a polycrystalline Pt electrode in Ar-saturated H_2SO_4 0.5 M showing the processes at each potential range (in roman numbers) and an atomistic model of the electrode/electrolyte interface structure in each region. The CV was taken at 50 mV/s with a reversible hydrogen electrode (RHE). Adapted from [70].

Many of these regions can be used to determine the electrochemical surface area (ECSA) of the electrode and thus allow for a direct comparison between different catalyst, which makes CVs a crucial electrochemical method for electrocatalysts characterization. The ECSA is usually calculated experimentally by using the charge associated with a given surface electrochemical process (Q) and the charge associated with the coverage of one monolayer (θ) by:

$$ECSA = \frac{Q}{\theta} \tag{4.13}$$

and Q is obtained from the integral of the region of interest in the CV by:

$$Q = \int I dt = \int I dE \frac{dt}{dE} \tag{4.14}$$

where $\frac{dt}{dE}$ is the inverse of the scan rate, which evidences the influence of the scan rate on the peak area. This methodology can be applied in several regions of the CV.

Hydrogen Underpotential Deposition (H_{UPD})

Charge associated with the adsorption of a hydrogen monolayer is the most commonly used method for ECSA calculation. The area over the two cathodic peaks (region I) after the subtraction of the non-faradaic currents (i.e. double layer) corresponds to 77% coverage of a hydrogen monolayer adsorbed on a polycrystalline Pt [86]. Then, by considering a θ_{Pt-H} of 210 µC/cm$_{Pt}^2$, the Pt ECSA can be extracted. This value is based on the assumption that θ of polycrystalline Pt corresponds to the averaged θ value over the three crystal base planes of Pt [86,87]. Besides the error associated with this assumption, the choice of valid integral limits also carries an error because of the presence of the hydrogen evolution peak at potentials close to 0 V vs. RHE. Overall, the ECSA determined by this method often corresponds to 90% of the actual ECSA value [87].

Capacitance

Non-faradaic currents arising from the EDL capacitance can also be used to calculate the ECSA, which is extracted from the dependence of the capacitive current (i_{DL}) on the scan rate ($\frac{\partial E}{\partial t}$) as:

$$ECSA = \frac{i_{DL}}{\frac{\partial E}{\partial t} C_M} \tag{4.15}$$

Thus, by plotting current vs. scan rate, the capacitance of the electrode is obtained, which can be converted to ECSA by dividing it by the specific capacitance found on the literature (C_M). For Pt, this value is usually reported to be 39.5 µF/cm^2 [88].

Metal Reduction

ECSA determination from H_{UPD} may become very inaccurate for metals that do not exhibit a well-defined hydrogen adsorption, such as Pd, whose H absorption complicates the integration of the area corresponding to a H monolayer formation [89]. For such metals, the area of the cathodic peak corresponding to the reduction of the metal oxide can be used instead. For this process, a θ value of 420 µC/cm$_M^2$ is taken, which corresponds to a 2:1 ratio compared to H adsorption/desorption. However, oxidation at higher potentials may lead to a higher oxide coverage, which in turn causes a surface rearrangement and, thus, a fluctuating ECSA during CVs [90].

In this thesis, the methods described above have been applied for the ECSA determination of electrocatalysts, mainly for the two types of hydrogen polymer electrolyte fuel cells: the proton exchange membrane fuel cell (PEMFC) and the anion exchange membrane fuel cell (AEMFC), whose working principles and reaction mechanisms are explained below.

4.7 Proton-Exchange Membrane Fuel Cell (PEMFC)

Hydrogen PEM fuel cells are, without doubt, the most widely studied and used today, mainly for automotive applications thanks to its high energy density. The schematic diagram of the PEMFC working principle is shown in Fig. 4.4. In a PEMFC, hydrogen enters the flow field pattern, diffuses through the gas diffusion layer (GDL) and oxidizes in the anode catalyst layer. Protons generated from the hydrogen oxidation then travel through the acidic polymeric membrane to the cathode catalyst layer, where they react with oxygen that is being reduced to form water in the cathode. Compensating charge in the form of electrons then flows through the external circuit and provides the useful work done by the fuel cell. The overall PEMFC electrochemical reaction can thus be written as:

Anode: $$H_2 \longrightarrow 2H^+ + 2e^- \tag{4.16}$$

Cathode: $$\frac{1}{2}O_2 + 2H^+ + 2e^- \longrightarrow H_2O \tag{4.17}$$

Overall: $$H_2 + \frac{1}{2}O_2 \longrightarrow H_2O \tag{4.18}$$

Since the electrochemical reactions required for the fuel cell to operate take place at the TPB in the catalyst layers, these are crucial for the good performance of the cell. The catalysts need to have contact with the electronic and the proton-conducting media, as well as with hydrogen and oxygen. For this, a large-area catalyst support and a proton-conducting ionomer are needed. The support is usually carbon-based, which allows for high electric conductivity and provides favorable porosity with a suitable balance between catalyst utilization and good mass transport. Similarly, the right amount of ionomer is needed to provide ionic conductivity to all active sites. A good ionomer and carbon support performance, however, cannot guarantee a good reaction rate if the catalytic material does not provide the correct reactant conversion. Thus, efficient and stable electrocatalysts need to be developed if the full potential of PEMFC is meant to be exploited. Moreover, their cost also needs to be reduced for their widespread commercialization. The first step in the development of new inexpensive catalysts, however, needs the correct understanding of both the ORR and the HOR mechanisms.

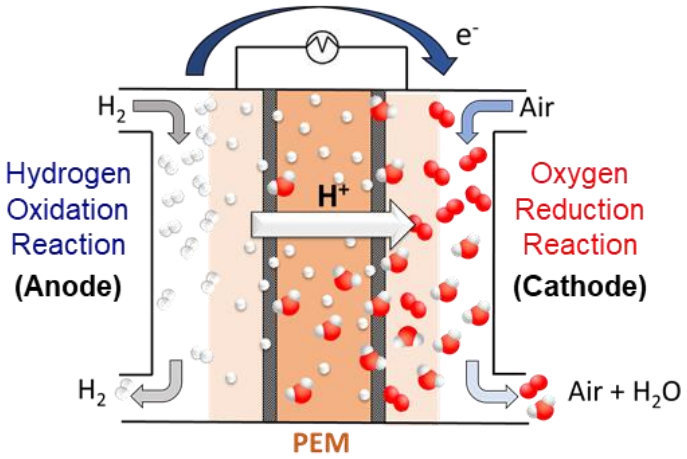

Figure 4.4 Schematic illustration of the PEMFC.

4.7.1 Oxygen Reduction Reaction (ORR)

As many other reactions, the oxygen reduction reaction (ORR) undergoes different pathways depending on the pH at which it takes place. In PEMFCs, which operate at low pH, the ORR is the largest single contributor to the potential loss of the fuel cell [91]. Thus, most of the research on PEMFC focuses on finding electrocatalysts more active than Pt, which is the current benchmark for this reaction in acidic media.

The ORR is a complex reaction to catalyze because it involves the transfer of 4 electrons and 4 protons to each O_2 molecule throughout a number of elementary steps, resulting in an exchange current density one order of magnitude lower than that of the HOR [37]. Moreover, the exact reaction mechanism is still not well understood, although it is believed to depend on the nature of the electrolyte, electrode and catalyst. In aqueous acidic solutions, there are two pathways through which the ORR may occur (at pH=0):

I) The direct 4-electron reduction pathway:

$$O_2 + 4H^+ + 4e^- \longrightarrow 2H_2O \qquad E°=1.23\ V \tag{4.19}$$

II) The 2-electron reduction pathway through H_2O_2:

$$O_2 + 2H^+ + 2e^- \longrightarrow H_2O_2 \qquad E°=0.70\ V \tag{4.20}$$

$$H_2O_2 + 2H^+ + 2e^- \longrightarrow 2H_2O \qquad E°=1.77\ V \tag{4.21}$$

Since generally the sluggish 2 electron pathway gives rise to a lower potential than the 4 electron one, the latter is preferred in hydrogen fuel cells. Moreover, the 2 electron pathway involves the formation of peroxide species, which is detrimental for the membrane [80].

Within a theoretical electrochemical framework, two possible ORR mechanisms are proposed for the 4 electron pathway: associative and dissociative mechanism [92]. In the associative mechanism, the pathway to form adsorbed O* intermediates proceeds as follows:

$$O_{2(g)} + * \longrightarrow O_2^* \tag{4.22}$$

$$O_2^* + H^+ + e^- \longrightarrow HOO^* \tag{4.23}$$

$$HOO^* + H^+ + e^- \longrightarrow O^* + H_2O_{(l)} \tag{4.24}$$

while in the dissociative route, O* is formed by:

$$O_{2(g)} + 2 * \longrightarrow 2O^* \tag{4.25}$$

Lastly, OH* is formed and reduced to water in both mechanisms by:

$$O^* + H^+ + e^- \longrightarrow HO^* \tag{4.26}$$

$$HO^* + H^+ + e^- \longrightarrow H_2O_{(l)} + * \tag{4.27}$$

The specific reaction pathway mainly depends on the catalyst used and the potential applied. However, the ORR can be summarized as follows [42,93]:

i) O_2 surface adsorption.
ii) electron transfer to adsorbed O* species.
iii) dissociation of O=O bond.
iv) desorption of the OH- formed.

Among these steps, three are considered to be the rate-limiting steps: i), ii) and iii), which depend on the cathode material.

The state-of-the-art catalyst for PEMFC is either platinum or platinum alloys supported on carbon black. The high ORR activity is attributed to the balance between the relatively weak adsorption of the oxygen species intermediates (O^*, HO^*, HOO^*) and the rather strong adsorption of O_2 on adjacent Pt sites, which enables the O=O bond breakage [94]. Thus, since the stability of oxygenated species scales linearly with the oxygen binding energy, the latter can be used as a descriptor for the ORR on different metals [85]. As explained in Section 3.1, rate-limiting intermediates in a catalytic reaction should bind neither too weak nor too strong to the surface for optimum activity, which is illustrated by the volcano plot. For metals that bind oxygen intermediates too strongly, the reaction 4.24 is the RDS and, for the ones who bind intermediates too weakly, it is found that the reactions 4.22 and 4.25 are the RDS [95]. Pt is found on the

"too strong" side of the oxygen intermediates binding of the volcano plot (Fig. 4.5) [92]. Thus, although Pt evidently has the highest activity for the ORR, an optimum catalyst should bind oxygen species approximately 0.1 eV weaker than Pt [92]. Furthermore, its high price and scarcity are additional motivations to reduce the amount of Pt used in the catalyst layer or, preferably, use Pt-free catalysts.

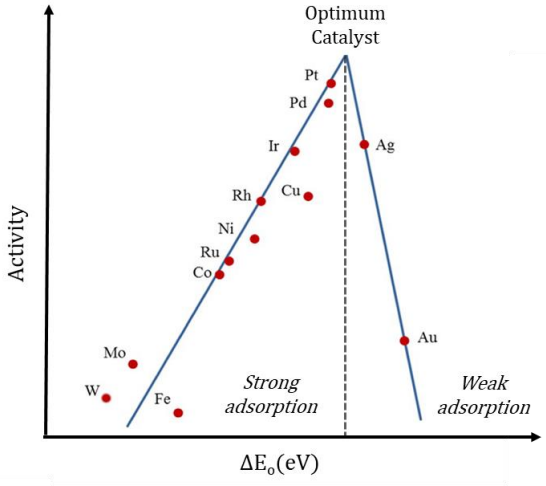

Figure 4.5 Volcano plot for the ORR activity on the oxygen binding energy for different catalysts. Data from [92].

The most common strategy to reduce Pt catalyst loading on the cathode is by alloying with other metal elements (often transition metals), such as Co, Ni, Fe, Ti, Cr, Ir or lanthanides [21,96–99], which can achieve higher intrinsic activities than pure Pt. The enhancement in the ORR activity has been attributed to different mechanisms, mainly ligand (electronic) and/or strain (structural) effects, that change the Pt electronic structure and thus the adsorption energy of reactants and intermediates. It has been proposed that structural effects may enhance the ORR by providing favorable active sites for the dissociative adsorption of oxygen. This is caused by the insertion of a second metal with a larger atomic radius into the Pt lattice, which results in a compressive lattice strain and thus a decrease in the Pt-Pt distance [100]. Hence, when Pt is alloyed with metals of dissimilar radii, the greater the difference radii is, the more strain is induced. This has been extensively investigated with Pt-rare earth metals (REM) alloys, in which the REM is more thermodynamically favored to stay in the bulk, causing a compressive strain on the Pt surface layer and consequently increasing its activity [98,101–103]. On the other hand, alloying Pt with low d-orbital occupancy transition metals cause the Pt to share its d-orbital electrons with the unfilled d-orbital of the transition metal, tunning its d-band center [104,105]. This electronic effect is considered to be the most significant in determining the adsorption strength of oxygen intermediates. This has been investigated for Pt_3Ni and PtCu, among other Pt alloys [106,107]. However, the metallic transition metal alloys are often not very stable in acidic

conditions, which leads to catalyst degradation [108]. For this reason, metal oxide catalysts have been investigated both as an alloying element with Pt or as a support in order to increase the stability of the catalyst layer. Other approaches involve switching to non-noble metal catalyst, such as M-N-C, where M corresponds to a non-PGM catalyst such as Fe or Co [109]. However, these are beyond the scope of this thesis, which focuses on Pt-REM alloys for the acidic ORR.

4.7.2 Hydrogen Oxidation Reaction (HOR)

In PEMFCs, most research has been focused on the development of cathode catalysts because the activation overpotential is mainly caused by the sluggish ORR kinetics. For this reason, much less attention has been paid to the anode reaction, in which Pt is also the most active catalyst. However, the HOR can also contribute to the PEMFC overpotential due to the high sensitivity of Pt towards CO impurities, which led to a vast research on CO-tolerant anode catalysts [110,111].

In acidic solution, the hydrogen oxidation is believed to be composed of two out of the three following steps (either Tafel-Volmer or Heyrovsky-Volmer):

Tafel $$H_2 + 2* \longrightarrow 2H_{ad} \tag{4.28}$$

Heyrovsky $$H_2 + * \longrightarrow H_{ad} + H^+ + e^- \tag{4.29}$$

Volmer $$H_{ad} \longrightarrow H^+ + e^- \tag{4.30}$$

Although the exact mechanism remains to be elucidated, the hydrogen adsorption is often considered to be the RDS in both the Tafel-Volmer and in the Heyrovsky-Volmer pathways. Several studies have reported that the RDS are individually applicable only in limited potential ranges, with some claiming that the Tafel-Volmer route is the RDS at low potentials and it switches to the Heyrovsky-Volmer mechanism at higher potentials [112–114]. Nevertheless, other studies consider the Tafel-Volmer mechanism applicable at all operating potentials [115], while others consider the HOR on Pt as a structure-sensitive and temperature-dependent reaction [116].

Although Pt is the most active catalyst for HOR, there is a lack of consensus in the literature concerning the exchange current density values. The main discrepancy arises from kinetic data measured in RDE, in which the exchange current density obtained is too small by at least a factor of 20, bringing concerns on the actual mechanism controlling the reaction in Pt catalysts, i.e. kinetics vs. hydrogen diffusion [117]. Parallel to these studies, a lot of research has focused on the development of stable CO-tolerant electrocatalysts, mainly by alloying Pt with Ru, Ni, Fe or Sn [111].

4.8 Anion-Exchange Membrane Fuel Cell (AEMFC)

Alkaline fuel cells (AFCs) were the first fuel cell technology to be put into practical service, proving the feasibility of using hydrogen as a fuel, when it was first used in spacecraft in the 1960s [68]. AFCs were further extended into anion exchange membrane fuel cells (AEMFCs), the most recent fuel cell technology, where a solid electrolyte was used instead of liquid. This technology operates under the same principles as that of PEMFCs, its acidic analog, with the main difference of hydroxyl ions serving as charge carriers instead of protons. The schematic diagram of the PEMFC working principle is shown in Fig. 4.6. In an AEMFC, the oxygen from air diffuses through the GDL and is reduced on the cathode, thereby forming hydroxide anions. These ions are then transferred through the alkaline membrane electrolyte to the anode, on which oxidation of hydrogen into water takes place [37]. The overall PEMFC electrochemical reaction can be written as:

Anode: $$H_2 + 2OH^- \longrightarrow 2H_2O + 2e^- \tag{4.31}$$

Cathode: $$\frac{1}{2}O_2 + H_2O + 2e^- \longrightarrow 2OH^- \tag{4.32}$$

Overall: $$H_2 + \frac{1}{2}O_2 \longrightarrow H_2O \tag{4.33}$$

The main advantage of AEMFCs over PEMFCs relies on the alkaline electrolyte, whose milder conditions enables the possibility to use electrocatalysts free of noble metals, thereby opening the door for low-cost polymer electrolyte fuel cells. Furthermore, the electrode kinetics of the cathode reduction are more facile in a high pH environment, which mitigates the activation overpotential attributed to the cathodic site [22]. Water flooding issues are also mitigated in AMEFCs compared to PEMFCs because the hydroxides and dragged water molecules generally migrate from the cathode to the anode, thereby suppressing hydrogen crossover [118]. They also present the advantage over AFCs of using an alkaline polymer electrolyte, which is less susceptible to carbonation issues that decrease the ionic conductivity, and avoids electrolyte leakage [119].

Nevertheless, AEMFCs have a few drawbacks compared to PEMFCs, mainly attributed to the nature of the electrolyte. A typical anion exchange membrane is composed of a polymer backbone with tethered cationic ion-exchange groups to facilitate the movement of free OH^- ions. However, the diffusion coefficient of hydroxide ions is approximately four times lower than that of the protons, which translates into conductivity issues. Although the carbonates precipitations are mitigated in AMEFCs due to cations being fixed to the membrane backbone, this also causes additional anion conductivity issues

[119]. Besides, there are no commercially available anion-exchange membranes that are as efficient as Nafion® for PEMFCs. Last but not least, the lower AEMFC performance compared to PEMFCs has been attributed to a slower hydrogen oxidation in alkaline media, which evidences the need for highly active HOR catalysts as well as a good understanding of its mechanism at high pH [117].

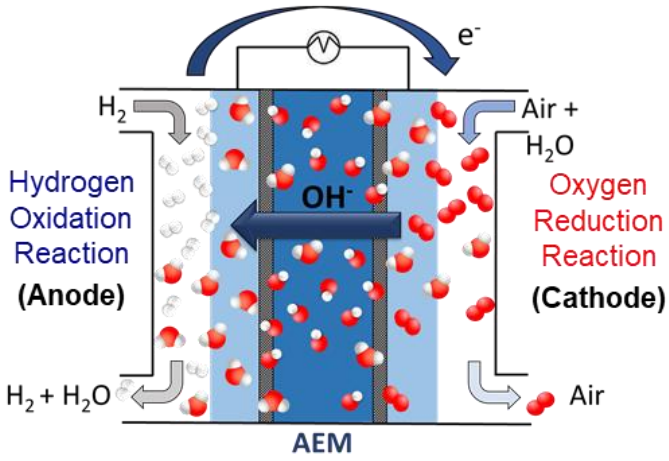

Figure 4.6 Schematic illustration of the AEMFC.

4.8.1 Oxygen Reduction Reaction (ORR)

Although the ORR kinetics in alkaline media is enhanced compared to acidic media, it is still far from being optimal and its exact sequence in AEMFC also remains to be elucidated. As in PEMFCs, the ORR is a multielectron reaction that undergoes two different pathways that include a number of elementary steps involving different reaction intermediates, which slightly differ from those in acidic media [120]:

I) The direct 4 electron pathway, in which O_2 is directly reduced to OH^-:

$$O_2 + 2H_2O + 4e^- \longrightarrow 4OH^- \qquad E°=0.41\ V \tag{4.34}$$

II) The 2+2 electron pathway through HO2- intermediate:

$$O_2 + H_2O + 2e^- \longrightarrow HO_2^- + OH^- \qquad E°=-0.065\ V \tag{4.35}$$

$$HO_2^- + H_2O + 2e^- \longrightarrow 3OH^- \qquad E°=0.87\ V \tag{4.36}$$

The peroxide produced may also undergo disproportionation:

$$2HO_2^- \longrightarrow 2OH^- + O_2 \tag{4.37}$$

Thus, in alkaline media, the following intermediate species are formed: O^{2-}, O, OH^-, HO_2^- and OOH, whose stability regulate the activity of the ORR catalyst. Although the exact

mechanism is still not well understood, it is known that the rate-determining step on metals such as Pt and Ag is the first electron transfer [121]:

$$O_{2(g)} + e^- \longrightarrow O_2^- \tag{4.38}$$

It is also known that the origin of the lower activation overpotential, i.e. higher voltage, in AEMFCs relies on the preferred formation of peroxide species in alkaline media, which desorb more easily than in their acidic analog [122]. The stabilization of HO_2^- due to its negative charge as opposed to its neutrality in acid solutions is believed to be the reason behind the more facile kinetics at high pH. Moreover, the dependence of the ORR on the pH was also explained by the presence of spectator species adsorbed on the catalyst surface, which at low pH block the active sites and lower the adsorption energy of the intermediates, thereby decreasing the overall reaction rate [123].

The decrease of the overpotential with increasing pH is one of the main factors permitting the use of Pt-free catalysts for the ORR in alkaline media, including noble metals, non-noble metals and metal-free catalysts [121]. Although the performance of Pt catalysts is not compensated for their expense, it remains the most commonly used and active catalyst for the ORR in alkaline conditions. Hence, considerable efforts have been devoted to decrease Pt content while maintaining a high ORR activity [23,124,125]. These catalysts have lower Pt loadings and increased activity and stability relative to bulk Pt, mainly due to: i) strain effects that reduce the Pt-Pt bond distance and thus favor the oxygen adsorption, ii) d-coupling effects that lower the d-band center of the 5d-orbital when alloying with transition metals such as Ni, Co or Cr and iii) the presence of surface oxide layers such as perovskites that enhance the covalency of the metal-oxygen bond [123,126,127].

With the need for comparatively cheap materials in AEMFCs, a number of substitutes to Pt have been considered, mainly in the PGM because they all promote the 4 electron pathway in alkaline media [126]. Pd and Ag-based electrocatalysts are more abundant noble metals than Pt that exhibit promising ORR activity via various modification methods. Pd has a similar electronic configuration to Pt and presents an optimum balance between the O=O bond breaking and the OH^- formation [128]. Moreover, Pd exhibits higher activity in alkaline than in acidic solutions due to a decrease in the anion poisoning effect in alkaline solutions [129]. However, its highly occupied d-orbital results in a too strong binding of oxygenated species, for which alloying with other transition metals is needed if the O binding energy is meant to be weakened. 3d transition metals are widely employed to enhance the catalytic activity of Pd catalysts, such as Cu, Ni, Fe and Co, which is highly dependent on the composition and structure of the alloy [126,128,130,131]. Ag has also been considered to substitute Pt in the cathode. The ORR

in Ag surfaces occurs through 2 and 4 electron pathways depending on the surface morphology and oxidation state [121]. As opposed to Pd, Ag binds oxygen adsorbates too weakly, for which alloying with 3d metals is also needed, being Pd a good candidate due to its strong bonding to adsorbed intermediate species [132].

Among non-noble metal ORR catalysts, Fe, Co, and Mn are the most widely studied. Manganese oxides represent an attractive inexpensive and active catalysts towards the ORR in alkaline media, especially MnO_2 and Mn_3O_4 [120]. Their higher activity has been attributed to the mediation process involving the reduction of Mn(IV) to Mn(III), followed by the electron transfer from Mn(III) to oxygen. However, the ORR activity of MnO_2 was found to vary depending on the crystalline structure, with amorphous manganese oxides providing more active sites [133]. Mn oxides led to a new approach of electrocatalyst bifunctionality, in which one catalyst is used for the reduction of O_2 through the formation of HO_2^- and is subsequently reduced to OH^- by MnO_2, leading to a 4 electron transfer [134].

4.8.2 Hydrogen Oxidation Reaction (HOR)

In the PEMFC anode, platinum is an excellent HOR electrocatalyst. Nevertheless, in alkaline conditions the exchange current density for HOR on Pt is slowed by approximately three order of magnitude [135]. Despite the reduced activity of Pt for HOR in alkaline electrolytes and its price, Pt is still the most commonly used anode catalyst for hydrogen AEMFCs, for which considerable amounts of Pt are still needed [136].

The correct understanding of the HOR mechanism at high pH is a cornerstone in the development of inexpensive catalysts. Thus, tailoring of new alkaline HOR electrocatalysts rely on the thorough understanding of the reaction mechanism. Similar to that in acid, the HOR is normally believed to proceed through the combination of the following steps (either Tafel-Volmer or Heyrovsky-Volmer) [137]:

Tafel $$H_2 + 2* \longrightarrow 2H_{ad} \tag{4.39}$$

Heyrovsky $$H_2 + OH^- + * \longrightarrow H_{ad} + H_2O + e^- \tag{4.40}$$

Volmer $$H_{ad} + OH^- \longrightarrow * + H_2O + e^- \tag{4.41}$$

As seen, the Tafel step, i.e. dissociative adsorption of H_2 without electron transfer, is the same as in acidic media. However, the exact mechanism of the Heyrovsky and Volmer steps remains under considerable debate so far. The Heyrovsky step can be described as the electron transfer from H_2 to the catalyst, either by OH^- or OH_{ad}. Similarly, the Volmer

step, i.e. the discharge of the adsorbed hydrogen, can also occur *via* OH^- or OH_{ad} [137]. Thus, the different beliefs can be classified into two categories: HOR pathway with OH^- in solution and HOR pathway with OH_{ad} on the electrocatalyst surface. However, the hydrogen atom desorption (Volmer step), is widely viewed as the rate-determining step.

Two descriptors governing the HOR activity of electrocatalysts have been proposed depending on whether the HOR pathway is assumed to rely on OH^- or OH_{ad}. One descriptor is the hydrogen binding energy (HBE), in which only OH^- from solution is involved in the alkaline HOR. It is therefore suggested that, in strong base, the HOR mechanism does not change except that the Heyrovsky or Volmer step are followed by the fast recombination of H^+ and the abundant OH^- in the electrolyte, and thus the HBE governs the HOR activities in the full range of pHs [138]. In this way, it is suggested that the OH^- in solution affects the HOR activities through tuning the HBE, although they do not directly participate in the reactions through adsorption [139]. This hypothesis is widely demonstrated on Pt and Pt alloys, for which it has been claimed that the rate-determining step is the Volmer step and that the HBE is the unique and sole descriptor for the HOR in alkaline electrolytes [140–143]. Others, however, describe the HBE as the *dominant* descriptor in HOR on PGMs, although other factors such as oxophilicity may also play a secondary role [144,145]. It has been reported that the HBEs of PGMs increase with increasing pH, and that the high HBEs in alkaline conditions are the underlying reason for the sluggish HOR [138,143]. Thus, when alloying Pt with other metals such as Ru, the HBE is weakened by down-shifting the d-band center of Pt through either structural or electronic effects, which leads to an enhanced HOR [146,147].

The other descriptor is the oxophilicity, i.e. the tendency of a certain element to abstract an oxygen atom from another molecule, in which adsorbed OH is involved. This hypothesis arose from the apparent beneficial effect of an added oxophilic metal in facilitating the hydrogen desorption (i.e. the assumed RDS), which has been interpreted as *bifunctional* activity. Thus, according to this hypothesis, alloying dissimilar metals in which one is a surface site with high affinity towards H_{ad} (M_1), and the other is an oxophilic metal that binds OH reversibly (M_2), results in a lowering of the energy barrier of the Volmer step and thus an enhanced HOR in alkaline media [148]. This process takes place on a bifunctional catalyst surface as follows:

$$H_2 + M_1 \longrightarrow 2M_1 - H_{ad} \tag{4.42}$$

$$OH^- + M_2 \longrightarrow M_2 - OH_{ad} + e^- \tag{4.43}$$

$$M_1 - H_{ad} + M_2 - OH_{ad} \longrightarrow H_2O + M_1 + M_2 \tag{4.44}$$

According to this model, the reason for slower HOR kinetics at high pH relies on the competitivity between H and OH for adsorption on active sites, which is dominated by OH due to its high concentration in alkaline electrolytes. Hence, with the aim to provide different adsorption sites and thus avoid competitivity, alloying of oxophilic metals with others with optimal HBE have been widely investigated for different morphologies, mainly involving bimetallic alloys such as PdNi [128,130,131,148]. For these alloys, it is yet not clear if the addition of a second metal results in an enhanced HOR through added oxophilicity or by tuning the HBE of the first metal. So far, however, there is no direct evidence that OH adsorption occurs at potentials near the HOR reversible potential, which is essential for this proposed mechanism [149].

Many examples have been provided for the beneficial effects of alloying to the HOR rate in alkaline media, either through electronic and structural effects modifying the HBE of PGMs or by added oxophilicity. Nonetheless, examples providing the existence of both mechanisms have also been given, which seems to be the most feasible occurrence. In summary, identifying the exact alkaline HOR pathway is indispensable for tailoring new highly-active inexpensive HOR electrocatalysts.

5. Model Electrodes

Fuel cell electrodes are complex materials, usually containing several components that contribute to overall activity. In order to identify the active part of the catalyst, being able to study a very small amount of material and reactants at the surface of these complex materials is needed, as well as the differentiation of its surface from its bulk. This requires employment of surface sensitive techniques and a variation in the complexity of the catalysts to isolate the contribution of each component. Thus, only by systematically adding complexity to a simple system, the ultimate real system may be approached. Model systems are well-defined systems that have been modified and structurally simplified in order to isolate the contribution from one or a few phenomena that are important for the real (and complex) system. In this work, different well-defined thin-film model electrodes have been fabricated and characterized (both physically and electro-chemically) in order to analyze specific and selected mechanisms that describe the catalyst behavior.

Physical vapor deposition (PVD) covers a range of thin-film deposition techniques. PVD processes involve individual atoms or clusters, which are not usually found in the gas phase, that are removed from a solid source and collide on a solid surface where atoms stick and form a film. The means to remove atoms or clusters from the source can occur through either sputtering (magnetron or ion beam), which utilizes energetic ions colliding with a target to sputter target material, or evaporation (thermal resistive and e-beam), which relies on heating a solid source material past its vaporization temperature. For this process to occur, an ultra-high vacuum (UHV) is needed to create the necessary mean free path for the vaporized metal to reach the substrate.

5.1 Fabrication

Since the complex structure of supported metal catalysts usually hinders the connection between macroscopic effects and microscopic processes at the surface, simpler structures are often preferred. Hence, the fabrication methods used for the sample preparation are critical to aim at fundamental questions about the correlation between structure and properties of catalytic materials. The methods used for the fabrication of model

electrodes are critical because a high catalytic activity relies on very fine and well dispersed catalyst particles, for which planar structures are preferred. Besides, a model electrode should also ensure a high degree of reproducibility and maximized mass activity in order to provide a reliable comparison between different catalyst materials. Physically deposited thin-film model electrodes fulfill all the above-mentioned requirements. Thus, in this work, thin-films have been fabricated by physical deposition techniques, such as evaporation and sputtering, which allow for high control of the composition and thickness that ensure minimal structural variation between samples. Thin-films have been deposited on both glassy carbon substrates (to be evaluated in Rotating Disk Electrode) and on conventional GDLs which are evaluated in single cell AEMFC.

5.1.1. E-beam Physical Vapor Deposition

E-beam PVD uses a high-voltage electron beam directed by a magnetic field to focus a large amount of energy into the evaporation source found in a water-cooled holder. The high-energy beam produces a very high temperature in the metal target, which allows the metal to be vaporized. The vaporized metal atoms or clusters then diffuse through an evacuated chamber and impinge on a solid surface used as a substrate, at which they condensate and form a thin-film (Fig. 5.1) [77,150].

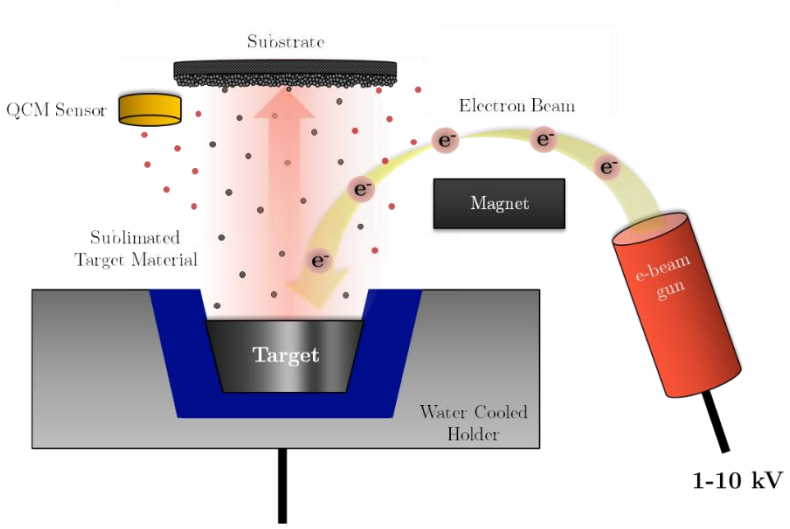

Figure 5.1 Schematic illustration of e-beam physical vapor deposition (PVD).

E-beam PVD can be used even on metals with high melting points, without compromising uniformity or material utilization. Moreover, this technique also presents the advantage of good directionality and low level of impurities, which are essential for the fabrication of well-defined model electrodes. Nonetheless, e-beam PVD also exhibits a few drawbacks that might affect the properties of ideal thin-films. Since thin-films are formed as a result of the much lower temperature of the substrate on which they are

being deposited at low deposition rates, they usually have a smaller grain size than the bulk materials [150]. The impact energy in PVD is generally rather low, which might result in low adhesion of evaporated films. Furthermore, this technique is not suited for depositing alloy thin-films because each alloying element has a different temperature-vapor pressure relation, which leads to different evaporation rates and thus a difficult control of the alloy composition [77]. Hence, other physical deposition techniques are used in order to obtain uniform and well-controlled alloy thin-films.

5.1.2 DC Magnetron Sputtering

As opposed to e-beam PVD, magnetron sputtering is a plasma-based technique that employs magnetron sputtering sources that use electric and magnetic fields to confine a plasma (typically composed of positively charged Ar particles) close to the surface of the source, or target material. The confined plasma collides with the negatively charge target material (cathode), thereby causing the ejection of atoms from the metal target (Fig. 5.2). These ejected atoms then travel through the UHV chamber under a magnetic field and are deposited onto the substrate material (anode) [150,151].

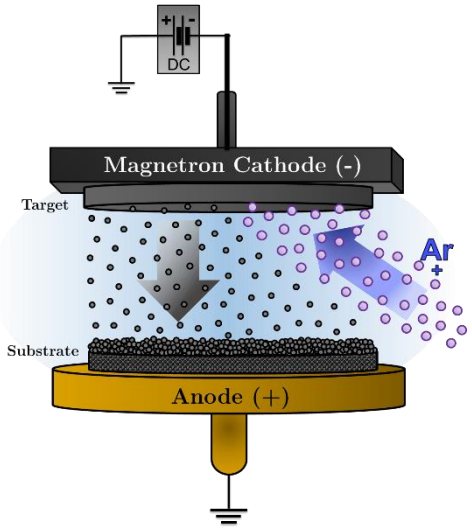

Figure 5.2 Schematic illustration of DC magnetron sputtering.

This method produces good film quality and uniformity, as well as very strong adhesion. Moreover, DC magnetron sputtering exhibits the highest scalability among all the physical deposition methods, which is very advantageous for industry applications [150,152]. More importantly, this method is very suitable for fabrication of alloy thin-films with compositions very close to that of the alloy target, either by placing clips of the alloying metal on top of the metal to be alloyed, by using an alloy target or by sputtering from multiple alloys.

5.2 Electrochemical Characterization

5.2.1 Rotating Disk Electrode (RDE)

In order to study electron transfer kinetics of HOR and ORR electrocatalysts and evaluate their catalytic activity, convective systems like the rotating disk electrode (RDE) are used. The RDE allows for the screening of catalysts under constant reactant flux and steady state. In this hydrodynamic technique, the mass transfer to the electrode surface is faster and more controllable than in case of stationary electrodes, where mass transport is governed solely by diffusion and migration. Thus, by setting an enhanced and well-defined mass transport, kinetic information such as rate constants, electron transfer coefficients and symmetry factors can be obtained [28,29]. In this work, RDE is the main tool to evaluate the performance of electrocatalysts.

The RDE is used in a conventional three electrode set-up, with a counter electrode, reference electrode and the disk of the RDE as working electrode, which consists of a circular conductive disk (5 mm diameter) embedded in an insulating PTFE sheath. The disk itself is generally made of catalytic material deposited onto glassy carbon, which are both conductive. The electrode rotates with a defined constant velocity, adjusted by the attached motor, around the rotating axis, which is perpendicular to the electrode surface (Fig. 5.3). The rotating disk then drags the electrolyte at its surface along with it and the centrifugal force propels the solution outwards in a radial direction, which increases with increasing rotation rate (ω) [29,30]. This results in a laminar flow of solution towards and across the electrode of which rate can be controlled by rotation speed.

Diffusion, convection and migration are the processes by which reactants are transported to the electrode surface. In a stagnant electrolyte, the dominant mechanism is diffusion, which induces limitations in the obtention of kinetic data of planar electrodes because the current in the kinetic region is dominated by mass transport, which is increasing with time. Forced convection can be applied in order to enhance mass transport, which is particularly important when dissolved gases with low solubility are used as reactants, such as in the ORR and HOR. Under forced convection, the net mass transport and thus the current is governed by the diffusion of reactants through the diffusion layer [28,30]. Hence, since the thickness of the diffusion layer is determined by the rotation speed, the current is also controlled by convection. The current density measured at the electrode surface is inversely proportional to the thickness of the double layer (δ), which is expressed by Fick's law:

$$j = nF\frac{D}{\delta}(c_0 - c^*) \tag{5.1}$$

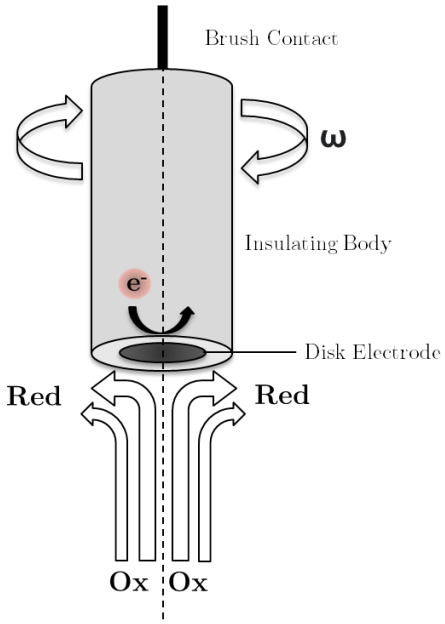

Figure 5.3 Schematic illustration of a rotating disk electrode and the radial flow of electrolyte during a reduction reaction.

where n is the number of moles of electrons transferred in the half reaction, F is the Faraday constant (C/mol), D is the diffusion constant, c_0 the concentration of reactants in the bulk and c^* is the concentration of reactants at the surface. High rotation speeds result in very thin diffusion layer thicknesses and, as a consequence, each species that arrive at the electrode surface are immediately converted (i.e. oxidized or reduced), leading to a surface concentration equal to zero. Eq. 5.1 can then be simplified to:

$$j = nF\frac{D}{\delta}c_0 \tag{5.2}$$

which relates the thickness of the diffusion layer to the current generated under convection. The relation between δ and the rotation speed (ω) of the electrode is expressed by an equation developed by Levich:

$$\delta = 1.61D^{\frac{1}{3}}\nu^{\frac{1}{6}}\omega^{-\frac{1}{2}} \tag{5.3}$$

where ν is the kinematic viscosity of the electrolyte (cm^2/s). According to Eq. 5.3, the thickness of the diffusion layer of a chosen system depends only on the rotation rate. By combining Eq. 5.2 and 5.3, the *Levich equation* for the diffusion limited current density (j_L) using RDE is obtained:

$$j_d = 0.62nFc_0D^{\frac{2}{3}}\nu^{-\frac{1}{6}}\omega^{\frac{1}{2}} \tag{5.4}$$

where the value of 0.62 is used when using rotation units of radians per second.

Before reaching the mass transport controlled regime, the current is also affected by the reaction kinetics in the so-called *mixed region*. Thus, in order to analyze the kinetics in this region, the kinetic and the diffusion current densities must be deconvoluted so they can be determined separately by:

$$\frac{1}{j} = \frac{1}{j_k} + \frac{1}{j_d} \tag{5.5}$$

where j_k and j_d are the kinetic and the diffusion-limited current density respectively. The diffusion-limited current can easily be determined from the diffusion region of the polarization curve at high overpotentials and the kinetic current density can be quantified by plotting $1/j$ vs. $1/j_d$, in which j_k corresponds to the intercept of the plot with the y axis. Kinetic parameters, such as the electron transfer coefficient (n), can be obtained by rearranging Eq. 5.4 and 5.5, which gives the *Koutecky-Levich equation*:

$$\frac{1}{j} = \frac{1}{j_k} + \frac{1}{0.62nFc_0D^{\frac{2}{3}}\nu^{-\frac{1}{6}}\omega^{\frac{1}{2}}} \tag{5.6}$$

By plotting $1/j$ vs. $\omega^{-\frac{1}{2}}$, a straight line is obtained, whose slope is used to determine kinetic parameters expressed in the Levich Equation [29,30].

5.2.2 Fuel Cell Measurements in Membrane Electrode Assembly (MEA)

Since the RDE provides conditions quite different from those in a real fuel cell, the measurement of electrocatalytic activity under conditions more relevant for fuel cells are highly needed. The membrane electrode assembly (MEA) is a more suitable choice for measuring model electrodes under conditions more similar to those in an actual fuel cell. The MEA is the heart of a polymer exchange fuel cell, i.e. PEMFC or AEMFC, and it consists of two catalytically active electrodes that form the anode and the cathode, and a polymer exchange electrolyte, forming a three-layer structure. However, the real electrode in real MEAs is very complicated to fabricate and complex to analyze, which makes the catalyst study and development very challenging. At the same time, the conditions in in the RDE are not the same as in the fuel cell and thus the catalyst evaluation is not ideal. An MEA model system relies between those, which can be seen as a combination of both. Thus, by using PVD fabrication methods on gas diffusion electrode (GDE) materials, is it possible to evaluate catalysts in a real fuel cell environment while having most of the advantages from thin-film fabrication. Similar to an actual MEA, the MEA model system also contains electrodes that facilitate transport of products and reactants through the setup, ions through the membrane, and electrons to and from the current collectors.

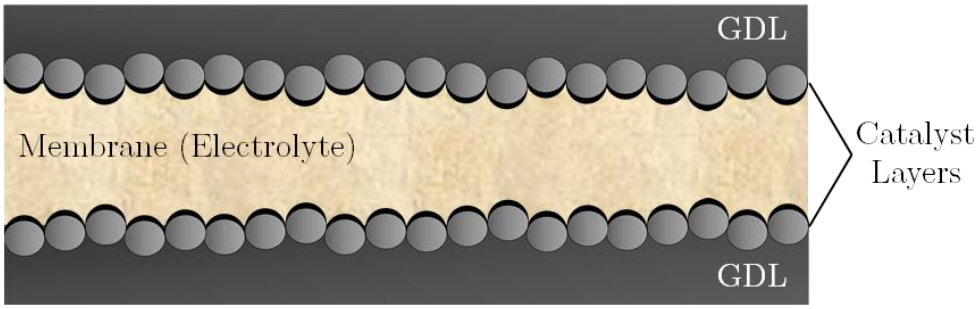

Figure 5.4 Schematic illustration of an MEA using nanoparticles as catalyst.

5.3 Physical Characterization

5.3.1 X-ray Photoelectron Spectroscopy

X-ray Photoelectron Spectroscopy (XPS) is a surface-sensitive technique that is used for qualitative and semi-quantitative analysis of the elements within a material, as well as their chemical state and the density of electronic states. Since it gives information about the chemical state of the material components, it is also called Electron Spectroscopy for Chemical Analysis (ECSA). The possibility to estimate the chemical composition and chemical state of elements, together with a small probing depth, makes XPS an important method for catalysts physical characterization [153].

The basic principle of XPS is based on energetic X-rays kicking out core electrons of an atom, whose energy is measured in an electron analyzer and compared to a reference library, SUCH AS Handbook of X-ray Photoelectron Spectroscopy [154]. Therefore, an XPS instrument consists of three critical components: the X-ray source, the electron energy analyzer and the detector. The X-ray source is composed of filaments that emit electrons, which are accelerated towards their respective anodes at 10-15 keV and bring about emission of X-rays. The choice of the anode material determines the energy of the X-rays emitted, which depends on the of surface analysis required. The most commonly used X-ray sources are Mg and Al due to their narrow full width at half maximum (FWHM), relatively high energy and intensity. The X-rays are then filtered by a monochromator and irradiated onto the material to be analyzed, which emits electrons whose kinetic energies are differentiated by the electron energy analyzer to allow for element identification. The material analyzed should be metallic and have a reasonably high melting point because the emission current creates a lot of heat on the material. The electrons are then accelerated to a certain energy (pass energy) and enter the detector, where they induce a detectable current that is registered by the detector itself.

Depending on the energy of the electrons, they will have different trajectories and can thus be differentiated for elemental identification [153,155].

In XPS, surface atoms are differentiated by tracing back the energy of the detected electrons to retrieve the kinetic energy of the incident electrons. This energy, together with the energy of the X-ray line, enables the calculation of the binding energy of the electrons (E_{BE}) by:

$$E_{BE} = h\nu - E_k - \phi_{sp} \tag{5.7}$$

Thus, for an electron kicked out with a photon energy $h\nu$, it has to overcome the binding energy (E_{BE}) and the spectrometer work function (ϕ_{sp}) in order to reach the detector with a kinetic energy E_k (Fig. 5.5). However, the kinetic energy of the electron in vacuum, i.e. in the XPS chamber, could be descried as:

$$E_{k-XPS} = h\nu - E_{BE} - \phi_s \tag{5.8}$$

where ϕ_s is the work function of the sample. Since both the sample and the analyzer are grounded, the contact potential between the two metals accelerates or decelerates the electron so that, at the end:

$$E_k - \phi_{sp} = E_{k-XPS} - \phi_s \tag{5.9}$$

Eq. 5.7 can now be written as:

$$E_{BE} = h\nu - E_{k-XPS} - \phi_{sp} \tag{5.10}$$

which is how the instrument derives the binding energy of a certain ejected electron. To detect the electrons, ultra-high vacuum (UHV) is needed to ensure that photoelectrons can travel from the sample to the detector without significant scattering [155]. Moreover, high vacuum is also needed to keep the surface of the sample clean, otherwise the surface can adsorb monolayers of hydrocarbons and water and the XPS signal can be stemmed from this contamination.

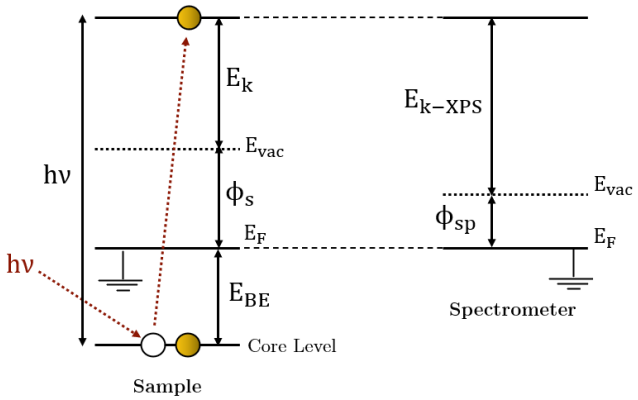

Figure 5.5 Schematic band diagram showing the energy of the photoemission process.

As far as every chemical element has a characteristic XPS spectrum, the chemical composition of a sample can be identified by the photoelectron energy. The position of a certain core-level photoelectron depends on the surrounding atoms. However, different binding energies in the same element in different chemical compounds might also be observed due to several reasons: difference in the oxidation state, different lattice parameters, *etc.* Thus, the binding energy shift due to the atomic environment effect, the so-called *chemical shift*, arises from different phenomena. In oxide samples, for instance, the strong electronegative oxygen atoms attract electron density, which causes the energy of the photoelectron to increase in order to be emitted and thus shifts the core-level energy peak to higher binding energies. In fact, binding to any atom with a higher electronegativity will result in a withdraw of electron density and thus a chemical shift towards higher binding energies. Other phenomena that might be seen in an XPS spectrum is *satellite peaks*, which appear at lower binding energies of the peak and are caused by the irradiation with the non-chromatic source. Moreover, *ghost peaks* arising from imperfections of the X-ray source might also be observed. Electrons that suffered an energy loss during the travel to the detector also give rise to XPS peaks, which include: *Auger peaks* and plasmon-loss features. Auger peaks emerge when an inner level hole is refilled by a more energetic electron from an outer level, which results in the emission of another electron from the outer energy level and a peak at very high binding energies is observed. Plasmon-losses originate from discreet energy losses and are observed at higher binding energies than the core-level photoelectron peak due to the interaction of the plasma oscillation of the outer shell with the photoelectron. In addition, some elements exhibit a spin-orbit splitting resulting in two peaks for p, d and f states, the so-called *spin-orbital coupling*. The ratio between the two peaks are different for each orbital shell (*p*, *d* and *f*) and the separation between the coupling states is characteristic of each element [153,154].

The shape and intensity of a core-level photoelectron peak are used for the qualitative and quantitative analysis of the sample constituents, which depend on the peak type as well as on the nature of the sample. Several components that overlap each other can be observed in a peak due to the coexistence of all the phenomena explained above. For this, deconvolution of each contribution is needed if each chemical state is meant to be quantified. The peak shape is usually well-defined by a Gauss-Lorentz profile for insulators and semiconductors, and by the Doniach-Sunjic line shape for metals. Moreover, the background arising from inelastically scattered photoelectrons should also be subtracted for the appropriate determination of the peak intensity and thus its quantification. Different background shapes can be used to better evaluate the line shape and stoichiometry, i.e. linear, Shirley or Tougaard, whose use depends on the nature of the photoelectron peak [153,156]. Lastly, XPS peaks should be calibrated to account for differences between the Fermi level of the spectrometer and the sample, which results in photoelectron kinetic energies differing from the actual value. The most common calibration peak is carbon 1s at a binding energy of 284.8 eV because every sample surface has a trace of adventitious carbon, i.e. carbon contamination.

Information from XPS beyond the surface can be obtained by performing a non-destructive depth profiling by means of synchrotron radiation XPS (SRXPS), which is carried out by tunning the excitation photon energy. Similarly, angular resolved photoelectron spectroscopy (ARPES) also allows for measuring a depth profile by tunning the angle between the perpendicular to the sample surface and the direction of the photoelectron detection, thereby changing the probing depth. However, in a lab XPS, depth profiling is usually obtained by destructive ion etching. By using an ion beam (usually Ar) to etch the layers of the surface or surface contamination, subsurface information can be revealed. The surface is etched by scanning an ion beam over an area of the sample (usually in the range of µm) and, after the etch cycle, an XPS spectrum is recorded from the surface of the sample. Thus, combining a sequence of ion gun etch cycles with XPS analysis provides both qualitative and quantitative information about the elemental composition throughout the sample, as well as the sample thickness.

5.3.2 Scanning Electron Microscopy/Energy-dispersive X-ray Spectroscopy (SEM/EDX)

Electron microscopy is a technique used to determine the size and shape of materials, as well as give information of the internal structure due to the different possible interactions between the electron beam and material. The interaction of the electron beam with a sample atom gives rise to, among others, back-scattered electrons (BSE) and emitted secondary electrons (SE)(Fig. 5.6), which are both used in scanning electron microscopy (SEM) to obtain information about the surface topography and composition. Moreover, the interaction between matter and an electron beam also produces characteristic X-rays, which might be used in energy-dispersive X-ray spectroscopy (EDX) for elemental analysis and chemical characterization of a sample [157].

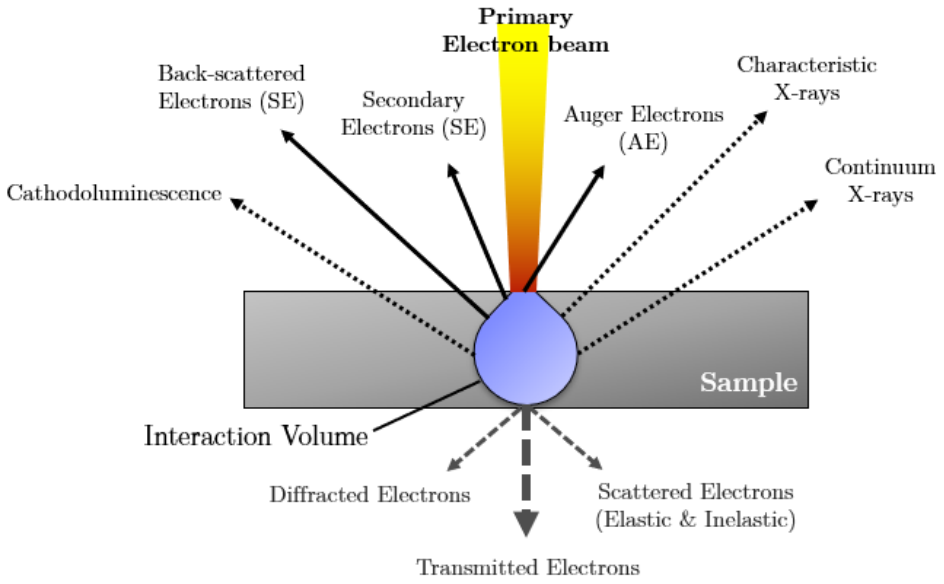

Figure 5.6 Electron-matter interaction volume and types of signal generated.

SEM is a type of electron microscopy that is used for imaging of samples by scanning them with a focused beam of electrons (typically 0.2-40 keV) and recording both the BSE and the SE emitted. BSE correspond to those electrons from the electron beam that have been bounced back out of the sample and, in contrast, low-energy SE are produced when electrons knock into atoms of the sample and displace electrons from the sample itself. The detection of these electrons allows for the investigation of the structure, morphology and crystallite size, as well as for determining surface defects. The BSE produced by the elastic scattering of electrons can also be collected in a different detector and, in combination with the evaluation of the characteristic X-rays, qualitative and quantitative elemental analysis can be obtained by EDX, which is an integrated characteristic of the SEM [157,158].

6. Summary and Outlook

The main long-term goal of my project is to investigate the catalytic activity and stability of electrocatalysts for both the hydrogen oxidation reaction and the oxygen reduction reaction in PEMFC and AEMFC with the aim to develop the next generation of efficient, durable and inexpensive catalysts for low-temperature hydrogen fuel cells. The work presented here represents the first progress towards achieving this goal.

6.1 Summary of Appended Papers

In **Paper I**, the electrocatalytic activity towards the oxygen reduction reaction (ORR) of thin-films of Pt and rare earth metals (REM) alloys (Pt_3Y, Pt_5Gd and Pt_5Tb) was evaluated in a membrane electrode assembly (MEA) of a PEMFC. The cathode thin-film electrodes were fabricated by deposition onto a gas diffusion layer (GDL) using DC magnetron sputtering and they were subsequently acid-treated to obtain a Pt overlayer covering the Pt-REM alloy bulk. Formation of a protective Pt skin over the Pt-REM alloy was confirmed by EDX and XPS/SRXPS, which was measured for as-sputtered, acid-treated and fuel cell measured samples. The thin-film catalysts performance was evaluated in a fuel cell environment by means of polarization curves in O_2/H_2. As the key result, it was found that the acid-treated alloys of Pt_3Y and Pt_5Gd catalysts show a specific activity enhancement of 2.5 times compared to pure Pt, and a 2.0 enhancement for acid-treated Pt_5Tb. The activity enhancement in Pt-REM alloys was attributed to a lattice strain effect caused by the underlying alloy on the Pt skin, which was found to be thicker for Pt_5Tb and thus the reason for its lower electroactivity. This study demonstrates the beneficial effects of alloying Pt with REM, which can lead to more active and less expensive catalysts compared to today's PEMFCs.

Electrocatalysts for the alkaline analog of the PEMFC, the AEMFC, were studied in **Paper II**, in which different radiation-induced chemically synthesized AgNi structured nanoparticles were evaluated for their activity towards the ORR in alkaline conditions. Two types of bimetallic AgNi nanocatalysts were synthesized by γ-radiation induced synthesis: Ag@Ni core-shells and Ag/Ni heterostructures. The structural and compositional analyses were carried out by microscopy (TEM, HRTEM and HAADF-

STEM), diffraction (XRD) and spectroscopy (XPS and EDS). The electrochemical characterization by RDE was used to evaluate the ORR activity, which for both structures was shown to be higher than their monometallic counterparts. Both alloy samples exhibited a very similar ORR enhancement, which was attributed to a ligand effect originating from the Ag-Ni interface for Ag@Ni, and to both a lattice strain effect and the presence of oxidized Ni species for Ag/Ni. Thus, in this paper, the study of the ORR performance was correlated with the nature of the electronic effects induced in the nanoparticles as a result of both ligand and structural effects.

In **Paper III**, electronic effects on both the HOR and the ORR for PdNi thin-film alloys were evaluated in alkaline media. The bimetallic alloys were fabricated by means of physical vapor deposition (PVD) and were subsequently annealed at different temperatures to induce the formation of different surface compositions. The samples were then acid-treated to remove Ni species on the surface and form a Pd overlayer, and both these and as-annealed samples were evaluated in RDE for HOR and ORR by means of polarization curves. Elemental surface composition and structure were evaluated by XPS and SEM respectively, which revealed different surface constituents at different temperatures, as well as a grain size dependent on temperature. It was found that, whereas the addition of surface Ni was beneficial for the HOR, the ORR activity showed an overall enhancement in acid-treated samples. The evaluation of the HOR activity and its correlation with the Hydrogen Binding Energy (HBE) of Pd provided clarifications on the HOR mechanism by confirming the HBE as the main descriptor of this reaction in alkaline media. Moreover, given the Tafel slopes obtained, the Volmer step was proposed as the rate-determining step in the HOR. The ORR, conversely, showed that electronic effects resulted in the largest enhancement when Ni was placed in the subsurface rather than on the surface, which induced an electronic effect that caused a shift of the d-band center of Pd and thus a weaker adsorption of oxygenated species.

6.2 Outlook

This project focuses on the development of electrocatalysts for low-temperature hydrogen fuel cells, which is currently hindered by the lack of mechanistic understanding. A versatile platform to study model system catalysts has been built to allow for reliable comparison among catalytic materials. Thus, the upcoming steps will focus on the fabrication and characterization, both physical and electrochemcial, of thoroughly tailored electrocatalysts. However, more importantly, the design of model catalysts will be oriented towards elucidating the mechanisms through which the HOR and ORR are

enhanced. For this, we have currently several pathways that could potentially be taken in order to find the new state-of-the-art catalysts for both PEMFCs and AEMFCs.

One route that this project will most likely take is based on deconvoluting the interplay between electronic effects, which are generally responsible for the enhanced activity of the catalysts already studied in this work. For this, rigorously fabricated thin-films with well-defined structures will be evaluated for both the HOR and ORR in order to pinpoint the exact effect responsible for the enhancement in both reactions, which will be correlated with their atomic distribution and thus their electronic environment. In this way, future catalysts can be carefully tailored in order to obtain the highest possible electroactivity. To have a better understanding of the structure and morphology effects on the catalytic activity, the HOR and ORR activity of thin-films fabricated by physical methods will be compared to the catalyst with the same composition but different structures fabricated by chemical methods by our collaborators.

Parallel to the evaluation of catalysts in our platform, physically-fabricated catalytic materials with the same composition and structure will also be evaluated in a membrane electrode assembly (MEA) model system. By studying their HOR and ORR performance in conditions more relevant for fuel cells, their performance can then be extrapolated to that in a real fuel cell, which is the actual aim of this work. Thus, by establishing a relation between different model systems, the influence of the reaction conditions can be elucidated, which is of crucial importance for the development of the new generation of efficient and inexpensive catalysts. In this context, the interaction between the catalysts and the other components in a fuel cell is essential to predict their behavior under real-life operation. For this, different ionomers used for ionic and reactants transport will also be also evaluated in combination with our electrocatalysts, which will provide a further comprehension of both the ionomer and the catalyst performance.

7. Acknowledgements

The work presented in this thesis was carried out at the Division of Chemical Physics at the Department of Physics, Chalmers University of Technology, Göteborg, Sweden from October 2018 through April 2021.

This work is financially supported by the Sweden Foundation for Strategic Research (*Stiftelsen för Strategisk Forskning*, SSF).

I would like to thank, first and foremost, my supervisor Björn Wickman, for his guidance and optimism, his patience, for putting his trust in me and for pushing me instead of pulling me back. You always offered opportunities to explore and develop to become an independent researcher, for which I am very grateful.

I would also like to thank my office and lab mate (and technically also co-supervisor) Rosemary Brown for all her guidance in those first steps and for all her patience when doing so. You are greatly missed.

I would also like to acknowledge all the help and support I received from the external collaborators at KTH and Lund University, from both professors and PhD students, who provided me with many opportunities to explore the research field we are in and to grow as a scientist.

A big thanks also to my examiner Henrik Grönbeck for all the help, support and discussions in a very relaxed and professional environment.

A huge thanks to everyone in the Division of Chemical Physics, current and former members, for creating a very nice, comfortable and professional work environment. Despite the times we are living, the environment at the Division makes it definitely worth to work here.

Thanks also to Lasse Urholm, Lars Hellberg and Lennart Norberg for always providing great, quick and generous support whenever it was needed.

Last but not least, I would like to thank my family for an unconditional and constant support. To all my great friends from Barcelona, Alió, DTU and all the ones across Europe, as well as all the new friends I made here in Göteborg. You all constantly reminded me who I am and what made me arrive until here. You truly make my life easier.

Bibliography

[1] G.W.Y. Melillo, J.M., T.C. Richmond, Climate change impacts in the United States: The third National Climate Assessment, U.S. Glob. Chang. Res. Progr. (2014).

[2] European Comission, A European Green Deal, (2021). https://ec.europa.eu/info/strategy/priorities-2019-2024/european-green-deal_en.

[3] T.A. of E.R.E.R.C. (EUREC), 2030: A binding 45% renewable energy target, (2020). https://eurec.be/2030-a-binding-45-renewable-energy-target/.

[4] W.M. Haynes; David R. Lide, ed., CRC Handbook of Chemistry and Physics, 92nd ed., CRC Press, 2011.

[5] G. Cipriani, V. Di Dio, F. Genduso, D. La Cascia, R. Liga, R. Miceli, G. Ricco Galluzzo, Perspective on hydrogen energy carrier and its automotive applications, Int. J. Hydrogen Energy. 39 (2014) 8482–8494. https://doi.org/10.1016/j.ijhydene.2014.03.174.

[6] S.E. Hosseini, M.A. Wahid, Hydrogen production from renewable and sustainable energy resources: Promising green energy carrier for clean development, Renew. Sustain. Energy Rev. 57 (2016) 850–866. https://doi.org/10.1016/j.rser.2015.12.112.

[7] R.M. Navarro, M.A. Peña, J.L.G. Fierro, Hydrogen production reactions from carbon feedstocks: Fossil fuels and biomass, Chem. Rev. 107 (2007) 3952–3991. https://doi.org/10.1021/cr0501994.

[8] P. Nikolaidis, A. Poullikkas, A comparative overview of hydrogen production processes, Renew. Sustain. Energy Rev. 67 (2017) 597–611. https://doi.org/10.1016/j.rser.2016.09.044.

[9] T. Nguyen, Z. Abdin, T. Holm, W. Mérida, Grid-connected hydrogen production via large-scale water electrolysis, Energy Convers. Manag. 200 (2019) 112108. https://doi.org/10.1016/j.enconman.2019.112108.

[10] A. Buttler, H. Spliethoff, Current status of water electrolysis for energy storage, grid balancing and sector coupling via power-to-gas and power-to-liquids: A review, Renew. Sustain. Energy Rev. 82 (2018) 2440–2454. https://doi.org/10.1016/j.rser.2017.09.003.

[11] S. Fang, D. Bresser, S. Passerini, Transition Metal Oxide Anodes for Electrochemical Energy Storage in Lithium- and Sodium-Ion Batteries, Adv. Energy Mater. 10 (2020). https://doi.org/10.1002/aenm.201902485.

[12] M. Cakici, K.R. Reddy, F. Alonso-Marroquin, Advanced electrochemical energy storage supercapacitors based on the flexible carbon fiber fabric-coated with uniform coral-like MnO2structured electrodes, Chem. Eng. J. 309 (2017) 151–158. https://doi.org/10.1016/j.cej.2016.10.012.

[13] Y. Wang, D.F. Ruiz Diaz, K.S. Chen, Z. Wang, X.C. Adroher, Materials, technological status, and fundamentals of PEM fuel cells – A review, Mater. Today. 32 (2020) 178–203. https://doi.org/10.1016/j.mattod.2019.06.005.

[14] H. Lohse-Busch, K. Stutenberg, M. Duoba, X. Liu, A. Elgowainy, M. Wang, T. Wallner, B. Richard, M. Christenson, Automotive fuel cell stack and system efficiency and fuel consumption based on vehicle testing on a chassis dynamometer at minus 18 °C to positive 35 °C temperatures, Int. J. Hydrogen

Energy. 45 (2020) 861–872. https://doi.org/10.1016/j.ijhydene.2019.10.150.

[15] Y. Wang, K.S. Chen, J. Mishler, S.C. Cho, X.C. Adroher, A review of polymer electrolyte membrane fuel cells: Technology, applications, and needs on fundamental research, Appl. Energy. 88 (2011) 981–1007. https://doi.org/10.1016/j.apenergy.2010.09.030.

[16] U.S. Department of Energy, DOE Technical Targets for Fuel Cell Systems and Stacks for Transportation Applications, Internet Publlication. (2017). https://www.energy.gov/eere/fuelcells/doe-technical-targets-fuel-cell-systems-and-stacks-transportation-applications.

[17] C.J. Yang, An impending platinum crisis and its implications for the future of the automobile, Energy Policy. 37 (2009) 1805–1808. https://doi.org/10.1016/j.enpol.2009.01.019.

[18] T. Abdel-Baset, T. Benjamin, R. Borup, K.E. Martin, N. Garland, S. Hirano, J. Kopasz, B. Lakshmanmn, D. Masten, M. Mehall, D. Myers, D. Papageorgopoulos, W. Podolski, T. Trabold, B. Vermeersch, J. Waldecker, The. US Deparment of Energy (DOE). Energy Efficiency and Renewable Energy https://energy.gov/eere/fuelcells/doe-technical-targets-polymer-electrolyte-membrane-fuel-cell-components, (2017) 30. https://doi.org/10.2172/1220127.

[19] M. Breitwieser, M. Klingele, B. Britton, S. Holdcroft, R. Zengerle, S. Thiele, Improved Pt-utilization efficiency of low Pt-loading PEM fuel cell electrodes using direct membrane deposition, Electrochem. Commun. 60 (2015) 168–171. https://doi.org/10.1016/j.elecom.2015.09.006.

[20] L. Ye, Y. Gao, S. Zhu, J. Zheng, P. Li, J.P. Zheng, A Pt content and pore structure gradient distributed catalyst layer to improve the PEMFC performance, Int. J. Hydrogen Energy. 42 (2017) 7241–7245. https://doi.org/10.1016/j.ijhydene.2016.11.002.

[21] V. Čolić, A.S. Bandarenka, Pt Alloy Electrocatalysts for the Oxygen Reduction Reaction: From Model Surfaces to Nanostructured Systems, ACS Catal. 6 (2016) 5378–5385. https://doi.org/10.1021/acscatal.6b00997.

[22] D.R. Dekel, Review of cell performance in anion exchange membrane fuel cells, J. Power Sources. 375 (2018) 158–169. https://doi.org/10.1016/j.jpowsour.2017.07.117.

[23] Q. He, E.J. Cairns, Review—Recent Progress in Electrocatalysts for Oxygen Reduction Suitable for Alkaline Anion Exchange Membrane Fuel Cells, J. Electrochem. Soc. 162 (2015) F1504–F1539. https://doi.org/10.1149/2.0551514jes.

[24] S. Gu, R. Cai, T. Luo, Z. Chen, M. Sun, Y. Liu, G. He, Y. Yan, A soluble and highly conductive ionomer for high-performance hydroxide exchange membrane fuel cells, Angew. Chemie - Int. Ed. 48 (2009) 6499–6502. https://doi.org/10.1002/anie.200806299.

[25] D.B. Hibbert, Introduction to electrochemistry, 1st ed., THE MACMILLAN PRESS LTD, 1993. https://doi.org/10.1007/978-1-349-22721-1.

[26] S. Petrovic, S. Petrovic, Basic Electrochemistry Concepts, 2021. https://doi.org/10.1007/978-3-030-61562-8_2.

[27] John Simpson; Edmund Weiner, Oxford English Dictionary: The definitive record of the English language, 3rd ed., Oxford University Press, 2018. https://www.oed.com/.

[28] W.V. Carl H. Hamann, Andrew Hamnet, Electrochemistry, 2nd Editio, WILEY-

VCH, 2007.

[29] A.J.B. and L.R. MFaulkner, Electrochemical Methods: Fundamentals and Applications, 2nd Editio, John Wiley & Sons, Ltd., 2001.

[30] D. Pletcher, A First Course in Electrode Processes, 2nd Editio, RSC Publishing, 2009.

[31] J. Staszak-Jirkovský, R. Subbaraman, D. Strmcnik, K.L. Harrison, C.E. Diesendruck, R. Assary, O. Frank, L. Kobr, G.K.H. Wiberg, B. Genorio, J.G. Connell, P.P. Lopes, V.R. Stamenkovic, L. Curtiss, J.S. Moore, K.R. Zavadil, N.M. Markovic, Water as a Promoter and Catalyst for Dioxygen Electrochemistry in Aqueous and Organic Media, ACS Catal. 5 (2015) 6600–6607. https://doi.org/10.1021/acscatal.5b01779.

[32] D. Strmcnik, K. Kodama, D. Van Der Vliet, J. Greeley, V.R. Stamenkovic, N.M. Marković, The role of non-covalent interactions in electrocatalytic fuel-cell reactions on platinum, Nat. Chem. 1 (2009) 466–472. https://doi.org/10.1038/nchem.330.

[33] A.J.B. and L.R. MFaulkner, Electrochemichal Methods, 2nd Ed, John Wiley & Sons, Ltd., 2001.

[34] M. Favaro, B. Jeong, P.N. Ross, J. Yano, Z. Hussain, Z. Liu, E.J. Crumlin, Unravelling the electrochemical double layer by direct probing of the solid/liquid interface, Nat. Commun. 7 (2016) 1–8. https://doi.org/10.1038/ncomms12695.

[35] Richard G. Compton and Craig E. Banks, Understanding Voltammetry, 3rd Editio, World Scientific Publishing Europe, 2018.

[36] A.J.B. and L.R. MFaulkner, Electrochemichal Methods, 2nd Editio, John Wiley & Sons, Ltd., 2001.

[37] Andrew L. Dicks; David A.J. Rand, Fuel Cell Systems Explained, 3rd Editio, 2018.

[38] J. Wisniak, The History of Catalysis. From the Beginning to Nobel Prizes, Educ. Quim. 21 (2010) 60–69. https://doi.org/10.1016/S0187-893X(18)30074-0.

[39] R. Winderlich, J.M. Moore, JONS JAKOB BERZELIUS, (1852).

[40] A. Camia, Birth of the catalytic concept, Catal. Letters. 67 (2000) 1–4. https://doi.org/10.1023/a:1016622806065.

[41] E. Auer, A. Freund, J. Pietsch, T. Tacke, Carbons as supports for industrial precious metal catalysts, Appl. Catal. A Gen. 173 (1998) 259–271. https://doi.org/10.1016/S0926-860X(98)00184-7.

[42] Z.W. Chen, L.X. Chen, Z. Wen, Q. Jiang, Understanding electro-catalysis by using density functional theory, Phys. Chem. Chem. Phys. 21 (2019) 23782–23802. https://doi.org/10.1039/c9cp04430b.

[43] C.J.H. Jacobsen, Novel class of ammonia synthesis catalysts, Chem. Commun. (2000) 1057–1058. https://doi.org/10.1039/b002930k.

[44] R.J. Farrauto, R.M. Heck, Catalytic converters: State of the art and perspectives, Catal. Today. 51 (1999) 351–360. https://doi.org/10.1016/S0920-5861(99)00024-3.

[45] IUPAC, Compendium of Chemical Terminology—The “Gold Book,” 2nd Editio, Blackwell Scientific Publications, Oxford. (2006-), 1997.

[46] J. Heveling, Heterogeneous catalytic chemistry by example of industrial applications, J. Chem. Educ. 89 (2012) 1530–1536.

https://doi.org/10.1021/ed200816g.

[47] I. Chorkendorff and J. W. Niemantsverdriet, Concepts of Modern Catalysis and kinetics, 3rd Editio, John Wisley & Sons, 2017.

[48] K. Taylor, Nitric oxide catalysis in automotive exhaust systems, Catal. Rev. 35 (1993) 457–481. https://doi.org/10.1080/01614949308013915.

[49] J.K. Nørskov, T. Bligaard, A. Logadottir, S. Bahn, L.B. Hansen, M. Bollinger, H. Bengaard, B. Hammer, Z. Sljivancanin, M. Mavrikakis, Y. Xu, S. Dahl, C.J.H. Jacobsen, Universality in heterogeneous catalysis, J. Catal. 209 (2002) 275–278. https://doi.org/10.1006/jcat.2002.3615.

[50] A.J. Medford, A. Vojvodic, J.S. Hummelshøj, J. Voss, F. Abild-Pedersen, F. Studt, T. Bligaard, A. Nilsson, J.K. Nørskov, From the Sabatier principle to a predictive theory of transition-metal heterogeneous catalysis, J. Catal. 328 (2015) 36–42. https://doi.org/10.1016/j.jcat.2014.12.033.

[51] I.E.L. Stephens, A.S. Bondarenko, U. Grønbjerg, J. Rossmeisl, I. Chorkendorff, Understanding the electrocatalysis of oxygen reduction on platinum and its alloys, Energy Environ. Sci. 5 (2012) 6744–6762. https://doi.org/10.1039/c2ee03590a.

[52] S.A. Park, H. Lim, Y.T. Kim, Enhanced Oxygen Reduction Reaction Activity Due to Electronic Effects between Ag and Mn3O4 in Alkaline Media, ACS Catal. 5 (2015) 3995–4002. https://doi.org/10.1021/acscatal.5b00495.

[53] H.E. Hoster, O.B. Alves, M.T.M. Koper, Tuning adsorption via strain and vertical ligand effects, ChemPhysChem. 11 (2010) 1518–1524. https://doi.org/10.1002/cphc.200900500.

[54] X. Wang, Y. Orikasa, Y. Takesue, H. Inoue, M. Nakamura, T. Minato, N. Hoshi, Y. Uchimoto, Quantitating the lattice strain dependence of monolayer Pt shell activity toward oxygen reduction, J. Am. Chem. Soc. 135 (2013) 5938–5941. https://doi.org/10.1021/ja312382h.

[55] B. Hammer, J.K. Nørskov, Electronic factors determining the reactivity of metal surfaces, Surf. Sci. 343 (1995) 211–220. https://doi.org/10.1016/0039-6028(96)80007-0.

[56] A. Nilsson, L.G.M. Pettersson, B. Hammer, T. Bligaard, C.H. Christensen, J.K. Nørskov, The electronic structure effect in heterogeneous catalysis, Catal. Letters. 100 (2005) 111–114. https://doi.org/10.1007/s10562-004-3434-9.

[57] J.K. Nørskov, F. Abild-Pedersen, F. Studt, T. Bligaard, Density functional theory in surface chemistry and catalysis, Proc. Natl. Acad. Sci. U. S. A. 108 (2011) 937–943. https://doi.org/10.1073/pnas.1006652108.

[58] A.S. Bandarenka, E. Ventosa, A. Maljusch, J. Masa, W. Schuhmann, Techniques and methodologies in modern electrocatalysis: evaluation of activity, selectivity and stability of catalytic materials, Analyst. 139 (2014) 1274–1291. https://doi.org/10.1039/c3an01647a.

[59] C.C.L. McCrory, S. Jung, I.M. Ferrer, S.M. Chatman, J.C. Peters, T.F. Jaramillo, Benchmarking Hydrogen Evolving Reaction and Oxygen Evolving Reaction Electrocatalysts for Solar Water Splitting Devices, J. Am. Chem. Soc. 137 (2015) 4347–4357. https://doi.org/10.1021/ja510442p.

[60] I. EG & G Technical Services, Fuel Cell Handbook, Seventh Ed, U.S. Department of Energy. National Energy Technology Laboratory., 2004.

[61] J. He, N.J.J. Johnson, A. Huang, C.P. Berlinguette, Electrocatalytic Alloys for CO2 Reduction, ChemSusChem. 11 (2018) 48–57.

https://doi.org/10.1002/cssc.201701825.

[62] B. Zhu, Advantages of intermediate temperature solid oxide fuel cells for tractionary applications, J. Power Sources. 93 (2001) 82–86. https://doi.org/10.1016/S0378-7753(00)00564-4.

[63] D. Bloch, Miniature fuel cells for portable applications, Low-Power Electron. Des. 106 (2004) 44-1-44–20. https://doi.org/10.1201/9781420039559.ch44.

[64] B.D. McNicol, D.A.J. Rand, K.R. Williams, Fuel cells for road transportation purposes - Yes or no?, J. Power Sources. 100 (2001) 47–59. https://doi.org/10.1016/S0378-7753(01)00882-5.

[65] K. Sopian, W.R. Wan Daud, Challenges and future developments in proton exchange membrane fuel cells, Renew. Energy. 31 (2006) 719–727. https://doi.org/10.1016/j.renene.2005.09.003.

[66] Grove - On a Gaseous Voltaic Battery.pdf, (n.d.).

[67] Grove - On Voltic Series and the Combination of Gases by Platinum.pdf, (n.d.).

[68] J.M. Andújar, F. Segura, Fuel cells: History and updating. A walk along two centuries, Renew. Sustain. Energy Rev. 13 (2009) 2309–2322. https://doi.org/10.1016/j.rser.2009.03.015.

[69] E.I. Ortiz-Rivera, A.L. Reyes-Hernandez, R.A. Febo, Understanding the history of fuel cells, 2007 IEEE Conf. Hist. Electr. Power, HEP 2007. 2 (2007) 117–122. https://doi.org/10.1109/HEP.2007.4510259.

[70] Marc. T.M. Koper, Fuel Cell Catalysis: A Surface Science Approach, 1st Editio, Andrzej Wieckowski, 2009.

[71] A. Larminie, J., & Dicks, 2 - Efficiency and Open Circuit Voltage, in: Fuel Cell Syst. Explain., Second Edi, John Wiley & Sons, Ltd., 2003.

[72] A. Hermann, T. Chaudhuri, P. Spagnol, Bipolar plates for PEM fuel cells: A review, Int. J. Hydrogen Energy. 30 (2005) 1297–1302. https://doi.org/10.1016/j.ijhydene.2005.04.016.

[73] H.W. Langmi, J. Ren, N.M. Musyoka, Nanomaterials for Fuel Cell Catalysis, 2016. http://link.springer.com/10.1007/978-3-319-29930-3.

[74] R.M. Ormerod, Solid oxide fuel cells, Chem. Soc. Rev. 32 (2003) 17–28. https://doi.org/10.1039/b105764m.

[75] N. Sammes, R. Bove, K. Stahl, Phosphoric acid fuel cells: Fundamentals and applications, Curr. Opin. Solid State Mater. Sci. 8 (2004) 372–378. https://doi.org/10.1016/j.cossms.2005.01.001.

[76] M. Neergat, A.K. Shukla, A high-performance phosphoric acid fuel cell, J. Power Sources. 102 (2001) 317–321. https://doi.org/10.1016/S0378-7753(01)00766-2.

[77] San Ping Jiang and Pei Kang Shen, Nanostructured and Advanced Materials for Fuel Cells, 1st Editio, CRC Press Taylor & Francis Group, 2017.

[78] R. Borup, J. Meyers, B. Pivovar, Y.S. Kim, R. Mukundan, N. Garland, D. Myers, M. Wilson, F. Garzon, D. Wood, P. Zelenay, K. More, K. Stroh, T. Zawodzinski, J. Boncella, J.E. McGrath, M. Inaba, K. Miyatake, M. Hori, K. Ota, Z. Ogumi, S. Miyata, A. Nishikata, Z. Siroma, Y. Uchimoto, K. Yasuda, K.I. Kimijima, N. Iwashita, Scientific aspects of polymer electrolyte fuel cell durability and degradation, Chem. Rev. 107 (2007) 3904–3951. https://doi.org/10.1021/cr0501821.

[79] C. Francia, V.S. Ijeri, S. Specchia, P. Spinelli, Estimation of hydrogen crossover

through Nafion® membranes in PEMFCs, J. Power Sources. 196 (2011) 1833–1839. https://doi.org/10.1016/j.jpowsour.2010.09.058.

[80] S.A. Vilekar, R. Datta, The effect of hydrogen crossover on open-circuit voltage in polymer electrolyte membrane fuel cells, J. Power Sources. 195 (2010) 2241–2247. https://doi.org/10.1016/j.jpowsour.2009.10.023.

[81] E. Alonso, F.R. Field, R.E. Kirchain, Platinum availability for future automotive technologies, Environ. Sci. Technol. 46 (2012) 12986–12993. https://doi.org/10.1021/es301110e.

[82] M.L.C.M. Henckens, P.P.J. Driessen, E. Worrell, Metal scarcity and sustainability, analyzing the necessity to reduce the extraction of scarce metals, Resour. Conserv. Recycl. 93 (2014) 1–8. https://doi.org/10.1016/j.resconrec.2014.09.012.

[83] N. Dubouis, A. Grimaud, The hydrogen evolution reaction: From material to interfacial descriptors, Chem. Sci. 10 (2019) 9165–9181. https://doi.org/10.1039/c9sc03831k.

[84] A.B. Anderson, O2 reduction and CO oxidation at the Pt-electrolyte interface. The role of H2O and OH adsorption bond strengths, Electrochim. Acta. 47 (2002) 3759–3763. https://doi.org/10.1016/S0013-4686(02)00346-8.

[85] I.E.L. Stephens, A.S. Bondarenko, L. Bech, I. Chorkendorff, Oxygen Electroreduction Activity and X-Ray Photoelectron Spectroscopy of Platinum and Early Transition Metal Alloys, ChemCatChem. 4 (2012) 341–349. https://doi.org/10.1002/cctc.201100343.

[86] S. Trasatti, O.A. Petrii, International Union of Pure and Applied Chemistry Physical Chemistry Division Commission on Electrochemistry: Real Surface Area Measurements in Electrochemistry, Pure Appl. Chem. 63 (1991) 711–734. https://doi.org/10.1351/pac199163050711.

[87] T. Biegler, D.A.J. Rand, R. Woods, Limiting oxygen coverage on platinized platinum; Relevance to determination of real platinum area by hydrogen adsorption, J. Electroanal. Chem. 29 (1971) 269–277. https://doi.org/10.1016/S0022-0728(71)80089-X.

[88] Cynthia G. Zoski, ed., Handbook of Electrochemistry, Elsevier B.V. and Science Press, 2007. https://doi.org/https://doi.org/10.1016/B978-0-444-51958-0.X5000-9.

[89] T. Mittermeier, A. Weiß, H.A. Gasteiger, F. Hasché, Monometallic Palladium for Oxygen Reduction in PEM Fuel Cells: Particle-Size Effect, Reaction Mechanism, and Voltage Cycling Stability, J. Electrochem. Soc. 164 (2017) F1081–F1089. https://doi.org/10.1149/2.0561712jes.

[90] A. Visintin, J.C. Canullo, W.E. Triaca, A.J. Arvia, Changes in real surface area, crystallographic orientation and morphology of platinum electrodes caused by periodic potential treatments: phenomenological approach, J. Electroanal. Chem. 239 (1988) 67–89. https://doi.org/10.1016/0022-0728(88)80270-5.

[91] G.S. Harzer, J.N. Schwämmlein, A.M. Damjanović, S. Ghosh, H.A. Gasteiger, Cathode Loading Impact on Voltage Cycling Induced PEMFC Degradation: A Voltage Loss Analysis, J. Electrochem. Soc. 165 (2018) F3118–F3131. https://doi.org/10.1149/2.0161806jes.

[92] J.K. Nørskov, J. Rossmeisl, A. Logadottir, L. Lindqvist, J.R. Kitchin, T. Bligaard, H. Jónsson, Origin of the overpotential for oxygen reduction at a fuel-cell cathode, J. Phys. Chem. B. 108 (2004) 17886–17892. https://doi.org/10.1021/jp047349j.

[93] E. Zamburlini, K.D. Jensen, I.E.L. Stephens, I. Chorkendorff, M. Escudero-Escribano, V. Čolić, A.S. Bandarenka, O. Ozturk, O.K. Ozdemir, I. Ulusoy, A.S. Ahsen, E. Slavcheva, N.M. Marković, T.J. Schmidt, V. Stamenković, P.N. Ross, M. Wesselmark, B. Wickman, C. Lagergren, G. Lindbergh, Oxygen Reduction Reaction on Pt and Pt Bimetallic Surfaces: A Selective Review, Electrochim. Acta. 111 (2013) 152–159. https://doi.org/10.1016/j.electacta.2013.07.108.

[94] A.J. Appleby, Electrocatalysis of aqueous dioxygen reduction, J. Electroanal. Chem. 357 (1993) 117–179. https://doi.org/10.1016/0022-0728(93)80378-U.

[95] V. Viswanathan, H.A. Hansen, J. Rossmeisl, J.K. Nørskov, Universality in oxygen reduction electrocatalysis on metal surfaces, ACS Catal. 2 (2012) 1654–1660. https://doi.org/10.1021/cs300227s.

[96] N.M. Marković, T.J. Schmidt, V. Stamenković, P.N. Ross, Oxygen Reduction Reaction on Pt and Pt Bimetallic Surfaces: A Selective Review, Fuel Cells. 1 (2001) 105–116. https://doi.org/10.1002/1615-6854(200107)1:2<105::aid-fuce105>3.3.co;2-0.

[97] O. Ozturk, O.K. Ozdemir, I. Ulusoy, A.S. Ahsen, E. Slavcheva, Effect of Ti sublayer on the ORR catalytic efficiency of dc magnetron sputtered thin Pt films, Int. J. Hydrogen Energy. 35 (2010) 4466–4473. https://doi.org/10.1016/j.ijhydene.2010.02.077.

[98] E. Zamburlini, K.D. Jensen, I.E.L. Stephens, I. Chorkendorff, M. Escudero-Escribano, Benchmarking Pt and Pt-lanthanide sputtered thin films for oxygen electroreduction: fabrication and rotating disk electrode measurements, Electrochim. Acta. 247 (2017) 708–721. https://doi.org/10.1016/j.electacta.2017.06.146.

[99] M. Wesselmark, B. Wickman, C. Lagergren, G. Lindbergh, The impact of iridium on the stability of platinum on carbon thin-filmmodel electrodes, Electrochim. Acta. 111 (2013) 152–159. https://doi.org/10.1016/j.electacta.2013.07.108.

[100] M.K. Min, J. Cho, K. Cho, H. Kim, Particle size and alloying effects of Pt-based alloy catalysts for fuel cell applications, Electrochim. Acta. 45 (2000) 4211–4217. https://doi.org/10.1016/S0013-4686(00)00553-3.

[101] J.N. Schwämmlein, G.S. Harzer, P. Pfändner, A. Blankenship, H.A. El-Sayed, H.A. Gasteiger, Activity and Stability of Carbon Supported Pt x Y Alloys for the ORR Determined by RDE and Single-Cell PEMFC Measurements , J. Electrochem. Soc. 165 (2018) J3173–J3185. https://doi.org/10.1149/2.0221815jes.

[102] N. Lindahl, E. Zamburlini, L. Feng, H. Grönbeck, M. Escudero-Escribano, I.E.L. Stephens, I. Chorkendorff, C. Langhammer, B. Wickman, High Specific and Mass Activity for the Oxygen Reduction Reaction for Thin Film Catalysts of Sputtered Pt3Y, Adv. Mater. Interfaces. 4 (2017) 1–9. https://doi.org/10.1002/admi.201700311.

[103] P. Malacrida, M. Escudero-Escribano, A. Verdaguer-Casadevall, I.E.L. Stephens, I. Chorkendorff, Enhanced activity and stability of Pt-La and Pt-Ce alloys for oxygen electroreduction: The elucidation of the active surface phase, J. Mater. Chem. A. 2 (2014) 4234–4243. https://doi.org/10.1039/c3ta14574c.

[104] V. Stamenkovic, B.S. Mun, K.J.J. Mayrhofer, P.N. Ross, N.M. Markovic, J. Rossmeisl, J. Greeley, J.K. Nørskov, Changing the activity of electrocatalysts for oxygen reduction by tuning the surface electronic structure, Angew. Chemie - Int. Ed. 45 (2006) 2897–2901. https://doi.org/10.1002/anie.200504386.

[105] F.H.B. Lima, J. Zhang, M.H. Shao, K. Sasaki, M.B. Vukmirovic, E.A. Ticianelli,

R.R. Adzic, Catalytic activity - d-band center correlation for the O2 reduction reaction on platinum in alkaline solutions, J. Phys. Chem. C. 111 (2007) 404–410. https://doi.org/10.1021/jp065181r.

[106] I.E.L. Stephens, A.S. Bondarenko, F.J. Perez-Alonso, F. Calle-Vallejo, L. Bech, T.P. Johansson, A.K. Jepsen, R. Frydendal, B.P. Knudsen, J. Rossmeisl, I. Chorkendorff, Tuning the activity of Pt(111) for oxygen electroreduction by subsurface alloying, J. Am. Chem. Soc. 133 (2011) 5485–5491. https://doi.org/10.1021/ja111690g.

[107] V.R. Stamenkovic, B. Fowler, B.S. Mun, G. Wang, P.N. Ross, C.A. Lucas, N.M. Markovic, Improved oxygen reduction activity on Pt3Ni(111) via increased surface site availability, Science (80-.). 315 (2007) 493–497. https://doi.org/10.1126/science.1135941.

[108] H.A. Gasteiger, S.S. Kocha, B. Sompalli, F.T. Wagner, Activity benchmarks and requirements for Pt, Pt-alloy, and non-Pt oxygen reduction catalysts for PEMFCs, Appl. Catal. B Environ. 56 (2005) 9–35. https://doi.org/10.1016/j.apcatb.2004.06.021.

[109] G. Wu, K.L. More, C.M. Johnston, P. Zelenay, High-performance electrocatalysts for oxygen reduction derived from polyaniline, iron, and cobalt, Science (80-.). 332 (2011) 443–447. https://doi.org/10.1126/science.1200832.

[110] L.J. Wan, Lattice-confined Ru clusters for hydrogen oxidation reaction with high CO-tolerance, Sci. China Chem. 63 (2020) 1169–1170. https://doi.org/10.1007/s11426-020-9774-3.

[111] S.J. Lee, S. Mukerjee, E.A. Ticianelli, J. McBreen, Electrocatalysis of CO tolerance in hydrogen oxidation reaction in PEM fuel cells, Electrochim. Acta. 44 (1999) 3283–3293. https://doi.org/10.1016/S0013-4686(99)00052-3.

[112] M. Wesselmark, B. Wickman, C. Lagergren, G. Lindbergh, Hydrogen oxidation reaction on thin platinum electrodes in the polymer electrolyte fuel cell, Electrochem. Commun. 12 (2010) 1585–1588. https://doi.org/10.1016/j.elecom.2010.08.037.

[113] S.A. Vilekar, I. Fishtik, R. Datta, Kinetics of the Hydrogen Electrode Reaction, J. Electrochem. Soc. 157 (2010) B1040. https://doi.org/10.1149/1.3385391.

[114] B. Babić, J. Gulicovski, L. Gajić-Krstajić, N. Elezović, V.R. Radmilović, N. V. Krstajić, L.M. Vračar, Kinetic study of the hydrogen oxidation reaction on sub-stoichiometric titanium oxide-supported platinum electrocatalyst in acid solution, J. Power Sources. 193 (2009) 99–106. https://doi.org/10.1016/j.jpowsour.2008.11.142.

[115] S. Chen, A. Kucernak, Electrocatalysis under conditions of high mass transport: Investigation of hydrogen oxidation on single submicron Pt particles supported on carbon, J. Phys. Chem. B. 108 (2004) 13984–13994. https://doi.org/10.1021/jp048641u.

[116] N.M. Marković, B.N. Grgur, P.N. Ross, Temperature-dependent hydrogen electrochemistry on platinum low-index single-crystal surfaces in acid solutions, J. Phys. Chem. B. 101 (1997) 5405–5413. https://doi.org/10.1021/jp970930d.

[117] W. Sheng, H.A. Gasteiger, Y. Shao-Horn, Hydrogen Oxidation and Evolution Reaction Kinetics on Platinum: Acid vs Alkaline Electrolytes, J. Electrochem. Soc. 157 (2010) B1529. https://doi.org/10.1149/1.3483106.

[118] S. Gottesfeld, D.R. Dekel, M. Page, C. Bae, Y. Yan, P. Zelenay, Y.S. Kim, Anion exchange membrane fuel cells: Current status and remaining challenges, J. Power Sources. 375 (2018) 170–184.

https://doi.org/10.1016/j.jpowsour.2017.08.010.

[119] J.R. Varcoe, R.C.T. Slade, Prospects for alkaline anion-exchange membranes in low temperature fuel cells, Fuel Cells. 5 (2005) 187–200. https://doi.org/10.1002/fuce.200400045.

[120] X. Ge, A. Sumboja, D. Wuu, T. An, B. Li, F.W.T. Goh, T.S.A. Hor, Y. Zong, Z. Liu, Oxygen Reduction in Alkaline Media: From Mechanisms to Recent Advances of Catalysts, ACS Catal. 5 (2015) 4643–4667. https://doi.org/10.1021/acscatal.5b00524.

[121] A. Qaseem, F. Chen, X. Wu, R.L. Johnston, Pt-free silver nanoalloy electrocatalysts for oxygen reduction reaction in alkaline media, Catal. Sci. Technol. 6 (2016) 3317–3340. https://doi.org/10.1039/c5cy02270c.

[122] M.T. Ergül, L. Türker, I. Eroğlu, An investigation on the performance optimization of an alkaline fuel cell, Int. J. Hydrogen Energy. 22 (1997) 1039–1045. https://doi.org/10.1016/s0360-3199(96)00244-3.

[123] J. Stacy, Y.N. Regmi, B. Leonard, M. Fan, The recent progress and future of oxygen reduction reaction catalysis: A review, Renew. Sustain. Energy Rev. 69 (2017) 401–414. https://doi.org/10.1016/j.rser.2016.09.135.

[124] M.G. Hosseini, P. Zardari, Electrocatalytical study of carbon supported Pt, Ru and bimetallic Pt-Ru nanoparticles for oxygen reduction reaction in alkaline media, Appl. Surf. Sci. 345 (2015) 223–231. https://doi.org/10.1016/j.apsusc.2015.03.146.

[125] K.D. Jensen, J. Tymoczko, J. Rossmeisl, A.S. Bandarenka, I. Chorkendorff, M. Escudero-Escribano, I.E.L. Stephens, Elucidation of the Oxygen Reduction Volcano in Alkaline Media using a Copper–Platinum(111) Alloy, Angew. Chemie - Int. Ed. 57 (2018) 2800–2805. https://doi.org/10.1002/anie.201711858.

[126] C.R. Raj, A. Samanta, S.H. Noh, S. Mondal, T. Okajima, T. Ohsaka, Emerging new generation electrocatalysts for the oxygen reduction reaction, J. Mater. Chem. A. 4 (2016) 11156–11178. https://doi.org/10.1039/c6ta03300h.

[127] Z.F. Pan, L. An, T.S. Zhao, Z.K. Tang, Advances and challenges in alkaline anion exchange membrane fuel cells, Prog. Energy Combust. Sci. 66 (2018) 141–175. https://doi.org/10.1016/j.pecs.2018.01.001.

[128] L. Zhang, Q. Chang, H. Chen, M. Shao, Recent advances in palladium-based electrocatalysts for fuel cell reactions and hydrogen evolution reaction, Nano Energy. 29 (2016) 198–219. https://doi.org/10.1016/j.nanoen.2016.02.044.

[129] M. Shao, Palladium-based electrocatalysts for hydrogen oxidation and oxygen reduction reactions, J. Power Sources. 196 (2011) 2433–2444. https://doi.org/10.1016/j.jpowsour.2010.10.093.

[130] M. Wang, W. Zhang, J. Wang, D. Wexler, S.D. Poynton, R.C.T. Slade, H. Liu, B. Winther-Jensen, R. Kerr, D. Shi, J. Chen, PdNi hollow nanoparticles for improved electrocatalytic oxygen reduction in alkaline environments, ACS Appl. Mater. Interfaces. 5 (2013) 12708–12715. https://doi.org/10.1021/am404090n.

[131] L. Chen, H. Guo, T. Fujita, A. Hirata, W. Zhang, A. Inoue, M. Chen, Nanoporous PdNi bimetallic catalyst with enhanced electrocatalytic performances for electro-oxidation and oxygen reduction reactions, Adv. Funct. Mater. 21 (2011) 4364–4370. https://doi.org/10.1002/adfm.201101227.

[132] J.A. Zamora Zeledón, M.B. Stevens, G.T.K.K. Gunasooriya, A. Gallo, A.T. Landers, M.E. Kreider, C. Hahn, J.K. Nørskov, T.F. Jaramillo, Tuning the electronic structure of Ag-Pd alloys to enhance performance for alkaline oxygen

reduction, Nat. Commun. 12 (2021) 1–9. https://doi.org/10.1038/s41467-021-20923-z.

[133] F. Cheng, Y. Su, J. Liang, Z. Tao, J. Chen, MnO2-based nanostructures as catalysts for electrochemical oxygen reduction in alkaline media, Chem. Mater. 22 (2010) 898–905. https://doi.org/10.1021/cm901698s.

[134] I. Roche, E. Chaînet, M. Chatenet, J. Vondrák, Carbon-supported manganese oxide nanoparticles as electrocatalysts for the Oxygen Reduction Reaction (ORR) in alkaline medium: Physical characterizations and ORR mechanism, J. Phys. Chem. C. 111 (2007) 1434–1443. https://doi.org/10.1021/jp0647986.

[135] P.J. Rheinländer, J. Herranz, J. Durst, H.A. Gasteiger, Kinetics of the Hydrogen Oxidation/Evolution Reaction on Polycrystalline Platinum in Alkaline Electrolyte Reaction Order with Respect to Hydrogen Pressure, J. Electrochem. Soc. 161 (2014) F1448–F1457. https://doi.org/10.1149/2.0501414jes.

[136] P. Rheinlander, S. Henning, J. Herranz, H.A. Gasteiger, Comparing Hydrogen Oxidation and Evolution Reaction Kinetics on Polycrystalline Platinum in 0.1 M and 1 M KOH, ECS Trans. 50 (2013) 2163–2174. https://doi.org/10.1149/05002.2163ecst.

[137] Y. Cong, B. Yi, Y. Song, Hydrogen oxidation reaction in alkaline media: From mechanism to recent electrocatalysts, Nano Energy. 44 (2018) 288–303. https://doi.org/10.1016/j.nanoen.2017.12.008.

[138] W. Sheng, Z. Zhuang, M. Gao, J. Zheng, J.G. Chen, Y. Yan, Correlating hydrogen oxidation and evolution activity on platinum at different pH with measured hydrogen binding energy, Nat. Commun. 6 (2015) 6–11. https://doi.org/10.1038/ncomms6848.

[139] E.S. Davydova, S. Mukerjee, F. Jaouen, D.R. Dekel, Electrocatalysts for Hydrogen Oxidation Reaction in Alkaline Electrolytes, ACS Catal. 8 (2018) 6665–6690. https://doi.org/10.1021/acscatal.8b00689.

[140] J. Ohyama, D. Kumada, A. Satsuma, Improved hydrogen oxidation reaction under alkaline conditions by ruthenium-iridium alloyed nanoparticles, J. Mater. Chem. A. 4 (2016) 15980–15985. https://doi.org/10.1039/c6ta05517f.

[141] J. Huang, P. Li, S. Chen, Quantitative Understanding of the Sluggish Kinetics of Hydrogen Reactions in Alkaline Media Based on a Microscopic Hamiltonian Model for the Volmer Step, J. Phys. Chem. C. 123 (2019) 17325–17334. https://doi.org/10.1021/acs.jpcc.9b03639.

[142] S. Lu, Z. Zhuang, Investigating the Influences of the Adsorbed Species on Catalytic Activity for Hydrogen Oxidation Reaction in Alkaline Electrolyte, J. Am. Chem. Soc. 139 (2017) 5156–5163. https://doi.org/10.1021/jacs.7b00765.

[143] J. Durst, A. Siebel, C. Simon, F. Hasché, J. Herranz, H.A. Gasteiger, New insights into the electrochemical hydrogen oxidation and evolution reaction mechanism, Energy Environ. Sci. 7 (2014) 2255–2260. https://doi.org/10.1039/c4ee00440j.

[144] L. fan Shen, B. an Lu, X. ming Qu, J. yu Ye, J. ming Zhang, S. hu Yin, Q. hui Wu, R. xiang Wang, S. yu Shen, T. Sheng, Y. xia Jiang, S. gang Sun, Does the oxophilic effect serve the same role for hydrogen evolution/oxidation reaction in alkaline media?, Nano Energy. 62 (2019) 601–609. https://doi.org/10.1016/j.nanoen.2019.05.045.

[145] J. Zheng, W. Sheng, Z. Zhuang, B. Xu, Y. Yan, Universal dependence of hydrogen oxidation and evolution reaction activity of platinum-group metals on pH and hydrogen binding energy, Sci. Adv. 2 (2016) 1–9.

https://doi.org/10.1126/sciadv.1501602.

[146] J. Hu, K.A. Kuttiyiel, K. Sasaki, C. Zhang, R.R. Adzic, Determination of Hydrogen Oxidation Reaction Mechanism Based on Pt−H ad Energetics in Alkaline Electrolyte , J. Electrochem. Soc. 165 (2018) J3355–J3362. https://doi.org/10.1149/2.0471815jes.

[147] Y. Wang, G. Wang, G. Li, B. Huang, J. Pan, Q. Liu, J. Han, L. Xiao, J. Lu, L. Zhuang, Pt-Ru catalyzed hydrogen oxidation in alkaline media: Oxophilic effect or electronic effect?, Energy Environ. Sci. 8 (2015) 177–181. https://doi.org/10.1039/c4ee02564d.

[148] M. Alesker, M. Page, M. Shviro, Y. Paska, G. Gershinsky, D.R. Dekel, D. Zitoun, Palladium/nickel bifunctional electrocatalyst for hydrogen oxidation reaction in alkaline membrane fuel cell, J. Power Sources. 304 (2016) 332–339. https://doi.org/10.1016/j.jpowsour.2015.11.026.

[149] M.T.M. Koper, Hydrogen electrocatalysis: A basic solution, Nat. Chem. 5 (2013) 255–256. https://doi.org/10.1038/nchem.1600.

[150] S.M. Rossnagel, Thin film deposition with physical vapor deposition and related technologies, J. Vac. Sci. Technol. A Vacuum, Surfaces, Film. 21 (2003) S74–S87. https://doi.org/10.1116/1.1600450.

[151] I. Safi, Recent aspects concerning DC reactive magnetron sputtering of thin films: A review, Surf. Coatings Technol. 127 (2000) 203–218. https://doi.org/10.1016/s0257-8972(00)00566-1.

[152] Y.S. Jung, J.Y. Seo, D.W. Lee, D.Y. Jeon, Influence of DC magnetron sputtering parameters on the properties of amorphous indium zinc oxide thin film, Thin Solid Films. 445 (2003) 63–71. https://doi.org/10.1016/j.tsf.2003.09.014.

[153] Paul van der Heide, X-ray Photoelectron Spectrocopy: An Introduction to Principles and Practices, John Wiley & Sons, Ltd., 2012.

[154] and K.D.B. J. F. Moulder, W. F. Stickle, P. E. Sobol, Handbook of x-ray photoelectron spectroscopy: a reference book of standard spectra for indentification and interpretation of XPS data, 1995.

[155] S. Hiifner, Photoelectron Spectroscopy: Principles and Applications, 3rd Editio, Springer US, 2003.

[156] J. Schnadt, J. Knudsen, N. Johansson, Present and new frontiers in materials research by ambient pressure x-ray photoelectron spectroscopy, J. Phys. Condens. Matter. 32 (2020). https://doi.org/10.1088/1361-648X/ab9565.

[157] Scanning Electron Microscopy 1928 – 1965 *, 17 (1995) 175–185.

[158] K.C.A. Smith, C.W. Oatley, The scanning electron microscope and its fields of application, Br. J. Appl. Phys. 6 (1955) 391–399. https://doi.org/10.1088/0508-3443/6/11/304.

Paper I

Enhanced oxygen reduction activity with rare earth metal alloy catalysts in proton exchange membrane fuel cells

B. Eriksson, G. Montserrat-Sisó, R. Brown, T. Skála, R. W. Lindström, G. Lindbergh, B. Wickman, C. Lagergren

Electrochimica Acta (In revision)

Enhanced oxygen reduction activity with rare earth metal alloy catalysts in proton exchange membrane fuel cells

Björn Eriksson[1*], Gerard Montserrat-Sisó[2], Rosemary Brown[2], Tomáš Skála[3], Rakel Wreland Lindström[1], Göran Lindbergh[1], Björn Wickman[2], Carina Lagergren[1]

[1]Applied Electrochemistry, Department of Chemical Engineering, School of Engineering Sciences in Chemistry, Biotechnology and Health, KTH Royal Institute of Technology, SE-100 44 Stockholm, Sweden

[2]Division of Chemical Physics, Department of Physics, Chalmers University of Technology, SE-412 96 Gothenburg, Sweden

[3]Faculty of Mathematics and Physics, Department of Surface and Plasma Science, Charles University, V Holešovičkách 2, CZ-18000 Prague, Czech Republic

Abstract

Alloying platinum is an approach to increase the oxygen reduction reaction (ORR) activity and at the same time reduce the amount of precious platinum catalyst in proton exchange membrane fuel cells (PEMFC). In this work the cathode activity of thin films of rare earth metals (REM) alloys, Pt_3Y, Pt_5Gd and Pt_5Tb, produced by sputter deposition onto gas diffusion layers, are evaluated in a fuel cell by means of polarization curves in O_2/H_2, and cyclic- and CO-stripping voltammetry in N_2/5 % H_2. Prior to evaluation, the model electrodes were acid-treated to obtain a Pt skin covering the PtREM alloy bulk, as was revealed by energy-dispersive X-ray spectroscopy (EDX) and X-ray photoelectron spectroscopy (XPS). The core shell alloys of Pt_3Y and Pt_5Gd catalysts show a specific activity enhancement at 0.9 V of 2.5 times compared to pure Pt. The slightly lower enhancement factor of 2.0 for Pt_5Tb is concluded to be due to leaching of the REM, that resulted in a thicker, and subsequently less strained, Pt overlayer. The high activity, combined with the minor changes in surface composition, achieved in the fuel cell environment shows that PtREM core shell catalysts are promising for the cathode reaction in PEMFC.

Keywords: Proton exchange membrane fuel cell, Platinum rare earth metal alloy, Oxygen reduction reaction

Highlights

- Sputter deposition of Pt_3Y, Pt_5Gd and Pt_5Tb as cathode catalysts in PEMFCs
- ORR enhancement factor of 2.5 for Pt_3Y and Pt_5Gd and 2.0 for Pt_5Tb
- Only minor changes in surface composition after fuel cell measurements

1. Introduction

For a sustainable energy society, not relying on combustion of fossil fuels, fuel cells will be important alternatives, especially within the transport sector, where high energy density is necessary. For fuel cells to reach full scale commercialization, a reduction of total cost is required [1]. One of the most expensive components in proton exchange membrane fuel cells (PEMFC) is the platinum catalyst.

High amounts of platinum catalyst are required for the sluggish oxygen reduction reaction (ORR). One approach to decrease the amount of platinum is to develop more active catalysts. While platinum is an efficient catalyst for ORR, it is not optimal. The kinetics of the ORR on platinum catalysts are limited by the strong OH binding energy, and by lowering the binding energy of OH on Pt(111) by approximately 0.1 eV, the activity could be increased by an order of magnitude [2,3]. The binding energy can be shifted by introducing an alloying material. This has been achieved with Ni, resulting in an increase in mass activity, compared to pure platinum, of an order of magnitude in rotating disk measurements (RDE) [4–7]. However, PtNi alloys are not completely stable in PEMFC, and can dealloy [8,9], leading to a decrease in activity with time and usage.

Alloying Pt with a rare earth metal (REM) is a promising alternative to PtNi catalysts. Due to the more negative energy of formation of the alloy, the REM should be more energetically favored to stay in the bulk, which should increase the stability compared to platinum alloys with late transition metals [3]. Several PtREM materials have been tested in RDE [2,10–16]. For these the activity increase has been reported to be between 6 and 7 times the specific activity of pure platinum, and up to an order of magnitude in mass activity, compared to platinum nanoparticles. Further, the cost of REM-oxides are several orders of magnitudes lower and their abundance several orders of magnitude higher than that of Pt [17]. However, even if the alloy catalysts perform well in RDE it is not certain that the same activity increase will be found in a fuel cell, as the conditions in RDE are not comparable with the PEMFC environment.

In our previous study in a real fuel cell setup, we found that model electrodes with sputtered thin films of Pt_3Y in contact with a Nafion membrane had approximately double the activity compared to sputtered platinum [18]. Part of the reason why the Pt_3Y films were less active in the fuel cell is likely due to the fact that they were sputtered on to the microporous layer (MPL) of the gas

diffusion layer (GDL), leading to uneven and non-optimal structure of the alloy. However, it is still not clear if this accounts for the whole difference in activity or if there are processes specific to the fuel cell environment that are mainly responsible. Previous studies with Pt_3Y in fuel cells have shown increase in specific activity by a factor between 2 and 3 compared to Pt/C [19,20]. It is also of great interest to see if other PtREM alloys, which display high activity in RDE, perform similarly under real fuel cell conditions [11].

In this study, thin film electrodes based on Pt_3Y, Pt_5Gd and Pt_5Tb are evaluated and compared in a PEMFC in a similar manner as in our previous work [18]. The thin-film electrodes can be seen as a two-dimensional model electrode used to study new catalyst in a more realistic fuel cell environment than for instance acid solutions used for RDE measurements. Thin-film electrodes allow for more accurate determination of oxygen reduction activity compared to a porous electrode, as effects from local mass transport, potential and humidity will not affect the electrodes to the same extent. The film thickness of 60 nm was chosen to give a relatively robust film. The MPL support was considered porous enough for sufficient supply of oxygen. Pt_3Y was chosen due to its high performance in our previous study [18], while Pt_5Gd and Pt_5Tb were chosen due to their reported high performance in RDE studies [2,10,21]. Physical characterization of the samples confirms the formation of a Pt overlayer after acid treatment, which leads to an increase in electrochemical activity. The overlayer and activity persists throughout the electrochemical testing, showing that these alloys are stable during fuel cell operation. These results highlight that PtREM catalysts are active and stable in an operating fuel cell.

2. Experimental

2.1 Sputter deposition of alloy catalysts

Thin films of Pt, Pt_3Y, Pt_5Tb and Pt_5Gd were deposited using single pure metal or alloy targets (from Goodfellow) using magnetron sputtering in a Nordiko 2000 sputter coater onto the MPL of the GDL (Carbel Cl). The base pressure of the sputtering system was lower than 1.0×10^{-6} mbar and sputtering was performed in 6.6 mbar under 50 sccm of argon flow. All sputtered films were 60 nm in thickness and thus the initial platinum loadings of the gas diffusion electrodes (GDEs) were 129 $\mu g_{Pt}/cm^2$ for Pt, 99 $\mu g_{Pt}/cm^2$ for Pt_3Y, 108.4 $\mu g_{Pt}/cm^2$ for Pt_5Gd and 108.8 $\mu g_{Pt}/cm^2$ for Pt_5Tb.

2.2 MEA assembly

For all PEMFC measurements the following membrane electrode assembly (MEA) preparation was used. An 11 mm diameter circular thin-film electrode was punched from the sputtered GDL. Prior to MEA assembly the GDE were treated in 0.1 M $HClO_4$ for a total of 45 min, and rinsed with water every 15 min. This step is required to remove surface oxides of the REM alloys and create a platinum skin on top of the alloy. To avoid the effects of hydrogen crossover in the fuel cell measurement, the model electrode was assembled with a double MEA [18]. A schematic of the double MEA configuration is shown in Figure S10 in the supporting information. The assembly consisted of a Sigracet 25BC GDL (20 mm in diameter) at the anode side, then a commercial MEA (loading of 0.45 and 0.4 $mg_{catalyst}cm^{-2}$) providing both the anode electrode and an interlayer of Pt catalyst. Finally, a Nafion 212 membrane was placed between the sputtered GDE and the commercial MEA, insulating the interlayer Pt from contact with the cathode GDE. Prior to any measurements, the MEA was pressed within the cell house using a clamping pressure of 12 bar at 80 °C for 30 s.

2.3 Electrochemical measurements

All measurements were performed using an in-house developed single cell with a spiral flow field [22,23]. First the cell was heated to 80 °C, with a humidifier temperature of 80 °C. To avoid

condensation, the pipes between humidifier and cell were heated to 84 °C. Activation was performed by cycling between 0.9 and 0.6 V, for 2000 cycles with a sweep rate of 20 mVs^{-1} with H_2 and O_2 gas with flow rates of 14.8 ml_n min^{-1} and 29.4 ml_n min^{-1}. After this the O_2 flow was lowered to 7.4 ml_n/min^{-1} and 100 cycles between 0.9 and 0.3 V were performed. Then the polarization curve was obtained by sweeping between 0.9 and 0.3 V with a sweep rate of 1 mVs^{-1} three times and taking the average of the forward sweeps. The setup was then cooled with nitrogen flow overnight. The next day the gases were switched to 5% H_2 in Ar at the anode (counter and reference electrode) and N_2 at the cathode (working electrode) in order to be able to do cyclic voltammetry (CV) and CO-stripping voltammetry in the fuel cell environment. The cyclic voltammetry was performed between 0.1 and 1.2 V, with a scan rate of 200 mV s^{-1} for 20 cycles, then with a sweep rate of 100 mV s^{-1} for 20 cycles, and finally with sweep rate of 20 mV s^{-1} for 2 cycles. Afterwards, CO-stripping was done by first recording a baseline CV between 0.1 and 1.2 V, with a scan rate of 200 mV s^{-1} for 5 cycles. This was followed by a potential hold at 0.15 V, where the gas at the cathode was switched to 2% CO in Ar for 2 min. The gas was then switched back to N_2 for 5 min purge at the same potential to ensure that all unreacted CO was removed before measuring the stripping curve in a CV as described above. The CO-stripping procedure was repeated four times. All electrochemical measurements were performed using a PAR 273A potentiostat.

2.4 Physical characterization

The X-ray photoelectron spectroscopy (XPS) (PerkinElmer PHI 5000 C ESCA system) analysis was used to study the surface composition of the four thin films (Pt, Pt_3Y, Pt_5Gd and Pt_5Tb). The surface analysis was performed using a monochromatic AlKα (1486.7 eV) X-ray source and the concentric hemispherical analyzer was positioned at a 45° angle with respect to the sample normal. Measurements with XPS were performed for as sputtered samples, acid treated, and after electrochemical testing in the single cell fuel cell setup. For all samples, the binding energy scale was adjusted by shifting the spectra with respect to the Pt $4f_{7/2}$-peak at 71.2 eV. We notice that this choice of binding energy adjustment placed the C1s peak around 284.4 eV on all samples.

Scanning electron microscopy (SEM) with energy-dispersive X-ray spectroscopy (EDX) was used to image and characterize the deposited catalysts. SEM was performed using a Zeiss Supra 60VP

field-emission microscope at 10 kV acceleration voltage and a working distance around 4 mm. EDX was performed in the same microscope with an IXRF spectroscopy unit. The working distance of the sample was increased to 23 mm and the acceleration voltage to 20 kV during EDX.

The synchrotron radiation photoelectron spectroscopy (SRXPS) measurements were carried out at the Materials Science Beamline (MSB) at the Elettra synchrotron light source in Trieste on an ultra-high vacuum (UHV) end-station with a base pressure below 5×10^{-10} mbar. With a bending magnet source, the MSB provides synchrotron light of a high intensity in the energy range of 21 – 1000 eV. The UHV experimental chamber is equipped with a hemispherical electron energy analyzer (Specs Phoibos 150). Pt_3Y, Pt_5Gd and Pt_5Tb on GDL were measured in the SRXPS before acid treatment (as-deposited), post acid treatment and after measurement in fuel cell. While conventional XPS allows for surface characterization of the samples the SRXPS measurements allow for both more accurate characterization, as well as allowing for depth probing by adjusting the photon energies.

The spectra of interest were Pt 4f, Y 3d, O 1s and C 1s acquired with photon energies of 250, 410, 650 and 990 eV, respectively. The total spectral resolutions were about 200 meV ($h\nu$ = 250 eV), 410 meV ($h\nu$ = 410 eV), 650 meV ($h\nu$ = 650 eV) and 1 eV ($h\nu$ = 990 eV).

Spectra were fitted using KolXPD software. Before fitting, each spectrum was charge corrected using the Fermi edge measured with the same photon energy. A linear background was subtracted from all data. In case of the core level Pt 4f spectra fitting procedure, the doublet separation for Pt 4f doublet components was set to 3.33 eV and the area ratio to 1.33 [18, 19], the energy position of the $4f_{7/2}$ peak was constrained to be between 70 and 71 eV. The metallic component of Pt 4f was fitted using a Donaich-Šunjić line shape setting the asymmetry to 0.19 [21]. The asymmetry contribution for the adsorbed CO component was allowed to vary from 0 to 0.19 and the oxide component was fitted with a Voigt line shape with no asymmetry.

The core level Y 3d spectra were fitted with Voigt line shapes with a doublet split of 2.1 eV and area ratio of 1.5 [22]. The Lorentzian and Gaussian line widths were kept equal for all components. The metallic peak ($3d_{5/2}$) was constrained to be between 155.9 and 156.2 eV and the oxide between 158 and 158.3 eV [24–28]. Substochiometric oxide was set to vary around 157 eV. Gadolinium 4d core level spectrum is reported to be composed of a broad multiplet structure but was fitted

using a single doublet with a doublet separation of 5.4 eV and doublet ratio of 1.5 for Gd $4d_{5/2}$-Gd $4d_{3/2}$ [29] Donaich-Šunjić line shapes were used for the fitting with no asymmetry. The metallic Gd peak ($4d_{5/2}$) was set at 140.6 eV (± 0.2 eV) and the Gd_2O_3 peak at 142.8 eV (± 0.2 eV), which are consistent with previously reported Gd peaks [30–32]. Likewise, terbium 4d spectrum presents a complex multiplet structure that was fit using singlets instead of doublets due to the lack of reliable literature for the doublet structure. It presents two different oxidation states (Tb^{3+} and Tb^{4+}) composing a mixed oxide (Tb_4O_7) [29,33,34].Voigt line shapes with no asymmetry were used for the fitting of the three states. The metallic Tb peak ($4d_{5/2}$) was constrained at 147.5 eV, Tb^{3+} at 150.7 eV and Tb^{4+} at 154.6 eV [35,36] . All Tb peaks were allowed to vary by ± 0.2 eV.

3 Results and discussion

3.1 Electrochemical characterization

As the introduction of an alloying element should affect the structure energy of Pt skin, CV and CO-stripping were employed to electrochemically investigate the catalyst surfaces. The shape and position of the hydrogen adsorption/desorption (HAD) and the PtO redox peaks in the base CV as well as the CO-oxidation peak in CO-stripping voltammetry give information about the surface structure of the platinum [37–40]. The cyclic voltammetry sweeps for all PtREM samples, compared to pure platinum, are shown in Figure 1. As can be seen the general features for all CVs are the same. This means that all alloy catalysts have pure platinum on their surfaces. Further, as no new peaks are visible in the alloyed samples, the REMs are not electrochemically active in the investigated potential region. Nevertheless, the alloyed catalysts have shifts in their potential responses, which indicate alterations of the surface properties compared to pure platinum. The main change that can be observed is the shift of the oxide reduction peak, which can be seen in the negative sweep between 0.9 and 0.6 V, Figure S9. For all alloys there is a negative shift in potential for the oxide reduction peak in comparison to pure Pt. For Pt_3Y and Pt_5Gd this shift is significant, on average 20 mV, while Pt_5Tb only exhibits a very slight shift of 10 mV to lower potentials.
The corresponding CO-stripping results are shown in Figure 2. The CO-oxidation peak for the pure Pt sample is split into two with a sharp spike at 0.75 V and a small peak at 0.80 V. For the alloys the second peak at 0.80 V is much smaller or absent. In most cases there is a slight shift to lower potentials for the onset of the CO-oxidation peak, when compared to pure platinum, but the variations between samples are relatively high. This is consistent with the shift in the oxide peaks and suggests that the surface has been modified by the presence of the alloy bulk. The shift for CO is smaller than for the oxides, which is expected. For Pt_5Gd and Pt_5Tb, samples with a more CO-oxidation charge at lower potentials had lower activity. This could be due to an increased number of surface defects for these samples, which might explain the lower oxygen reduction activity [40].

The polarization curves for three samples of the Pt_3Y and Pt_5Gd, and Pt_5Tb thin film alloys are shown in Figure 3. To ensure proper alloy composition the sputtered films were intentionally made flat and thick. This results in low electrochemical active surface area per mass platinum, and

subsequently poor platinum utilization. As such these electrodes give a good model system for studying catalytic activity in a fuel cell, but are not optimal electrodes for an operating fuel cell. As the main focus of the study is primarily the kinetic activity of the catalyst in a fuel cell, all results will be reported in specific current density based on the measured Pt electrochemical surface area from the CO-stripping measurements, as shown in Figure 2. Polarization curves of geometric surface area and mass activity are shown in Figure S6 and Figure S7 in the supporting information. CO-stripping was chosen to measure the electrochemical surface area (ECSA) due to hydrogen adsorption/desorption (HAD) often underestimates the ECSA, especially when measuring alloy catalysts and MEAs [38,39]. For all the investigated samples the ECSA obtained from HAD was approximately 50% lower than that obtained from CO-stripping.

As can be seen, the specific activity for all alloys is higher than that of pure platinum. The activity increases, shown in Table 1, are approximately 2.5 times higher for Pt_3Y and Pt_5Gd, and about 2 times higher for Pt_5Tb. The lower activity for Pt_5Tb, compared to Pt_3Y and Pt_5Gd, could be due to the lower stability of Pt_5Tb [2]. While the stabilities of the alloy catalysts have not been specifically measured, it should be noted that all samples have been cycling between 0.9 and 0.6 V for ~16 h before the activity measurement. As seen in Table 1, the activity increase at 0.75 V is lower than at 0.9 V. This is most likely due to other effects, such as local mass transport, affecting the measurement. Nevertheless, all the alloys show higher activity, at 0.75 V, with improvements of 1.7 for Pt_3Y, 1.5 for Pt_5Gd and 1.6 for Pt_5Tb. The previously reported activity for Pt/C nanoparticles is approximately 200 μAcm^{-2}_{Pt} [41]. The sputtered films of pure platinum have a higher activity of 280 μAcm^{-2}_{Pt}, compared to nanoparticles, which was also observed in RDE measurements [11]. This is attributed to strains in the platinum films from substrate interactions [42]. Comparing the measured alloys to the activity of platinum nanoparticles gives improvement factors of 3.5 for Pt_3Y and Pt_5Gd, and 2.7 for Pt_5Tb. The mass activities, at 0.9 V, of the sputtered electrodes are 0.011 (Pt), 0.026 (Pt_3Y), 0.028 (Pt_5Gd) and 0.018 A/mg_{Pt} (Pt_5Tb). The low values compared to 0.15 A/mg_{Pt} for Pt/C electrodes [8] is due to that the sputtered 60 nm catalyst has a much lower surface to volume ratio compare to nanoparticle catalysts. Even so, the corresponding mass-activity increase of the alloyed films at 0.9 V is significant, compared to the platinum film, being a factor of 2.8 (Pt_3Y), 1.7 (Pt_5Gd), and 2.2 (Pt_5Tb).

Considering the large variation of activity between samples, the activity increase as a function of mean oxide peak position and ECSA were investigated more closely. When comparing the mean oxide reduction peak position, calculated from the reduction charge from Figure 1, with activity it can be seen that the more active samples exhibit a peak position at slightly lower potentials, as shown in Figure 4a. However, a shift to lower potentials would indicate an increase in binding energy, not the expected decrease [2,3,21]. The shifts detected here are most likely due to the presence of several crystal planes of platinum. Exactly what is causing the negative shift in peak position is still unclear, but the shift has been reported previously for sputtered PtREM catalysts [10,11,43,44]. Figure 4b shows the activity increase as a function of the ECSA. The cause of the large in-sample variance of ECSA for the Pt-REM samples is at present not fully understood. Possible explanations could be variations of the MPL causing changes in the sputtered layers. The results indicate a trend that the lower the ECSA, the higher the measured activity. Previous studies have shown that sputter deposition onto an MPL creates particles with varying size, with regions that are less than 3 nm [16]. These thin regions fully leach out the REM during acid treatment, and become pure platinum. As such, a high ECSA could indicate that the sample has more of these pure platinum regions, which lowers the overall activity of the sample. Further, the ECSA value is an indication of the surface roughness of the samples, meaning that a low ECSA indicates flatter surface. This result suggests that if the surface becomes too rough, the macrostrain caused by the alloy become less significant, lowering the expected activity increase. A rougher surface could indicate that the surface has more disordered platinum, which is less active compared to the ordered structure [40,45].

The electrochemical results show that the presence of an alloying element affects the electrochemical properties of platinum, which results in higher intrinsic activity. The shifts in potential can be seen in the CVs and CO-stripping measurements, however, due to the polycrystalline nature of the sputtered films, the exact cause of the shifts is difficult to quantify.

3.2 Physical characterization

The samples were physically characterized by energy-dispersive X-ray spectroscopy (EDX), which has a sensing depth in the micrometer range and, thus, gives information about the bulk composition of the sputtered films. Figure 5a shows the Pt:REM bulk composition ratio of the three different alloys as sputtered, after acid treatment, and after electrochemical test. The EDX analysis confirms that the bulk nominal composition obtained is very close to that of the sputter target alloys with the ratios 3:1 (Pt_3Y) and 5:1 (Pt_5Gd and Pt_5Tb). The spread in REM content after acid treatment and fuel cell operation, falls into the EDX error margin expected for samples supported onto porous surfaces [46]. Therefore, it appears all alloys maintain their bulk composition after acid treatment and fuel cell operation, indicating that the bulk alloy is mostly unchanged and the platinum overlayer, which forms after acid treatment, is so thin it does not affect the bulk composition.

The samples were also characterized by X-ray photoelectron spectroscopy (XPS), which has a probing depth of a few nanometers, meaning only the surface elemental composition of these films is determined. The XPS results for all tested alloys are shown in Figure 5b. The as-sputtered samples all showed a much larger Pt:REM surface relative amount than given by nominal ratios, which is also considerably larger than the ratio measured in EDX, thereby suggesting that there is a surface enrichment of REM during sputtering. During acid treatment the surface REMs that oxidized, due to contact with air, were removed. This is the cause for the large reduction of REM seen in the XPS, more pronounced than in EDX. After the electrochemical tests, all alloys show a decrease in their total surface REM content to only between 5 and 7% remaining close to the surface. This can be attributed to the further leaching of the alloy and an increase in overlayer thickness as a result of the exposure to the acidic fuel cell environment and the electrochemical reactions taking place during fuel cell evaluation [11,18].

To present the oxide and metallic REM XPS data in more detail, the fitted spectra for the REM components Y 3d (Pt_3Y), Gd 4d (Pt_5Gd) and Tb 4d (Pt_5Tb), as sputtered, after acid treatment, and after fuel cell measurements are shown in Figure 6. For all alloys, similar trends can be observed. The as-sputtered samples all have peaks corresponding mainly to the non-metallic state of the

REM. The non-metallic peaks in the as-sputtered samples are attributed to the formation of oxides as a result of exposure to ambient atmosphere after sputter deposition [13]. After acid treatment, the amount of REM to platinum decreases as oxidized REM is removed from the surface resulting in a significant reduction in intensity of the Y 3d, Gd 4d, and Tb 4d core level peaks. Before treatment, all REM in contact with the air is oxidized so the surface contains mostly REM-oxide and some metallic REM in the layers below. Acid treatment removes the REM-oxides, leaving only metallic REM in the bulk material. Thus, a layer of platinum is formed where the REM-oxides were leached. This is also in accordance with previous results showing the formation of a protective Pt overlayer when PtREM samples are immersed in an acidic solution, in accordance with previous RDE studies [2,21,43]. The REM peaks in the XPS spectra of Pt_5Gd and Pt_5Tb are reduced in amplitude as they contain much less REM than Pt_3Y. Additionally, the XPS cross-sections for Tb and Gd are also lower than Y which further decreases signal making quantitative analysis of the peak constituents difficult to perform. The amount of oxides remaining after acid treatment seems to be higher for Pt_5Gd and Pt_5Tb, compared to Pt_3Y, which can be attributed to either subsurface REM-oxides present also after acid treatment or some REM–O coordination in the thin film surface [10,47].

After fuel cell operation, the amount of REM-oxide decreases for all samples. This result suggests that the electrochemical measurements cause additional leaching from beneath the surface. There were no significant changes observed in the Y 3d and Gd 4d peaks for Pt_3Y and Pt_5Gd, only a slight reduction in the total amount of REM near the surface. For Pt_5Tb, a slight decrease in the total and metallic amount of Tb is observed. The relatively low amount of metallic Tb observed in XPS, compared to the others, might explain the somewhat lower fuel cell performance of this alloy. The differences between the XPS data after acid treatment and electrochemical measurements suggest that the alloys are affected differently by the fuel cell environment. As such, there might be different optimal activation strategies for each type of alloy, which can lead to higher ORR activities.

In general, the overlayer thickness increases after fuel cell use as the total amount of REM decreases for all alloys. Films sputtered on a porous and particulate GDL are not flat and have thickness variation, this is shown in Figure S4 and Figure S5 in the supporting information, so

some areas of the sputtered films are thin and allow complete oxidation of the REM [18]. Regions under 3 nm in thickness are less active, as the REM leaches from the bulk to become pure Pt after acid treatment [11]. Fuel cell operation causes further leaching and an increase in the areas of pure Pt. Hence, catalyst layers sputtered onto GDL have lower increases in activity, compared to the RDE measurements of the same alloys on flat glassy carbon substrates [11].

Synchrotron radiation can provide a depth profile of the surface composition through changing beam energy and can reveal surface impurities. In a synchrotron, lower photon energies than in lab-XPS are used to reduce the depth probed and gain more surface sensitivity. In general, Tb and Gd produce less signal than Y as they have lower photoionization cross-sections, so it is harder to measure them with low photon energies provided by a synchrotron, especially in the low alloy concentrations used in this study. Therefore, it was only possible to measure Pt_3Y in this manner. Measurements of the Y 3d core level peak in Pt_3Y samples are presented in Figure 7.

Before acid treatment, all yttrium at the surface is oxidized, as indicated by the two oxide doublets present in the Y 3d core level in Figure 7a, that are seen at higher eV compared to metallic yttrium. Pure yttrium oxide is the doublet at 158.3 eV and a substochiometric oxide is the doublet at 157.5 eV. As photon energy is increased there is more contribution from metallic yttrium as the relative amount of substochiometric oxide is reduced. Notably there is still a large contribution from yttrium oxide even at 990 eV corresponding to a depth of approximately 2.4 nm.

The acid treatment in 0.1 M $HClO_4$ removes most of the yttrium from the surface, shown in Figure 7b, as higher photon energies show only metallic yttrium remains due to the yttrium oxide being leached out. This confirms the formation of the platinum overlayer. Our previous work studying flat sputtered Pt_3Y in the synchrotron showed more yttrium underneath the surface compared to the porous GDL substrates in this study [28]. This is due to the GDL structure, where Pt_3Y will also be sputtered around the edges of the carbon particles [11]. Acid treatment removes more yttrium on a GDL substrate compared to a flat substrate, as described above alongside lab-XPS [28]. Subsequent fuel cell exposure appears to remove a little more yttrium, nevertheless, the surface is mostly unchanged by the electrochemical testing and no additional surface impurities were observed.

Comparing the content of the surface for each photon energy reveals features of the catalyst layer on the GDL. Figure 8 summarizes the results of the fitting of the spectra showing the relative amount of Pt 4f and Y 3d corrected using the spectrometer transmission and elemental cross-section. There is an enrichment of surface REM and REM-oxides in the as-deposited sample, in agreement with the conventional XPS results presented in Figure 5b. At 990 eV the stoichiometry of the alloy is as expected. There is little difference between the amount of Pt:Y in the acid treated and fuel cell tested sample. On first glance it seems that there is slightly less yttrium in the fuel cell tested sample, observed by no REM being detected at 650 eV. However, due to the large noise and error in fitting it can be concluded that both samples have a very similar surface. Fuel cell tests conducted in the manner presented in this paper do not alter the catalyst surface significantly.

The presented results show that the specific activity for sputtered thin-film PtREM catalysts is superior to that of a thin film of pure Pt. The electrochemical and physical characterization both show that an overlayer has been formed, and that it remains after electrochemical testing. Further, after testing additional leaching of REM is minor. This leaching is most likely occurring in areas of the MPL where the deposited film is thinner and results in areas of pure Pt, which may be one of the explanations to the lower activities observed in the fuel cell compared to RDE. This is supported by the depth profiles in Figure 8, where no increase in overlayer thickness was observed. Further, the electrochemical measurements do not cause a significant change in the Pt_3Y, which has a nearly constant composition before and after the electrochemical testing. This suggests this alloy is stable in the operating range of a fuel cell. This is further supported by the SEM images, Figure S5 in supporting information, where no significant changes in morphology is observed after electrochemical testing. The effect of acid treatment and electrochemical evaluation in the fuel cell on the Pt_3Y surface properties was evaluated in detail by transmission electron microscopy (TEM) in our previous paper [18]. We expect that the other alloys have a similar behavior as Pt_3Y in that case. A more in-depth evaluation of the surface changes of Pt_3Y films during long-term fuel cell measurements including TEM and SRXPS is currently being carried out. Pt_5Gd shows similar trends as Pt_3Y with a similar amount of metallic REM before and after electrochemical testing. The lower measured activity of Pt_5Tb is most likely due to leaching of the REM, which causes a thicker, and subsequently less strained, Pt overlayer. Further studies are required to fully determine the stability of these materials. The large variation between samples as well as the similar values

between the investigated PtREM alloys suggests that the uneven substrate and the presence of undefined areas with no REM content are significantly affecting the catalyst activity. If these regions could be removed, even higher activities should be obtainable. Nevertheless, all evaluated alloy samples have higher activity compared to pure platinum, indicating that PtREM alloy catalysts can achieve high activity in an active fuel cell.

4 Conclusion

In this work the activity of sputtered thin films of Pt_3Y, Pt_5Gd and Pt_5Tb in a PEMFC were evaluated. It was found that the specific activity of Pt_3Y and Pt_5Gd were approximately 2.5 times that of pure platinum. The slightly lower activity enhancement of Pt_5Tb, approximately 2 times that of pure platinum, was due to lower amounts of metallic REM found after the electrochemical tests, most likely due to the formation of a thicker platinum layer. This suggests that Pt_5Tb is less stable than Pt_5Gd and Pt_3Y in PEMFC environment. Cyclic voltammetry and CO-stripping curves showed small potential shifts to higher binding energies for the oxide peaks. This is attributed to changes in the bulk composition of the alloys, caused by the introduction of the alloying element. XPS and EDX measurements showed that acid treatment removes surface REM-oxides. However, after electrochemical tests all alloys had different amounts of REM as well as different ratios between metallic and oxidized REM, suggesting that there might be different optimal activation strategies for the different alloys. If these strategies can be found, even higher activities could be achieved. Pt_3Y showed no significant change in the surface composition, suggesting that this alloy is the most stable under the experimental conditions. The high activity, combined with the low changes in surface composition, achieved in an operating fuel cell shows that PtREM catalysts are promising as ORR catalysts in PEMFC.

Acknowledgments

This work was supported by the Strategic Vehicle Research and Innovation program (FFI) (Project No. P37806-3), the Swedish Foundation for Strategic Research (SSF) (Project No. EM16-0060), the Swedish governmental initiative StandUp for Energy and the Swedish Research Council (Project No. 2018-03927). Sample fabrication was performed in part at Myfab, Chalmers. Dr. Niklas Lindahl is acknowledged for the initial sputter deposition of the PtREM samples. We thank CERIC-ERIC for access to the synchrotron facilities and for financial support.

References

[1] J. Marcinkoski, J. Spendelow, A. Wilson, D. Papageorgopoulos, P. Reviewed, R. Ahluwalia, B. James, C. Houchins, J. Moton, Fuel cell system cost -2015, DOE Hydrog. Fuel Cells Progr. Rec. Rec. (2015) 15015. https://www.hydrogen.energy.gov/pdfs/15015_fuel_cell_system_cost_2015.pdf.

[2] M. Escudero-Escribano, P. Malacrida, H.M. Hansen, U. Vej-Hansen, A. Velazquez-Palenzuela, V. Tripkovic, J. Schiøtz, J. Rossmeisl, I.E.L. Stephens, I. Chorkendorff, Tuning the activity of Pt alloy electrocatalysts by means of the lanthanide contraction, Science (80-.). 352 (2016) 73–76.

[3] J. Greeley, I.E.L. Stephens, a S. Bondarenko, T.P. Johansson, H. a Hansen, T.F. Jaramillo, J. Rossmeisl, I. Chorkendorff, J.K. Nørskov, Alloys of platinum and early transition metals as oxygen reduction electrocatalysts., Nat. Chem. 1 (2009) 552–6. https://doi.org/10.1038/nchem.367.

[4] R. Sakamoto, K. Omichi, T. Furuta, M. Ichikawa, Effect of high oxygen reduction reaction activity of octahedral PtNi nanoparticle electrocatalysts on proton exchange membrane fuel cell performance, J. Power Sources. 269 (2014) 117–123. https://doi.org/10.1016/j.jpowsour.2014.07.011.

[5] C. Chen, Y. Kang, Z. Huo, Z. Zhu, W. Huang, H.L. Xin, J.D. Snyder, D. Li, J.A. Herron, M. Mavrikakis, M. Chi, K.L. More, Y. Li, N.M. Markovic, G.A. Somorjai, P. Yang, V.R. Stamenkovic, Highly crystalline multimetallic nanoframes with three-dimensional electrocatalytic surfaces, Science (80-.). 343 (2014) 1339–1343. https://doi.org/10.1126/science.1249061.

[6] M. Li, Z. Zhao, T. Cheng, A. Fortunelli, C.Y. Chen, R. Yu, Q. Zhang, L. Gu, B. V. Merinov, Z. Lin, E. Zhu, T. Yu, Q. Jia, J. Guo, L. Zhang, W.A. Goddard, Y. Huang, X. Duan, Ultrafine jagged platinum nanowires enable ultrahigh mass activity for the oxygen reduction reaction, Science (80-.). 354 (2016) 1414–1419. https://doi.org/10.1126/science.aaf9050.

[7] D. Van Der Vliet, C. Wang, M. Debe, R. Atanasoski, N.M. Markovic, V.R. Stamenkovic, Platinum-alloy nanostructured thin film catalysts for the oxygen reduction reaction, Electrochim. Acta. 56 (2011) 8695–8699. https://doi.org/10.1016/j.electacta.2011.07.063.

[8] A. Kongkanand, M.F. Mathias, The priority and challenge of high-power performance of low-Platinum proton-exchange membrane fuel cells, J. Phys. Chem. Lett. 7 (2016) 1127–1137. https://doi.org/10.1021/acs.jpclett.6b00216.

[9] K.J.J. Mayrhofer, K. Hartl, V. Juhart, M. Arenz, Degradation of carbon-supported Pt bimetallic nanoparticles by surface segregation, J. Am. Chem. Soc. 131 (2009) 16348–16349. https://doi.org/10.1021/ja9074216.

[10] E. Zamburlini, K.D. Jensen, I.E.L. Stephens, I. Chorkendorff, M. Escudero-Escribano, Benchmarking Pt and Pt-lanthanide sputtered thin films for oxygen electroreduction: fabrication and rotating disk electrode measurements, Electrochim. Acta. 247 (2017) 708–721. https://doi.org/10.1016/j.electacta.2017.06.146.

[11] N. Lindahl, E. Zamburlini, L. Feng, H. Grönbeck, M. Escudero-Escribano, I.E.L. Stephens, I. Chorkendorff, C. Langhammer, B. Wickman, High specific and mass activity for the oxygen reduction reaction for thin film catalysts of sputtered Pt3Y, Adv. Mater. Interfaces. 4 (2017) 1–9. https://doi.org/10.1002/admi.201700311.

[12] R. Sandström, E. Gracia-Espino, G. Hu, A. Shchukarev, J. Ma, T. Wågberg, Yttria stabilized and surface activated platinum (PtxYOy) nanoparticles through rapid microwave assisted synthesis for oxygen reduction reaction, Nano Energy. 46 (2018) 141–149. https://doi.org/10.1016/j.nanoen.2018.01.038.
[13] F. Masini, P. Hernández-Fernández, D. Deiana, C.E. Strebel, D.N. McCarthy, A. Bodin, P. Malacrida, I. Stephens, I. Chorkendorff, Exploring the phase space of time of flight mass selected Pt $_x$ Y nanoparticles, Phys. Chem. Chem. Phys. 16 (2014) 26506–26513. https://doi.org/10.1039/C4CP02144D.
[14] P. Hernandez-Fernandez, F. Masini, D.N. McCarthy, C.E. Strebel, D. Friebel, D. Deiana, P. Malacrida, A. Nierhoff, A. Bodin, A.M. Wise, J.H. Nielsen, T.W. Hansen, A. Nilsson, I.E.L. Stephens, I. Chorkendorff, Mass-selected nanoparticles of PtxY as model catalysts for oxygen electroreduction, Nat. Chem. (2014) 1–23. https://doi.org/10.1038/nchem.2001.
[15] R. Brandiele, A. Guadagnini, L. Girardi, G. Dražić, M.C. Dalconi, G.A. Rizzi, V. Amendola, C. Durante, Climbing the oxygen reduction reaction volcano plot with laser ablation synthesis of Pt: xY nanoalloys, Catal. Sci. Technol. 10 (2020) 4503–4508. https://doi.org/10.1039/d0cy00983k.
[16] R. Brandiele, C. Durante, E. Gradzka, G.A. Rizzi, J. Zheng, D. Badocco, P. Centomo, P. Pastore, G. Granozzi, A. Gennaro, One step forward to a scalable synthesis of platinum-yttrium alloy nanoparticles on mesoporous carbon for the oxygen reduction reaction, J. Mater. Chem. A. 4 (2016) 12232–12240. https://doi.org/10.1039/c6ta04498k.
[17] Y. Hu, J. Oluf Jensen, L. Nilausen Cleemann, B. Axel Brandes, Q. Li, Synthesis of Pt–rare earth metal nanoalloys, J. Am. Chem. Soc. 142 (2019) 953–961. https://doi.org/10.1021/jacs.9b10813.
[18] N. Lindahl, B. Eriksson, H. Grönbeck, R. Wreland Lindström, G. Lindbergh, C. Lagergren, B. Wickman, Fuel cell measurements with cathode catalysts of sputtered Pt3Y thin films, ChemSusChem. 11 (2018) 1438–1445. https://doi.org/10.1002/cssc.201800023.
[19] J.N. Schwämmlein, G.S. Harzer, P. Pfändner, A. Blankenship, H.A. El-Sayed, H.A. Gasteiger, Activity and stability of carbon supported PtxY alloys for the ORR determined by RDE and single-cell PEMFC measurements, J. Electrochem. Soc. 165 (2018) J3173–J3185. https://doi.org/10.1149/2.0221815jes.
[20] S.J. Yoo, K.-S. Lee, S.J. Hwang, Y.-H. Cho, S.-K. Kim, J.W. Yun, Y.-E. Sung, T.-H. Lim, Pt3Y electrocatalyst for oxygen reduction reaction in proton exchange membrane fuel cells, Int. J. Hydrogen Energy. 37 (2012) 9758–9765. https://doi.org/10.1016/j.ijhydene.2012.03.089.
[21] M. Escudero-Escribano, A.F. Pedersen, E.T. Ulrikkeholm, K.D. Jensen, M.H. Hansen, J. Rossmeisl, I.E.L. Stephens, I. Chorkendorff, Active-phase formation and stability of Gd/Pt(111) electrocatalysts for oxygen reduction: An in situ grazing incidence X-Ray diffraction study, Chem. - A Eur. J. 24 (2018) 12280–12290. https://doi.org/10.1002/chem.201801587.
[22] J. Ihonen, M. Mikkola, G. Lindbergh, Flooding of gas diffusion backing in PEFCs: Physical and electrochemical characterization, J. Electrochem. Soc. 151 (2004) 1152–1161. https://doi.org/10.1149/1.1763138.
[23] A. Oyarce, N. Holmström, A. Bodén, C. Lagergren, G. Lindbergh, Operating conditions affecting the contact resistance of bi-polar plates in proton exchange membrane fuel cells,

J. Power Sources. 231 (2013) 246–255. https://doi.org/10.1016/j.jpowsour.2012.12.100.
[24] J. Moulder, W. Stickle, P. Sobol, K. Bomben, Handbook of X-ray photoelectron spectroscopy, Perkin-Elmer Corp., Physical Electronics Division, Eden Prairie, Minnesota, USA, 1992. https://doi.org/10.1002/sia.740030412.
[25] A. Mesarwi, A. Ignatiev, X-ray photoemission study of Y-promoted oxidation of the Si(100) surface, Surf. Sci. 244 (1991) 15–21. https://doi.org/10.1016/0039-6028(91)90165-O.
[26] J.S. Kanady, P. Leidinger, A. Haas, S. Titlbach, S. Schunk, K. Schierle-Arndt, E.J. Crumlin, C.H. Wu, A.P. Alivisatos, Synthesis of Pt3Y and other early-late intermetallic nanoparticles by way of a molten reducing agent, J. Am. Chem. Soc. 139 (2017) 5672–5675. https://doi.org/10.1021/jacs.7b01366.
[27] R. Cui, L. Mei, G. Han, J. Chen, G. Zhang, Y. Quan, N. Gu, L. Zhang, Y. Fang, B. Qian, X. Jiang, Z. Han, Facile synthesis of nanoporous Pt-Y alloy with enhanced electrocatalytic activity and durability, Sci. Rep. 7 (2017) 1–10. https://doi.org/10.1038/srep41826.
[28] R. Brown, M. Vorokhta, I. Khalakhan, M. Dopita, T. Vonderach, T. Skála, N. Lindahl, I. Matolínová, H. Grönbeck, K.M. Neyman, V. Matolín, B. Wickman, Unraveling the surface chemistry and structure in highly active sputtered Pt3Y catalyst films for the oxygen reduction reaction, ACS Appl. Mater. Interfaces. 12 (2020) 4454–4462. https://doi.org/10.1021/acsami.9b17817.
[29] S.P. Kowalczyk, N. Edelstein, F.R. McFeely, L. Ley, D.A. Shirley, X-ray photoemission spectra of the 4d levels in rare-earth metals, Chem. Phys. Lett. 29 (1974) 491–495. https://doi.org/10.1016/0009-2614(74)85076-1.
[30] A. Velázquez-Palenzuela, F. Masini, A.F. Pedersen, M. Escudero-Escribano, D. Deiana, P. Malacrida, T.W. Hansen, D. Friebel, A. Nilsson, I.E.L. Stephens, I. Chorkendorff, The enhanced activity of mass-selected PtxGd nanoparticles for oxygen electroreduction, J. Catal. 328 (2015) 297–307. https://doi.org/10.1016/j.jcat.2014.12.012.
[31] D. Raiser, J.P. Deville, Study of XPS photoemission of some gadolinium compounds, J. Electron Spectros. Relat. Phenomena. 57 (1991) 91–97. https://doi.org/https://doi.org/10.1016/0368-2048(91)85016-M.
[32] J. L. M. Rupp, T. Drobek, A. Rossi, L. J. Gauckler, Chemical analysis of spray pyrolysis Gadolinia-doped Ceria electrolyte thin films for solid oxide fuel cells, Chem. Mater. 19 (2007) 1134–1142. https://doi.org/10.1021/cm061449f.
[33] L.M.W. and D.J.F. B. D. Padalia, W. C. Lang, P. R. Norris, X-Ray photoelectron core-level studies of the heavy rare-earth metals and their oxides, Proc. R. Soc. Lond. A. 425 (1989) 73–90.
[34] D.D. Sarma, C.N.R. Rao, XPES studies of oxides of second- and third-row transition metals including rare earths, J. Electron Spectros. Relat. Phenomena. 20 (1980) 25–45. https://doi.org/10.1016/0368-2048(80)85003-1.
[35] H. Yin, Y. Gao, H. Guo, C. Wang, C. Yang, Effect of B2O3 content and microstructure on Verdet constant of Tb2O3-doped GBSG magneto-optical glass, J. Phys. Chem. C. 122 (2018) 16894–16900. https://doi.org/10.1021/acs.jpcc.8b04989.
[36] S. Saini, H.S. Yaddanapudi, K. Tian, Y. Yin, D. Magginetti, A. Tiwari, Terbium ion doping in Ca3Co4O9: A step towards high-performance thermoelectric materials, Sci. Rep. 7 (2017) 44621. https://doi.org/10.1038/srep44621.
[37] O. Diaz-Morales, T.J.P. Hersbach, C. Badan, A.C. Garcia, M.T.M. Koper, Hydrogen adsorption on nano-structured platinum electrodes, Faraday Discuss. 210 (2018) 301–315.

https://doi.org/10.1039/c8fd00062j.
[38] T.R. Garrick, T.E. Moylan, M.K. Carpenter, A. Kongkanand, Electrochemically active surface area measurement of Aged Pt alloy catalysts in PEM fuel cells by CO stripping, J. Electrochem. Soc. 164 (2017) F55–F59. https://doi.org/10.1149/2.0381702jes.
[39] D.F. Van Der Vliet, C. Wang, D. Li, A.P. Paulikas, J. Greeley, R.B. Rankin, D. Strmcnik, D. Tripkovic, N.M. Markovic, V.R. Stamenkovic, Unique electrochemical adsorption properties of Pt-skin surfaces, Angew. Chemie - Int. Ed. 51 (2012) 3139–3142. https://doi.org/10.1002/anie.201107668.
[40] R. Chattot, I. Martens, M. Scohy, J. Herranz, J. Drnec, F. Maillard, L. Dubau, Disclosing Pt-bimetallic alloy nanoparticle surface lattice distortion with electrochemical probes, ACS Energy Lett. 5 (2020) 162–169. https://doi.org/10.1021/acsenergylett.9b02287.
[41] H. a. Gasteiger, S.S. Kocha, B. Sompalli, F.T. Wagner, Activity benchmarks and requirements for Pt, Pt-alloy, and non-Pt oxygen reduction catalysts for PEMFCs, Appl. Catal. B Environ. 56 (2005) 9–35. https://doi.org/10.1016/j.apcatb.2004.06.021.
[42] T. Daio, A. Staykov, L. Guo, J. Liu, M. Tanaka, S. Matthew Lyth, K. Sasaki, Lattice strain mapping of Platinum nanoparticles on carbon and SnO2 supports, Sci. Rep. 5 (2015) 1–10. https://doi.org/10.1038/srep13126.
[43] M. Escudero-Escribano, A. Verdaguer-Casadevall, P. Malacrida, U. Grønbjerg, B.P. Knudsen, A.K. Jepsen, J. Rossmeisl, I.E.L. Stephens, I. Chorkendorff, Pt5Gd as a highly active and stable catalyst for oxygen electroreduction., J. Am. Chem. Soc. 134 (2012) 16476–9. https://doi.org/10.1021/ja306348d.
[44] I.E.L. Stephens, A.S. Bondarenko, L. Bech, I. Chorkendorff, Oxygen electroreduction activity and X-ray photoelectron spectroscopy of platinum and early transition metal alloys, ChemCatChem. 4 (2012) 341–349. https://doi.org/10.1002/cctc.201100343.
[45] R. Chattot, O. Le Bacq, V. Beermann, S. Kühl, J. Herranz, S. Henning, L. Kühn, T. Asset, L. Guétaz, G. Renou, J. Drnec, P. Bordet, A. Pasturel, A. Eychmüller, T.J. Schmidt, P. Strasser, L. Dubau, F. Maillard, Surface distortion as a unifying concept and descriptor in oxygen reduction reaction electrocatalysis, Nat. Mater. 17 (2018) 827–833. https://doi.org/10.1038/s41563-018-0133-2.
[46] D.E. Newbury, N.W.M. Ritchie, Is scanning electron microscopy/energy dispersive X-ray spectrometry (SEM/EDS) quantitative?, Scanning. 35 (2013) 141–168. https://doi.org/10.1002/sca.21041.
[47] P. Malacrida, M. Escudero-Escribano, A. Verdaguer-Casadevall, I.E.L. Stephens, I. Chorkendorff, Enhanced activity and stability of Pt–La and Pt–Ce alloys for oxygen electroreduction: the elucidation of the active surface phase, J. Mater. Chem. A. 2 (2014) 4234. https://doi.org/10.1039/c3ta14574c.

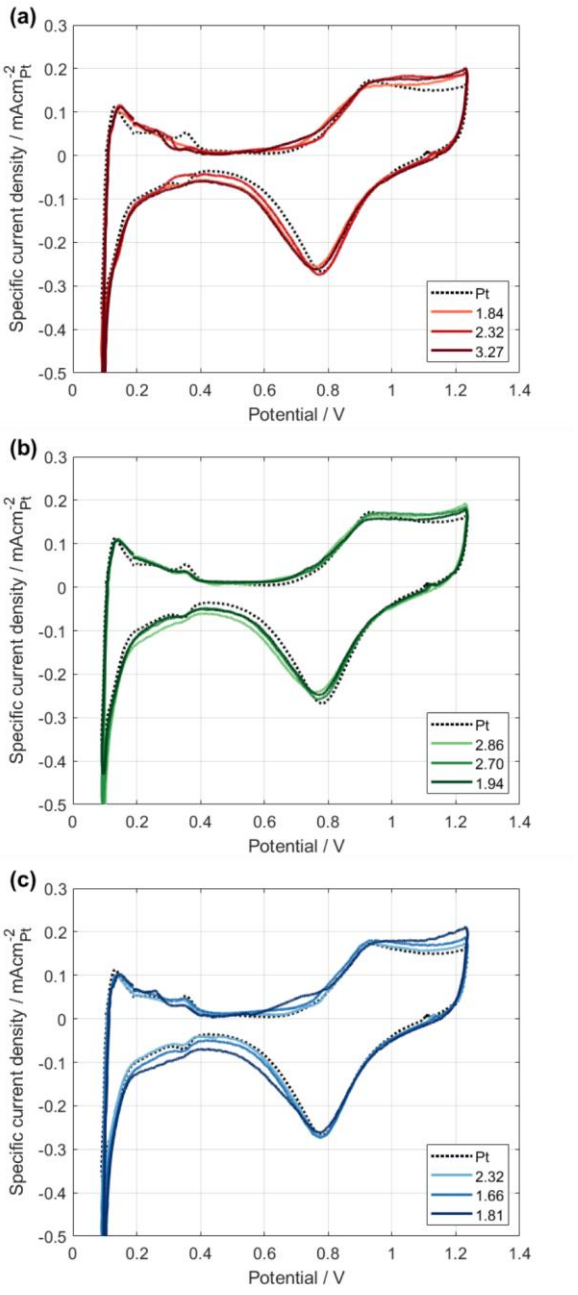

Figure 1: Cyclic voltammetry for three repetitions of a) Pt_3Y b) Pt_5Gd c) Pt_5Tb. The values in the legend are the specific activity increase at 0.9 V for each sample compared to thin-film platinum. Measured with 5% H_2 in Ar and N_2, a cell temperature of 30 °C and 100% RH, and a sweep rate of 200 mVs^{-1}.

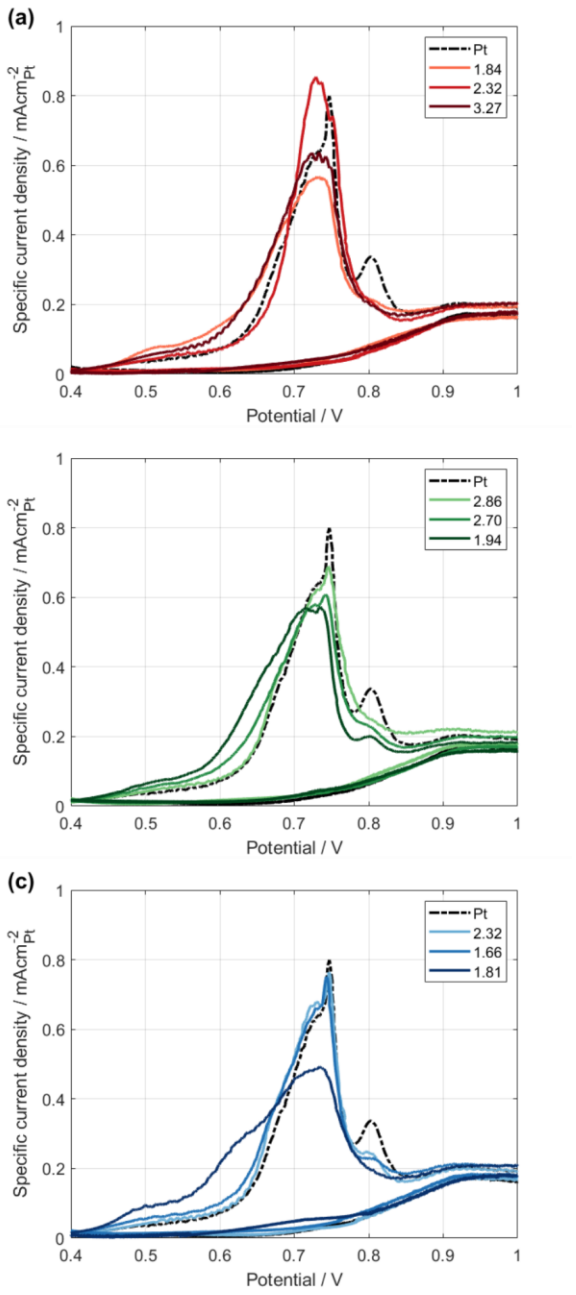

Figure 2: CO-stripping curves for three repetitions of a) Pt_3Y, b) Pt_5Gd, and c) Pt_5Tb. The values in the legend are the specific activity increase for each sample compared to thin-film platinum. Measured with 5% H_2 in Ar and N_2, a cell temperature of 30 °C and 100% RH, and a sweep rate of 200 mVs^{-1}.

Sample	$I_{0.9V}$ μAcm^{-2}_{Pt}	$I_{0.75V}$ $mAcm^{-2}_{Pt}$	Improvement factor compared to thin film Pt
Pt	280 ± 30	12.6 ± 1.5	-
Pt_3Y	692 ± 200	21.3 ± 4.3	2.48 ± 0.78
Pt_5Gd	699 ± 140	18.4 ± 4.6	2.50 ± 0.56
Pt_5Tb	539 ± 100	19.8 ± 2.6	1.93 ± 0.41

Table 1: Mean specific current density, at 0.9 V and 0.75 V, and standard deviation between repeated experiments for different samples. The improvement factor is compared to sputtered platinum and calculated from the specific activity at 0.9 V.

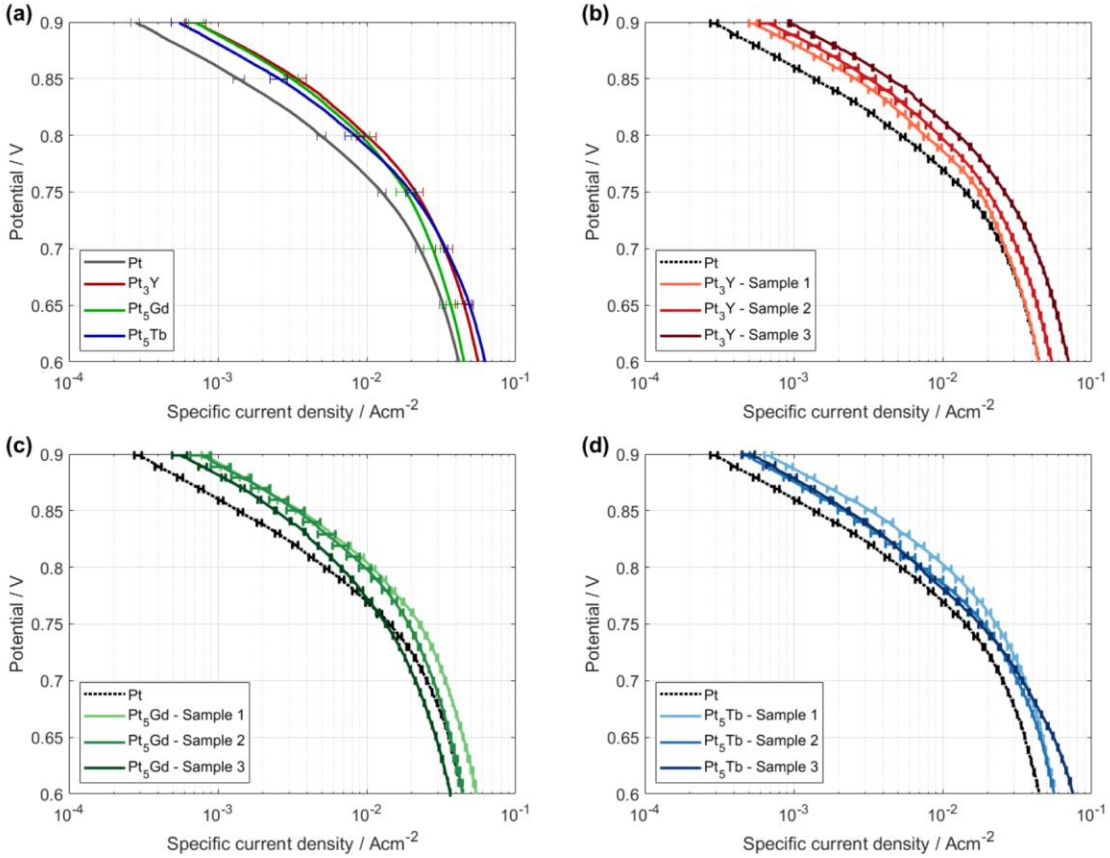

Figure 3: Specific activity of the different tested alloy catalysts, a) Mean value for all measurements. Error bars show the standard error for each alloy. b-d) Specific activity for three repetitions of b) Pt_3Y c) Pt_5Gd d) Pt_5Tb. Measured with 14.8 $ml_n min^{-1}$ H_2 and 7.4 $ml_n min^{-1}$ O_2, a cell temperature of 80 °C, 100% RH, and a sweep rate of 1 mVs^{-1}. The electrochemical surface area was calculated from CO-stripping. The error bars represent the standard deviation of the three forward sweeps.

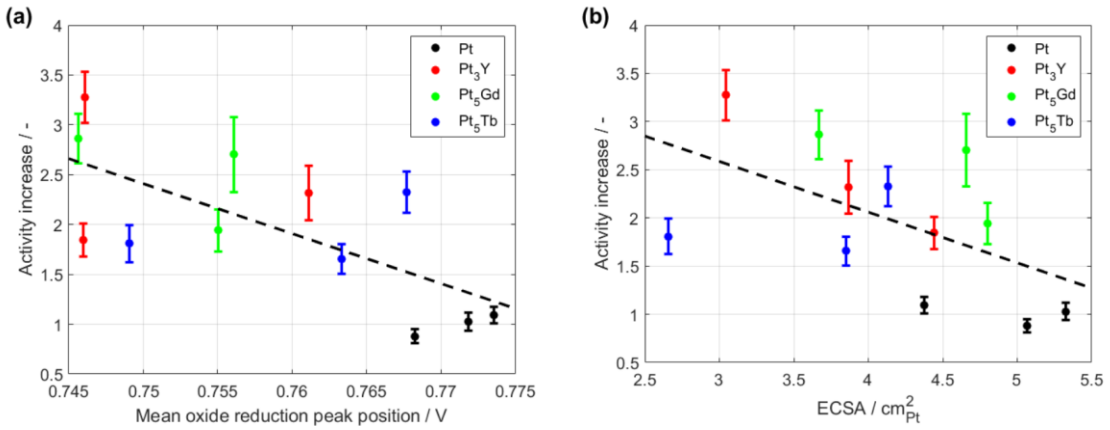

Figure 4: Activity increase as a function of mean oxide reduction peak position (a) and the electrochemical active surface area (b). Measured with 5% H_2 in Ar and N_2, a cell temperature of 30 °C and 100% RH, and a sweep rate of 200 mVs^{-1}. The different shades of the same color correspond to the same colors in Figure 1, Figure 2, and Figure 3. Trend line is for visual aid only.

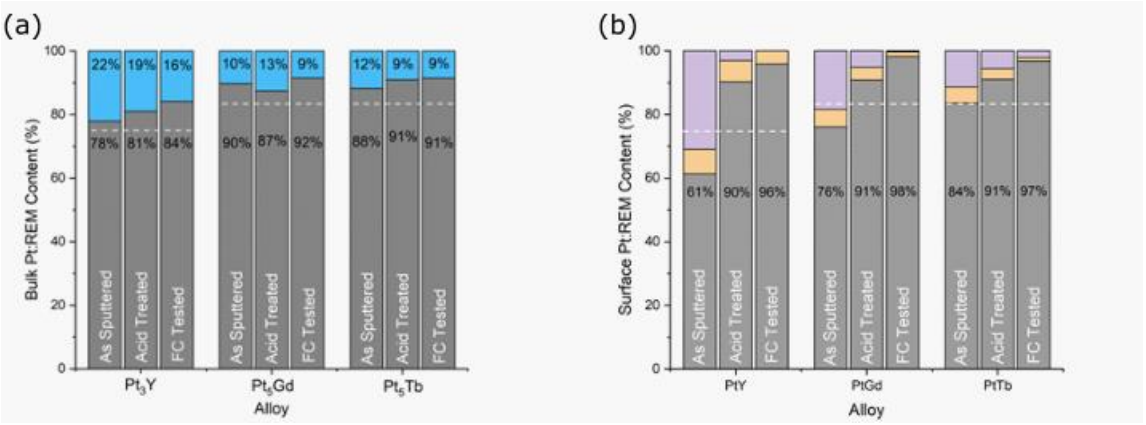

Figure 5: (a) The bulk content of Pt:REM for each sample measured by EDX. Gray colored columns indicate Pt and blue the REM of each alloy. (b) The surface content of Pt:REM for each sample measured by XPS. Gray corresponds to Pt, orange metallic REM and purple REM-oxide. Numeric percentages of each alloy are found in Table S2 in Supporting Information. Dashed white lines indicate the composition of the sputter target for the different alloys.

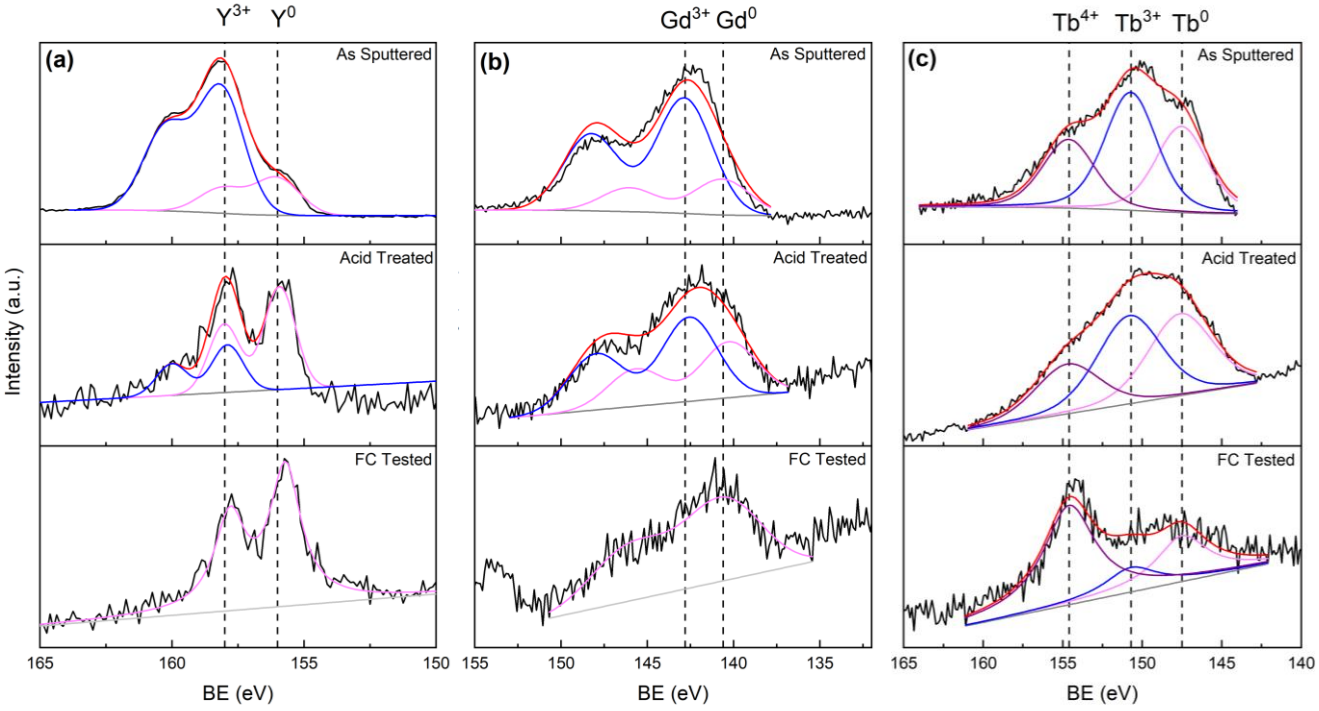

Figure 6: XPS spectra of a) Y 3d (Pt_3Y) b) Gd 4d (Pt_5Gd) and c) Tb 4d (Pt_5Tb) for as sputtered, acid cleaned and post electrochemical measurements. All 3d orbitals shown correspond to $3d_{5/2}$ orbitals. The red line corresponds to the fitted spectrum, pink the metallic REM and blue and purple the REM oxide.

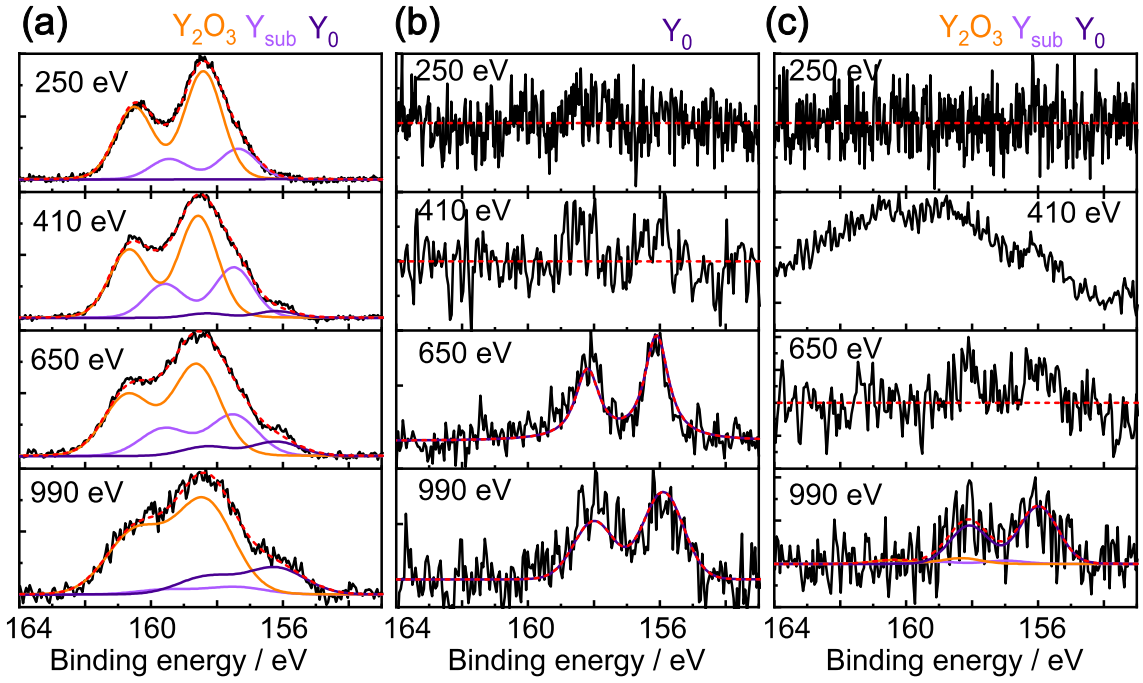

Figure 7: The catalyst surface seen through the Y 3d core level; a) as sputtered Pt_3Y, b) acid treated and c) post-fuel cell test. Yttrium oxide (orange), substochiometric oxide (light purple) and metallic yttrium (dark purple) are present in the as-deposited sample. Only metallic yttrium (dark purple) is present in the acid treated and fuel cell tested samples.

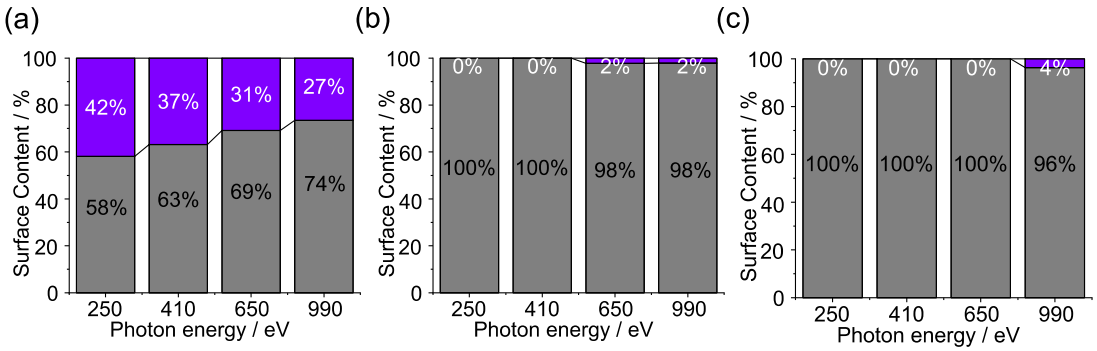

Figure 8: The percentage content of Pt 4f (gray) and Y 3d (purple) for a) as-deposited, b) acid treated and c) post-fuel cell test at each photon energy.

Supporting information

Specific activity and electrochemical surface area

The specific activity towards the oxygen reduction reaction and electrochemical active surface area (ECSA) for each sample is shown in Table 1.

Sample	ECSA	$I_{0.9V}$ μAcm^{-2}_{Pt}	$I_{0.75V}$ $mAcm^{-2}_{Pt}$
Pt	5.33 ± 0.07	287 ± 17	14.3 ± 0.2
Pt	5.06 ± 0.14	245 ± 7	11.4 ± 0.2
Pt	4.38 ± 0.12	304 ± 4	11.9 ± 0.2
Pt_3Y	4.44 ± 0.09	515 ±33	17.6 ± 0.2
Pt_3Y	3.87 ± 0.09	647 ± 80	20.1 ± 0.3
Pt_3Y	3.04 ± 0.08	914 ± 18	26.0 ± 0.3
Pt_5Gd	3.67 ± 0.07	800 ± 46	22.6 ± 0.2
Pt_5Gd	4.66 ± 0.14	755 ± 124	19.1 ± 0.2
Pt_5Gd	4.80 ± 0.10	542 ± 60	13.5 ± 0.2
Pt_5Tb	4.13 ± 0.21	649 ± 40	22.8 ± 0.3
Pt_5Tb	3.85 ± 0.17	462 ± 29	18.9 ± 0.3
Pt_5Tb	2.66 ± 0.04	505 ± 47	17.8 ± 0.3

Table S1: ECSA and specific activity towards the oxygen reduction reaction for all tested samples.

Fitting of XPS data

X-ray photoelectron spectroscopy (XPS) peak fitting was used to quantify the amount of oxide and metallic rare earth metal (REM) (Figure S1) and thus facilitate comparison among samples before and after electrochemical measurement. Nonetheless, it is necessary to mention that there is a lack of a well-stablished validated model for the fitting of the XPS REM peaks and this might lead to an erroneous quantification of both metallic and oxide REM. While the peak positions of both metallic (156 eV) and oxide (158 eV) yttrium 3d doublets is well known [1–4], Gd and Tb peak energies still remain unexplored. It has been demonstrated before that Gd 4d peak is composed of a complex broad multiplet structure resulting from both core spin-orbit and spin-spin interactions with a broadening resulting from the 4d-4f-4f decay process [5–7]. Due to the high spectra complexity such a complex multiplet, other methods for peak fitting utilized in the literature have been used instead [8–11]. Thus, the binding energies for both Gd and Gd_2O_3 have been set at 140.6 eV and 142.8 eV respectively, and the results obtained agree with previous articles reporting similar studies [12,13]. Similarly to Gd 4d, Tb 4d peak exhibits a complex multiplet structure arising from the spin-orbit coupling between its 4d core-hole and the open 4f-shell [14,15] and they present a two different oxidized states (Tb^{3+} and Tb^{4+}) that result from its mixed oxide (Tb_4O_7)[16]. Again, previous articles deconvoluted Tb 4d have been used to carry out fitting [17–19].

Table S2: Percentage of Pt, metallic REM and REM oxide of each sample for every allow.

Sample	As sputtered			Acid Treated			FC Tested		
	% Pt	%REM (metal)	%REM (oxide)	% Pt	%REM (metal)	%REM (oxide)	% Pt	%REM (metal)	%REM (oxide)
Pt_3Y	61.30	7.74	30.96	90.3	6.9	2.8	95.91	4.09	0.0
Pt_5Gd	76.10	5.58	18.32	90.9	4.1	5.0	98.2	1.5	0.3
Pt_5Tb	83.50	5.10	11.40	91.05	3.33	5.62	96.7	1.0	2.4

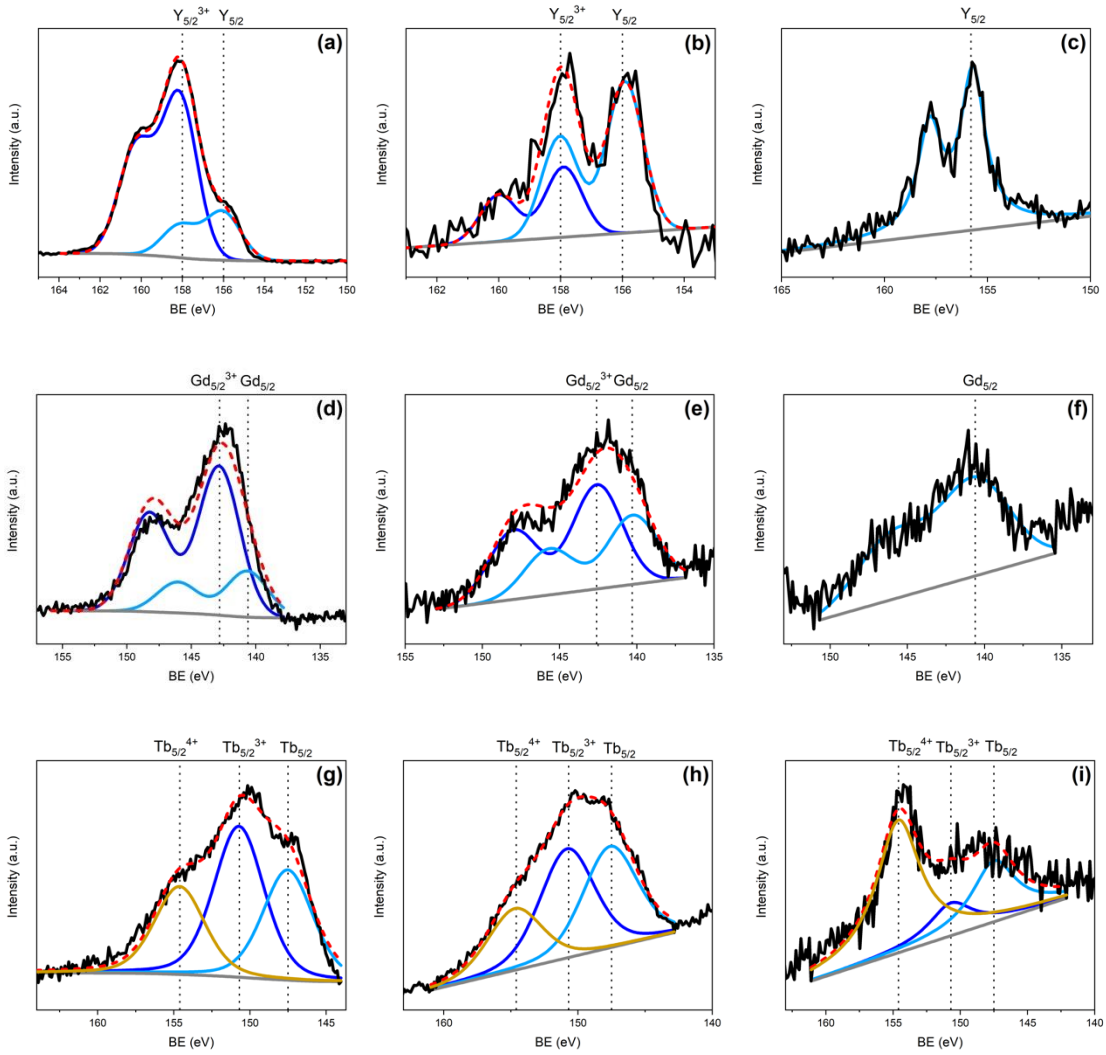

Figure S1 XPS spectra deconvolution of (a-c) Y 3d (Pt_3Y) (d-f) Gd 4d (Pt_5Gd) and (g-i) Tb 4d (Pt_5Tb) for as sputtered (a, d, g), acid cleaned (b, e, h) and post electrochemical measurements (c, f, i).

Most of the platinum at the surface of Pt_3Y is metallic in all samples, shown in the Pt 4f spectra in Figure S2. Additionally, all samples show an additional doublet that is attributed to adsorbed CO. The very small shoulder at after acid treatment and post-fuel cell testing indicates that some platinum oxide is present only at the very surface. After acid treatment and post-fuel cell tests the signal from the Pt 4f is approximately the double of that as-sputtered which is due to the formation of the platinum overlayer (not seen as all the spectra have been normalized for image clarity).

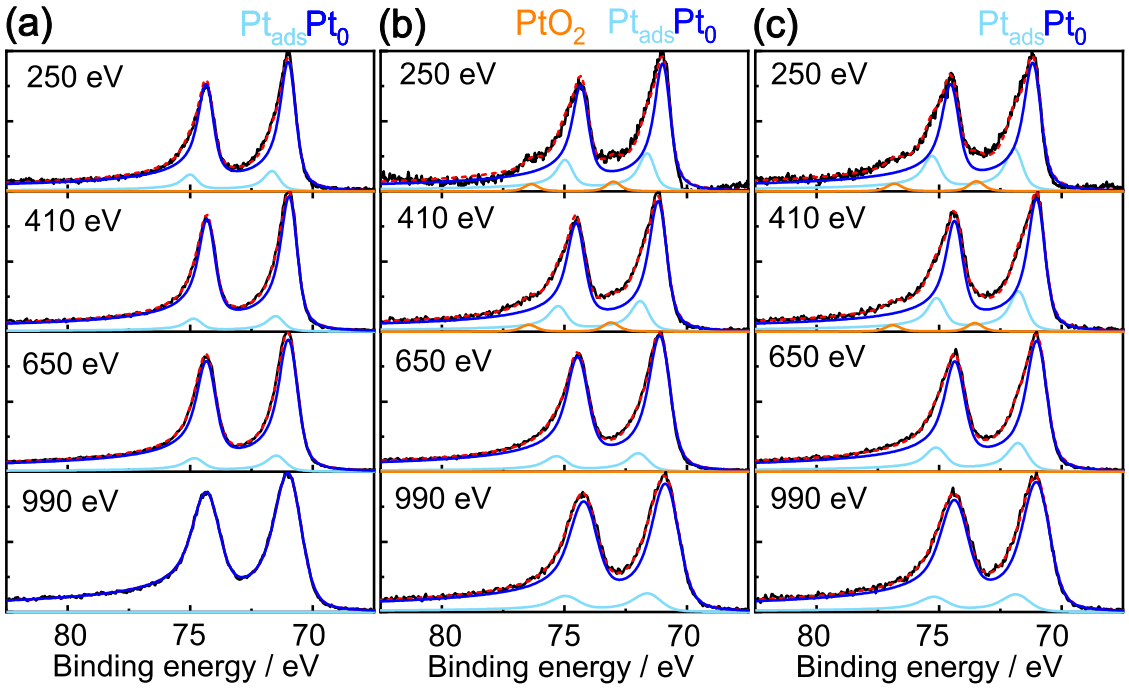

Figure S2: The Pt 4f core level of the surface of as-deposited (a), acid treated (b) and post-fuel cell (c) Pt_3Y sputtered on GDE. Metallic platinum (dark blue) and adsorbed CO (light blue) are present in the surface of all samples. The acid treated and fuel cell tested GDL shows platinum oxide (orange) at the lower photon energies.

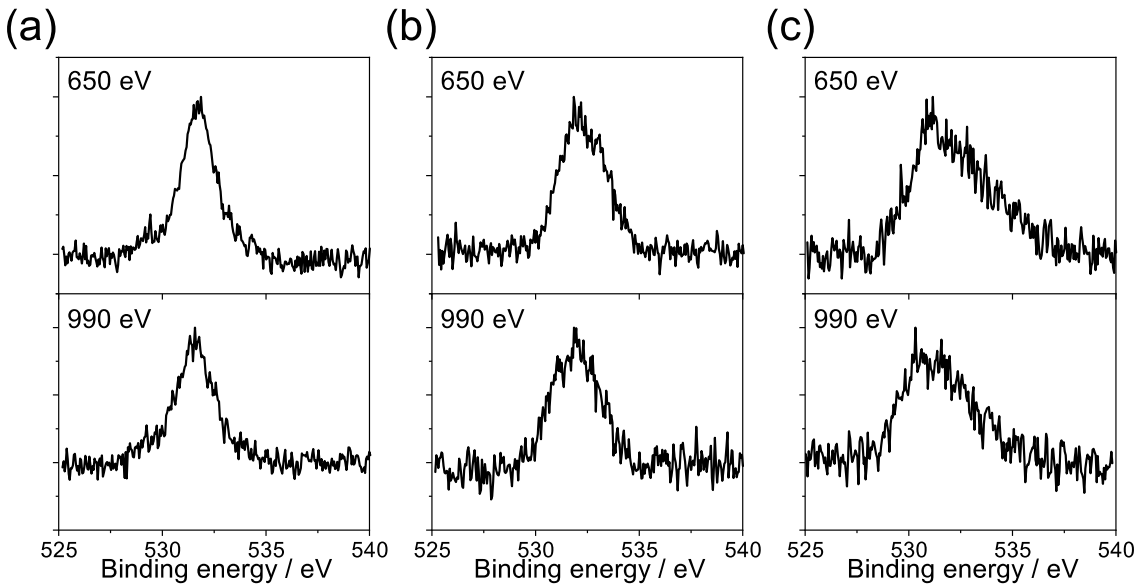

Figure S3. The O 1s spectra from synchrotron XPS measurements on Pt_3Y films sputtered onto GDL, (a) as deposited, (b) after acid treatment and (c) post fuel cell tests. The peaks are normalized to the maximum intensity.

The corresponding O 1s spectra from synchrotron XPS measurements on the Pt_3Y samples presented in the manuscript are shown in figure S3. These are the same samples as presented in figure S2 also. Figure S3(a) shows the as-deposited material, the O 1s peak seems to be organic oxygen from adsorbates (large peak above 530 eV) and yttrium oxide which falls around 530 eV [3,19–22]. After acid treatment in (b) and post-fuel cell testing (c), there is less signal from the oxygen in total, little to no contribution from yttrium oxide as it has been leached. There is an appearance of a peak shoulder towards higher binding energies which could be organic molecules on the surface, which corroborates the adsorbed CO present in the Pt 4f spectra in figure S2. Only the 650 eV and 990 eV photon energies produced O 1s signal as these binding energies cannot be measured using synchrotron radiation with lower energies.

The scanning electron microscope (SEM) image of the microporous layer of the gas diffusion layer (GDL) (Carbel CL) is shown in Figure S4. As can be seen the morphology of the electrode is due to the microporous layer (MPL) structure. The SEM images for all samples are shown in Figure S5. As can be seen no significant changes have occurred for any samples.

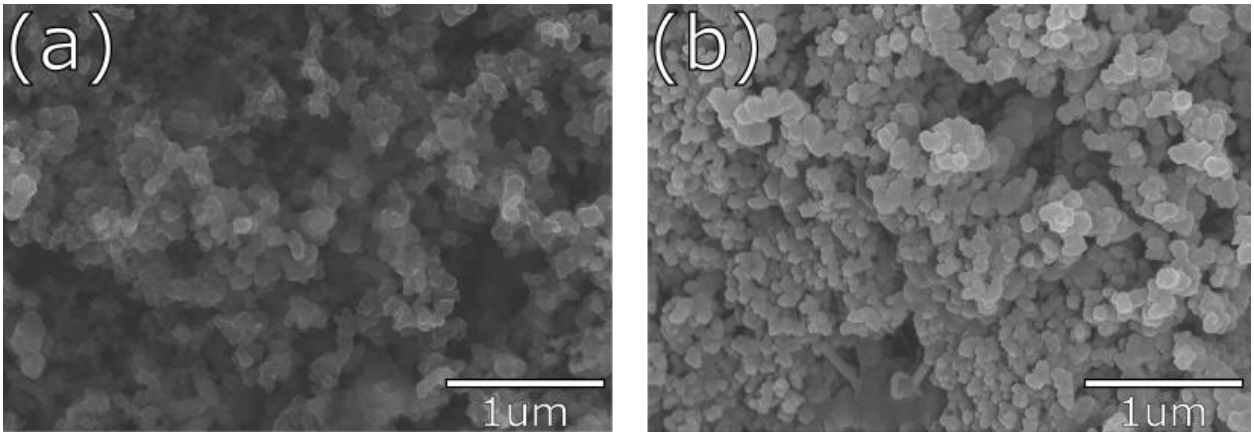

Figure S4: SEM images of a) Carbel Cl and b) Pt_3Y as sputtered.

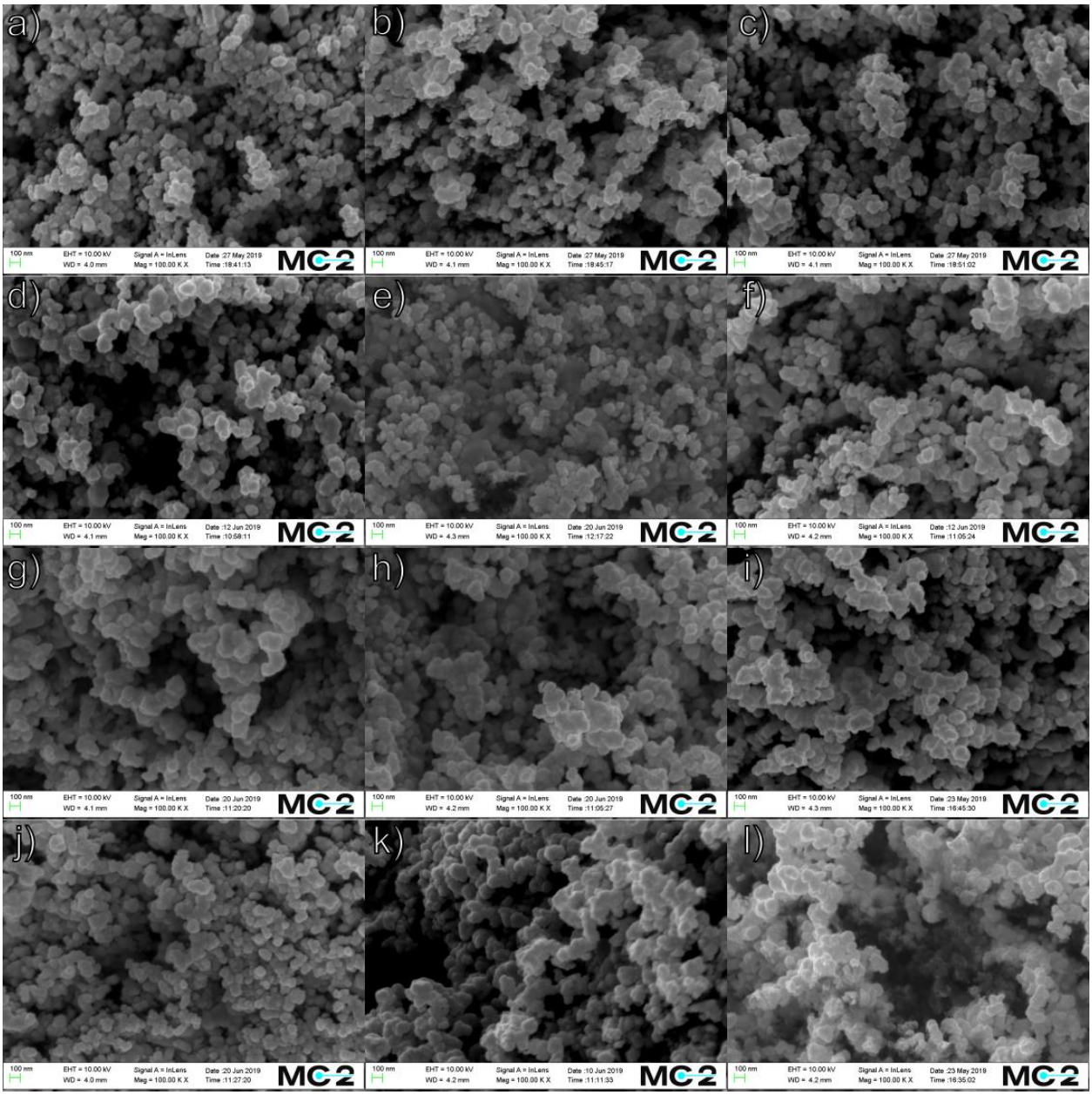

Figure S5: SEM images of Pt (a,b,c) Pt_3Y (d,e,f), Pt_5Gd(g,h,i), and Pt_5Tb(j,k,l) samples as sputtered (a,d,g,j), after acid treatment (b,e,h,k) and after fuel cell testing (c,f,i,l).

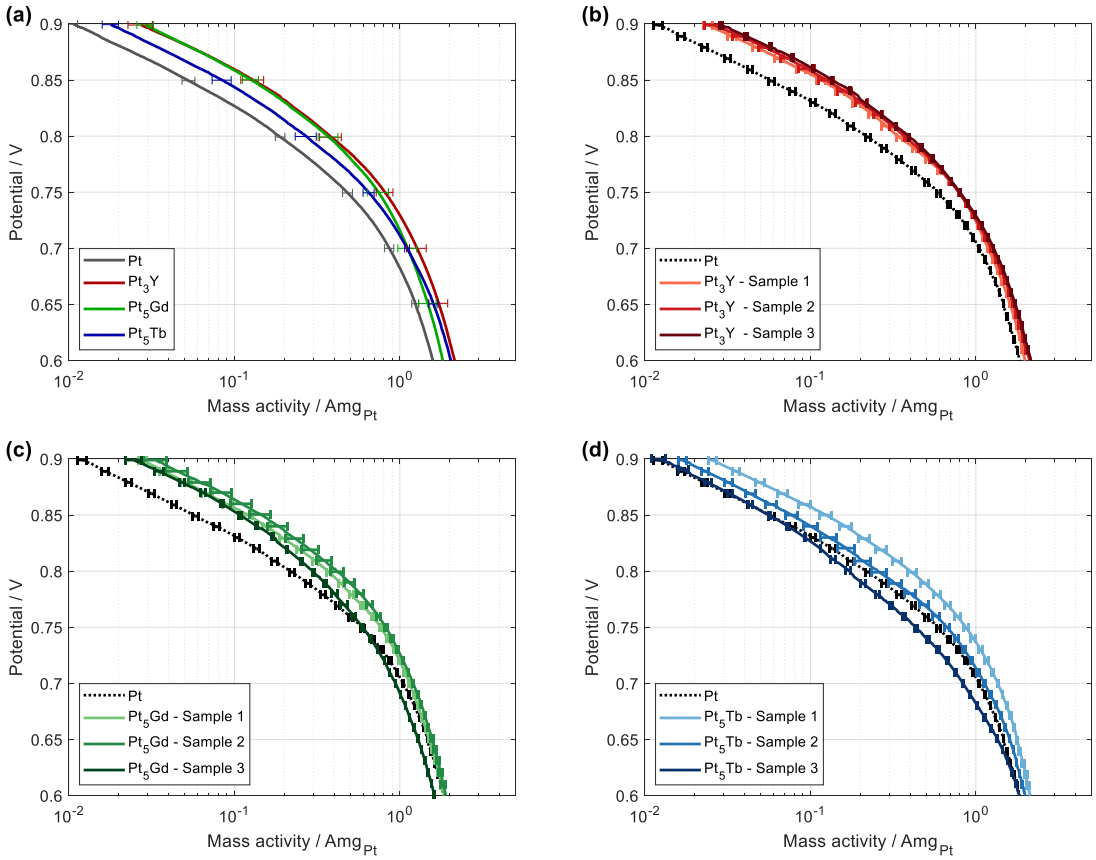

Figure S6: Mass activity of the different tested alloy catalysts, a) Mean value for all measurements. Error bars show the standard error for each alloy. b-d) Specific activity for three repetitions of b) Pt_3Y c) Pt_5Gd d) Pt_5Tb. Measured with 14.8 $ml_n min^{-1}$ H_2 and 7.4 $ml_n min^{-1}$ O_2, a cell temperature of 80 °C, 100% RH, and a sweep rate of 1 mVs^{-1}. The mass of platinum was calculated from the initial deposited mass. The error bars represent the standard deviation of the three forward sweeps.

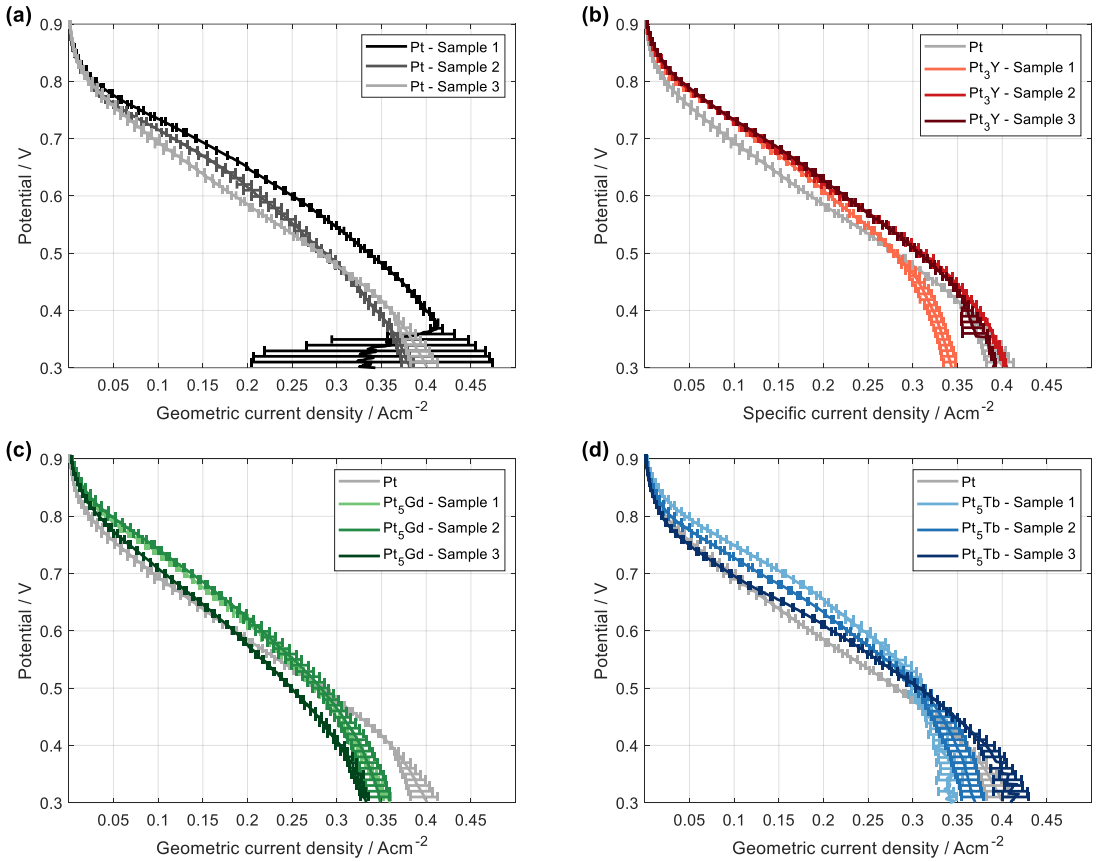

Figure S7: Polarization curves of the different tested alloy catalysts, a) Mean value for all measurements. Error bars show the standard error for each alloy. b-d) Specific activity for three repetitions of b) Pt_3Y c) Pt_5Gd d) Pt_5Tb. Measured with 14.8 ml_nmin^{-1} H_2 and 7.4 ml_nmin^{-1} O_2, a cell temperature of 80 °C, 100% RH, and a sweep rate of 1 mVs^{-1}. The error bars represent the standard deviation of the three forward sweeps.

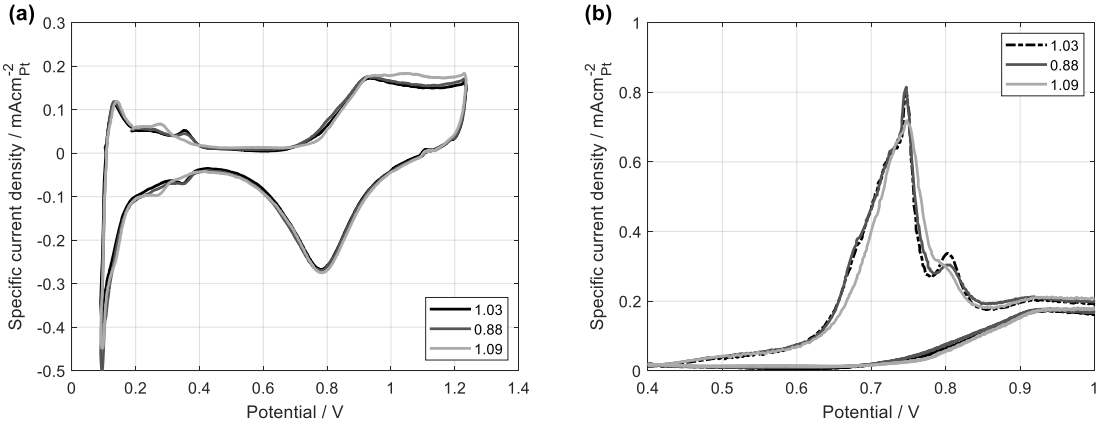

Figure S8: CV (a) and CO-stripping curves (b) for three repetitions of Pt. The values in the legend are the specific activity increase for each sample compared to the average of thin film platinum. Measured with 5% H_2 in Ar and N_2, a cell temperature of 30 °C and 100% RH, and a sweep rate of 200 mVs^{-1}.

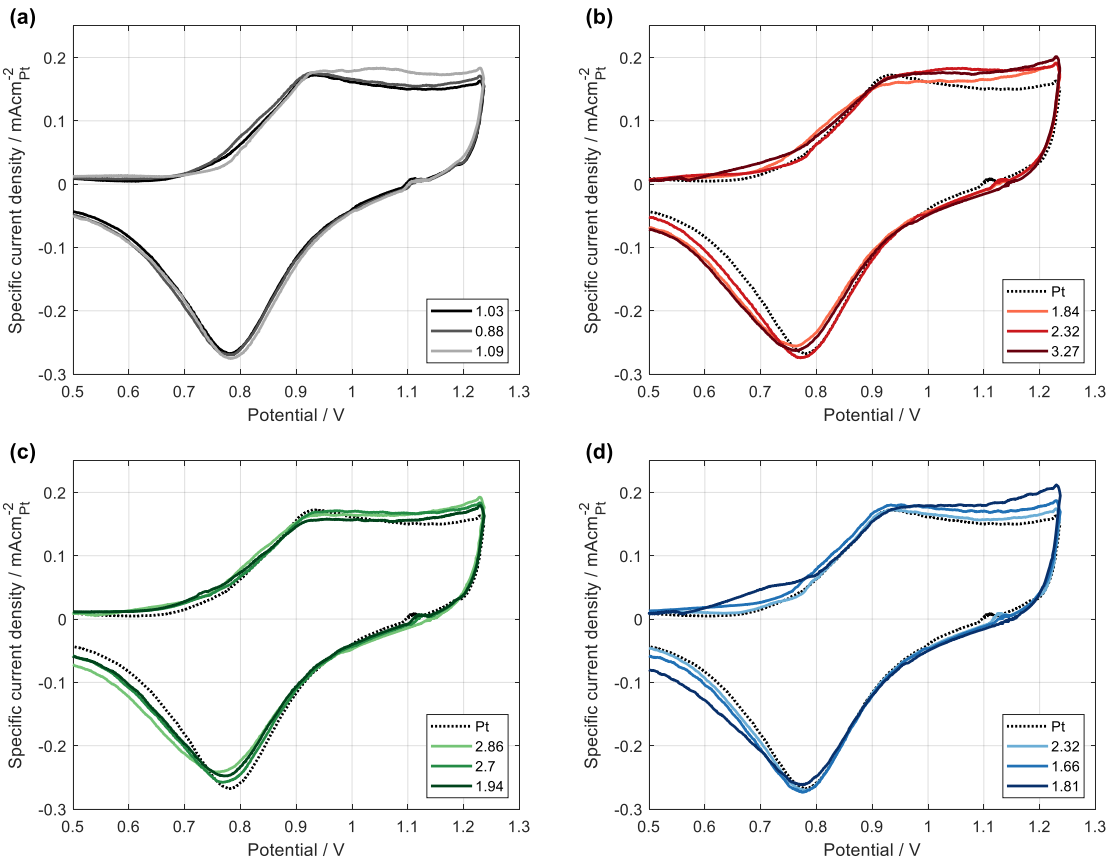

Figure S9: Cyclic voltammetry in the oxide region for three repetitions of a) Pt b) Pt_3Y c) Pt_5Gd d) Pt_5Tb. The values in the legend are the specific activity increase at 0.9 V for each sample compared to thin-film platinum. Measured with 5% H_2 in Ar and N_2, a cell temperature of 30 °C and 100% RH, and a sweep rate of 200 mVs^{-1}.

Double MEA configuration

The difference between a common single MEA and a double MEA configuration used in this work is shown in Figure S10. As can be seen the catalyst coated membrane has an additional membrane placed at on the cathode catalyst layer (CCL) making that layer a platinum interlayer (IL). The thin film gas diffusion electrode (GDE) is then placed on the additional membrane. The IL reduces the effects of hydrogen crossover by chemically allowing hydrogen and oxygen to react.

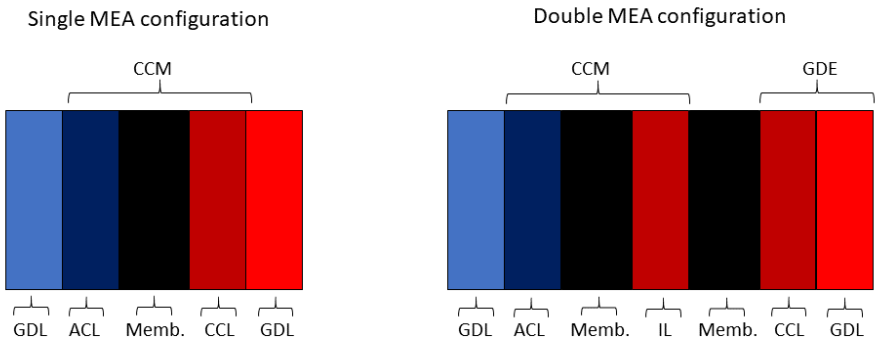

Figure S10: Schematic of a standard single MEA configuration and a double MEA configuration utilized in this work.

X-Ray diffraction

XRD spectra were collected on a Bruker D8 Discover equipped with a Cu source and an Eiger2 R 500K detector. Measurements were carried out in a Bragg Brentano configuration, with 0.04° step size and 3s exposure per step. An anti-scatter knife was used to eliminate background at low angles, and a motorized primary slit was used to regulate the beam size in order to achieve fixed sample illumination area during the entire scan. 2.5° soller slits were used on the source as well as the detector side. A 0.02 mm Ni filter on the source side was used to eliminate K-beta radiation.

The GDL supported Pt, Pt_3Y, Pt_5Gd and Pt_5Tb thin films were structurally characterized by XRD. Figure S11 shows the resulting XRD spectra for all as sputtered samples. As can be seen, the carbon GDL used as a substrate gives rise to a large diffraction peak at 25° found in all samples, as well as a large background signal. Although pure Pt is a very strong X-Ray scatterer, the characteristic peaks for pure Pt are rather weak, due to that the amount of material in a 60 nm film is quite low, and probably also that the crystallite size of sputtered Pt is very small [Brown et al. ACS Appl. Mater. Interfaces 2020, 12, 4454−4462]. However, the clearly visible diffraction peaks of pure Pt are characteristic of an FCC crystal structure, and confirms the presence of crystalline domains in this sample. Conversely, the PtREM samples show almost no or very small peaks associated with Pt or an alloy crystalline structure. Thus, both the alloy formation and the presence of a lattice strain cannot be confirmed from these measurements. However. the fact that the characteristic Pt-peaks are not visible in Pt_3Y and Pt_5Gd indicate that, at least, there are no pure Pt domains and that the REM-component is distributed throughout the metal film, likely as an alloy.

Pt_5Tb shows a small peak at around 40° corresponding to a (111) plane, which could indicate the presence of pure Pt domains, but in that case much smaller than for the pure Pt sample.

Whether the absence of clear diffraction peaks in PtREM alloy samples is due to a small grain size or to the absence of an ordered crystal structure cannot be elucidated with this type of samples. Previous studies on sputtered Pt_5Gd thin film alloys with a similar amount of alloy but sputtered on a flat substrate have shown the presence of ordered crystal structures.

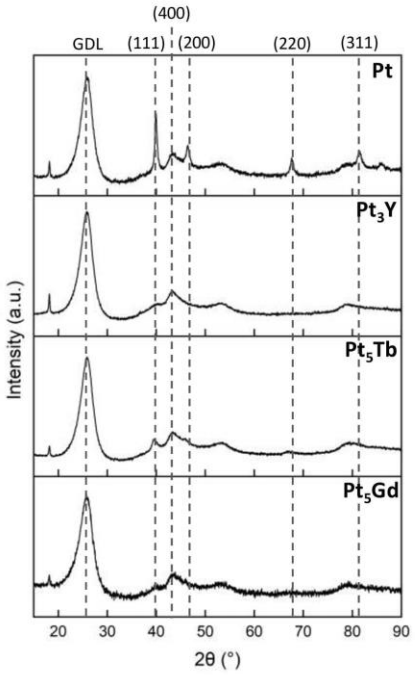

Figure S11: XRD spectra for 60 nm sputtered films of Pt, Pt_3Y, Pt_5Gd, and Pt_5Tb on GDL.

References

[1] C. Roy, B.P. Knudsen, C.M. Pedersen, A. Velázquez-Palenzuela, L.H. Christensen, C.D. Damsgaard, I.E.L. Stephens, I. Chorkendorff, Scalable synthesis of carbon-supported platinum-lanthanide and -rare-earth alloys for oxygen reduction, ACS Catal. 8 (2018) 2071–2080. https://doi.org/10.1021/acscatal.7b03972.

[2] P. Malacrida, H.G. Sanchez Casalongue, F. Masini, S. Kaya, P. Hernández-Fernández, D. Deiana, H. Ogasawara, I.E.L. Stephens, A. Nilsson, I. Chorkendorff, Direct observation of the dealloying process of a platinum-yttrium nanoparticle fuel cell cathode and its oxygenated species during the oxygen reduction reaction, Phys. Chem. Chem. Phys. 17 (2015) 28121–28128. https://doi.org/10.1039/c5cp00283d.

[3] R. Reichl, K.H. Gaukler, An investigation of air-grown yttrium oxide and experimental determination of the sputtering yield and the inelastic mean free path, Appl. Surf. Sci. 26 (1986) 196–210. https://doi.org/10.1016/0169-4332(86)90005-X.

[4] P. Hernandez-Fernandez, F. Masini, D.N. McCarthy, C.E. Strebel, D. Friebel, D. Deiana, P. Malacrida, A. Nierhoff, A. Bodin, A.M. Wise, J.H. Nielsen, T.W. Hansen, A. Nilsson, I.E.L. Stephens, I. Chorkendorff, Mass-selected nanoparticles of PtxY as model catalysts for oxygen electroreduction, Nat. Chem. 6 (2014) 732–738. https://doi.org/10.1038/nchem.2001.

[5] E. Talik, A. Guzik, M. Oboz, J. Kusz, P. Zajdel, M. Zubko, Influence of nickel on the electronic structure and magnetic properties in Gd7Pd3-xNix, Philos. Mag. 96 (2016) 1073–1092. https://doi.org/10.1080/14786435.2016.1154620.

[6] G. van der Laan, E. Arenholz, E. Navas, A. Bauer, G. Kaindl, Magnetic circular dichroism and orbital momentum coupling in photoemission from Gd(0001), Phys. Rev. B - Condens. Matter Mater. Phys. 53 (1996) R5998–R6001. https://doi.org/10.1103/PhysRevB.53.R5998.

[7] S.P. Kowalczyk, N. Edelstein, F.R. McFeely, L. Ley, D.A. Shirley, X-ray photoemission spectra of the 4d levels in rare-earth metals, Chem. Phys. Lett. 29 (1974) 491–495. https://doi.org/10.1016/0009-2614(74)85076-1.

[8] J. Vinoth Kumar, R. Karthik, S.M. Chen, K. Natarajan, C. Karuppiah, C.C. Yang, V. Muthuraj, 3D flower-like gadolinium molybdate catalyst for efficient detection and degradation of organophosphate pesticide (Fenitrothion), ACS Appl. Mater. Interfaces. 10 (2018) 15652–15664. https://doi.org/10.1021/acsami.8b00625.

[9] D.N. Durgasri, T. Vinodkumar, P. Sudarsanam, B.M. Reddy, Nanosized CeO2-Gd2O3 mixed oxides: Study of structural characterization and catalytic CO oxidation activity, Catal. Letters. 144 (2014) 971–979. https://doi.org/10.1007/s10562-014-1223-7.

[10] Y. Luo, A. Habrioux, L. Calvillo, G. Granozzi, N. Alonso-Vante, Yttrium oxide/gadolinium oxide-modified platinum nanoparticles as cathodes for the oxygen reduction reaction, ChemPhysChem. 15 (2014) 2136–2144. https://doi.org/10.1002/cphc.201400042.

[11] P. Terzieff, K. Lee, Electron spectroscopy studies on amorphous GdFe and GdCo alloys, J. Appl. Phys. 50 (1979) 3565–3569. https://doi.org/10.1063/1.326302.

[12] A. Velázquez-Palenzuela, F. Masini, A.F. Pedersen, M. Escudero-Escribano, D. Deiana, P. Malacrida, T.W. Hansen, D. Friebel, A. Nilsson, I.E.L. Stephens, I. Chorkendorff, The enhanced activity of mass-selected PtxGd nanoparticles for oxygen electroreduction, J. Catal. 328 (2015) 297–307. https://doi.org/10.1016/j.jcat.2014.12.012.

[13] M. Escudero-Escribano, A. Verdaguer-Casadevall, P. Malacrida, U. Grønbjerg, B.P. Knudsen, A.K. Jepsen, J. Rossmeisl, I.E.L. Stephens, I. Chorkendorff, Pt5Gd as a highly active and stable catalyst for oxygen electroreduction., J. Am. Chem. Soc. 134 (2012) 16476–9. https://doi.org/10.1021/ja306348d.

[14] H.O. and A. Kotani, Lifetime effect on the multiplet structure of 4d x-ray-photoemission spectra in heavy rare-earth elements., 50 (1994) 332–341.

[15] L.M.W. and D.J.F. B. D. Padalia, W. C. Lang, P. R. Norris, X-Ray photoelectron core-level studies of the heavy rare-earth metals and their oxides, Proc. R. Soc. Lond. A. 425 (1989) 73–90.

[16] D.D. Sarma, C.N.R. Rao, XPES studies of oxides of second- and third-row transition metals including rare earths, J. Electron Spectros. Relat. Phenomena. 20 (1980) 25–45. https://doi.org/10.1016/0368-2048(80)85003-1.

[17] H. Taz, T. Sakthivel, N.K. Yamoah, C. Carr, D. Kumar, S. Seal, R. Kalyanaraman, Transparent ferromagnetic and semiconducting behavior in Fe-Dy-Tb based amorphous oxide films, Sci. Rep. 6 (2016) 1–8. https://doi.org/10.1038/srep27869.

[18] H. Yin, Y. Gao, H. Guo, C. Wang, C. Yang, Effect of B2O3 content and microstructure on Verdet constant of Tb2O3-doped GBSG magneto-optical glass, J. Phys. Chem. C. 122 (2018) 16894–16900. https://doi.org/10.1021/acs.jpcc.8b04989.

[19] Y. Uwamino, T. Ishizuka, H. Yamatera, X-ray photoelectron spectroscopy of rare-earth compounds, J. Electron Spectros. Relat. Phenomena. 34 (1984) 67–78.

[20] J. Moulder, W. Stickle, P. Sobol, K. Bomben, Handbook of X-ray photoelectron spectroscopy, Perkin-Elmer Corp., Physical Electronics Division, Eden Prairie, Minnesota, USA, 1992. https://doi.org/10.1002/sia.740030412.

[21] O. Durand, Characterization of multilayered materials for optoelectronic components by high-resolution X-ray diffractometry and reflectometry: Contribution of numerical treatments, Thin Solid Films. 450 (2004) 51–59. https://doi.org/10.1016/j.tsf.2003.10.052.

[22] T. Gougousi, Z. Chen, Deposition of yttrium oxide thin films in supercritical carbon dioxide, Thin Solid Films. 516 (2008) 6197–6204. https://doi.org/10.1016/j.tsf.2007.11.104.

Paper II

γ-Radiation Induced Engineering of Interfaces in Bimetallic Ag-Ni Nanocomposites for Oxygen Reduction in Alkaline Media

Y. Yang, G. Montserrat-Sisó, B. Wickman, P. Nikolaychuk, I. Soroka

ACS Applied Nano Materials (Submitted)

γ-Radiation Induced Engineering of Interfaces in Bimetallic Ag-Ni Nanocomposites for Oxygen Reduction in Alkaline Media

Yi Yang[1*], Gerard Montserrat-Sisó[2], Björn Wickman[2], Pavel Anatolyevich Nikolaychuk[3], Inna L. Soroka[1*]

[1]*Applied Physical Chemistry, Department of Chemistry, School of Engineering Sciences in Chemistry, Biotechnology and Health, KTH Royal Institute of Technology, S-100 44 Stockholm, Sweden*

[2]*Chemical Physics, Department of Physics, Chalmers University of Technology, 412 96 Gothenburg, Sweden*

[3]*Microhydrodynamic Technologies Laboratory, Tyumen State University, 625003 Tyumen, Russian Federation*

[*]*Corresponding Authors*

Abstract

Anion exchange membrane fuel cells (AEMFCs) are currently receiving increasing attention since the alkaline conditions allow the usage of cheaper catalysts, such as Ag. However, monometallic Ag is generally not sufficiently active for the oxygen reduction reaction (ORR). Herein, using a facile γ-radiation induced synthesis approach, bimetallic Ag-Ni nanocatalysts of two types: core shells, Ag@Ni and heterostructures, Ag/Ni are fabricated. Due to the introduced interfaces both bimetals materials demonstrate a similar but enhanced alkaline ORR activity as compared to the monometallic nanocatalysts. Detailed structural, compositional and electrochemical analyses on the as-prepared nanocatalysts are presented. The Ag@Ni catalyst consists of an amorphous Ni oxide layer about 2 nm thick as a shell and a crystalline facetted Ag particle as a core, the average size of Ag core is about 160 nm. The enhanced ORR activity of core-shell nanoparticles is attributed mainly to a ligand effect that originates from the changing atomic surroundings at the Ag-Ni interface. Meanwhile, Ag/Ni heterostructures comprise polycrystalline Ni-based clusters, with diameters ranging from 10 to 205 nm, adjacent to the surface of metallic Ag particles (average size of 45 nm). As confirmed by structural analysis, the composition of the clusters corresponds to metallic Ni covered with Ni (oxy-hydro) oxides, $Ni(OH)_2/Ni_2O_3/NiOOH$. The large lattice mismatch between Ni (oxy-hydro) oxides and Ag, of about 11%, may imply a significant lattice strain of the Ag surface layers, which in turn, is responsible for the enhanced catalytic activity of Ag/Ni heterostructures. Moreover, Ag/Ni exhibits good stability under the operation conditions, that is attributed to the existence of stable crystalline Ni^{3+} compounds ($Ni_2O_3/NiOOH$) in the heterostructures. Our study brings up fundamental and practical insights into the electronic effects in alkaline ORR electrocatalysis and highlights an unconventional approach to the controllable synthesis of active and durable nanocatalysts.

1. Introduction

Anion exchange membrane fuel cell (AEMFCs) are considered as the next generation fuel cell and show great potential to be an alternative for acidic proton exchange membrane fuel cells (PEMFCs).[1] The alkaline conditions in AEMFCs allow the usage of less expensive, non-platinum

based catalysts for the oxygen reduction reaction (ORR). Possible candidates include many abundant transition metals, which dramatically reduces the cost per kilowatt of power in fuel cell devices.[2] One such candidate is Ag, that has a market price approximately 50 times lower than Pt and 90 times lower than Pd and Au.[3] Moreover, it has been reported that Ag can display a high electrocatalytic activity for the ORR, especially for HO_2^- disproportionation.[4–6] In addition, Ag has good electrochemical stability in alkaline solutions according to the Pourbaix diagram.[7] For ORR in alkaline medium, it is believed that two dominant factors will govern ORR catalytic activity: (i) adsorption strength of the oxygen species on the catalyst surface and (ii) O–O bond breakage tendency.[8,9] However, with fully occupied d-band, pure Ag is difficult to provide unpaired electrons from the d-band for bond formation with oxygen, thus leading to low oxygen coverage.[10] Meanwhile, Ag shows slow kinetics of the O–O bond split.[9] These facts result in much lower ORR activity of Ag than that of e.g. Pt.

To decrease d-band charge density in Ag and realize an improved ORR activity, a lot of efforts have been done, among which, introducing another metal to form bimetallic composites[6,7] , using carbon[5] or metal oxides[11] as support, to achieve improved ORR activity. Mixing Ag with other metal could result in a lower d-band center. Ni is one of the most widely used elements in metal based catalysts.[12] Moreover, it is known for its low d-band occupancy and high alloying ability with some noble metals as well as with many transition metals. As shown in the literature, alloying effect may contribute to the enhanced catalytic activity of the constituents.[7,13] Although Ag and Ni is a thermally immiscible system, which makes them quite difficult to form the alloy, several studies on Ag-Ni alloy nanomaterials synthesis by using different approaches were reported[14–17]. As shown in the literature, during synthesis and operation the metastable AgNi alloys may undergo structural reorganization followed by atomic segregation.[18,19] Thus, Ag atoms tend to segregate at the surface of Co, Cu and Ni, in favor of forming the thermodynamically stable phase-segregated structures.[20–23] Unlike the metastable alloy of metallic Ag and Ni, a mixture of Ag and Ni oxides or mixed oxides, such as $AgNiO_2$ and Ag_2NiO_2, are stable and common compounds in Ag-Ni-O system.[24–26]

Nanocatalysts with phase segregated structures such as near-surface alloys[27], core-shell[28,29], janus-[30,31] and hetero-structures[32], demonstrate improved kinetics mainly due to the electronic effects induced from the segregated phases. Electronic effect can be categorized into two major types[9,33]: (i) ligand effect originates from the atomic vicinity of two different metal atoms, leading to charge transfer between them and results in modification of the electronic structure at the interface between two compounds. Thereby surface chemical properties can be altered, for instance, O-O breaking is facilitated.[27,33] (ii) strain effect, compressive or tensile, caused by the lattice mismatch between constituents in the composition. During compressive strain, the d-orbital overlapping index increases, resulting in a broadening of the d-band and lowering of its average energy, thereafter, the adsorption energies of oxygenated adsorbates are expected to decrease.[34] Generally, ligand effects together with strain effects can synergistically alter the ORR activity of catalysts and the two effects usually co-exist and work as cumulative electronic effects.[35] Achieving a deconvolution of these two effects with theoretical calculation is feasible but generally difficult with experimental methods.

In addition to achieve the activity enhancement, stability of the catalyst under operation condition is of equal importance. Recently, Bark *et al.*[36] used density functional theory calculations to predict the stability and activity of a series of noble-metal supported transition metal (oxy-hydro) oxide nanocatalysts. It was suggested the NiOOH|Ag composite is one of the most promising candidates for alkaline ORR catalysts with an enhanced activity and stability. Given these facts, phase-segregated Ag-Ni nanocomposites with well-defined interfaces could be promising candidates for alkaline ORR catalysts with an enhanced activity as well as good stability. However, it is still challenging to synthesize Ag-Ni nanocomposites with desired structural properties under mild conditions.

In this study, we fabricate bimetallic Ag-Ni nanocomposites (core shell- and hetero-structures) as well as monometallic Ag and Ni nanoparticles, using a facile γ-radiation induced synthesis method[37] in aqueous solutions and at ambient conditions. Essential structural, chemical and electrochemical characterizations of the synthesized materials are performed to emphasize the effect of compositional and structural modulation on electrocatalytic activity and stability.

2. Materials and methods

2.1 Chemicals

Ag nitrate, $AgNO_3$ (≥99.0%), Nickel (II) acetate tetrahydrate, $Ni(CH_3COO)_2{\cdot}4H_2O$ (98%), Poly vinyl alcohol, $[-CH_2CHOH^-]_n$ (PVA, Mw 70000, 87-90% hydrolyzed), propan-2-ol, $(CH_3)_2CHOH$ (IPA, 99.9%), KOH (pellets, 99.99%), $Pb(NO_3)_2$ (99.999%), Nafion-117 (5% in a mixture of lower aliphatic alcohols and water) was purchased from Sigma Aldrich. The water used in all the experiment was Milli-Q water (Millipore, 18.2 MΩ cm at 25 °C).

2.2 Synthesis procedure

For ionizing radiation induced synthesis, Cs-137 gamma source, MDS Nordion 1000 Elite, was used. The total irradiation dose was varying by the time of the samples exposure to irradiation. The dose rate estimated with ferrous sulfate dosimetry is 0.15 Gy s^{-1}. The nanoparticles were synthesized using metal salt solutions with 5 mM of corresponding precursor concentration. IPA was added as OH radicals' scavenger and PVA was used as a surfactant. Prior to irradiation all mixtures are deaerated with N_2 (99.999 % purity) for 30 min and sealed with septum in glass vials. The irradiation time is 40 hours for all samples. It corresponds to the total dose of 21.6 kGy. The initial pH of the solution was about 5.5, after irradiation pH decreases to about 3. The obtained Ni precipitates were separated from solutions by using magnet in the glove-box under Ar atmosphere with oxygen content < 0.1 ppm, Ag-contained precipitates were separated by centrifugation at 8000 rpm for 15 min, then washed with IPA/Milli-Q water for three times, and dispersed in IPA.

Ag and Ni nanoparticles were synthesized from the aqueous solution of $AgNO_3$ and $Ni(CH_3COO)_2{\cdot}4H_2O$, respectively. Core-shell Ag@Ni nanoparticles were synthesized by one-step seeding growth, which includes irradiation of mixture containing Ag and Ni salts with 5 mM concentration of each precursor. Ag/Ni heterostructures were obtained by successive reduction where Ni nanoparticles in a form of suspension were obtained by γ radiation induced reduction from the corresponding precursor solution first. Thereafter $AgNO_3$ stock solution (0.1 M) was injected dropwise into the sealed vial with the Ni suspension, the concentration of precursor Ni^{2+}

and Ag^+ in solution was controlled at the same level 5 mM. The vial then was slightly shaken and left for 20 hours in glove-box.

2.3 Structural and compositional characterization

Powder X-ray diffraction (XRD) patterns were recorded on a PANanalytical X'Pert PRO diffractometer with CuKα radiation (λ = 1.5418 Å). Transmission electron microscopy (TEM) and high-resolution transmission electron microscopy (HRTEM) images were obtained with FEI Tecnai G2 F20 operating at 200 kV. The ratio of Ag/Ni of the bimetallic samples as well as the actual amount of Ag on glass carbon (GC) electrode were determined by inductively coupled plasma optical emission spectroscopy (ICP-OES) measurements with a iCAP 6000 series instrument (Thermo Fisher Scientific). X-ray photoelectron spectroscopy (XPS) was performed with a PerkinElmer PHI 5000C ESCA system. Al Kα radiation (hv = 1486.7 eV) as excitation source was used, the chamber pressure was kept below 6×10^{-10} Torr. The binding energy of the spectra was calibrated using the C 1s core level at 284.8 eV from adventitious carbon. The details of curve fitting are described in Supporting Information (SI).

2.4 Calculation of potential – pH diagram of Ni-Ag system

The chemical and electrochemical equilibria of the Ni–Ag–NO_3^-–AcO^-–H_2O system is calculated basing on the thermodynamic activities of nickel, Ag, nitrate and acetate ions in aqueous solutions at T=298.15 K, atmospheric pressure and at solution pH ranging from 1 to 6. The partial pressure of methane was considered to be equal to 2×10^{-6} bar that corresponds to the average concentration of methane in the air.[38] The standard Gibbs energy of formation of nickel hydride Ni_2H was taken from the literature[39]. The calculation details are given in SI.

2.4 Electrochemical Measurement

Rotating disc electrode (RDE) measurement was used to evaluate the ORR performance and carried out on mirror polished glassy carbon electrodes (GC) with the surface area of 0.196 cm^2. The catalyst ink was prepared by mixing 10 µL Nafion-117 with specific volume of the as-prepared nanoparticle dispersions. The metal concentration of the nanoparticle dispersions was measured by ICP-OES before ink preparation. Then a specific volume of the ink (10-20 µL) was taken with a pipette and casted on GC mirror surface. The electrodes were then dried naturally at ambient environment. To obtain a relatively accurate electrochemically active surface area (ECSA) value, the actual amount of catalyst on modified GC was quantified by ICP-OES using solutions obtained via ultrasonic stripping and dissolution in acid of the catalyst layer after the electrochemical test. ECSA of Ag-contained samples was determined by Pb under potential deposition (Pb_{upd}) stripping method[7,40,41]. Specifically, the electrolyte solution 0.1 M KOH was purged with high purity N_2 for 30 minutes followed by adding 125 µM $Pb(NO_3)_2$, hold the potential at 0.20 V for Pb underpotential deposition for 300 s and sweep to 0.7 V at 10 mV s^{-1}. The area under the Pb_{upd} stripping peak of the stable voltammogram was integrated to calculate the electrochemical surface area using the theoretical Pb_{upd} surface charge on Ag of 280 µC cm^{-2}.[7] The calculated surface area (cm^2) and surface area are then normalized to mass of Ag (m^2 g^{-1}). ECSA measurement of Ni can refer to our previous work[42], hydrogen underpotential deposition (H_{upd}) method[43] was used to measure the ECSA of commercial Pt/C. All electrochemical measurements were performed in a three-electrode system using a potentiostat

(BioLogic SP-300) with a graphite rod as a counter electrode and Ag/AgCl in saturated KCl solution as a reference electrode. All the potential reported here were corrected with 85% iR-compensation and calibrated to reversible hydrogen electrode (RHE) according to E(RHE) = E(Ag/AgCl) + 0.964 V in 0.1 M KOH.

3. Results and discussions

3.1 γ-radiation induced synthesis of nanoparticles

General concept: Synthesis of materials by γ-radiation induced methods involves the redox reactions of metal precursor salts with the products of water radiolysis. Upon absorbing ionizing radiation, water molecules undergo decomposition to form free radicals and active molecular species. The main radicals products formed as a result of water radiolysis are hydroxyl radicals, $OH^{\bullet}$, and solvated electrons, e_{aq}^{-}. In neutral water those radicals are formed in equal amounts, of 0.28 μmol J^{-1} and readily react with each other.[44,45] OH radicals are strong oxidants while solvated electrons are strong reductants (Table S1). Thus, in order to tune redox conditions of the solution to either reductive or oxidative, the undesired radical needs to be scavenged. To produce metallic nanomaterials reductive conditions are created by adding, for example, propan-2-ol as an OH radical's scavenger. The reaction between propan-2-ol and $OH^{\bullet}$ results in formation of reductive 2-hydroxyl-2-propyl radicals, which standard potential *vs* SHE is -1.8 V.[46]

$$HO^{\bullet} + (CH_3)_2CHOH \rightarrow H_2O + (CH_3)_2COH^{\bullet} \quad (1)$$

These radicals together with solvated electrons are main agents which are responsible for metal atoms formation from monovalent metal ions.[47]

$$Me^{+} + e_{aq}^{-} / (CH_3)_2COH^{\bullet} \rightarrow Me^{0} \quad (2)$$

For divalent ions the reduction may occurs by the following sequence:

$$Me^{2+} \rightarrow Me^{+} \rightarrow Me^{0} \quad (3)$$

Considering the oxidation state of Ag and Ni in the precursor solutions, the reduction of Ag^{+} ions and Ag atoms formation occurs via Reaction (2), while the reduction of Ni^{2+} to Ni^{0} may follow the route shown in Reaction (3). The details on γ-radiation induced synthesis of metallic Ni are given elsewhere (Ref.[42]). Since the binding energy between metal atoms is stronger than that between atom and solvent, the metal atoms tend to form dimers and subsequently clusters. Metal ions in solution can also adsorb to the clusters and be reduced on the cluster surface.[48] The size of the metal clusters can be controlled by adding polymers and surfactants.[49] The final size of the clusters or nanoparticles is dependent on the initial polymer/ion ratio and thus, polymer concentration in solutions.

3.2 Structural and compositional investigation

To approach the aim of the current study, the following samples were produced and analysed: monometallic nanoparticles (Ag, Ni) and bimetallic composites: core-shells, Ag@Ni, and heterostructures, Ag/Ni. The morphology and structure of the obtained nanomaterials are investigated using TEM and XRD, respectively, and the surface atomic composition is obtained by XPS.

3.2.1 Electron microscopy studies.

Ag nanoparticles:

X-ray diffraction studies performed on the material synthesized from aqueous Ag nitrate solution reveal that the obtained precipitate consists of *fcc* Ag (see Figure 1d). The lattice constant

calculated from XRD pattern is a = 4.096 ± 0.008 Å, which is slightly larger than that for the bulk Ag (a = 4.086 Å)[50]. The Ag precipitate consists of spherical particles which diameters follow a bimodal size distribution where the smaller particles, with average size of 7.4 ± 1.6 nm coexist stably with the larger ones with average diameters 18.0 ± 2.5 nm. The particles size distribution fitted to a lognormal function is shown in Figure 1b. Such a bimodal ensemble may occur in solutions containing surfactants (in our case it is PVA) and is attributed to the difference in interaction energies of polymers with particles which have different diameters.[51] The obtained Ag nanoparticles show five-fold twinned morphology. These structures are often noticeable in *fcc* noble metals.[15,52,53] The shape of such crystals can be described as five single crystal *fcc* subunits sharing their {111} planes[54] and leads to a tensile lattice strain and surface defects. Both defects types may contribute for the enhanced ORR activity of the catalyst.[55–57]

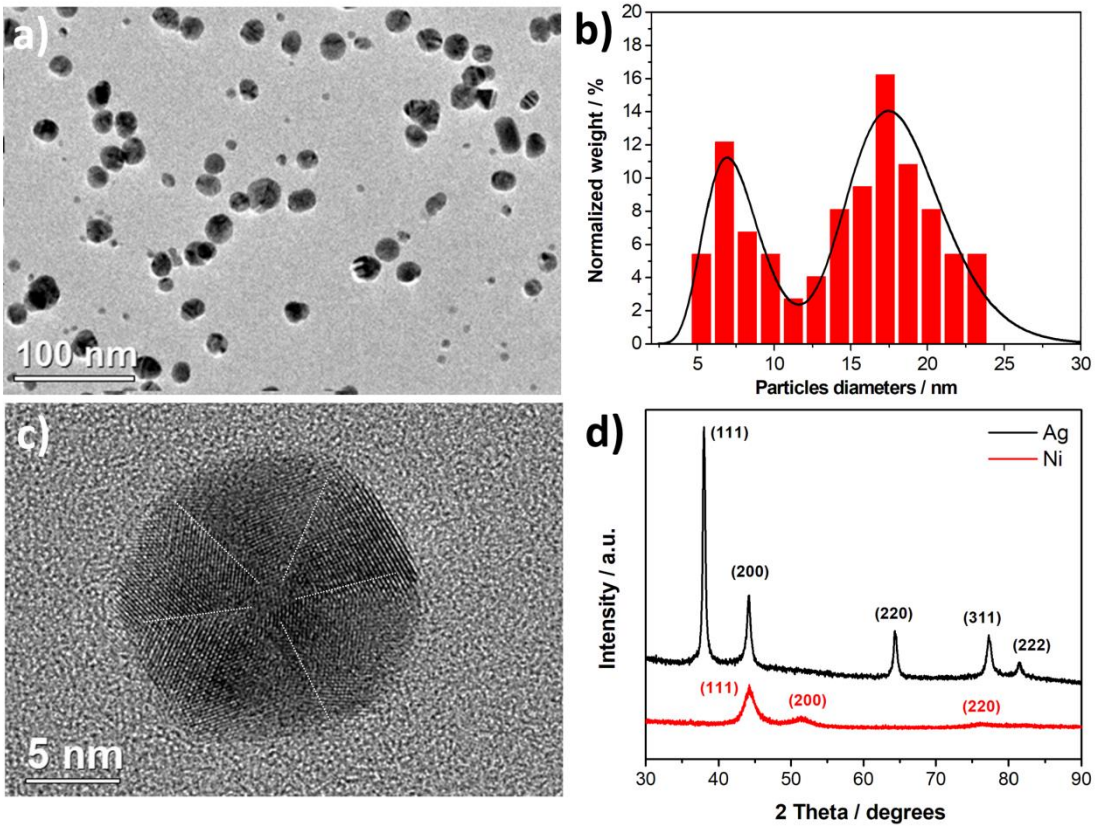

Figure 1 a) TEM image of Ag nanoparticles. b) Sizes distribution histogram calculated from TEM images, fitted to lognormal function. c) HRTEM image of Ag nanoparticle, dash lines reveal the stacking faults and five-fold twined structure. d) XRD patterns of Ag and Ni, Miller indices of corresponding planes in fcc Ag and fcc Ni are labeled.

Ni nanoparticles:

Ni nanomaterial was synthesized from Ni acetate aqueous solution in a form of a black precipitate. In Figure 1c, X-ray diffractogram recorded from the obtained Ni precipitate is presented. As seen in the figure, the XRD pattern contains peaks that belong only to *fcc* Ni, no other XRD peaks are present, indicating the absence of any other crystalline phases in the precipitate. Thus, one can assume that the synthesized material contains mainly metallic *fcc* Ni. The detailed description structure, composition, morphology, magnetic and electrochemical

properties of the metallic Ni nanoparticles obtained by the γ-radiation induced synthesis is provided in our previous study. As shown in Ref.[42], Ni precipitate consists of metallic Ni nanoparticles with diameters of about 3 nm agglomerated to larger clusters. The clusters sizes are between 15 and 40 nm. The surfaces of Ni agglomerates are covered with $NiO/Ni(OH)_2$ poor-crystalline/amorphous layers.

Core-shell nanoparticles, Ag@Ni:

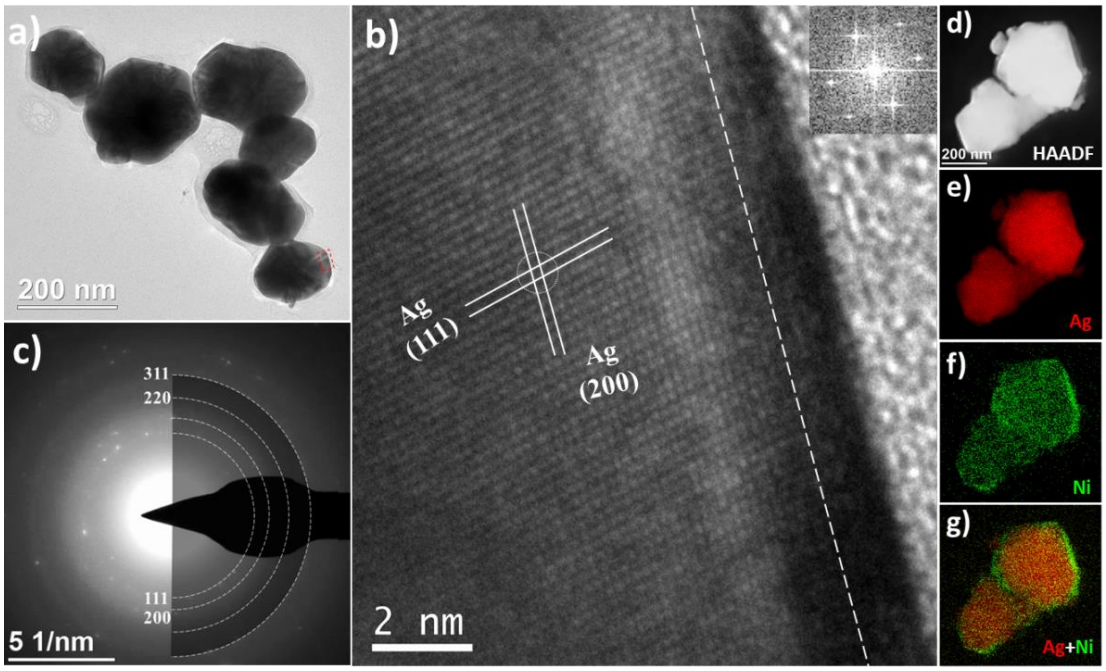

Figure 2 a) TEM image of the synthesized core-shell Ag@Ni nanoparticles. b) HRTEM image recorded from the marked region in a), the interface between Ag core and Ni-based shell is schematically denoted with dashed white line. Miller indices of corresponding fcc Ag planes are denoted. Insert image is FFT patterns taken from the circle-marked region in (b). C) Selected area diffraction (SAED) pattern of the nanoparticles. Miller indices are denoted for fcc Ag. (d) HAADF-STEM image and EDS elemental mappings (e-g), elemental Ag and Ni are labeled with red and green colors, respectively.

Core-shell Ag@Ni nanostructures were obtained in a form of black precipitate by irradiating a mixture containing Ag and Ni salts in equal amount. The morphology of the precipitate was studied using TEM and the results are presented in Figure 2. The core-shell structure is confirmed by EDS mapping shown in see Figure 2(d-g), where the Ag-containing core and Ni-containing shell are clearly visible. The Ag@Ni nanoparticles consist of large (162 nm on average) faceted particles (core) surrounded by thin layer/shell (of about 2 nm thick), as demonstrated in Figure 2(a-b). The composition of the core corresponds to metallic Ag, that has *fcc* structure as determined from SAED pattern (Figure 2c). The presence of *fcc* Ag is confirmed by XRD studies (Figure 4a). The interatomic distances determined from high resolution image and FFT pattern, shown in Figure 2b, correspond to (111) and (200) planes in metallic Ag. The lattice parameter of Ag core calculated using the XRD pattern is 4,105 ± 0.007 Å, (all lattice parameters of Ag obtained from XRD and SAED are presented in Table S2). The shell represents an adjacent Ni containing amorphous layer/shell of about 2 nm at the surface of the Ag core. As demonstrated in Figure 2b,

the interfaces between the crystalline Ag core and amorphous Ni-based shell are continuous and do not contain any pores or voids.

Ag-Ni heterostructures, Ag/Ni:

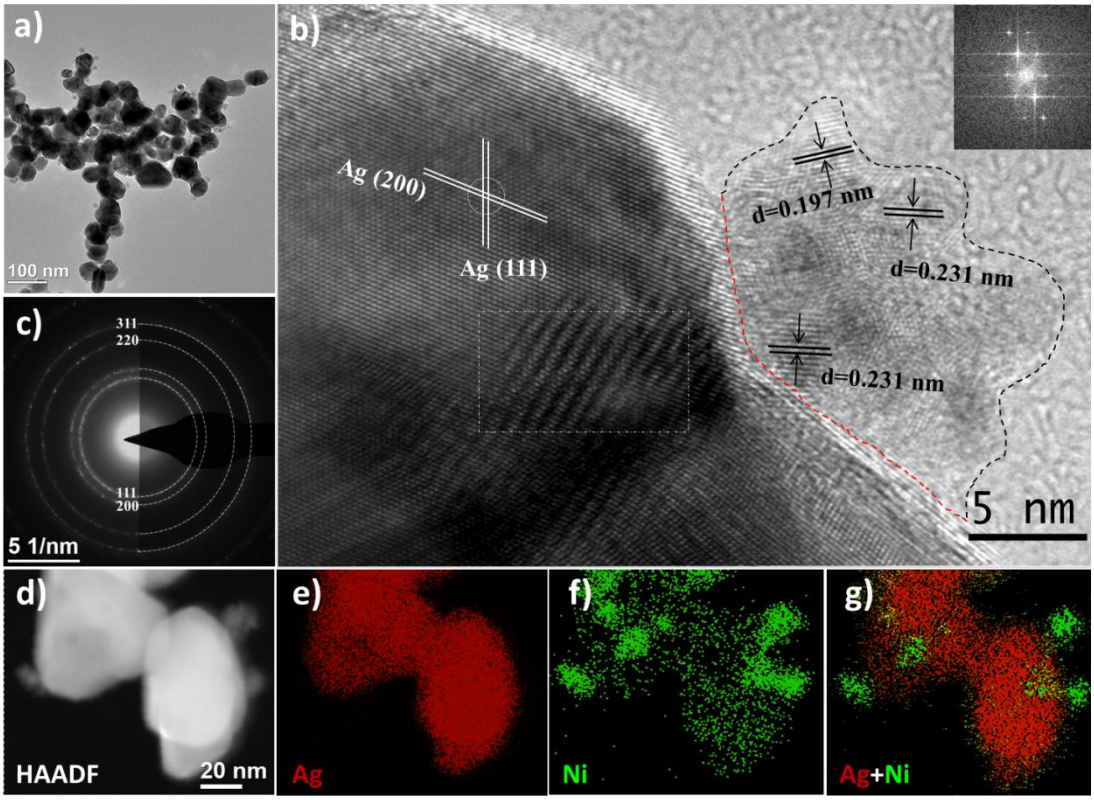

Figure 3. Ag-Ni heterostructures: a) TEM image; b) HRTEM image, the insert is FFT patterns taken from the circle-marked region in (b). The crystallographic planes and corresponding Miller indices are denoted, the interface between and Ni compound is schematically denoted with dashed red line; c) SAED pattern. The reflection indices corresponding to fcc Ag are labeled d) HAADF-STEM image and EDS mappings (e-g), elemental Ag and Ni are denoted with red and green color, respectively.

Ag/Ni heterostructures constitute of single crystal Ag nanoparticles (the average size of 45 nm) with adjacent Ni-containing polycrystalline clusters, as seen in Figure 3. These clusters, which diameters are ranging from 10 to 20 nm, consist of primary particles (with the size of 3 nm). SAED pattern shown in Figure 3c corresponds solely to the diffraction pattern from metallic *fcc* Ag. No clear signal from Ni compounds is registered by the electron diffraction technique. However, the interatomic distances of Ni-containing crystals, determined from HRTEM image (Figure 3b), are 0.231 nm and may correspond to either (101) planes in $Ni(OH)_2$, or (102) planes in Ni_2O_3 / NiOOH, while d = 0.197 nm corresponds to Ni (111).[58,59] Thus, the epitaxial relationship between Ag and Ni (oxy-hydro) oxide can be the following: Ag [100] // $Ni(OH)_2$ [101] or/and Ag [100] // Ni_2O_3(NiOOH) [102]. The calculated lattice mismatch is about 11 %, where Ni (oxy-hydro) oxide undergoes a compressive strain at the surface of Ag. Except for the conventional lattice plane, a Moiré pattern is observed (the area is labeled with a rectangular in Figure 3b). Moiré pattern is an optical phenomenon that indicates the coexistence of two sub-lattices which are either

disoriented with respect to each other or have slightly different lattice constants.[60] Thus, the appearance of Moiré pattern can be ascribed to interferences from two randomly oriented Ag crystals and/or from the heterostructure formed at the interfaces between the Ag nanoparticles and the Ni-based nanoclusters.

3.2.2. X-ray diffraction study

The X-ray diffraction patterns of Ag@Ni core-shell, Ag/Ni heterostructure and reference Ag samples are presented in Figure 4. The high intensity diffraction peaks corresponding to *fcc* Ag[50] are visible for all samples. Meanwhile several low intensity peaks at 2θ range from 20 to 37° have been detected only on the diffractograms recorded from the bimetallic samples but not from the reference ones. Although, the main crystalline phase formed during the synthesis is metallic Ag, the low intensity XRD peaks recorded for both Ag@Ni and Ag/Ni samples indicate the presence of other, Ag- and/or Ni-based compounds. Thus, XRD peaks at 2θ ≈ 34° and 36.2°, shown in Figure 4b, can be ascribed to Ag oxides Ag_2O_6[61], Ag_2O (Ag_2F type)[62] and/or to a mixed oxide Ag_2NiO_2[63]. While in Ag/Ni sample the low intensity peaks at 2θ = 27.6° and 31.9° can be attributed to rhombohedral Ni_2O_3[64]. Possible compounds detected with XRD are listed in Table S3. Note, the diffraction peaks neither from metallic Ni nor from NiO are observed. This may happen due to the fact that the main XRD peaks positions for *fcc* Ni[65] and *fcc* NiO[66] are overlapping with those for Ag. Thus, diffraction peak from Ni (111) appears at 2θ = 44.5° and almost overlapping with that from Ag (200) (2θ = 44.3°). As confirmed by TEM, Ni-based compounds in our samples have much poorer crystallinity as compared to Ag: Ni-based compounds are present in the samples either as thin amorphous layers (Ag@Ni) or as clusters which consist of primary particles with 2-3 nm in diameters. Therefore, X-ray diffraction is less sensitive to the Ni-based compounds in our samples.

In addition, as seen in the insert to Figure 4a, the positions Ag(111) peaks recorded from Ag@Ni and Ag/Ni are shifted by 0.09° towards lower 2θ with regard to that recorded from the metallic Ag sample (used as a reference). This indicates the presence of small crystal lattice distortions in Ag-Ni samples. Those distortions correspond to Ag crystal lattice expansion of 0.65% in Ag@Ni and Ag/Ni as compared to the reference Ag sample. Thus, the X-ray diffraction study reveals that both Ag-Ni nanocomposites consist of crystalline Ag and phases with low crystallinity which contain Ag- and Ni-based oxides.

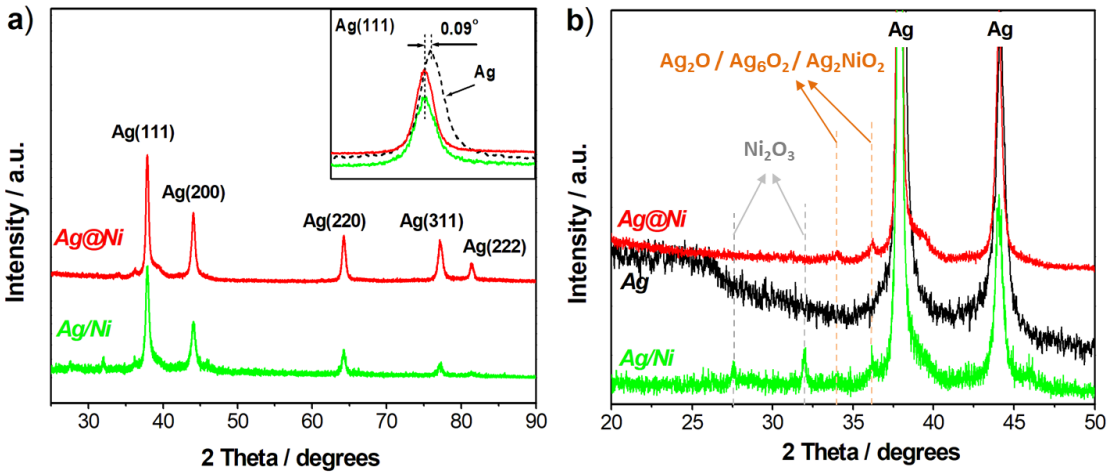

Figure 4 (a) X-ray diffraction patters of Ag@Ni, core-shell and Ag/Ni heterostructure. Miller

indices of corresponding Ag peaks are denoted. The details of Ag (111) peaks are presented in the insert. Black dashed curve corresponds to XRD pattern recorded for Ag nanoparticles. (b) The magnified (2θ = 20-50°) part of XRD patterns containing low intensity peaks, recorded from Ag@Ni, Ag/Ni and Ag nanoparticles. Possible compounds with low density peaks are labeled in Figure 4b.

3.2.3. XPS analysis

To further verify the composition and structure of the studied samples, XPS analysis was performed and the resulting spectra are shown in Figure 5. The binding energies (BE) of O1s, Ag 3d and Ni 2p core levels and atomic ratio of Ag and Ni in the samples measured with XPS are given in the Table S4. The structural and compositional studies of free standing Ni nanoparticles, produced by γ-radiation induced synthesis, were given in our previous work. Therefore, we suggest using Ref.[42] *Y. Yang et al*. for further details on XPS analysis of Ni nanoparticles presented in the current study.

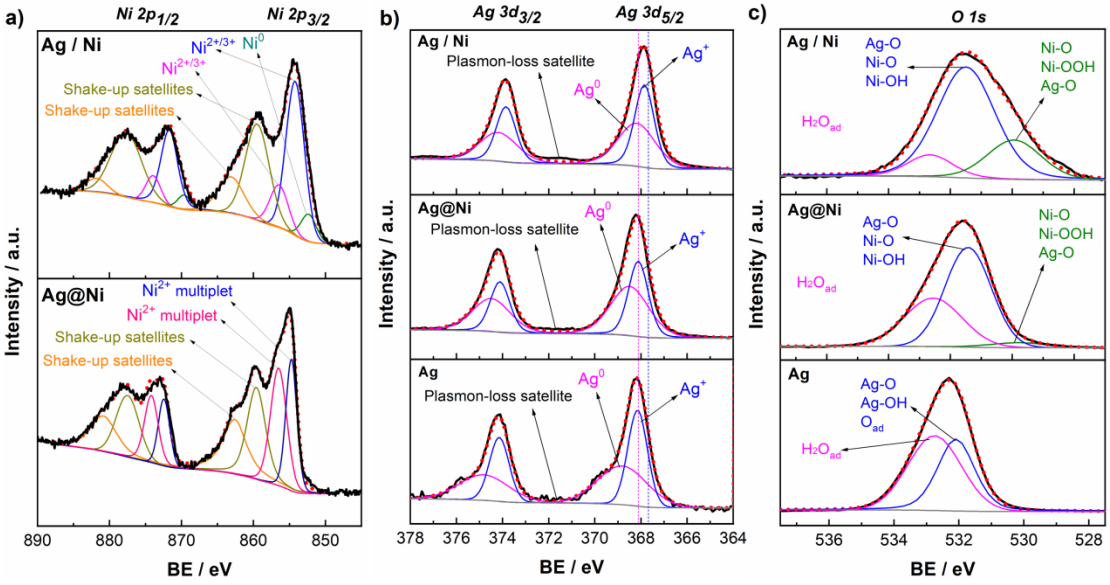

Figure 5 XPS spectra of Ag@Ni and Ag/Ni sample for Ni 2p (a), Ag, Ag@Ni, and Ag/Ni NPs for Ag 3d (b) and O 1s (c). The black solid lines are the original spectra and red dot lines are the fits to the data. The dash lines in (b) at 368.1 eV and 367.7 eV correspond to the BEs of bulk Ag^0 and Ag^+, respectively.

Ag nanoparticles: As reported in the literature, the binding energy (BE) that corresponds to Ag $3d_{5/2}$ spectral line is 368.1 eV for bulk Ag[67]. For bulk Ag_2O this energy is shifted towards lower values, 367.7 eV[67]. In nanomaterials, such as thin films, nanoparticles, atomic clusters and others, Ag $3d_{5/2}$ BE level for both Ag^0 and Ag^+ have tendency to shift towards the higher values due to changes in the electronic structure, by 0.4-0.8 eV[68–72]. Deconvolution of the Ag 3d spectral lines performed in the current study reveals binding energies of 368.8 and 368.2 eV for the Ag $3d_{5/2}$, which may correspond to Ag^0 and Ag^+, respectively. However, both values are higher as compared to those for the bulk metallic Ag and Ag_2O. Since the BE shift is rather large, an unambiguous interpretation of the spectra is difficult, therefore, the results from the structural studies should be considered here. The shift in BE may be partially attributed to the size effect[73] since the

studied Ag sample consists of nanoparticles which have bi-modal size distribution with average diameters of 7.4 nm and 18.0 nm. So far as the sizes of the nanoparticles presented in our study are still rather large to significantly affect the energy of core level electrons[74], other factors are to be considered. Thus, as shown by structural analysis, Ag nanoparticles possess five-fold twinned morphology which may lead to an induced tensile strain that may, in turn, contribute to the BE shift towards higher values. Thus, Ag nanoparticles consist of metallic Ag with Ag_2O formed at the surface. Another possibility is the formation of non-stoichiometric surface and sub-surface Ag-O compounds. The latter statement is supported by the fact that oxygen signal at 532.1 eV may correspond to the BE for the adsorbed/absorbed oxygen on the Ag surface[67,75]. Note that the existence of AgO can be neither confirmed nor disproved since AgO may be reduced by the X-ray beam. The existence of Ag^0 in all studied samples is further confirmed by the presence of plasmon-loss structures at 371.5 and 377.4 eV which are exclusive to metallic Ag[75,76].

Ag@Ni core-shell structures: Analysis of the XPS spectra reveals Ag $3d_{5/2}$ BE peaks located at 368.6 eV and 368.2 eV. Note, that the lower value is close to the BE of Ag-Ag bonds in bulk[67]. Since the diameter of the Ag@Ni core-shell structures is much larger than that of Ag nanoparticles, the size effect on the electronic structure can be neglected. Hence, BE 368.2 eV is attributed to metallic Ag. The higher energy peak may belong to Ag in bimetallic compounds. As reported in the literature, binding energies for Ag 3d in Ag-$Ni(OH)_2$ composites may shift between 0.2 eV to 0.55 eV towards higher energies[77,78] with respect to those in a pure Ag. Ni $2p_{3/2}$ photoelectron lines exhibit a shoulder towards high BEs which is characteristics of NiO[79]. The asymmetry of the peak arises from the partial overlapping of the multiplet splitting of NiO, and its $2p_{3/2}$ peaks found at 854.7 eV and 856.5 eV together with its $2p_{1/2}$ peaks at 872.4 eV and 874.2 eV are in good agreement with literature[80].

Ag/Ni heterostructures: The deconvoluted spectrum of Ni 2p for Ag/Ni sample presents several photoelectron peaks, both primary and secondary. There are three primary peaks resulting from the ejection of a core level electron located at 852.4 eV, 854.3 eV, and 856.5 eV. The first peak are attributed to $2p_{3/2}$ spectral line from metallic Ni[81] ,while second and third peaks may belong to Ni (oxy-hydro) oxides (Ni_2O_3 and/or NiOOH)[82,83]. Likewise, primary peaks at 869.7 eV, 871.8 eV, and 874 eV are attributed to $2p_{1/2}$ peaks of the same compounds. Higher energy singlet broad peaks at 859.4 eV, 863.1 eV, 877.6 eV and 881.8 eV are reported to correspond to a plasmon-loss peak from metallic Ni and shake-up satellite peaks emerging from Ni-O-H compounds[83]. Integration of the primary peaks reveals that 90% of the Ni found within the probing depth, of about 6 nm, corresponds to Ni^{2+}/Ni^{3+} and the remaining 10% to metallic Ni. It is known that Ni is easily oxidized by water, consequently, Ni^{2+}/Ni^{3+} oxide/hydroxide layers cover the surface of metallic Ni particles.[42] Note, that the other Ni compounds such as Ni_2O_3[84] or mixed oxides Ag-Ni-O[24,63], which Ni 2p BEs are within the same range as those for Ni-O and Ni-O-H, may also be present in both Ag@Ni and Ag/Ni nanomaterials. Peaks at BEs of 367.9 and 368.2 eV are attributed to Ag $3d_{5/2}$ of Ag_2O and metallic Ag, respectively.[67] Plasmon-loss satellites at 371.5 and 377.4 eV confirmed the existence of metallic Ag as described above. The presence of the Ag_2O may be ascribed to the adjacent Ni (oxy-hydro) oxides ($Ni(OH)_2/Ni_2O_3$/NiOOH) with strong electronic affinity which would promote the electron-depleted Ag to be oxidized.[11]

3.3 Bimetallic nanoparticles formation

To understand the bimetallic Ag-Ni compounds formation in aqueous solutions, the chemical and electrochemical equilibria of the Ni–Ag–NO_3^-–AcO^-–H_2O system is calculated and shown in Figure 6. The chosen pH range at the diagram covers the experimental pH values, between 5.5 and 3, measured before and after irradiation, respectively. As seen in the diagram, no hydrolysis of metal cations occurs at the chosen pH range. No bimetallic Ag-Ni compounds or mixed oxides are formed as a result of homogeneous reactions in solutions, indicating the interactions between Ag and Ni species occurs heterogeneously via the surface reactions. The redox potential values for Ag and Ni calculated using actual experimental conditions correspond to 0.67 and -0.29 V, respectively. This indicates affinity of the ions for the electrons and the species' tendency to be reduced is much higher in Ag as compared to that in Ni. The calculation details and parameters are presented in SI.

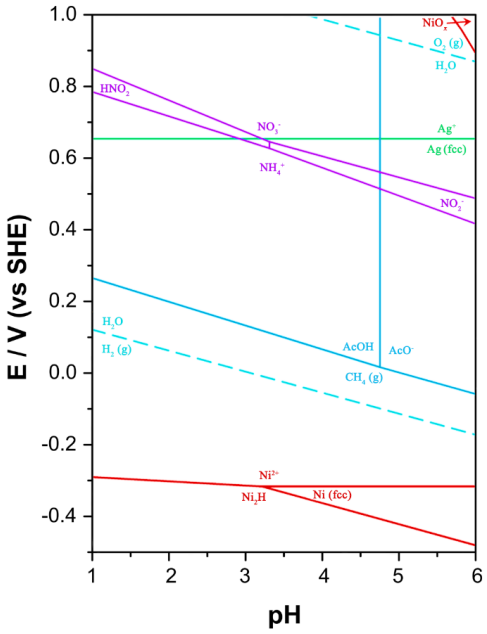

Figure 6 The potential – pH diagram calculated for Ni–Ag–NO_3^-–AcO^-–H_2O system containing 5 mM of Ni^{2+} and Ag^+ ions at T=298,15 K and at atmospheric pressure of 1 bar.

Ag@Ni nanoparticles formation: Core-shell nanoparticles were synthesized by co-reduction method where the aqueous solution containing both Ag and Ni salts are subjected to γ-radiation. Since the reduction potential of Ag is much more positive than that of Ni (Table S1), there will be a thermodynamic driving force to selective reduction of Ag ions first, reduction of Ni will take place only when the system is depleted of Ag^+ ions.[85] Hence, the reduction of Ni^{2+} in solution and homogeneous nucleation of Ni cluster occurs in a less extent. The nucleation of Ag particles occurs according to the following reactions[48]:

$Ag^0 + Ag^0 \rightarrow Ag_2$ (4)

$Ag^0 + Ag^+ \rightarrow Ag_2^+$ (5)

Dimers formed in Reaction (4) later coalescent into the larger clusters. The unreacted remaining Ag ions adsorb on the cluster surface (Reaction 5) and are reduced provided that the reducing agents are continuously supplied into the solution. Moreover, the reduced Ag particles act as seeds over which the Ni-rich phase nucleates and grows. The resulting particles will have a core

with noble metal (Ag) and a shell layer with less noble metal (Ni). This is in agreement with the mechanism of bimetallic nanoparticles formation in solutions exposed to γ-irradiation proposed by Belloni *et al.*[48,86], that implies at low dose rate the electron transfer from less noble metal to more noble one and core-shell structures form. The strong oxidative ability of Ag^+ lead to oxidation of metallic Ni in the shell and Ni oxide formation, the latter is confirmed by XPS studies. The reaction between Ni and Ag can be described as Reaction (6)

$$2Ag^+ + Ni^0 \rightarrow (Ag_2Ni)^{2+} \rightarrow 2Ag^0 + Ni^{2+} \quad (6)$$

The formation of Ni oxide can occur due to reaction of Ni species with molecular oxygen, the latter is formed as a result of decomposition of H_2O_2 (one of the products of water radiolysis) on the solid surface.

***Ag/Ni heterstructures formation*:** Heterostructures were obtained by a successive reduction where Ni nanoparticles were obtained first by γ-radiation induced reduction from the corresponding precursor solution. The details about γ-radiation induce synthesis of Ni nanoparticles performed under the similar conditions as in current study, are given in our previous work[42]. Thereafter Ag acetate solution was added and no further irradiation has been performed. Thus, Ni-containing clusters can act as seeds for heterogeneous nucleation and further growth of Ag nanoparticles. The charge transfer between Ag and Ni, Reaction (6) that results in oxidation of Ni surface layers, leads to formation of Ni (oxy-hydro) oxides clusters.

3.4 Electrochemical studies

To verify the effect of structural and compositional modifications on the catalytic activity of the Ag-Ni composites, detailed electrochemical studies were performed.

3.4.1 Cyclic voltammetry (CV)

CV measurements were conducted in N_2 saturated 0.1 M KOH solution at a scan rate of 50 mV s^{-1}. The results are presented in Figure 7a. As can be seen in the CV curve for the nickel nanoparticles, there are distinct peaks at around 1.35 V and 1.5 V which can be ascribed to redox potentials of a Ni(II)/Ni(III) couple in alkaline media[87,88]. The CV curve measured for the Ag sample exhibits a pair of peaks at around 1 V and 1.35 V corresponding a Ag/Ag(I) redox couple.[89] The cyclic voltammetry curves for both bimetallic samples have distinct double oxidation peaks indicating sequential oxidation Ni and Ag. The electrochemical surface areas of Ag, Ag@Ni and Ag/Ni samples determined from Pb_{upd}-stripping voltammogram are shown in Figure 7b, where a pair of typical Pb-stripping peaks appear between 0.2 – 0.5 V. The ESCA for Ag/Ni and Ag@Ni is found to be 41.90 $m^2 g^{-1}$ and 30.38 $m^2 g^{-1}$, respectively. The ECSA of monometallic Ag is a bit larger (43.6 $m^2 g^{-1}$), which could be ascribed to decreased particle sizes (bimodal particle size distribution with 7.4 nm and 18.0 nm) in the monometallic Ag sample (Table S5 shows the ECSA of Ni and detailed calculation parameters). Besides that, the five-fold twinned structure of Ag nanoparticles may also contribute to their electrochemical activity due to the increased amount of active sites because of the additional edges appearing between twins and induced lattice strain[90].

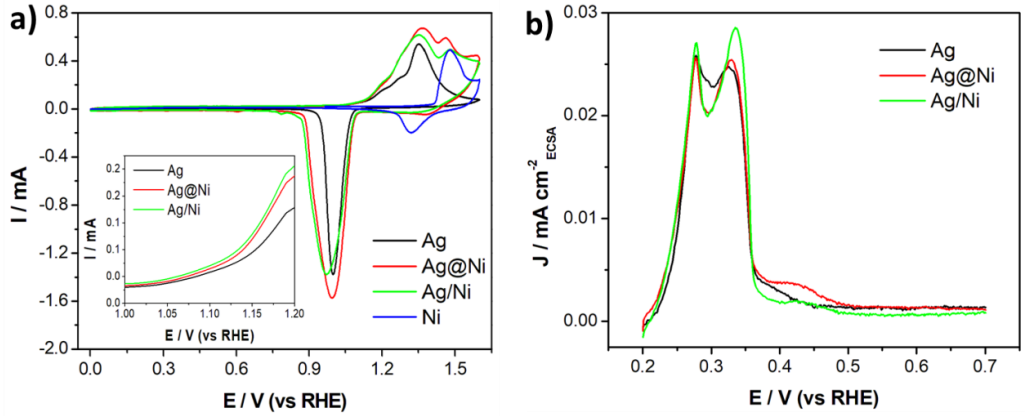

Figure 7. a) Cyclic voltammetry (CV) curves of the Ag, Ag@Ni, Ag-Ni and Ni recorded in 0.1 M N_2 saturated KOH solution at a scan rate of 50 mV s^{-1}, Inset is the magnifying curves showing onset oxidation potential of Ag, Ag@Ni, and Ag/Ni. b) Stripping voltammogram of Pb_{upd} on Ag, Ag@Ni, Ag-Ni in N_2 saturated 0.1 M KOH + 125 µM $Pb(NO_3)_2$ solution at scan rate of 10 mV s^{-1}, the current was normalized with ECSA.

3.4.2 Oxygen Reduction Reaction

The electrocatalytic performance for ORR of the obtained catalysts was investigated. The ORR polarization curves of different catalysts are shown in Figure 8a. The measurements are done at the scan rate of 10 mV s^{-1} and rotation speed of 1600 rpm. The ORR onset potential, E_{onset}, and half-wave potential, $E_{1/2}$, derived from polarization curves are presented in Figure 8b. The data were summarized in Table 1. E_{onset} of both bimetallic Ag-Ni samples (around 0.82 V) is higher than that for the monometallic Ag and Ni, although it is lower than that of commercial Pt/C. This result can be confirmed with the onset oxidation potentials of Ag@Ni, and Ag/Ni (shown in the insert in Figure 7a). It is clear that the onset oxidation potentials of the bimetallic Ag-Ni are lower compared to these in a pure Ag, thus, indicating that the surface of bimetallic Ag-Ni nanoparticles is oxidized more readily than that of Ag. The increased E_{onset} for Ag@Ni and Ag/Ni could be attributed to the enhanced water-activation ability of Ni compounds (NiO and Ni (oxy-hydro) oxides in Ag@Ni and Ag/Ni samples, respectively).[33,91] Similarly, the two bimetallic samples also show larger $E_{1/2}$ values than that of monometallic materials. However, the difference is no as distinct as that in E_{onset}.

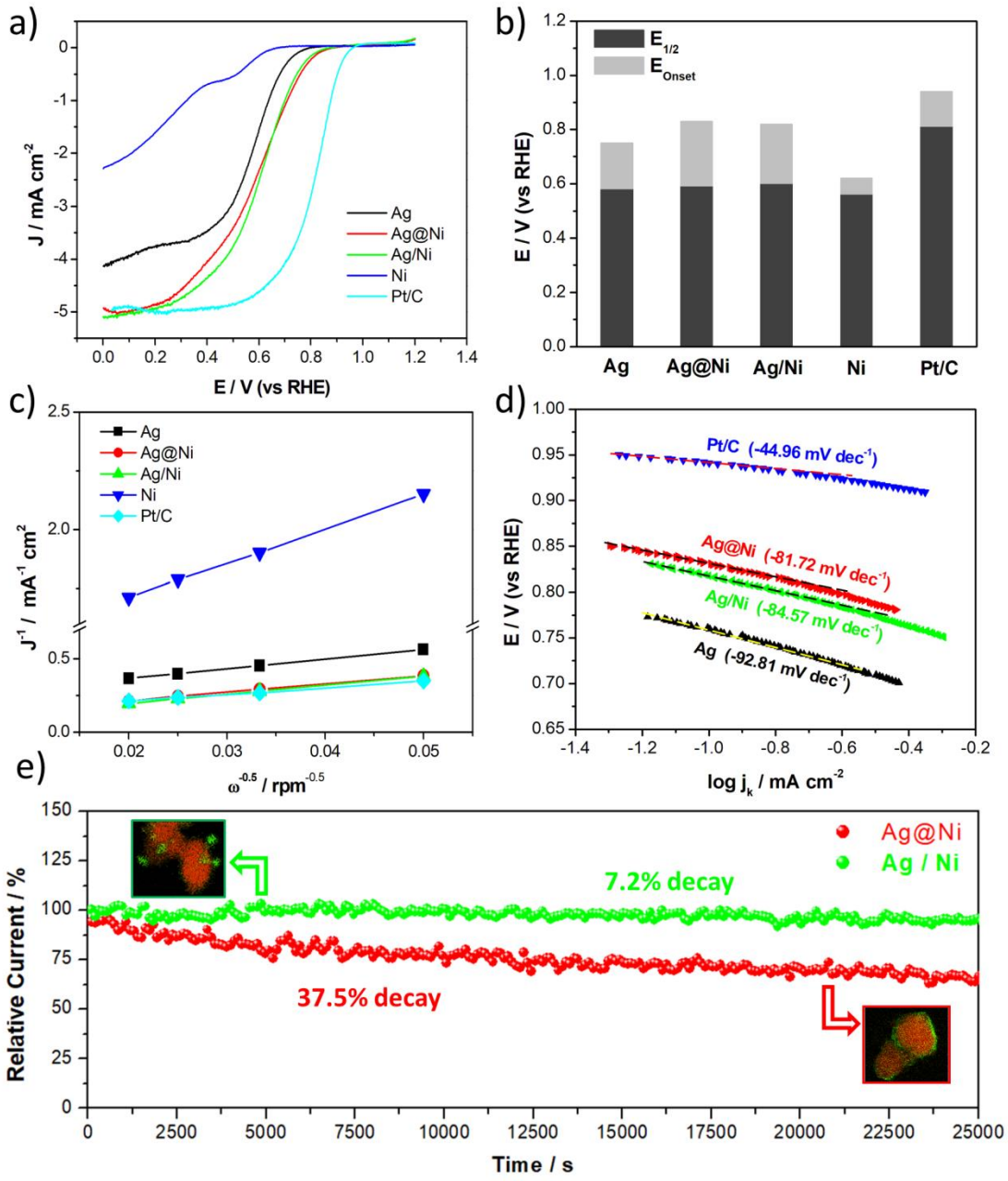

Figure 8 Electrocatalytic performance of Ag, Ag@Ni, Ag/Ni, Ni, Commercial Pt/C (20 wt. %, ETEK) used as a reference. a) ORR polarization curves obtained at the rotation speed of 1600 rpm in O_2-saturated 0.1 M KOH. b) Histograms of onset potentials (E_{onset}) and half-wave potentials ($E_{1/2}$) for all studied samples, c) K–L plots at 0.5 V, d) Tafel plots for geometric surface area normalized kinetic oxygen reduction current with absolute slope values labeled. **All the polarization curves were recorded at the scan rate of 10 mV s^{-1}.** ***e) Chronoamperometric responses (percentage of the current retained versus operation time) of Ag@Ni and Ag/Ni at 0.65 V in O_2-saturated 0.1 M KOH.***

The ORR kinetics were investigated by collecting polarization curves at various rotation speeds (Figure S1(a-d)). Based on those polarization curves, the electron transfer number (n) that reflects the first order ORR kinetics is then calculated using the Koutecky–Levich (K–L) equation[43]. K-L plots at 0.5 V for the studied samples, including commercial Pt/C (20 wt. %, ETEK) used as a reference, are shown in Figure 8c. The calculation details and K-L plots at different potential

(inserts in Figure S1 (a-d)) are shown in SI. The calculated electron transfer number is listed in Table 1. As seen in the table, all Ag-based samples including Ag, Ag@Ni and Ag/Ni possess an electron transfer number over 3.5, demonstrating a mainly four-electron oxygen reduction pathway, which is comparable to that of Pt. A commercial Pt/C was used as the reference catalyst in this work and it has been confirmed in our previous study[92] that the obtained electrochemical parameters are within the normal region of Pt/C catalyst (E_{onset}=0.94 V, $E_{1/2}$=0.82 V). The diffusion limiting current density, J_d values (shown in Table 1) for bimetallic Ag@Ni and Ag/Ni are higher (at about 5.0 mA cm^{-2}) than those for the monometallic compounds and are quite close to that for Pt/C. The specific activity, *SA*, the current per unit catalyst surface area, is commonly used to reflect the intrinsic activity of the catalysts.[93] SA for all prepared samples is calculated at 0.65 V. The bimetallic Ag-Ni display an enhanced SA which was around 3× times improvement relative to monometallic Ag and 175× times higher than that of Ni prepared with the same condition. *SA* for Pt/C is calculated at 376 μA $cm^{-2}{}_{Pt}$ at 0.85 V, a commonly used potential to evaluate SA.[94] It should be noted that the catalytic performance of the as-prepared samples may be affected by PVA, used as a surfactant in the Ag nanoparticles production, which is difficult to remove completely from the catalysts surface (see Figure S2 in SI). Examples of similar effects of protecting surfactants on the ORR was reported by Lu *et al*.[95], where they found that the ORR current density of Ag nanorods was remarkably enhanced when the surfactant had been removed from the material surface. Therefore, the intrinsic ORR activity of our samples is likely to be a bit higher after complete removing the surfactants. The surfactant removal is a complicated procedure[96] that could influences physical and chemical parameters of the materials and thus, it may be a matter of a separate study. Therefore, to minimize the systematic uncertainty in the experiment, in the current work we provide similar post-irradiation treatment for all the samples.

Table 1 Electrochemical parameters of the studied nanocatalysts and Pt/C, used as a reference. The parameters are derived from Figure 8a.

Catalyst	Onset Potential E_{onset} (V)	Half-wave Potential $E_{1/2}$ (V)	Diffusion Limiting Current Density i_d (mA $cm^{-2}{}_{GEO}$)	Specific Activity @0.65V (μA $cm^{-2}{}_{ECSA}$)	Electron Transfer Number *n*
Ag	0.75	0.55	3.76	21.58	3.5
Ag@Ni	0.83	0.59	4.86	60.84	3.9
Ag/Ni	0.82	0.60	4.94	72.61	3.6
Ni	0.62	0.52	0.65	0.39	2.2
Pt/C	0.94	0.81	5.01	376 (@0.85V)	4.0

Tafel plots, used for further analysis of the ORR kinetics of all catalysts, are presented in Figure 8d. Tafel slope of pure Ag was -81.81 mV dec^{-1}, which was within the reported range of -80 to -120 mV dec^{-1} for Ag-based catalysts.[97] The absolute value of Tafel slope decreased in the following sequence: Ag > Ag/Ni ≈ Ag@Ni > Pt/C, indicating the faster oxygen reduction dynamics of bimetallic Ag-Ni catalysts as compared to the monometallic Ag. From the practical application point of view, in addition to the activity, the catalysts should possess a good stability under operation conditions. Chronoamperometry (CA) method was used to evaluate and compare the stability of the obtained two bimetallic Ag-Ni samples. As seen in Figure 8e, Ag/Ni showed superior stability with only 7.2% current decay after 25000 s at 0.65 V in O_2-saturated 0.1 M KOH,

which is around 5 times lower that in Ag@Ni (37.5 % decay).

4. Discussion on the mechanisms of the enhanced ORR performance on Ag-Ni nanocatalysts

The electrochemical studies reveal that both bimetallic Ag-Ni and monometallic Ag catalysts, demonstrate close to four electron transfer pathway. Meanwhile, bimetallic Ag-Ni compounds showed enhanced specific activity compared to that of the separate Ag and Ni catalysts. Evidently, the modulation of the catalysts' structures carried out in the current study is the main reason for the enhanced electrochemical performance. Although the electrochemical parameters measured for both bimetallic samples are quite close to each other, the cause behind the enhanced ORR activity may be different.

As shown above, the Ag@Ni core shell structure consists of metallic Ag nanoparticles covered by amorphous NiO layers. The interactions at the Ag-Ni interfaces imply changes in the atomic surrounding which leads to either partial alloying or to new structures, like mixed oxide Ag-Ni-O, formation. The introduced modifications the electronic structure of the constituents may lead to a ligand effect, which would accelerate the charge transfer between Ag and NiO, thus changing the interface chemical properties. Since the Ni-based shell layers are amorphous, the introduced Ag lattice strain at the interfaces is negligible. However, the individual atoms around the interface may still experience a strain-like environment, and therefore, display a different activity than a crystalline film, as has been observed on Pt in acidic solution.[98] Besides, an amorphous film will have very different interactions with species on the surface compared to a crystalline one, which can affect the rate of catalytic reactions. To sum up, in the Ag@Ni sample, both electronic effects are assumed to contribute to the improved ORR activity, while the strong ligand effect induced by the amorphous Ni-O layers may play the prominent role.

Ag/Ni heterostructures, as revealed by the structural analysis, contain clusters of metallic Ni covered by Ni (oxy-hydro) oxides. These clusters are attached to the surface of Ag nanoparticles. Since Ag and Ni-based clusters are crystalline, and they may grow epitaxial with respect to each other. The large lattice mismatch, of about 11%, established between Ag and Ni_2O_3/NiOOH (oxy-hydro) oxides may result in a tensile lattice strain of silver surface layers which, in turn, leads to changes in electronic structure of Ag. Note that an interface induced ligand effect in the Ag/Ni sample would also contribute to the catalytic performance even though the interface sites are disrupted. Moreover, a high-valence Ni (≥ 2) with even less d-electrons forming in a Ag/Ni sample would imply changes in the electronic structure of a metal-adsorbate type and, thus, might also contribute to the enhanced ORR activity.[99] The latter would need detailed investigation that is beyond the scope of the present study. Therefore, in Ag/Ni sample, the improved ORR activity could be also attributed to a cumulative effect of both ligand and strain effects. Because of the large lattice mismatch between Ag and Ni (oxy-hydro) oxides, strain effect may be considered as a dominant contribution to the activity enhancement.

The superior ORR stability of the Ag/Ni heterostructure as compared to core-shell Ag@Ni, could be ascribed to the possible presence of a stable crystalline NiOOH compound in the former. The

result is consistent with the prediction from DFT calculation by Bark *et al.*[36], where the authors claimed that the presence of a stable NiOOH compound results in the enhanced stability of the catalyst for ORR. Indeed, in the Ag@Ni sample, the metallic Ag nanoparticles are covered by amorphous Ni oxide, that is a metastable phase may undergo recrystallization under the operation conditions, which in turn can lead to the lower stability of the catalyst.

It should be noted that monometallic Ag has been widely reported as an ORR catalyst with two-electron transfer pathway in alkaline solution because of the weak affinity to oxygen.[98,100,101] In this work, however, the electron transfer number was calculated at 3.5, indicating a close to four electron transfer pathway. The increased ORR kinetics in metallic Ag observed in the current study could be attributed to surface defects originated from the five-twinned structure and the induced tensile lattice strain.[55]

5. Conclusions

The effects of structure and composition on catalytic performance of Ag-Ni nanocomposites are investigated. For this purpose, bimetallic Ag-Ni nanocomposites and monometallic Ni and Ag nanoparticles were fabricated using γ radiation induced synthesis approach. The following types of structures are obtained: (i) metallic Ni nanoparticles with diameters of about 3 nm agglomerated to larger clusters, which surfaces are covered with Ni oxide/hydroxide poor-crystalline layers; (ii) The Ag nanoparticles which diameters follow a bimodal size distribution with average diameters of 7.4 ± 1.6 nm and 18.0 ± 2.5 nm. The obtained nanoparticles possess five-fold twinned morphology, typical for fcc Ag (iii) core-shell structure Ag@Ni with metallic Ag with average diameter of about 160 nm, as a core covered by an amorphous Ni oxide (Ni(II)) layer of about 2nm thick; (iv) Heterostructures Ag/Ni which consist of Ag nanoparticles (average diameter of 45 nm) and Ni-containing clusters with the sizes ranging from 10 to 20 nm attached to the Ag surface. The clusters consist of metallic Ni covered with Ni (oxy-hydro) oxide (Ni (II)/Ni (III)) layers. The lattice mismatch at the interfaces between Ag and Ni(oxy-hydro) oxide layers in Ag/Ni heterostructures is about 11%. Basing on the potential – pH diagram calculated for the real Ni–Ag–NO_3^-–AcO^-–H_2O system, a possible formation mechanism of bimetallic Ag-Ni compounds induced by γ-radiation in solutions was discussed.

The catalytic activities of those 4 types of catalysts were compared. Electrochemical studies showed that both monometallic Ag and bimetallic Ag-Ni nanocatalysts demonstrated a close to four electron transfer pathway. Comparing with conventional Ag with a two electron transfer pathway, Ag nanoparticles prepared in this work display faster ORR kinetics due to the defects and lattice strain originated from the five-twinned structure. The bimetallic Ag-Ni display an enhanced SA which is around 3× times improvement relative to monometallic Ag and 175× times higher than that of Ni prepared with the same condition.

The enhanced ORR activity of core-shell Ag@Ni nanoparticles is attributed mainly to a ligand effect that originates from the changing atomic surroundings at Ag-Ni interfaces. Meanwhile a tensile strain induced at Ag surface in Ag/Ni heterostructures leads to the changes in the electronic structure of the constituents, thus, causing the enhanced activity of the catalyst. In addition, good stability of Ag/Ni under the operation conditions as compared to that of Ag@Ni

may be ascribed to the existence of a stable crystalline Ni^{3+} (oxy-hydro) oxide in the heterostructures. The findings presented in the current study demonstrate, among others, the advantages of using γ-radiation induced approaches for the engineering of bimetallic nanocatalysts with a well-defined interfacial structure, an enhanced catalytic activity and good operational stability.

Conflicts of interest

There are no conflicts to declare.

Acknowledgements

The authors would like to acknowledge Swedish Foundation for Strategic Research (SSF) for the financial support of the current study. B. W. thanks the Swedish Research Council (Project No. 2018- 03927). In addition, Y. Y. acknowledges the support for samples test work by Ceshigou Research Service.

Reference

(1) Gottesfeld, S.; Dekel, D. R.; Page, M.; Bae, C.; Yan, Y.; Zelenay, P.; Kim, Y. S. Anion Exchange Membrane Fuel Cells: Current Status and Remaining Challenges. *J. Power Sources* **2018**, *375*, 170–184.

(2) Dekel, D. R. Review of Cell Performance in Anion Exchange Membrane Fuel Cells. *J. Power Sources* **2018**, *375*, 158–169.

(3) United States Geological Survey (USGS). *Mineral Commodity Summaries 2020*; 2020.

(4) Blizanac, B. B.; Ross, P. N.; Marković, N. M. Oxygen Reduction on Silver Low-Index Single-Crystal Surfaces in Alkaline Solution: Rotating Ring Disk Ag(Hkl) Studies. *J. Phys. Chem. B* **2006**, *110*, 4735–4741.

(5) Guo, J.; Hsu, A.; Chu, D.; Chen, R. Improving Oxygen Reduction Reaction Activities on Carbon-Supported Ag Nanoparticles in Alkaline Solutions. *J. Phys. Chem. C* **2010**, *114*, 4324–4330.

(6) Slanac, D. A.; Hardin, W. G.; Johnston, K. P.; Stevenson, K. J. Atomic Ensemble and Electronic Effects in Ag-Rich AgPd Nanoalloy Catalysts for Oxygen Reduction in Alkaline Media. *J. Am. Chem. Soc.* **2012**, *134*, 9812–9819.

(7) Holewinski, A.; Idrobo, J. C.; Linic, S. High-Performance Ag-Co Alloy Catalysts for Electrochemical Oxygen Reduction. *Nat. Chem.* **2014**, *6*, 828–834.

(8) Lima, F. H. B.; Zhang, J.; Shao, M. H.; Sasaki, K.; Vukmirovic, M. B.; Ticianelli, E. A.; Adzic, R. R. Catalytic Activity - d-Band Center Correlation for the O_2 Reduction Reaction on Platinum in Alkaline Solutions. *J. Phys. Chem. C* **2007**, *111*, 404–410.

(9) Park, S. A.; Lim, H.; Kim, Y. T. Enhanced Oxygen Reduction Reaction Activity Due to Electronic Effects between Ag and Mn_3O_4 in Alkaline Media. *ACS Catal.* **2015**, *5*, 3995–4002.

(10) Appleby, A. J. Electrocatalysis and Fuel Cells. *Catal. Rev.* **1971**, *4*, 221–244.

(11) Liu, J.; Liu, J.; Song, W.; Wang, F.; Song, Y. The Role of Electronic Interaction in

the Use of Ag and Mn_3O_4 Hybrid Nanocrystals Covalently Coupled with Carbon as Advanced Oxygen Reduction Electrocatalysts. *J. Mater. Chem. A* **2014**, *2*, 17477–17488.

(12) De, S.; Zhang, J.; Luque, R.; Yan, N. Ni-Based Bimetallic Heterogeneous Catalysts for Energy and Environmental Applications. *Energy Environ. Sci.* **2016**, *9*, 3314–3347.

(13) Yang, Y.; Luo, L. M.; Guo, Y. F.; Dai, Z. X.; Zhang, R. H.; Sun, C.; Zhou, X. W. In Situ Synthesis of PtPd Bimetallic Nanocatalysts Supported on Graphene Nanosheets for Methanol Oxidation Using Triblock Copolymer as Reducer and Stabilizer. *J. Electroanal. Chem.* **2016**, *783*, 132–139.

(14) Song, X.; Zhang, D. Bimetallic Ag-Ni/C Particles as Cathode Catalyst in AFCs (Alkaline Fuel Cells). *Energy* **2014**, *70*, 223–230.

(15) Majee, R.; Kumar, A.; Das, T.; Chakraborty, S.; Bhattacharyya, S. Tweaking Nickel with Minimal Silver in a Heterogeneous Alloy of Decahedral Geometry to Deliver Platinum-like Hydrogen Evolution Activity. *Angew. Chemie Int. Ed.* **2020**, *59*, 2881–2889.

(16) Zhang, Z.; Nenoff, T. M.; Huang, J. Y.; Berry, D. T.; Provencio, P. P. Room Temperature Synthesis of Thermally Tmmiscible Ag-Ni Nanoalloys. *J. Phys. Chem. C* **2009**, *113*, 1155–1159.

(17) Tang, M. H.; Hahn, C.; Klobuchar, A. J.; Ng, J. W. D.; Wellendorff, J.; Bligaard, T.; Jaramillo, T. F. Nickel-Silver Alloy Electrocatalysts for Hydrogen Evolution and Oxidation in an Alkaline Electrolyte. *Phys. Chem. Chem. Phys.* **2014**, *16*, 19250–19257.

(18) Bonventre, D.; Panizon, E.; Ferrando, R. Phase Separation in AgCu and AgNi Core-Shell Icosahedral Nanoparticles: A Harmonic Thermodynamics Study. *Part. Part. Syst. Charact.* **2018**, *35*, 1700425.

(19) Rossi, G.; Rapallo, A.; Mottet, C.; Fortunelli, A.; Baletto, F.; Ferrando, R. Magic Polyicosahedral Core-Shell Clusters. *Phys. Rev. Lett.* **2004**, *93*, 105503.

(20) Delogu, F. Free Energy Differences between Ag-Cu Nanophases with Different Chemical Order. *J. Phys. Chem. C* **2010**, *114*, 19946–19951.

(21) Rapallo, A.; Rossi, G.; Ferrando, R.; Fortunelli, A.; Curley, B. C.; Lloyd, L. D.; Tarbuck, G. M.; Johnston, R. L. Global Optimization of Bimetallic Cluster Structures. I. Size-Mismatched Ag-Cu, Ag-Ni, and Au-Cu Systems. *J. Chem. Phys.* **2005**, *122*, 194308.

(22) Parsina, I.; Baletto, F. Tailoring the Structural Motif of AgCo Nanoalloys: Core/Shell versus Janus-Like. *J. Phys. Chem. C* **2010**, *114*, 1504–1511.

(23) Panizon, E.; Ferrando, R. Strain-Induced Restructuring of the Surface in Core@shell Nanoalloys. *Nanoscale* **2016**, *8*, 15911–15919.

(24) Svintsitskiy, D. A.; Lazarev, M. K.; Kardash, T. Y.; Fedorova, E. A.; Slavinskaya, E. M.; Boronin, A. I. Mixed Silver-Nickel Oxide $AgNiO_2$: Probing by CO during XPS Study. *J. Chem. Phys.* **2020**, *152*, 044707.

(25) Sörgel, T.; Jansen, M. $Ag_3Ni_2O_4$-A New Stage-2 Intercalation Compound of 2H-$AgNiO_2$ and Physical Properties of 2H-$AgNiO_2$ above Ambient Temperature. *J. Solid State Chem.* **2007**, *180*, 8–15.

(26) Schreyer, M.; Jansen, M. Synthesis and Characterization of Ag_2NiO_2 Showing an Uncommon Charge Distribution. *Angew. Chemie Int. Ed.* **2002**, *114*, 665–668.
(27) Jensen, K. D.; Tymoczko, J.; Rossmeisl, J.; Bandarenka, A. S.; Chorkendorff, I.; Escudero-Escribano, M.; Stephens, I. E. L. Elucidation of the Oxygen Reduction Volcano in Alkaline Media Using a Copper-Platinum(111) Alloy. *Angew. Chemie Int. Ed.* **2018**, *57*, 2800–2805.
(28) Gorzkowski, M. T.; Lewera, A. Probing the Limits of D-Band Center Theory: Electronic and Electrocatalytic Properties of Pd-Shell-Pt-Core Nanoparticles. *J. Phys. Chem. C* **2015**, *119*, 18389–18395.
(29) Asara, G. G.; Paz-Borbón, L. O.; Baletto, F. "Get in Touch and Keep in Contact": Interface Effect on the Oxygen Reduction Reaction (ORR) Activity for Supported PtNi Nanoparticles. *ACS Catal.* **2016**, *6*, 4388–4393.
(30) Lai, J.; Huang, B.; Tang, Y.; Lin, F.; Zhou, P.; Chen, X.; Sun, Y.; Lv, F.; Guo, S. Barrier-Free Interface Electron Transfer on PtFe-Fe_2C Janus-like Nanoparticles Boosts Oxygen Catalysis. *Chem* **2018**, *4*, 1153–1166.
(31) Kuttiyiel, K. A.; Sasaki, K.; Park, G. G.; Vukmirovic, M. B.; Wu, L.; Zhu, Y.; Chen, J. G.; Adzic, R. R. Janus Structured Pt-FeNC Nanoparticles as a Catalyst for the Oxygen Reduction Reaction. *Chem. Commun.* **2017**, *53*, 1660–1663.
(32) Bhalothia, D.; Chen, P.-C.; Yan, C.; Wang, K.-W.; Chen, T.-Y. Heterogeneous NiO_2-to-Pd Epitaxial Structure Performs Outstanding Oxygen Reduction Reaction Activity . *J. Phys. Chem. C* **2020**, *124*, 2295–2306.
(33) Park, S. A.; Lee, E. K.; Song, H.; Kim, Y. T. Bifunctional Enhancement of Oxygen Reduction Reaction Activity on Ag Catalysts Due to Water Activation on $LaMnO_3$ Supports in Alkaline Media. *Sci. Rep.* **2015**, *5*, 1–14.
(34) Mavrikakis, M.; Hammer, B.; Nørskov, J. K. Effect of Strain on the Reactivity of Metal Surfaces. *Phys. Rev. Lett.* **1998**, *81*, 2819–2822.
(35) Kitchin, J. R.; Nørskov, J. K.; Barteau, M. A.; Chen, J. G. Role of Strain and Ligand Effects in the Modification of the Electronic and Chemical Properties of Bimetallic Surfaces. *Phys. Rev. Lett.* **2004**, *93*, 156801.
(36) Back, S.; Hansen, M. H.; Garrido Torres, J. A.; Zhao, Z.; Nørskov, J. K.; Siahrostami, S.; Bajdich, M. Prediction of Stable and Active (Oxy-Hydro) Oxide Nanoislands on Noble-Metal Supports for Electrochemical Oxygen Reduction Reaction. *ACS Appl. Mater. Interfaces* **2019**, *11*, 2006–2013.
(37) Soroka, I. L.; Tarakina, N. V.; Hermansson, A.; Bigum, L.; Widerberg, R.; Andersson, M. S.; Mathieu, R.; Paulraj, A. R.; Kiros, Y. Radiation-Induced Synthesis of Nanoscale Co- and Ni-Based Electro-Catalysts on Carbon for the Oxygen Reduction Reaction. *Dalt. Trans.* **2017**, *46*, 9995–10002.
(38) Schiermeier, Q. Global Methane Levels Soar to Record High. *Nature* **2020**.
(39) Baranowski, B.; Bocheńska, K. The Free Energy and Entropy of Formation of Nickel Hydride. *Zeitschrift fur Phys. Chemie* **1965**, *45*, 140–152.
(40) Wiberg, G. K. H.; Mayrhofer, K. J. J.; Arenz, M. Investigation of the Oxygen Reduction Activity on Silver - A Rotating Disc Electrode Study. *Fuel Cells* **2010**, *10*, 575–581.

(41) Wiberg, G.; Mayhofer, K.; Arenz, M. Investigation of the Oxygen Reduction Activity of Non-Platinum Catalysts - a RDE Methodology. *ECS Trans.* **2019**, *19*, 37–46.

(42) Yang, Y.; Johansson, M.; Wiorek, A.; Tarakina, N. V.; Sayed, F.; Mathieu, R.; Jonsson, M.; Soroka, I. L. Gamma-Radiation Induced Synthesis of Freestanding Nickel Nanoparticles. *Dalt. Trans.* **2021**, *50*, 376–383.

(43) Vidal-Iglesias, F. J.; Arán-Ais, R. M.; Solla-Gullón, J.; Herrero, E.; Feliu, J. M. Electrochemical Characterization of Shape-Controlled Pt Nanoparticles in Different Supporting Electrolytes. *ACS Catal.* **2012**, *2*, 901–910.

(44) Schwarz, H. A. Free Radicals Generated by Radiolysis of Aqueous Solutions. *J. Chem. Educ.* **1981**, *58*, 101–105.

(45) Swallow, A. J. An Introduction to Radiation Chemistry. *Int. J. Radiat. Biol. Relat. Stud. Physics, Chem. Med.* **1976**, *30*, 399–399.

(46) Schwarz, H. A.; Dodson, R. W. Reduction Potentials of CO_2- and the Alcohol Radicals. *J. Phys. Chem.* **1989**, *93*, 409–414.

(47) Belloni, J.; Mostafavi, M.; Remita, H.; Marignier, J. L.; Delcourt, M. O. Radiation-Induced Synthesis of Mono- and Multi-Metallic Clusters and Nanocolloids. *New J. Chem.* **1998**, *22*, 1239–1255.

(48) Belloni, J. Nucleation, Growth and Properties of Nanoclusters Studied by Radiation Chemistry. *Catal. Today* **2006**, *113*, 141–156.

(49) Mostafavi, M.; Keghouche, N.; Delcourt, M. O.; Belloni, J. Ultra-Slow Aggregation Process for Silver Clusters of a Few Atoms in Solution. *Chem. Phys. Lett.* **1990**, *167*, 193–197.

(50) Jette, E. R.; Foote, F. Precision Determination of Lattice Constants. *J. Chem. Phys.* **1935**, *3*, 605–616.

(51) Shih, C. Y.; Streubel, R.; Heberle, J.; Letzel, A.; Shugaev, M. V.; Wu, C.; Schmidt, M.; Gökce, B.; Barcikowski, S.; Zhigilei, L. V. Two Mechanisms of Nanoparticle Generation in Picosecond Laser Ablation in Liquids: The Origin of the Bimodal Size Distribution. *Nanoscale* **2018**, *10*, 6900–6910.

(52) Liu, T.; Jiang, P.; You, Q.; Ye, S. Five-Fold Twinned Pentagonal Gold Nanocrystal Structure Exclusively Bounded by {110} Facets. *CrystEngComm* **2013**, *15*, 2350–2353.

(53) Liu, S.; Mu, X.; Li, W.; Lv, M.; Chen, B.; Chen, C.; Mu, S. Cation Vacancy-Modulated PtPdRuTe Five-Fold Twinned Nanomaterial for Catalyzing Hydrogen Evolution Reaction. *Nano Energy* **2019**, *61*, 346–351.

(54) Sun, Y.; Ren, Y.; Liu, Y.; Wen, J.; Okasinski, J. S.; Miller, D. J. Ambient-Stable Tetragonal Phase in Silver Nanostructures. *Nat. Commun.* **2012**, *3*, 1–6.

(55) Liu, S.; Zhang, Q.; Li, Y.; Han, M.; Gu, L.; Nan, C.; Bao, J.; Dai, Z. Five-Fold Twinned Pd_2NiAg Nanocrystals with Increased Surface Ni Site Availability to Improve Oxygen Reduction Activity. *J. Am. Chem. Soc.* **2015**, *137*, 2820–2823.

(56) Erikson, H.; Sarapuu, A.; Tammeveski, K. Oxygen Reduction Reaction on Silver Catalysts in Alkaline Media: A Minireview. *ChemElectroChem* **2019**, *6*, 73–86.

(57) Dietze, E. M.; Grönbeck, H. Structure-Dependent Strain Effects. *ChemPhysChem* **2020**, *21*, 2407–2410.

(58) Manukyan, K. V; Tan, W.; Deboer, R. J.; Stech, E. J.; Aprahamian, A.; Wiescher, M.; Rouvimov, S.; Overdeep, K. R.; Shuck, C. E.; Weihs, T. P.; Mukasyan, A. S. Irradiation-Enhanced Reactivity of Multilayer Al/Ni Nanomaterials. *ACS Appl. Mater. Interfaces* **2015**, *7*, 11272–11279.

(59) Zhou, W.; Cao, X.; Zeng, Z.; Shi, W.; Zhu, Y.; Yan, Q.; Liu, H.; Wang, J.; Zhang, H. One-Step Synthesis of Ni_3S_2 Nanorod@$Ni(OH)_2$ Nanosheet Core-Shell Nanostructures on a Three-Dimensional Graphene Network for High-Performance Supercapacitors. *Energy Environ. Sci.* **2013**, *6*, 2216–2221.

(60) Kobayashi, K. Moiré Pattern in Scanning Tunneling Microscopy: Mechanism in Observation of Subsurface Nanostructures. *Phys. Rev. B - Condens. Matter Mater. Phys.* **1996**, *53*, 11091–11099.

(61) Beesk, W.; Jones, P. G.; Rumpel, H.; Schwarzmann, E.; Sheldrick, G. M. X-Ray Crystal Structure of Ag_6O_2. *J. Chem. Soc. Chem. Commun.* **1981**, No. 14, 664–665.

(62) Kabalkina, S. S.; Popova, S. V.; Serebryanaya, N. R.; Vereshchagin, L. F. A New Ag_2O Modification with Stratified Structure. *Dokl. Akad. Nauk SSSR* **1963**, *152*, 853–854.

(63) Wedig, U.; Adler, P.; Nuss, J.; Modrow, H.; Jansen, M. Studies on the Electronic Structure of Ag_2NiO_2, an Intercalated Delafossite Containing Subvalent Silver. *Solid State Sci.* **2006**, *8*, 753–763.

(64) Aggarwal, P. S.; Goswami, A. An Oxide of Tervalent Nickel. *J. Phys. Chem.* **1961**, *65*, 2105–2105.

(65) Taylor, A. Lattice Parameters of Binary Nickel Cobalt Alloys. *J. Inst. Met.* **1950**, *77*, 585–594.

(66) Ana Walt, J. D. H.; Rinn, H. W.; Frevel, L. K. Chemical Analysis by X-Ray Diffraction: Classification and Use of X-Ray Diffraction Patterns. *Ind. Eng. Chem. - Anal. Ed.* **1938**, *10*, 457–512.

(67) Schön, G.; Tummavuori, J.; Lindström, B.; Enzell, C. R.; Enzell, C. R.; Swahn, C.-G. ESCA Studies of Ag, Ag_2O and AgO. *Acta Chem. Scand.* **1973**, *27*, 2623–2633.

(68) Chen, Y. Y.; Yu, S. H.; Yao, Q. Z.; Fu, S. Q.; Zhou, G. T. One-Step Synthesis of Ag_2O@$Mg(OH)_2$ Nanocomposite as an Efficient Scavenger for Iodine and Uranium. *J. Colloid Interface Sci.* **2018**, *510*, 280–291.

(69) Shi, L.; Liang, L.; Ma, J.; Wang, F.; Sun, J. Enhanced Photocatalytic Activity over the Ag_2O-g-C_3N_4 Composite under Visible Light. *Catal. Sci. Technol.* **2014**, *4*, 758–765.

(70) Sumesh, E.; Bootharaju, M. S.; Anshup; Pradeep, T. A Practical Silver Nanoparticle-Based Adsorbent for the Removal of Hg^{2+} from Water. *J. Hazard. Mater.* **2011**, *189*, 450–457.

(71) Weaver, J. F.; Hoflund, G. B. Surface Characterization Study of the Thermal Decomposition of Ag_2O. *Chem. Mater.* **1994**, *6*, 1693–1699.

(72) Firet, N. J.; Blommaert, M. A.; Burdyny, T.; Venugopal, A.; Bohra, D.; Longo, A.; Smith, W. A. Operando EXAFS Study Reveals Presence of Oxygen in Oxide-Derived Silver Catalysts for Electrochemical CO_2 Reduction. *J. Mater.*

Chem. A **2019**, *7*, 2597–2607.

(73) Lopez-Salido, I.; Lim, D. C.; Kim, Y. D. Ag Nanoparticles on Highly Ordered Pyrolytic Graphite (HOPG) Surfaces Studied Using STM and XPS. *Surf. Sci.* **2005**, *588*, 6–18.

(74) Dietsche, R.; Lim, D. C.; Bubek, M.; Lopez-Salido, I.; Ganteför, G.; Kim, Y. D. Comparison of Electronic Structures of Mass-Selected Ag Clusters and Thermally Grown Ag Islands on Sputter-Damaged Graphite Surfaces. *Appl. Phys. A Mater. Sci. Process.* **2008**, *90*, 395–398.

(75) Hoflund, G. B.; Hazos, Z. F.; Salaita, G. N. Surface Characterization Study of Ag, AgO, and Ag_2O Using X-Ray Photoelectron Spectroscopy and Electron Energy-Loss Spectroscopy. *Phys. Rev. B* **2000**, *62*, 11126–11133.

(76) Leiro, J.; Minni, E.; Suoninen, E. Study of Plasmon Structure in XPS Spectra of Silver and Gold. *J. Phys. F Met. Phys.* **1983**, *13*, 215–221.

(77) Lv, S.; Yang, F.; Chu, X.; Wang, H.; Yang, J.; Chi, Y.; Yang, X. In Situ Construction of Ag/Ni(OH)2 Composite Electrode by Combining Electroless Deposition Technology with Electrodeposition. *Metals.* **2019**, *9*, 826.

(78) Bao, F.; Tan, F.; Wang, W.; Qiao, X.; Chen, J. Facile Preparation of Ag/$Ni(OH)_2$ Composites with Enhanced Catalytic Activity for Reduction of 4-Nitrophenol. *RSC Adv.* **2017**, *7*, 14283–14289.

(79) Kim, K. S.; Winograd, N. X-Ray Photoelectron Spectroscopic Studies of Nickel-Oxygen Surfaces Using Oxygen and Argon Ion-Bombardment. *Surf. Sci.* **1974**, *43*, 625–643.

(80) Dubey, P.; Kaurav, N.; Devan, R. S.; Okram, G. S.; Kuo, Y. K. The Effect of Stoichiometry on the Structural, Thermal and Electronic Properties of Thermally Decomposed Nickel Oxide. *RSC Adv.* **2018**, *8*, 5882–5890.

(81) Andrews, P. T.; Collins, T.; Weightman, P. The Influence of the Number of Unoccupied 3d States on the L 3M4,5M4,5 Auger Spectrum of Ni. *J. Phys. C Solid State Phys.* **1981**, *14*, L957.

(82) Payne, B. P.; Biesinger, M. C.; McIntyre, N. S. The Study of Polycrystalline Nickel Metal Oxidation by Water Vapour. *J. Electron Spectros. Relat. Phenomena* **2009**, *175*, 55–65.

(83) Biesinger, M. C.; Payne, B. P.; Grosvenor, A. P.; Lau, L. W. M.; Gerson, A. R.; Smart, R. S. C. Resolving Surface Chemical States in XPS Analysis of First Row Transition Metals, Oxides and Hydroxides: Cr, Mn, Fe, Co and Ni. *Appl. Surf. Sci.* **2011**, *257*, 2717–2730.

(84) Grosvenor, A. P.; Biesinger, M. C.; Smart, R. S. C.; McIntyre, N. S. New Interpretations of XPS Spectra of Nickel Metal and Oxides. *Surf. Sci.* **2006**, *600*, 1771–1779.

(85) Tsuji, M.; Hikino, S.; Matsunaga, M.; Sano, Y.; Hashizume, T.; Kawazumi, H. Rapid Synthesis of Ag@Ni Core-Shell Nanoparticles Using a Microwave-Polyol Method. *Mater. Lett.* **2010**, *64*, 1793–1797.

(86) Treguer, M.; De Cointet, C.; Remita, H.; Khatouri, J.; Mostafavi, M.; Amblard, J.; Belloni, J.; De Keyzer, R. Dose Rate Effects on Radiolytic Synthesis of Gold-Silver Bimetallic Clusters in Solution. *J. Phys. Chem. B* **1998**, *102*,

4310–4321.

(87) Zhang, C.; Qian, L.; Zhang, K.; Yuan, S.; Xiao, J.; Wang, S. Hierarchical Porous Ni/NiO Core-Shells with Superior Conductivity for Electrochemical Pseudo-Capacitors and Glucose Sensors. *J. Mater. Chem. A* **2015**, *3*, 10519–10525.

(88) Chen, L.; Liu, L.; Guo, Q.; Wang, Z.; Liu, G.; Chen, S.; Hou, H. Preparation of $Ni(OH)_2$ Nanoplatelet/Electrospun Carbon Nanofiber Hybrids for Highly Sensitive Nonenzymatic Glucose Sensors. *RSC Adv.* **2017**, *7*, 19345–19352.

(89) Yuan, L.; Jiang, L.; Liu, J.; Xia, Z.; Wang, S.; Sun, G. Facile Synthesis of Silver Nanoparticles Supported on Three Dimensional Graphene Oxide/Carbon Black Composite and Its Application for Oxygen Reduction Reaction. *Electrochim. Acta* **2014**, *135*, 168–174.

(90) Stenlid, J. H.; Brinck, T. Extending the σ-Hole Concept to Metals: An Electrostatic Interpretation of the Effects of Nanostructure in Gold and Platinum Catalysis. *J. Am. Chem. Soc.* **2017**, *139*, 11012–11015.

(91) Subbaraman, R.; Tripkovic, D.; Chang, K. C.; Strmcnik, D.; Paulikas, A. P.; Hirunsit, P.; Chan, M.; Greeley, J.; Stamenkovic, V.; Markovic, N. M. Trends in Activity for the Water Electrolyser Reactions on 3d M(Ni,Co,Fe,Mn) Hydr(Oxy)Oxide Catalysts. *Nat. Mater.* **2012**, *11*, 550–557.

(92) Li, Z.; Yang, Y.; Relefors, A.; Kong, X.; Siso, G. M.; Wickman, B.; Kiros, Y.; Soroka, I. L. Tuning Morphology, Composition and Oxygen Reduction Reaction (ORR) Catalytic Performance of Manganese Oxide Particles Fabricated by γ-Radiation Induced Synthesis. *J. Colloid Interface Sci.* **2021**, *583*, 71–79.

(93) Wei, C.; Sun, S.; Mandler, D.; Wang, X.; Qiao, S. Z.; Xu, Z. J. Approaches for Measuring the Surface Areas of Metal Oxide Electrocatalysts for Determining Their Intrinsic Electrocatalytic Activity. *Chem. Soc. Rev.* **2019**, *48*, 2518–2534.

(94) Jiang, L.; Hsu, A.; Chu, D.; Chen, R. Oxygen Reduction Reaction on Carbon Supported Pt and Pd in Alkaline Solutions. *J. Electrochem. Soc.* **2009**, *156*, B370.

(95) Lu, Y.; Wang, Y.; Chen, W. Silver Nanorods for Oxygen Reduction: Strong Effects of Protecting Ligand on the Electrocatalytic Activity. *J. Power Sources* **2011**, *196*, 3033–3038.

(96) Niu, Z.; Li, Y. Removal and Utilization of Capping Agents in Nanocatalysis. *Chem. Mater.* **2014**, *26*, 72–83.

(97) Zhou, R.; Qiao, S. Z. Silver/Nitrogen-Doped Graphene Interaction and Its Effect on Electrocatalytic Oxygen Reduction. *Chem. Mater.* **2014**, *26*, 5868–5873.

(98) Wang, Q.; Chen, F.; Liu, Y.; Zhang, N.; An, L.; Johnston, R. L. Bifunctional Electrocatalysts for Oxygen Reduction and Borohydride Oxidation Reactions Using Ag_3Sn Nanointermetallic for the Ensemble Effect. *ACS Appl. Mater. Interfaces* **2017**, *9*, 35701–35711.

(99) Li, Y.; Wu, Z.; Lu, P.; Wang, X.; Liu, W.; Liu, Z.; Ma, J.; Ren, W.; Jiang, Z.; Bao, X. High-Valence Nickel Single-Atom Catalysts Coordinated to Oxygen Sites for Extraordinarily Activating Oxygen Evolution Reaction. *Adv. Sci.* **2020**, *7*, 1903089.

(100) Lu, Y.; Chen, W. Size Effect of Silver Nanoclusters on Their Catalytic Activity for Oxygen Electro-Reduction. *J. Power Sources* **2012**, *197*, 107–110.
(101) Singh, P.; Buttry, D. A. Comparison of Oxygen Reduction Reaction at Silver Nanoparticles and Polycrystalline Silver Electrodes in Alkaline Solution. *J. Phys. Chem. C* **2012**, *116*, 10656–10663.

Supplementary Information

γ-Radiation Induced Engineering of Interfaces in Bimetallic Ag-Ni Nanocomposites for Oxygen Reduction in Alkaline Media

Yi Yang[1*], Gerard Montserrat-Sisó[2], Björn Wickman[2], Pavel Anatolyevich Nikolaychuk[3], Inna L. Soroka[1*]

[1]*Applied Physical Chemistry, Department of Chemistry, School of Engineering Sciences in Chemistry, Biotechnology and Health, KTH Royal Institute of Technology, S-100 44 Stockholm, Sweden*

[2]*Chemical Physics, Department of Physics, Chalmers University of Technology, 412 96 Gothenburg, Sweden*

[3]*Microhydrodynamic Technologies Laboratory, Tyumen State University, 625003 Tyumen, Russian Federation*

[*]*Corresponding Authors*

Table S1 Reduction potential of chemicals involved in the material synthesis.

Reduction Potential	H_2O/e_{aq}^-	$HO^•/H_2O$	$(CH_3)_2C^·OH/(CH_3)_2CHOH$	Ag^+/Ag^0	Ni^{2+}/Ni^0
E_0 / V(vs *SHE*)	–2.7	+1.8	–1.8	+0.799	–0.257

Table S2 Structural parameters of Ag-Ni compounds obtained from XRD and TEM studies

Catalyst	Composition/morphology	Lattice parameter, a in [Å], from SAED	Lattice parameter, a in [Å] from XRD
		Ag, fcc	Ag, fcc
Ag@Ni	Ag – core; Ni – based - shell (core-shell structure)	4.177±0.018	4.105±0.007
Ag/Ni	Ag large monocrystalline particles and Ni-based small particles forming clusters (heterostructures)	4.175±0.047	4,105±0.007
Ag	Metallic Ag particles having five twinned structure		4.096±0.008

Table S3. XRD peak positions indicated in 2θ range from 20° to 45° and corresponding Ag- and Ni-based compounds.

Ag/Ni		Ag@Ni	
2 Theta	Compound	2 Theta	Compound
27.6	Ni_2O_3 [1]	29.6	$Ag(NiO_2)$ (29.2°)[2]
31.9	Ni_2O_3 [1]	31.2	N/A
34.0	Ag_6O_2(33.7°)[3];Ag_2O(33.7°)[4]; Ag_2NiO_2 (33.5°) [5]	34.0	Ag_6O_2(2θ=33.7°)[3];Ag_2O(33.7°)[4]; Ag_2NiO_2 (33.5°) [5]
36.2	Ag_6O_2(36.3°)[3], Ag_2O(36.4°)[4]; Ag_2NiO_2 (36.2°) [5]	36.3	Ag_6O_2(2θ=36.3°) [3]; Ag_2O(36.4°) [4]; $Ag(NiO_2)$ (36.1°) [2]; Ag_2NiO_2 (36.2°) [5]
37.9	Ag metal [6]	37.9	Ag metal [6]
44.0	Ag metal [6]	44.1	Ag metal [6]

Table S4 Binding energies (BE) of O, Ag and Ni core levels measured with XPS on Ag, Ag@Ni core-shell and Ag/Ni heterostructure nanocatalysts

	Ag BE, eV	Ag@Ni BE, eV	Ag/Ni BE,eV	Possible Compounds
O 1s		529.8	529.9	Ni-O; Ni-OOH, Ag-O [7]
		531.4	531.5	Ag-O, Ni-O, Ni-OH
	532.1			O adsorbed [8], Ag-O [9], Ag-OH [10]
	532.8	532.5	532.6	Adsorbed H_2O [9]
Ag	368.2 (50%)			Ag(I); AgOx [7]
$3d_{5/2}$	368.8 (50%)			Ag (0) metal [11]
	371.5			Plasmon-loss satellite [12]
	374.2			
	374.8			
$3d_{3/2}$	377.4			
Ag		368.2 (17 %)		Ag (0) [8],
$3d_{5/2}$		368.6 (19 %)		Ag in Ag-Ni compounds [13 14]
		371.5		Plasmon-loss satellite
		374.2		
$3d_{3/2}$		374.6		
		377.4		
Ag			367.9 (32 %)	Ag (I) (Ag_2O) [8]
$3d_{5/2}$			368.2 (30 %)	Ag (0) [8]
			371.5	Plasmon-loss satellite
			373.9	
$3d_{3/2}$			374.2	
			377.4	
Ni $2p_{3/2}$		854.7; 856.5		Ni (II) multiplet (NiO) [15]
		(64 %)		
		859.6; 862.5		Shake-up satellites [16]
$2p_{1/2}$		872.4;		
		874.2		
		877.6; 881.0		
Ni $2p_{3/2}$			852.4 (4 %)	Ni^0 (metal) [17]
			854.3; 856.5 (34 %)	Ni(II)/Ni(III) [18]
			859.4; 863.1	Shake-up satellites [16]
$2p_{1/2}$			869.7	
			871.8; 874	
			877.6; 881.8	

Table S5 Ag, Ni molar ratio, metal amount on electrode (m_{GC}) and the calculated ECSA based on the data from Pb-stripping and ICP-OES. ECSA of Ni was measured and calculated by the double-layer capacitance (C_{dl}) method, hydrogen underpotential deposition (H_{upd}) method was used to measure the ECSA of commercial Pt/C.

Catalyst	Ag_xNi_y	m_{GC}	ECSA	
			cm^2	$m^2 g^{-1}$
Ag	/	10 μg $_{Ag}$	4.36	43.60
Ag@Ni	Ag_4Ni_1	18 μg $_{Ag}$	5.47	30.38
Ag/Ni	Ag_3Ni_1	11 μg $_{Ag}$	4.61	41.90
Ni	/	50 μg $_{Ni}$	19.56	39.20
Pt/C	/	2 μg $_{Pt}$	0.86	43.1

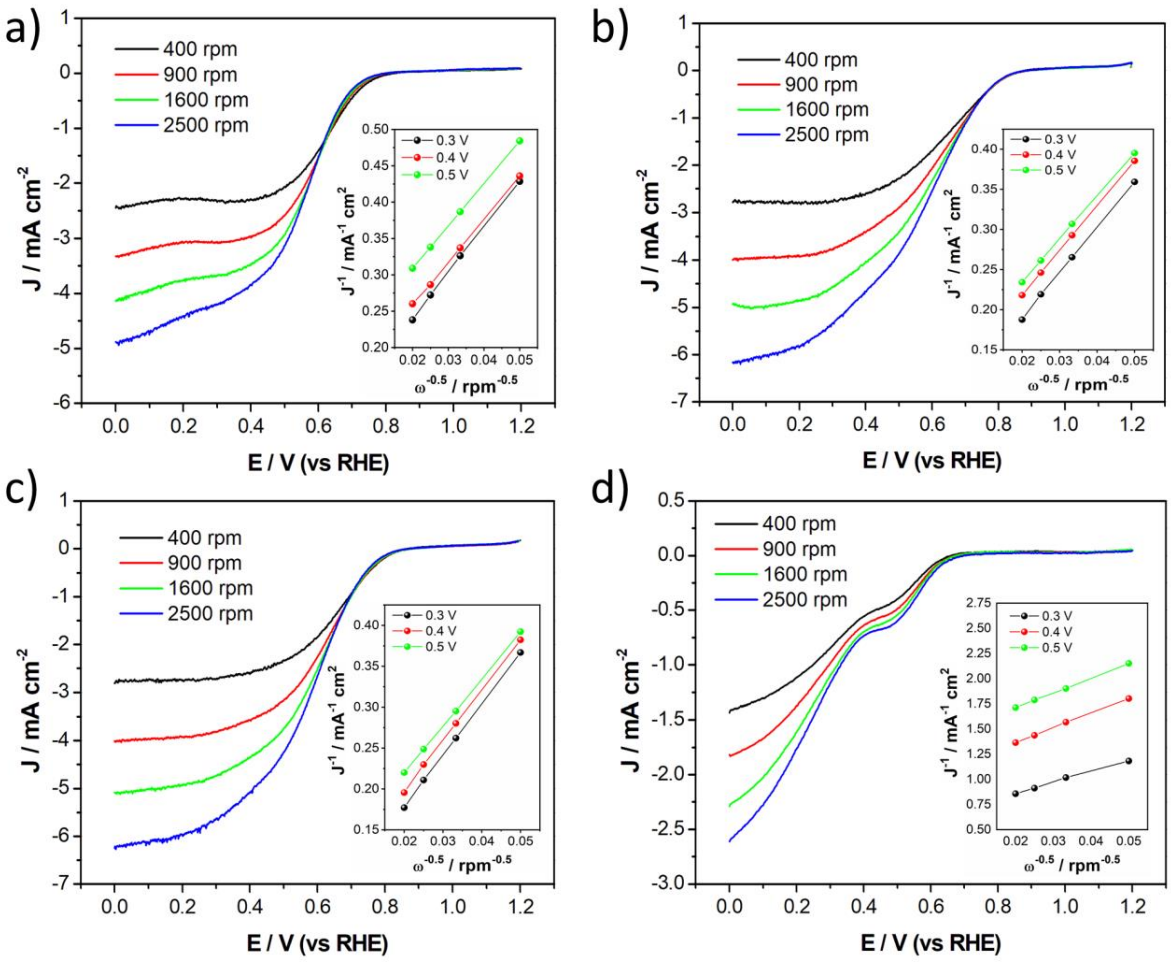

Figure S1 ORR Polarization curves of Ag (a), Ag@Ni (b), Ag/Ni (c) and Ni (d) at different rotation speed with K–L plots insert at 0.3 V, 0.4 V and 0.5 V respectively.

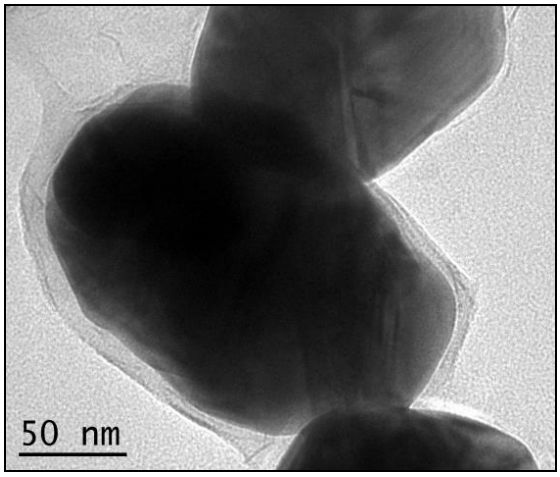

Figure S2 Typical Ag@Ni nanoparticles covered with surfactant PVA (layer with light color) on the surface.

1. Details for XPS fitting

For the curve fitting of both Ni-2p and Ag-3d a standard Shirley background was used, together with a Gaussian-Lorentzian peak profiles. All peaks emerging from core level photoelectrons were fitted using a doublet with a ratio suitable for the orbital (2:1 for Ni-2p and 2:3 for Ag-3d). The binding energy values were allowed to shift by ±0.3 eV to account for error associated with referencing to adventitious carbon. The study of the oxidation state of the Ni 2p core level spectrum is known to be compromised by the presence of secondary peaks emerging from multiplet splitting, plasmon loss structures and satellite peaks overlapping with the primary structure of the spectrum. Overlapping of the high binding energy satellite and plasmon-loss Ni structures with the $2p_{1/2}$ photoelectron lines make the curve fitting by doublets very problematic. The deconvolution is focused on the fitting of the $2p_{3/2}$ lines to ensure secondary photoelectrons are not taken into account for the quantification. Similarly, Ag-3d peaks also show the presence of plasmon-loss structures at higher binding energies, but they do not interfere with Ag primary peaks. All these secondary peaks were fitted with singlets and were not taken into account for the quantification of the oxidation states. To further prove the existence of the oxidation states found by fitting Ni and Ag peaks, deconvolution of the O-1s peak could also be carried out. This option has been dismissed due to the presence of too many oxygenated compounds in Ni and Ag, as well as adsorbed oxygen.

Study of Ag-3d spectra is much less problematic due to the sufficient energy difference between primary and secondary peaks. However, the close proximity of all its oxide peaks can make the peak assignment deceptive.

2. Details for Koutecky–Levich plots and calculation of electron transfer number.

The ORR measurement was performed in 0.1 M KOH by using rotating disk electrode (RDE) setup.

The ORR kinetics of the freestanding catalysts was investigated by collecting polarization curves at various rotation speeds. Based on those polarization curves, the electron transfer number (n) which reflects the first order ORR kinetics was then calculated using the Koutecky–Levich (K–L) equation[19]:

$$\frac{1}{i}=\frac{1}{i_k}+\frac{1}{i_d}=\frac{1}{n\cdot F\cdot \kappa\cdot C_0}+\frac{1}{0.2\cdot n\cdot F\cdot C_0\cdot D_0^{2/3}\cdot v^{-1/6}\cdot \omega^{1/2}}$$

where i is the current density measured experimentally, i_K and i_d represent the kinetic and the limiting diffusion current density, respectively, F is the Faraday constant (96485 C·mol^{-1}), κ is the electrochemical rate constant for O_2 reduction (cm s^{-1}) at a specific potential, C_0 is the dissolved concentration of O_2 (1.2×10^{-6} mol·cm^{-3}), D_0 is the diffusion coefficient of O_2 (1.9×10^{-5} cm^2 s^{-1}), v is the kinetic viscosity of the electrolyte (0.01 cm^2 s^{-1}) and ω is rotating rate (rpm) of the electrode.

3. Details for calculation of potential vs pH diagram of Ni-Ag system

3.1 Phase equilibria in the Ag – Ni system at 25 °C

According to phase diagram of the Ag–Ni system[20], silver and nickel are only very slightly soluble in each other in the solid state. Both solid solutions of Ag in (Ni) and Ni in (Ag) have the same face centered cubic crystal structure.

The maximum solid solubility at 298 K might be estimated by considering the equilibrium condition of equality of chemical potentials of both silver and nickel in both solutions:

$$\begin{cases}\mu_{Ag}^{(Ag)}=\mu_{Ag}^{(Ni)},\\ \mu_{Ni}^{(Ag)}=\mu_{Ni}^{(Ni)},\end{cases}$$

where $\mu_i^{(j)}$ is the chemical potential of the component i in the phase (j), the subscript i denotes the component (Ag or Ni), and the superscript (j) denotes the solvent in the solid solution ((Ag) or (Ni)).

Any chemical potential might be expressed as:

$$\mu_i^{(j)}=\mu_i^{0,(j)}+R\cdot T\cdot \ln x_i^{(j)}+\mu_i^{E,(j)},$$

where $\mu_i^{0,(j)}$ is the chemical potential of the pure substance i in the phase (j). $x_i^{(j)}$ is the mole fraction of the component i in the phase (j), and $\mu_i^{E,(j)}$ is the excess chemical potential of the component i in the phase (j).

Because both solid solutions have the same crystal structure, the chemical potentials of both pure silver and nickel in both phases are equal to each other:

$$\begin{cases} \mu_{Ag}^{0,(Ag)} = \mu_{Ag}^{0,(Ni)}, \\ \mu_{Ni}^{0,(Ag)} = \mu_{Ni}^{0,(Ni)}. \end{cases}$$

Moreover, the excess Gibbs energies of both phases are also the same:

$$G^{E,(Ag)} = G^{E,(Ni)} = G^{E}.$$

According to [20], the excess Gibbs energy of the fcc solid solution in the Ag – Ni system might be expressed in form of Redlich-Kister power series[21]:

$$G^{E} = x_{Ag} \cdot x_{Ni} \cdot (L_1 \cdot (x_{Ag} - x_{Ni}) + L_0).$$

From this expression the excess chemical potentials of the components might be expressed as follows:

$$\mu_{Ag}^{E} = A_1 \cdot x_{Ni}^2 + B_1 \cdot x_{Ni}^3,$$

$$\mu_{Ni}^{E} = A_2 \cdot x_{Ag}^2 + B_2 \cdot x_{Ag}^3,$$

where,

$$A_1 = L_0 + 3 \cdot L_1,$$

$$A_2 = L_0 - 3 \cdot L_1,$$

$$B_1 = -4 \cdot L_1,$$

$$B_2 = 4 \cdot L_1.$$

According to the data of [20]:

$$L_0 = (3{,}1 \cdot T + 54620{,}4), \text{ J/mol},$$

$$L_1 = 2800, \text{ J/mol}.$$

By substituting aforementioned equations into the equilibrium condition, the following system of equation might be derived:

$$\begin{cases} R \cdot T \cdot \ln x_{Ag}^{(Ag)} + A_1 \cdot \left(x_{Ni}^{(Ag)}\right)^2 + B_1 \cdot \left(x_{Ni}^{(Ag)}\right)^3 = R \cdot T \cdot \ln x_{Ag}^{(Ni)} + A_1 \cdot \left(x_{Ni}^{(Ni)}\right)^2 + B_1 \cdot \left(x_{Ni}^{(Ni)}\right)^3, \\ R \cdot T \cdot \ln x_{Ni}^{(Ag)} + A_1 \cdot \left(x_{Ag}^{(Ag)}\right)^2 + B_1 \cdot \left(x_{Ag}^{(Ag)}\right)^3 = R \cdot T \cdot \ln x_{Ni}^{(Ni)} + A_1 \cdot \left(x_{Ag}^{(Ni)}\right)^2 + B_1 \cdot \left(x_{Ag}^{(Ni)}\right)^3, \\ x_{Ag}^{(Ag)} + x_{Ni}^{(Ag)} = 1, \\ x_{Ag}^{(Ni)} + x_{Ni}^{(Ni)} = 1. \end{cases}$$

Solving this system at T = 298,15 K gives the following values:

$$\begin{cases} x_{Ni}^{(Ag)} = 6{,}004 \cdot 10^{-11}, \\ x_{Ag}^{(Ag)} \approx 1, \\ x_{Ag}^{(Ni)} = 5{,}758 \cdot 10^{-10}, \\ x_{Ni}^{(Ni)} \approx 1. \end{cases}$$

The activities of the components of both solid solutions might be calculated as follows:

$$R \cdot T \cdot \ln a_{Ag} = R \cdot T \cdot \ln x_{Ag} + A_1 \cdot x_{Ni}^2 + B_1 \cdot x_{Ni}^3,$$

$$R \cdot T \cdot \ln a_{Ni} = R \cdot T \cdot \ln x_{Ni} + A_2 \cdot x_{Ag}^2 + B_2 \cdot x_{Ag}^3.$$

According to calculations:

$$\begin{cases} a_{Ni}^{(Ag)} \approx 1, \\ a_{Ag}^{(Ag)} \approx 1, \\ a_{Ag}^{(Ni)} \approx 1, \\ a_{Ni}^{(Ni)} \approx 1. \end{cases}$$

Both solid solutions exhibit strong positive deviations from ideal behaviour.
As calculations show, at the standard temperature the solid solubility of both components in each other is vanishingly small. Even despite nanosized particles usually are more soluble than bulk phases, this solubility might be definitely neglected. Therefore, both solid silver and nickel will be treated as pure compounds in further calculations.

3.2 The oxides of silver and nickel

Silver forms a variety of oxides, namely, Ag_2O, Ag_2O_2 and Ag_2O_3. Nickel forms a continuous series of oxides with the formula NiO_x, where $1 \le x \le 2$. Silver and nickel could form a variety of mixed oxides[22], including $AgNiO_2$, Ag_2NiO_2 and $Ag_3Ni_2O_4$. However, there is a lack of thermodynamic information concerning these compounds, and, therefore, the ternary silver–nickel oxides will be excluded from further thermodynamic calculations.

3.3 Thermodynamic data on silver and nickel oxides and aqueous species

Compound	The standard Gibbs energy of formation, $^{J}/_{mol}$				
	Ref.[23]	Ref.[24]	Ref.[25]	Ref.[26]	Value used in further calculations
Ni^{2+} (aq)	–45 800	–46 400	–	–45 600	–45 800
NiO (s)	–211 700	–	–212 300	–211 700	–211 700
$NiOH^+$ (aq)	–228 500	–227 300	–226 500	–227 600	–227 300
$Ni(OH)_2$ (aq)	–	–	–399 400	–360 200	–399 400
$Ni(OH)_2$ (s)	–457 100	–446 900	–457 600	–447 200	–457 600

$Ni(OH)_3^-$ (aq)	–590 500	–	–	–	–590 500
Ni_2OH^{3+} (aq)	–268 200	–	–268 300	–	–268 300
$Ni_4(OH)_4^{4+}$ (aq)	–974 600	–	–972 600	–	–972 600
$HNiO_2^-$ (aq)	–	–350 000	–	–	–350 000
NiOOH (aq)	–	–316 900	–	–	–316 900
$Ni(OAc)^+$ (aq)	–	–	–	–422 900	–422 900
$Ni(OAc)_2$ (aq)	–	–	–	–801 900	–801 900
Ag^+ (aq)	–	77 100	77 100	77 100	77 100
Ag^{2+} (aq)	–	268 600	–	269 000	268 600
AgO^- (aq)	–	–22 600	–	–	–22 600
Ag_2O (s)	–	–11 300	–11 400	–11 200	–11 300
Ag_2O_2 (s)	–	27 600	–	27 600	27 600
Ag_2O_3 (s)	–	–	–	121 400	121 400
$AgNO_3$ (aq)	–	–33 500	–	–32 500	–33 500
AgOAc (s)	–	–	–	–307 700	–307 700
AgOAc (aq)	–	–296 200	–	–296 400	–296 200
$Ag(OAc)_2^-$ (aq)	–	–	–	–665 200	–665 200
AgOH (aq)	–	–	–93 000	–92 000	–93 000
$Ag(OH)_2^-$ (aq)	–	–	–258 300	–260 200	–258 300
NO_3^- (aq)	–110 800	–110 900	–	–108 700	–110 800
HNO_2 (aq)	–	–55 700	–	–50 600	–55 700
NO_2^- (aq)	–	–36 800	–	–32 200	–36 800
NH_4^+ (aq)	–	–79 500	–	–79 300	–79 500
NH_4OH (aq)	–	–264 000	–	–263 700	–264 000
AcO^- (aq)	–	–369 500	–	–369 300	–369 500
AcOH (aq)	–	–396 600	–	–396 500	–396 500
CH_4 (g)	–	–50 600	–	–50 500	–50 600

3.4 Thermodynamic activities of aqueous species

The extended Debye – Hückel equation parameters[27]:

T = 298.15 K.

$$\varepsilon = 87,74 - 0,4008 \cdot (T - 273,15) +$$
$$+9,398 \cdot 10^{-4} \cdot (T - 273,15)^2 + 1,41 \cdot 10^{-6} \cdot (T - 273,15)^3 = 78,3294.$$

$$A = \frac{1{,}825 \cdot 10^6}{(\varepsilon \cdot T)^{\frac{3}{2}}} = \frac{1{,}825 \cdot 10^6}{(78{,}3294 \cdot 298{,}15)^{\frac{3}{2}}} = 0{,}5114 \ {}^{\mathrm{L}^{\frac{1}{2}}}\!/_{\mathrm{mol}^{\frac{1}{2}}},$$

$$B = \frac{5{,}029 \cdot 10^{11}}{(\varepsilon \cdot T)^{\frac{1}{2}}} = \frac{5{,}029 \cdot 10^{11}}{(78{,}3294 \cdot 298{,}15)^{\frac{1}{2}}} = 3{,}291 \cdot 10^9 \ {}^{\mathrm{L}^{\frac{1}{2}}}\!/_{\mathrm{m \cdot mol}^{\frac{1}{2}}}.$$

The electrostatic radii of the individual ions[28]

Ion	a_i, Å
Ag^+ (aq)	2,5
Ni^{2+} (aq)	3,0
NO_3^-(aq)	3,0
AcO^- (aq)	4,5

The ionic strength of the solution:

$$\mathrm{I} = \frac{z^2_{Ni^{2+}} \cdot c_{Ni^{2+}} + z^2_{AcO^-} \cdot c_{AcO^-} + z^2_{Ag^+} \cdot c_{Ag^{2+}} + z^2_{NO_3^-} \cdot c_{NO_3^-}}{2} =$$

$$= \frac{4 \cdot 0{,}005 \ \mathrm{M} + 1 \cdot 0{,}010 \ \mathrm{M} + 1 \cdot 0{,}005 \ \mathrm{M} + 1 \cdot 0{,}005 \ \mathrm{M}}{2} = 0{,}020 \ \mathrm{M}.$$

The thermodynamic activities of the ions:

$$\lg \gamma_{Ni^{2+}} = -0{,}5114 \ {}^{\mathrm{L}^{\frac{1}{2}}}\!/_{\mathrm{mol}^{\frac{1}{2}}} \cdot (+2)^2 \cdot \frac{\sqrt{0{,}020 \ {}^{\mathrm{mol}}\!/_{\mathrm{L}}}}{1 + 3{,}291 \cdot 10^9 \ {}^{\mathrm{L}^{\frac{1}{2}}}\!/_{\mathrm{m \cdot mol}^{\frac{1}{2}}} \cdot 3{,}0 \cdot 10^{-10} \ \mathrm{m} \cdot \sqrt{0{,}020 \ {}^{\mathrm{mol}}\!/_{\mathrm{L}}}} = -0{,}254,$$

$$\gamma_{Ni^{2+}} = 10^{-0{,}254} = 0{,}557,$$

$$a_{Ni^{2+}} = 0{,}005 \ \frac{\mathrm{mol}}{\mathrm{L}} \cdot 0{,}557 = 0{,}00279 \ \frac{\mathrm{mol}}{\mathrm{L}}.$$

$$\lg \gamma_{AcO^-} = -0{,}5114 \ {}^{\mathrm{L}^{\frac{1}{2}}}\!/_{\mathrm{mol}^{\frac{1}{2}}} \cdot (-1)^2 \cdot \frac{\sqrt{0{,}020 \ {}^{\mathrm{mol}}\!/_{\mathrm{L}}}}{1 + 3{,}291 \cdot 10^9 \ {}^{\mathrm{L}^{\frac{1}{2}}}\!/_{\mathrm{m \cdot mol}^{\frac{1}{2}}} \cdot 4{,}5 \cdot 10^{-10} \ \mathrm{m} \cdot \sqrt{0{,}020 \ {}^{\mathrm{mol}}\!/_{\mathrm{L}}}} = -0{,}0598,$$

$$\gamma_{AcO^-} = 10^{-0{,}0598} = 0{,}871,$$

$$a_{AcO^-} = 0{,}010 \ \frac{\mathrm{mol}}{\mathrm{L}} \cdot 0{,}871 = 0{,}00871 \ \frac{\mathrm{mol}}{\mathrm{L}}.$$

$$\lg \gamma_{Ag^+} = -0,5114 \,{}^{L^{\frac{1}{2}}}\!/_{mol^{\frac{1}{2}}} \cdot (+1)^2 \cdot \frac{\sqrt{0,020\ {}^{mol}\!/_{L}}}{1 + 3,291 \cdot 10^9 \,{}^{L^{\frac{1}{2}}}\!/_{m \cdot mol^{\frac{1}{2}}} \cdot 2,5 \cdot 10^{-10}\ m \cdot \sqrt{0,020\ {}^{mol}\!/_{L}}} = -0,0648,$$

$$\gamma_{Ag^+} = 10^{-0,0648} = 0,861,$$

$$a_{Ag^+} = 0,005\ \frac{mol}{L} \cdot 0,861 = 0,0043\ \frac{mol}{L}.$$

$$\lg \gamma_{NO_3^-} = -0,5114 \,{}^{L^{\frac{1}{2}}}\!/_{mol^{\frac{1}{2}}} \cdot (-1)^2 \cdot \frac{\sqrt{0,020\ {}^{mol}\!/_{L}}}{1 + 3,291 \cdot 10^9 \,{}^{L^{\frac{1}{2}}}\!/_{m \cdot mol^{\frac{1}{2}}} \cdot 3,0 \cdot 10^{-10}\ m \cdot \sqrt{0,020\ {}^{mol}\!/_{L}}} = -0,0637,$$

$$\gamma_{NO_3^-} = 10^{-0,0637} = 0,864,$$

$$a_{NO_3^-} = 0,005\ \frac{mol}{L} \cdot 0,864 = 0,00432\ \frac{mol}{L}.$$

3.5 Chemical equilibria in aqueous solution

3.5.1. Equilibria involving silver-acetate complexation

For the equilibrium

$$CH_3COOH\ (aq) \rightleftharpoons CH_3COO^-\ (aq) + H^+\ (aq)$$

the pK_a value is equal to 4,76[29]. This means that at pH < 4,76 the predominant form in solution is $CH_3COOH\ (aq)$, and at pH > 4,76 the acetate-ion $CH_3COO^-\ (aq)$ predominates.

For the equilibrium

$$CH_3COOAg\ (s) \rightleftharpoons CH_3COO^-\ (aq) + Ag^+\ (aq)$$

the solubility product value K_{sp} is equal to 1,94[29]. Using the activities of silver and acetate ions, calculated afore, one might calculate that

$$a_{CH_3COO^-\,(aq)} \cdot a_{Ag^+\,(aq)} = 0,00871\ {}^{mol}\!/_{L} \cdot 0,0043\ {}^{mol}\!/_{L} = 1,78 \cdot 10^{-5}\ {}^{mol^2}\!/_{L^2}$$
$$< K_{sp}(CH_3COOAg\ (s)),$$

and, consequently, silver acetate does not precipitate at the reaction conditions. Solid silver acetate is excluded from further consideration.

For the equilibria

$$\begin{cases} Ag^+\ (aq) + CH_3COO^-\ (aq) \rightleftharpoons CH_3COOAg\ (aq), \\ CH_3COOAg\ (aq) + CH_3COO^-\ (aq) \rightleftharpoons Ag(CH_3COO)_2^-\ (aq), \\ H^+\ (aq) + CH_3COO^-\ (aq) \rightleftharpoons CH_3COOH\ (aq) \end{cases}$$

the standard Gibbs energies of reaction and the corresponding equilibrium constants might be calculated from the data, presented afore.

The activities of the species are related to each other according to the following equations:

$$\begin{cases} \dfrac{a_{CH_3COOAg\,(aq)}}{a_{Ag^+\,(aq)} \cdot a_{CH_3COO^-\,(aq)}} = 5{,}021\ {}^{L}/_{mol}, \\ \dfrac{a_{Ag(CH_3COO)_2^-\,(aq)}}{a_{CH_3COOAg\,(aq)} \cdot a_{CH_3COO^-\,(aq)}} = 1{,}470 \cdot 10^{-5}\ {}^{L}/_{mol}, \\ \dfrac{a_{CH_3COOH\,(aq)}}{a_{H^+\,(aq)} \cdot a_{CH_3COO^-\,(aq)}} = 5{,}594 \cdot 10^{4}\ {}^{L}/_{mol}, \\ a_{Ag^+\,(aq)} + a_{CH_3COOAg\,(aq)} + a_{Ag(CH_3COO)_2^-\,(aq)} = 0{,}0043\ {}^{mol}/_{L}, \\ a_{CH_3COOH\,(aq)} + a_{CH_3COO^-\,(aq)} + a_{CH_3COOAg\,(aq)} + 2 \cdot a_{Ag(CH_3COO)_2^-\,(aq)} = 0{,}00871\ {}^{mol}/_{L}. \end{cases}$$

By solving this system of equations, the dependencies of thermodynamic activities of ions might be expressed as the functions of pH value. These dependencies are shown in the diagram below.

The activity of the complex ion $Ag(CH_3COO)_2^-\,(aq)$ is very low, and the corresponding line lies outside the diagram range.

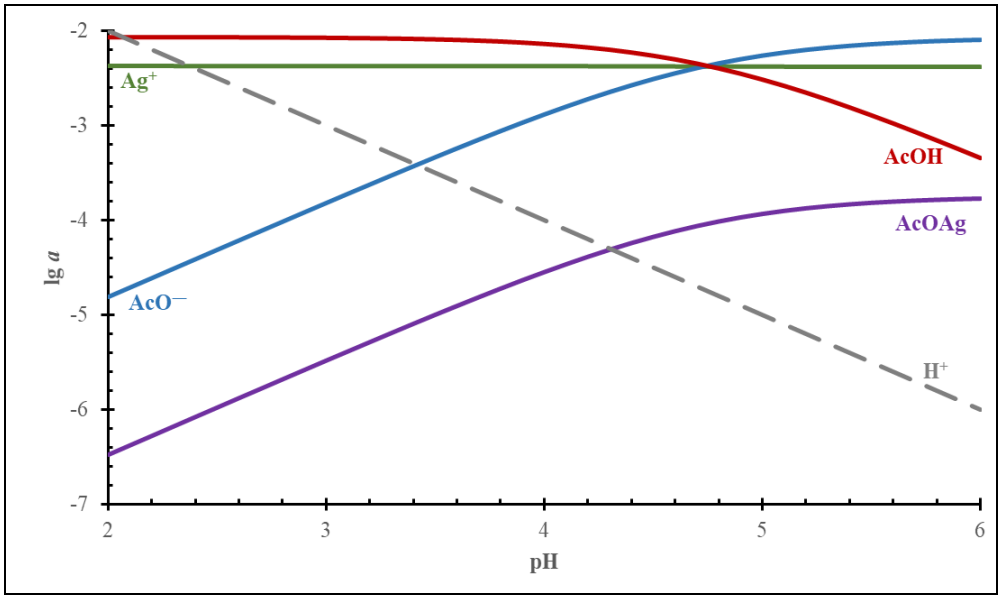

3.5.2. Equilibria involving nickel-acetate complexation

For the equilibria

$$\begin{cases} Ni^{2+}\,(aq) + CH_3COO^-\,(aq) \rightleftharpoons CH_3COONi^+\,(aq), \\ CH_3COONi^+ + CH_3COO^-\,(aq) \rightleftharpoons Ni(CH_3COO)_2\,(aq), \\ H^+\,(aq) + CH_3COO^-\,(aq) \rightleftharpoons CH_3COOH\,(aq) \end{cases}$$

the activities of the species are related to each other according to the following equations:

$$\begin{cases} \dfrac{a_{CH_3COONi^+(aq)}}{a_{Ni^{2+}(aq)} \cdot a_{CH_3COO^-(aq)}} = 23{,}254\ {}^{L}/_{mol}, \\ \dfrac{a_{Ni(CH_3COO)_2(aq)}}{a_{CH_3COONi^+(aq)} \cdot a_{CH_3COO^-(aq)}} = 48{,}067\ {}^{L}/_{mol}, \\ \dfrac{a_{CH_3COOH(aq)}}{a_{H^+(aq)} \cdot a_{CH_3COO^-(aq)}} = 5{,}594 \cdot 10^4\ {}^{L}/_{mol}, \\ a_{Ni^{2+}(aq)} + a_{CH_3COONi^+(aq)} + a_{Ni(CH_3COO)_2(aq)} = 0{,}00279\ {}^{mol}/_{L}, \\ a_{CH_3COOH(aq)} + a_{CH_3COO^-(aq)} + a_{CH_3COONi^+(aq)} + 2 \cdot a_{Ni(CH_3COO)_2(aq)} = 0{,}00871\ {}^{mol}/_{L}. \end{cases}$$

The dependencies of thermodynamic activities of ions on pH value are shown on the diagram below.

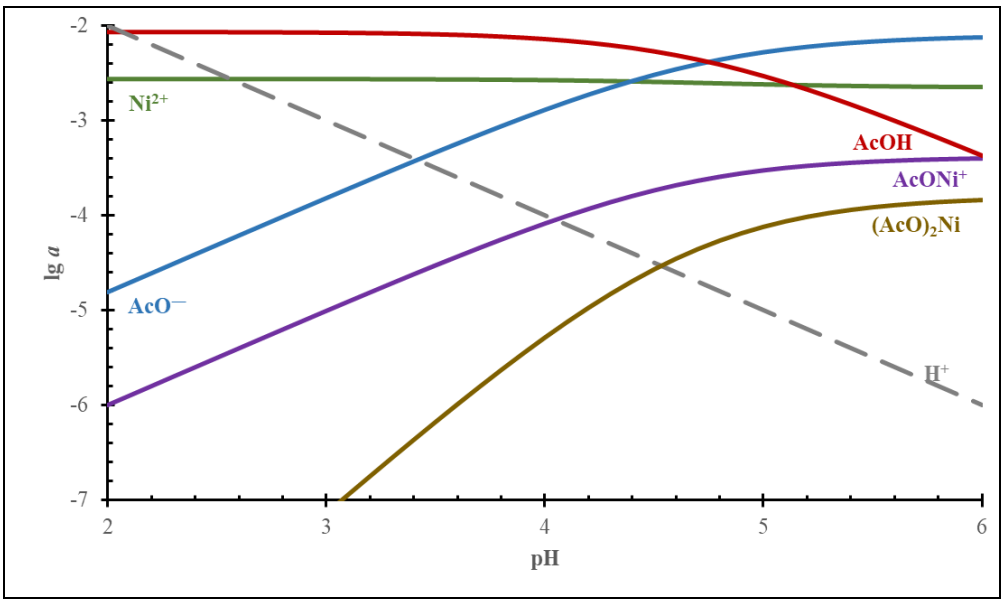

The diagrams in sections 5.1 and 5.2 show that at the reaction conditions simple nickel, silver and acetate-ions (or undissociated acetic acid) predominate in a solution, and complex ions are present in very small quantities and do not affect the electrochemical reactions of metals.

3.5.3 Electrochemical equilibria in aqueous solution

The chemical and electrochemical equilibria in the Ni–Ag–NO_3^-–AcO^-–H_2O system were calculated at 298,15 K, air pressure of 1 bar and the activities of nickel, silver, nitrate and acetate ions in the solution as was calculated in the section 4. The diagram is presented below. The partial pressure of methane according to its average atmospheric concentration[30] is equal to $2 \cdot 10^{-6}$ bar. The standard Gibbs energy of formation of nickel hydride Ni_2H was taken from[31]. This shows that at the reaction conditions no hydrolysis of metal cations or formation of metal oxides occurs. The nickel and silver ions are reduced independently of each other.

Reference

(1) Aggarwal, P. S.; Goswami, A. An Oxide of Tervalent Nickel. *J. Phys. Chem.* **1961**, *65*, 2105–2105.

(2) Sörgel, T.; Jansen, M. Eine Neue, Hexagonale Modifikation von $AgNiO_2$. *Zeitschrift für Anorg. und Allg. Chemie* **2005**, *631*, 2970–2972.

(3) Beesk, W.; Jones, P. G.; Rumpel, H.; Schwarzmann, E.; Sheldrick, G. M. X-Ray Crystal Structure of Ag_6O_2. *J. Chem. Soc. Chem. Commun.* **1981**, No. 14, 664.

(4) Kabalkina, S. S.; Popova, S. V.; Serebryanaya, N. R.; Vereshchagin, L. F. A New Ag_2O Modification with Stratified Structure. *Dokl. Akad. Nauk SSSR* **1963**, *152*, 853–854.

(5) Svintsitskiy, D. A.; Lazarev, M. K.; Kardash, T. Y.; Fedorova, E. A.; Slavinskaya, E. M.; Boronin, A. I. Mixed Silver-Nickel Oxide $AgNiO_2$: Probing by CO during XPS Study. *J. Chem. Phys.* **2020**, *152*, 044707.

(6) Jette, E. R.; Foote, F. Precision Determination of Lattice Constants. *J. Chem. Phys.* **1935**, *3*, 605–616.

(7) Firet, N. J.; Blommaert, M. A.; Burdyny, T.; Venugopal, A.; Bohra, D.; Longo, A.; Smith, W. A. Operando EXAFS Study Reveals Presence of Oxygen in Oxide-Derived Silver Catalysts for Electrochemical CO_2 Reduction. *J. Mater. Chem. A* **2019**, *7*, 2597–2607.

(8) Schön, G.; Tummavuori, J.; Lindström, B.; Enzell, C. R.; Enzell, C. R.; Swahn, C.-G. ESCA Studies of Ag, Ag_2O and AgO. *Acta Chem. Scand.* **1973**, *27*, 2623–2633.

(9) Chen, Y. Y.; Yu, S. H.; Yao, Q. Z.; Fu, S. Q.; Zhou, G. T. One-Step Synthesis of Ag_2O@$Mg(OH)_2$ Nanocomposite as an Efficient Scavenger for Iodine and Uranium. *J. Colloid Interface Sci.* **2018**, *510*, 280–291.

(10) Prieto, P.; Nistor, V.; Nouneh, K.; Oyama, M.; Abd-Lefdil, M.; Díaz, R. XPS Study of Silver, Nickel and Bimetallic Silver-Nickel Nanoparticles Prepared by Seed-Mediated Growth. *Appl. Surf. Sci.* **2012**, *258*, 8807–8813.

(11) Lopez-Salido, I.; Lim, D. C.; Kim, Y. D. Ag Nanoparticles on Highly Ordered Pyrolytic Graphite (HOPG) Surfaces Studied Using STM and XPS. *Surf. Sci.* **2005**, *588*, 6–18.

(12) Leiro, J.; Minni, E.; Suoninen, E. Study of Plasmon Structure in XPS Spectra of Silver and Gold. *J. Phys. F Met. Phys.* **1983**, *13*, 215–221.

(13) Lv, S.; Yang, F.; Chu, X.; Wang, H.; Yang, J.; Chi, Y.; Yang, X. In Situ Construction of Ag/$Ni(OH)_2$ Composite Electrode by Combining Electroless Deposition Technology with Electrodeposition. *Metals.* **2019**, *9*, 826.

(14) Bao, F.; Tan, F.; Wang, W.; Qiao, X.; Chen, J. Facile Preparation of Ag/$Ni(OH)_2$ Composites with Enhanced Catalytic Activity for Reduction of 4-Nitrophenol. *RSC Adv.* **2017**, *7*, 14283–14289.

(15) Kim, K. S.; Winograd, N. X-Ray Photoelectron Spectroscopic Studies of Nickel-Oxygen Surfaces Using Oxygen and Argon Ion-Bombardment. *Surf. Sci.* **1974**, *43*, 625–643.

(16) Dubey, P.; Kaurav, N.; Devan, R. S.; Okram, G. S.; Kuo, Y. K. The Effect of Stoichiometry on the Structural, Thermal and Electronic Properties of

Thermally Decomposed Nickel Oxide. *RSC Adv.* **2018**, *8*, 5882–5890.
(17) Andrews, P. T.; Collins, T.; Weightman, P. The Influence of the Number of Unoccupied 3d States on the L 3M4,5M4,5 Auger Spectrum of Ni. *J. Phys. C Solid State Phys.* **1981**, *14*, L957.
(18) Biesinger, M. C.; Payne, B. P.; Grosvenor, A. P.; Lau, L. W. M.; Gerson, A. R.; Smart, R. S. C. Resolving Surface Chemical States in XPS Analysis of First Row Transition Metals, Oxides and Hydroxides: Cr, Mn, Fe, Co and Ni. *Appl. Surf. Sci.* **2011**, *257*, 2717–2730.
(19) Ong, A. L.; Inglis, K. K.; Whelligan, D. K.; Murphy, S.; Varcoe, J. R. Effect of Cationic Molecules on the Oxygen Reduction Reaction on Fuel Cell Grade Pt/C (20 Wt%) Catalyst in Potassium Hydroxide (aq, 1 mol dm^{-3}). *Phys. Chem. Chem. Phys.* **2015**, *17*, 12135–12145.
(20) Liu, X. J.; Gao, F.; Wang, C. P.; Ishida, K. Thermodynamic Assessments of the Ag-Ni Binary and Ag-Cu-Ni Ternary Systems. *J. Electron. Mater.* **2008**, *37*, 210–217.
(21) Redlich, O.; Kister, A. T. Algebraic Representation of Thermodynamic Properties and the Classification of Solutions. *Ind. Eng. Chem.* **1948**, *40*, 345–348.
(22) Sörgel, T.; Jansen, M. $Ag_3Ni_2O_4$-A New Stage-2 Intercalation Compound of 2H-$AgNiO_2$ and Physical Properties of 2H-$AgNiO_2$ above Ambient Temperature. *J. Solid State Chem.* **2007**, *180*, 8–15.
(23) Gamsjäger, H.; Mompean, F. J.; Issy-les-Moulineaux (France); NEA Data Bank.; OECD Nuclear Energy Agency. *Chemical Thermodynamics of Nickel*; 2005.
(24) Schweitzer, G. K.; Pesterfield, L. L. *The Aqueous Chemistry of the Elements*; Oxford University Press: USA, 2010.
(25) Brown, P.; Ekberg, C. Hydrolysis of Metal Ions at 25°C. In *Kinetics of Inorganic Reactions*; Elsevier, 1966; p 280.
(26) Wagman, D. D.; Evans, W. H.; Parker, V. B.; Schumm, R. H.; Halow, I.; Bailey, S. M.; Churney, K. L.; Nuttall, R. L. The NBS Tables of Chemical Thermodynamic Properties. Selected Values for Inorganic and C_1 and C_2 Organic Substances in SI Units. *J. Phys. Chem. Ref. Data* **1982**, *11*, 2–61
(27) Debye, P.; Hückel, E. The Theory of Electrolytes. I. Freezing Point Depression and Related Phenomena (Engl. Transl.). **2019**; Zur Theorie der Elektrolyte. I. Gefrierpunktserniedrigung und verwandte Erscheinungen. *Physikalische Zeitschrift* **1923**, *24*, 185−206.
(28) Kielland, J. Individual Activity Coefficients of Ions in Aqueous Solutions. *J. Am. Chem. Soc.* **1937**, *59*, 1675–1678.
(29) *CRC Handbook of Chemistry and Physics, 93rd Edition*; CRC Press, 2016.
(30) Schiermeier, Q. Global Methane Levels Soar to Record High. *Nature* **2020**.
(31) Baranowski, B.; Bocheńska, K. The Free Energy and Entropy of Formation of Nickel Hydride. *Zeitschrift fur Phys. Chemie* **1965**, *45*, 140–152.

Paper III

PdNi Thin Films for Hydrogen Oxidation Reaction and Oxygen Reduction Reaction in Alkaline Media

G. Montserrat-Sisó and B. Wickman

In Manuscript

PdNi Thin Films for Hydrogen Oxidation Reaction and Oxygen Reduction Reaction in Alkaline Media

Gerard Montserrat-Sisó, Björn Wickman

Division of Chemical Physics, Department of Physics, Chalmers University of Technology, SE-412 96 Gothenburg, Sweden

Abstract

Pd-based catalysts are considered to be among the most promising electrocatalysts for both the hydrogen oxidation reaction (HOR) and oxygen reduction reaction (ORR) in alkaline media. Although major progress in finding effective catalysts has been made, the reasons for the activity enhancement in alkaline conditions remain to be elucidated. Herein, we report the fabrication of alloyed PdNi thin films as important Pt-free catalysts for HOR and ORR reactions. Annealing of physically evaporated PdNi thin films resulted in different surface compositions, which led to a range of HOR and ORR activities in 0.1 M KOH. Moreover, all annealed samples were acid treated to remove the surface Ni and the HOR and ORR were investigated in terms of subsurface composition. For the HOR, it was found that the addition of Ni induces an electronic effect that modifies the hydrogen binding energy (HBE) of Pd, whose role as the main HOR descriptor was confirmed. In addition, it was found that surface Ni also had a positive effect on the HOR activity by providing OH^- adsorption sites. In contrast to HOR, it was concluded that surface Ni was disadvantageous for the ORR. However, subsurface Ni was found to induce an electronic effect on the electronic structure of Pd that resulted in a boosting of the ORR kinetics by improving its oxygen desorption. These results provide insights for the more tailored design of electrocatalysts in alkaline media by lightening the mechanisms through which the HOR and ORR kinetics are improved in alkaline media.

1. Introduction

Low-temperature fuel cells have been recognized during the last decades as promising power generation technologies for both stationary and portable applications. Because of their high energy density, small size, and lightweight, Polymer Electrolyte Membrane Fuel Cells (PEMFC) have become the current leading low-temperature fuel cell for automotive applications[1,2]. However, the widespread commercialization of PEMFC in automotive vehicles is currently impeded by their high cost and limited lifetime. Both limitations are greatly attributed to the catalyst layer, whose contribution to the total cost of the fuel cell stack for large-scale energy production is nearly half[3,4]. This high cost is due to the scarcity of platinum, of which high amounts are needed to catalyze the hydrogen oxidation reaction (HOR) in the anode and to improve the sluggish oxygen reduction reaction (ORR) kinetics in the cathode[5,6]. Thus, the problems of Pt-based catalysts rely on their limited availability and activity in acidic media far from being sufficient to meet the required efficiency[7,8]. In contrast to acidic media, the rather mild alkaline conditions in the Alkaline Electrolyte Membrane Fuel Cell (AEMFC) allow the use of Pt-free electrocatalysts, which brings up new possibilities of finding abundant and inexpensive electrocatalysts without compromising the power density of the fuel cell[9,10]. A high pH environment implies different electrode reaction mechanisms. The kinetics of the ORR in alkaline media is remarkably more facile than in acid[11] and the overpotential for the ORR is substantially diminished at high pH environments, which allows the use of non-Pt metals[12]. Despite the activity enhancement in alkaline media, the ORR activity is still far from being optimal and affordable catalyst with high activity and stability are yet to be found.

Similar to that in acidic media, an ideal catalyst for the ORR in alkaline media would weaken the adsorption energy of hydroxides by about 0.1 eV compared to pure Pt[13]. One strategy to modify the OH^- adsorption is through alloying with metals with different d-orbital occupancies. It has been reported that through changes in the d-orbital overlap that change the d-band center, the breakage of the O–O bond, as well as the desorption of oxygenated intermediates, can be tuned[14]. By coupling a metal with low occupancy of d-orbitals with another highly occupied d-orbital metal, the d-band center of the fully occupied d-orbital metal is lowered, resulting in an ORR enhancement[15]. This enhancement is caused by the significant decrease in the Gibbs free energy of key electron transfer steps, which results in an optimal balance between the O_2 bond breaking and the adsorption of oxygenated species[15,16]. Thus, this electronic effect induced with alloying plays a crucial role in the enhancement of the ORR activity of metals in both alkaline and acidic conditions.

In contrast to the ORR, the HOR kinetics at the anode is greatly hindered in alkaline conditions compared to acidic[17]. The anodic reaction on Pt under alkaline conditions is around two orders of magnitude slower than that in acid[18,19]. Although the HOR mechanism in alkaline media is not fully understood, it is believed to proceed through either Tafel-Volmer or Heyrovsky-Volmer mechanism:

(Tafel) $$H_2 + 2^* \longrightarrow 2H_{ad} \quad (1)$$

(Heyrovsky) $$H_2 + OH^- + * \longrightarrow H_{ad} + H_2O + e^- \quad (2)$$

(Volmer) $$H_{ad} + OH^- \longrightarrow H_2O + e^- + * \quad (3)$$

Regardless of the mechanism, it is known that one reason behind the much slower HOR mechanism is the adsorption of oxygenated species blocking H_2 adsorption sites[20]. However, the hydrogen binding energy (HBE) is considered to be a highly important factor controlling the HOR kinetics. The reason for this is that the initial dissociative adsorption of hydrogen is likely to be the rate determining step, also in the presence of oxygenated species[10,21,22]. Thus, finding catalysts with both oxophilic sites that facilitate the OH^- adsorption and with an optimal HBE is crucial to boost the HOR kinetics at the anode.

Palladium has been intensively investigated as a potential candidate to substitute Pt in high pH environments and several reviews of Pd-based catalysts have been published to date[23–25]. Pd represents a good alloying material for ORR due to its fully occupied d-orbitals that could promote the electronic effect, as well as for HOR because of its close to optimal HBE[26]. To improve both anodic and cathodic kinetics, Pd needs to be alloyed with a metal with low d-orbital occupancy to optimize the oxygen adsorption for ORR and enough oxophilicity to promote the adsorption of hydroxide and avoid the blockage of Pd sites for hydrogen adsorption in HOR. Nickel is a very inexpensive and abundant metal that fulfills both requirements. Thus, a catalyst containing both Pd and Ni could potentially exhibit promising electrocatalytic activity for both reactions[27–31].

Both structural and electronic effects play a crucial role in enhancing the electrocatalytic activity of PdNi catalysts. The mechanism through which the HOR activity is enhanced in alkaline media when alloying Pd with Ni remains to be elucidated. The role of Ni in boosting the HOR kinetics is believed to occur either by providing oxophilic sites for the adsorption of hydroxyl species (structural effect) or by tuning the HBE (electronic effect)[32–34]. It has been found that the HOR activity is dependent on the coverage of Ni oxidated species because of their higher oxophilicity when compared to metallic Ni[35,36]. Thus, structural effects need the correct surface distribution of

Pd and Ni if the bifunctional electrocatalytic mechanism is meant to be observed, with OH^- binding on Ni and hydrogen binding on adjacent Pd[27,37]. For ORR, instead, the electronic effects require Pd to be on the surface and Ni in the contiguous subsurface for the correct bimetallic synergy and thus an enhancement of the oxygen adsorption on Pd[29]. With the aim to corroborate the mechanisms of bifunctionality for HOR and bimetallic coupling for ORR, PdNi alloys[27,28], core-shells[37], and PdNi nanoparticles[38] have been well investigated in the literature. However, there are still many questions regarding the mechanisms through which the enhancement takes place in both reactions, whose exploration is hindered by the lack of knowledge about the elementary steps. For HOR it is often claimed that the HBE is the only descriptor affecting the alkaline activity[39], while other investigations suggest that the adsorption of OH also influences the activity, albeit to a lesser extent[40]. Thus, the role of adsorbed H and OH is crucial to completely understand the HOR mechanism in alkaline media[41]. For the ORR, instead, the discussion arises from which are the mechanisms through which the intermediate species promote the desired 4-electron pathway rather than the 2-electron pathway[42,43]. Using PdNi thin films model electrodes should be a good strategy to answer these questions. Thin films present the advantage of being well defined, making the fabrication of different alloy stoichiometries more facile due to the high control over composition. They also have large surface areas with minimized loadings compared to their polycrystalline analogs and they are straightforward to characterize, which means they offer a good platform for mechanistic studies.

This study presents a comprehensive electrochemical and compositional characterization of PdNi annealed thin film alloys linked with their catalytic activity for both HOR and ORR reactions in 0.1 M KOH. Physically evaporated thin films are annealed at different temperatures and the differences in electrocatalytic activity for HOR and ORR are discussed for different XPS surface compositions. The results suggest that, although HBE is the main descriptor, the presence of surface Ni is still favorable for the HOR activity, while the ORR is impeded by Ni present on the surface. Instead, the ORR activity can be improved by an electronic effect if Ni is situated in the subsurface layers.

2. Experimental

2.1. Fabrication and Annealing of PdNi Thin Films

Fabrication of thin films was carried out in cleanroom facilities of Fed. Std.209E Class 10-100. Electron-beam evaporation (PVD 225/Lesker) was used to evaporate PdNi thin films on glassy carbon substrates (5 mm diameter diamond polished Sigradur G disks from HTW Gmbh). The carbon disks were first sonicated-cleaned in acetone, isopropanol, and Milli-Q water for 10 minutes in each solvent followed by plasma-etching cleaning with O_2 at 150 W (Plasma-Therm). In order to avoid oxidation of Ni in air, 12 nm of Ni was first evaporated on the carbon substrate followed by evaporation of 28 nm of Pd, resulting in a 40 nm thin film with an atomic ratio of 1:1. In order to induce alloy formation, the samples were subsequently annealed at different temperatures in a flow reactor for 48 h in 4% H_2 in Ar carrier gas at a flow rate of 500 mL min^{-1} to avoid oxidation as depicted in Fig. 1. Annealed samples were additionally acid treated with 0.1 M HCl for 10 min with the aim of forming a protective Pd overlayer by removing Ni oxide on the surface. Below, we shall refer to the samples as PdNi-X for annealed samples (being "X" the annealing temperature) and PdNi-X-AT for acid treated samples annealed at the same temperature. Both annealed and annealed + acid treated samples were electrochemically characterized in RDE for both HOR and ORR activity.

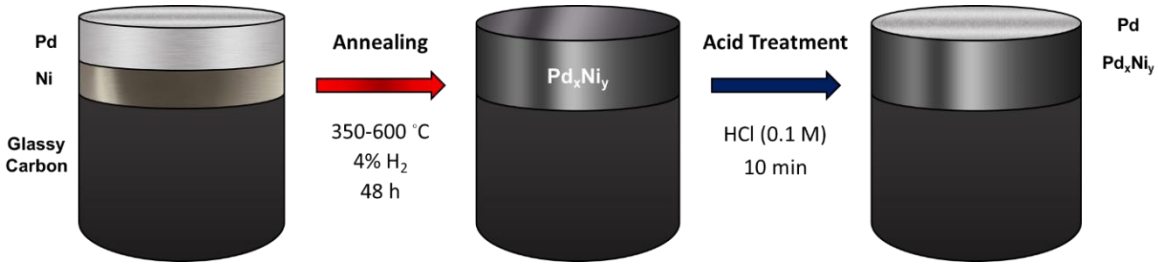

Figure 1 *Schematic illustration of the fabrication, annealing and acid treatment of PdNi thin films.*

2.2. Electrochemical Measurements

A three-electrode rotating disk electrode (RDE) cell was used to perform all the electrochemical measurements. The RDE cell (Pine Instruments) was equipped with a graphite rod (Sigma-Aldrich, 150 mm length and 3 mm diameter) as a counter electrode (CE). Graphite was chosen as CE to avoid metal contamination of the working electrode (WE), a very likely event in alkaline electrolytes[44–46]. A PTFE HydroFlex® Hydrogen Reference Electrode (Gaskatel) was used as a reference electrode (RE) and all the potentials in this study refer to that of the RHE. The reliability of the RHE potential was continuously tested experimentally by bubbling H_2 over a Pt WE in the same electrolyte and measuring the intersection of zero current by cycling the potential between -0.02 V to 0.02 V vs RHE at 2 mV/s.

The setup was also equipped with a gas inlet on the side of the cell to allow the electrolyte to be saturated with gasses. The potentiostat used was an SP-300 from Bio-Logic® controlled with the EC-lab software. The samples were mounted on an RDE PTFE tip from Pine Instruments using PTFE U-cups. Although the recommended practice is using a PTFE cell for alkaline electrolytes[22], a glass cell was used for the RDE measurements due to the short period and rather mild alkaline conditions of the measurements.

The electrochemical cell and the glassware were cleaned prior to the measurements in piranha solution (98% H_2SO_4 (Sigma-Aldrich, Emsure) and 33% H_2O_2 (VWR Chemicals, Technical), 3:1 v/v) for at least 24h. The cell was then thoroughly rinsed with ultrapure water (18.2 MΩ cm, <3 ppb TOC, Milli-Q® IQ 7000, Merck) at least 10 times before each measurement. The electrolyte used for ORR and HOR measurements consisted of 0.1 M KOH prepared from KOH pellets (KOH hydrate ≥99.995%, Suprapur®, Merck) and ultrapure water. The electrolyte was prepared and stored in a PFA volumetric flask (BRAND®) to prevent contamination over time from glass corrosion[47]. A 0.1 M HCl solution prepared from 30% HCl (Suprapur®, Merck) was used for the acid treatment of the samples. The Ar used for de-oxygenation of the electrolyte was supplied by AGA with instrument 5.0 purity, O_2 by Strandmøllen (≥ 99,6 vol %) and H_2 by Air Liquide (≥ 99,999 mol %).

In order to measure on a stable surface free of impurities, a conditioning scheme was conducted for every sample before every measurement. Conditioning was conducted under inert atmosphere after Ar purging, no rotation and consisted of 150 cycles between 0.1 and 1.2 V vs RHE at 150 mV/s. A cyclic voltammetry between 0.05 and 1.35 V vs RHE at 50 mV/s until stabilization of the voltammogram was recorded after conditioning. After CV, the electrolyte was saturated with either H_2 or O_2 and HOR/ORR polarization curves were measured at 50 mV/s at different electrode rotation speeds varied between 400 and 2500 rpm. The electrolyte was then Ar-saturated and another CV under the same conditions was recorded to evaluate changes of the surface from HOR/ORR. All potentials were corrected for ohmic losses by iR-compensation. The Ohmic resistance was determined by electrochemical impedance spectroscopy (EIS) from the intercept in the Nyquist plot[48]. The intersection of the imaginary impedance between 10 and 20,000 Hz on the real impedance is used to calculate the uncompensated resistance of the solution, which depends on the ionic conductivity of the electrolyte and geometry of the cell[49]. The typical measured resistance in 0.1 M KOH ranged from 40 to 50 Ω and was measured prior to each experiment in Ar-saturated electrolyte with no rotation. The iR-compensation was applied after obtaining the I-V polarization curve.

2.3. Physical Characterization

Scanning electron microscopy (SEM) was used to image the annealed samples. SEM was performed using a Zeiss Supra 60VP field-emission microscope with an in-lens detector at 5 kV acceleration voltage and a working distance around 3 mm.

A PHI 5000 VersaProbe III Microprobe X-ray Photoelectron Spectroscopy (XPS) instrument (Physical Electronics) was used to study the surface composition of the thin films. The instrument is equipped with a monochromatic Al K-α X-Ray excitation source (1486.6 eV) operated at 50 W as well as a dual charge compensation: an electron neutralizer (negative charge compensation) and an ion gun (positive charge compensation). Surface composition was evaluated by a survey scan in the binding energy range between 0 and 1400 eV with an energy step width of 0.4 eV. The chemical states of Pd-3d, Ni-2p, C-1s and O-1s core level spectra were studied in the narrow scan, which were recorded with an energy step of 0.1 eV and a pass energy of 55 eV. The measuring area was about 200 µm in diameter. The chamber pressure was always lower than 5.0×10^{-7} Pa during measurements. XPS measurements were performed for annealed samples, after dipping in 0.1 M HCl and after RDE testing. For all samples, the binding energy scale was corrected by shifting the spectra with respect to the adventitious C-1s peak of the C–C bond to 284.8 eV. Depth profiling was used in the same XPS instrument to map the elemental composition through the layers of the thin films and detect a potential thickness loss after RDE measurement. It was carried out by successive 2 kV Ar^+ ion etchings over a 2 x 2 mm^2 area at a rate of 4 nm/min. Both survey and narrow scans were recorded every 5 nm throughout a 45 nm depth. For the layer analysis narrow scans were recorded with 69 eV pass energy and 0.2 eV/step.

Relative sensitivity factors from the PHI-Multipak software were used for the concentration quantification. Concentrations were determined with the effective peak areas after Shirley background subtraction. For the electronic structure and chemical state analysis, the core level spectra of Ni-2p and Pd-3d were curve-fitted with the Multipak software. The fitting routine of the peaks was performed using an asymmetric Gaussian-Lorentzian sum function with a Shirley background.

3. Results & Discussion

3.1. Characterization of annealed and acid treated PdNi Thin Films

Physically evaporated PdNi thin films were thermally annealed in 4% H_2 in Ar at temperatures between 350 and 600 °C. Different Pd:Ni surface and subsurface atomic compositions were obtained as a result of different diffusion behaviors at different annealing temperatures. Fig. 2 shows the Pd:Ni atomic concentrations throughout the annealed thin films investigated by ion etching depth profiling in XPS. The depth profile shows the effect of annealing temperature on both surface and subsurface Pd:Ni concentrations. The as-prepared samples were fabricated with a 28 nm Pd film evaporated on top of a 12 nm Ni film to achieve 50/50 atomic ratio of Pd and Ni. The sample annealed at 350 °C shows a Pd:Ni composition at the surface of about 60% Pd (40% Ni), which indicates that Ni diffuses through the Pd film and reach the surface already at this temperature. The PdNi-350 profile shows that the Ni content decreases when going from 0 to 5 nm depth, indicating the preference of Ni to be at the surface at 350 °C. After depths of 10 nm, the amount of Pd gradually decreases. At 45 nm depth the amount of Pd is over 40%, confirming that at this temperature Pd mobility is already sufficient to diffuse throughout the entire film. At 400 °C a similar behavior is observed, with Ni accumulating on the surface rather than in subsurface layers and increasing concentration throughout the sample depth. This lower Ni content on the subsurface can be explained by the preferential sputtering event in XPS depth profiling. Ion sputtering of binary alloys gives rise to surface enrichment of the heavier component due to lighter elements having a larger cross-section and consequently, more of them are set into motion when hit by an incoming Ar^+ ion[50]. Thus, concentration profiles recorded after ion etching in Fig. 2 display larger Pd atomic concentrations than as-annealed samples.

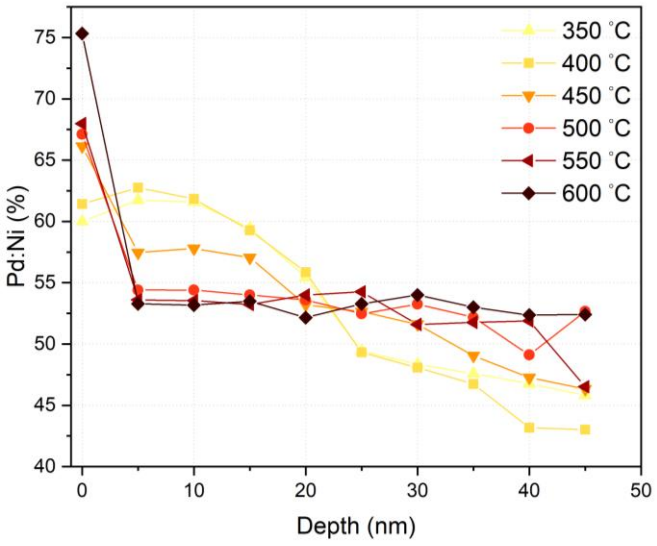

Figure 2 *Pd:Ni composition profile of thin films at different annealing temperatures obtained from Ar^+ ion etching depth profile in XPS.*

Higher annealing temperatures resulted in similar concentration profiles. Very similar compositions were achieved between 5 and 45 nm after annealing at 450 °C, where depth profiles revealed Pd:Ni subsurface stoichiometries close to 1:1 throughout the film. From 400 to 450 °C the amount of Pd on the surface significantly increased, indicating that Pd has a stronger driving force to be at the surface at this temperature. Further Pd enrichment on the surface was limited after annealing from 450 to 550 °C. The attained surface ratio of Pd and Ni is explained by their difference in surface energy[51]. At 600 °C there is an abrupt increase of surface Pd to 75% while subsurface concentrations remain unchanged.

The effect of temperature on the grain size of annealed samples is evidenced by SEM images (Fig.3). As shown in the insets, the grains increase as increasing annealing temperature. The grain size ranged from 20 nm (PdNi-350) to 200 nm (PdNi-600).

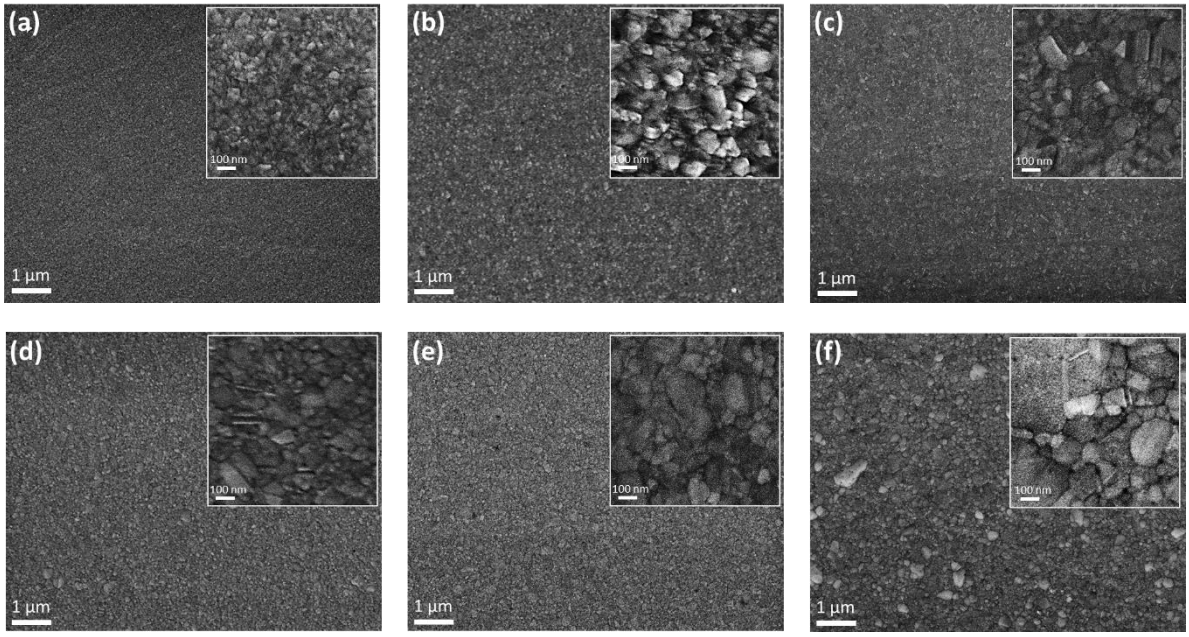

Figure 3 *SEM images of samples annealed at (a) 350 °C; (b) 400 °C; (c) 450 °C; (d) 500 °C; (e) 550 °C and (f) 600 °C.*

Cyclic voltammograms (CVs) of Pd, Ni, PdNi-400, and PdNi-400-AT in Ar-saturated 0.1 M KOH solution are shown in Fig. 3. All samples were annealed at 400 °C to relax the surface and enable better comparison. As seen, the PdNi-400 CV, set as a representative example, differs from that of pure Pd and pure Ni. Firstly, although only Pd is active for hydrogen adsorption, the annealed PdNi alloy exhibited a higher amount of charge involved in the hydrogen adsorption/desorption region (between 0.05 and 0.4 V vs. RHE). Possible reasons for this are either the alloying effect, which leads to an increase in lattice spacing and hence may facilitate the hydrogen absorption into the metal lattice[52]; or the overlapping of Ni(II) reduction currents with hydrogen adsorption[53]. Secondly, the peaks emerging at 0.7 – 0.8 V exhibit different intensities and shapes for PdNi and pure Pd. This peak

corresponds to the chemisorption of OH^- ions on Pd, followed by plateau-shaped currents ascribed to the oxidation of Pd-OH to higher valence Pd oxides (both PdO and $Pd(OH)_2$)[54,55]. This plateau also comprises currents attributed to the formation of a β-$Ni(OH)_2$ layer[53,56]. The formation of other Ni(II) species is not displayed in the CV due to a potential window not wide enough to entail the potential at which these processes occur[57]. Although the surface of PdNi-400-AT is composed solely of Pd, it does not present the OH^- adsorption peak. In addition, the reduction peak at 0.7 V is attributed to the reduction of Pd(II) compounds during the cathodic sweep[53–55]. As seen, the Pd(II) reduction takes place at different potentials for pure Pd, PdNi-400 and PdNi-400-AT. As expected, PdNi-400 shows a lower amount of charge involved on the Pd(II) reduction, indicating less amount of surface Pd. Upon acid treatment, the reduction peak increase in intensity due to the removal of Ni species from the surface, forming a completely Pd covered surface. The reduction peak for PdNi-400-AT is shifted negatively with respect to pure Pd. This suggests that the Pd on the surface of the PdNi-400-AT is affected by the Ni in the alloy below the surface.

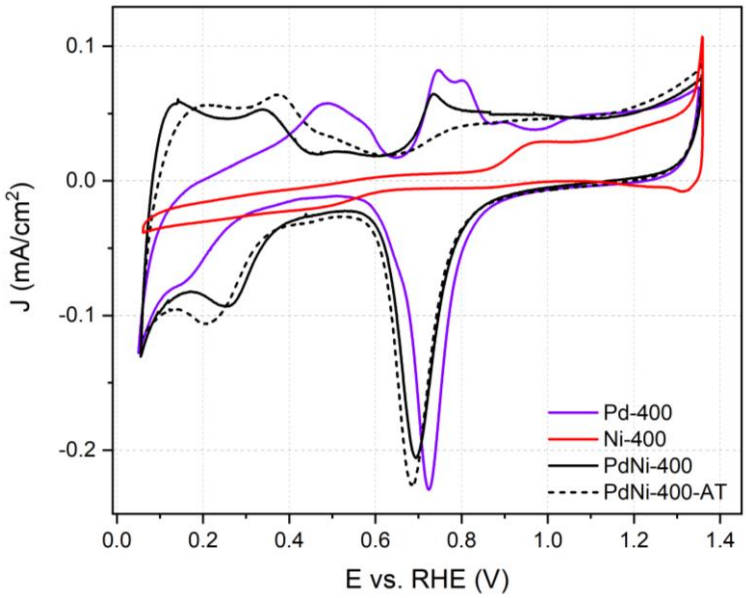

Figure 4 *Cyclic voltammograms in Ar-saturated 0.1 M KOH of Pd, Ni, PdNi annealed at 400 ◦C and acid treated 40 nm thin films. Scan rate 50 mV/s; room temperature.*

Fig. 4 shows both the Pd:Ni XPS atomic concentration and Pd electrochemical active surface area (ECSA) before and after the acid treatment. Since the hydrogen adsorption is accompanied by the absorption of hydrogen into the palladium bulk, ECSA of Pd alloys cannot be readily calculated from the hydrogen underpotential deposition region (H_{UPD})[58,59]. Instead, we chose to derive the Pd surface area from the charge corresponding to surface oxide reduction region. Hence, the Pd ECSA was calculated by measuring the charge involved in the surface PdO reduction from the peak at 0.7 V vs. RHE and dividing it by the charge density associated to the reduction of a PdO monolayer (424 $\mu C/cm^2$)[60,61]. As seen in Fig. 2, Pd atomic concentration on the top layers of the films increased with

increasing annealing temperature, ranging from 60 to 75%. After HCl cleaning for 10 min, all samples exhibited an increase of surface Pd regardless of the Pd:Ni atomic concentration prior to the acid treatment. Pd atomic concentration increased to about 80 % of the total surface composition. Pd ECSA, instead, is not dependent on the annealing temperature and it exhibits its maximum at 450 °C. The Pd ECSA increase between 350 and 450 °C can be confidently assigned to a surface Pd enrichment. Nevertheless, it must be mentioned that surface roughness decreases with increasing temperature, making the decrease of the Pd ECSA after 450 °C attributable to a smoothening of the total surface area. The effect of temperature on the surface roughness can be seen on the Pd ECSA of the acid treated samples. Since HCl effectively removes oxidated Ni species, it is assumed that the surfaces of all acid treated samples are entirely composed of Pd. Hence, the constant decrease of Pd ECSA with increasing temperature in the acid treated samples is utterly ascribed to a decrease of the total surface area. In this way, for annealed samples the contribution of the surface smoothening on the decrease of the Pd ECSA after 450 °C can be subtracted from the decrease due to Pd diffusion into the subsurface. Hence, it is easily observable that increasing temperature above 500 °C results in a Pd withdrawal from the surface as evidenced by the more pronounced decay of Pd ECSA for the annealed samples. Surface atomic distributions can be inferred by comparing surface compositions obtained in XPS with Pd ECSA profiles. For annealed samples, Pd concentration in both surface layers and on the total surface area increases proportionally until 450 °C, indicating similar atomic distributions in both regions. After 450 °C, the amount of Pd in the outermost layers keeps increasing while Pd ECSA decreases drastically after 500 °C. This trend indicates the formation of a Ni-rich surface with a Pd-rich subsurface at high annealing temperatures. For the acid treated samples, the amount of surface Pd remains constant and the decrease in Pd ECSA is merely attributed to smoothening of the surface with thermal annealing.

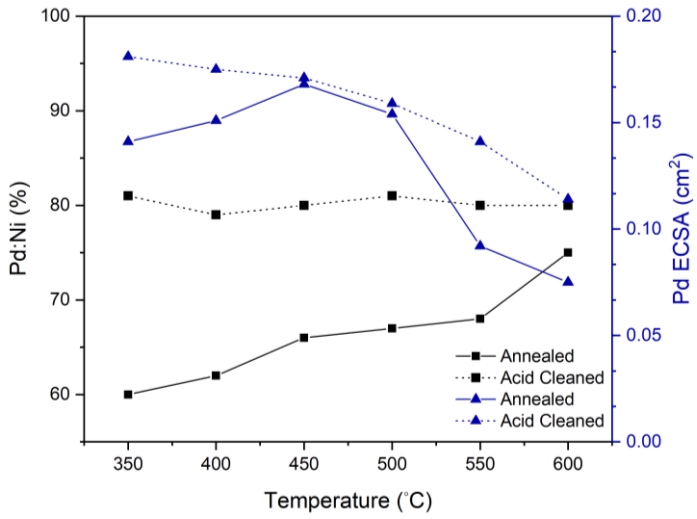

Figure 5 *Pd:Ni surface concentrations from XPS and Pd ECSA of annealed samples before and after the acid treatment.*

3.2. HOR

Fig. 6a shows the cathodic scan of HOR polarization curves of the annealed PdNi thin films together with a pure Pd thin film as a reference. The polarization curve of pure Ni is not shown as the HOR activity of pure Ni is more or less negligible[27]. With an onset potential at 0.17 V, the pure Pd film shows very low HOR activity, which is most likely due to a weaker HBE on Pd hydride that forms in H_2 atmosphere[62,63]. All annealed thin films show very low onset potentials, close to 0 V vs RHE. The HOR electroactivity exhibits slightly different potential responses, which are caused by slightly different Pd:Ni surface alloy compositions as a consequence of the different varying rates of Pd and Ni atoms throughout the film at the different annealing temperatures.

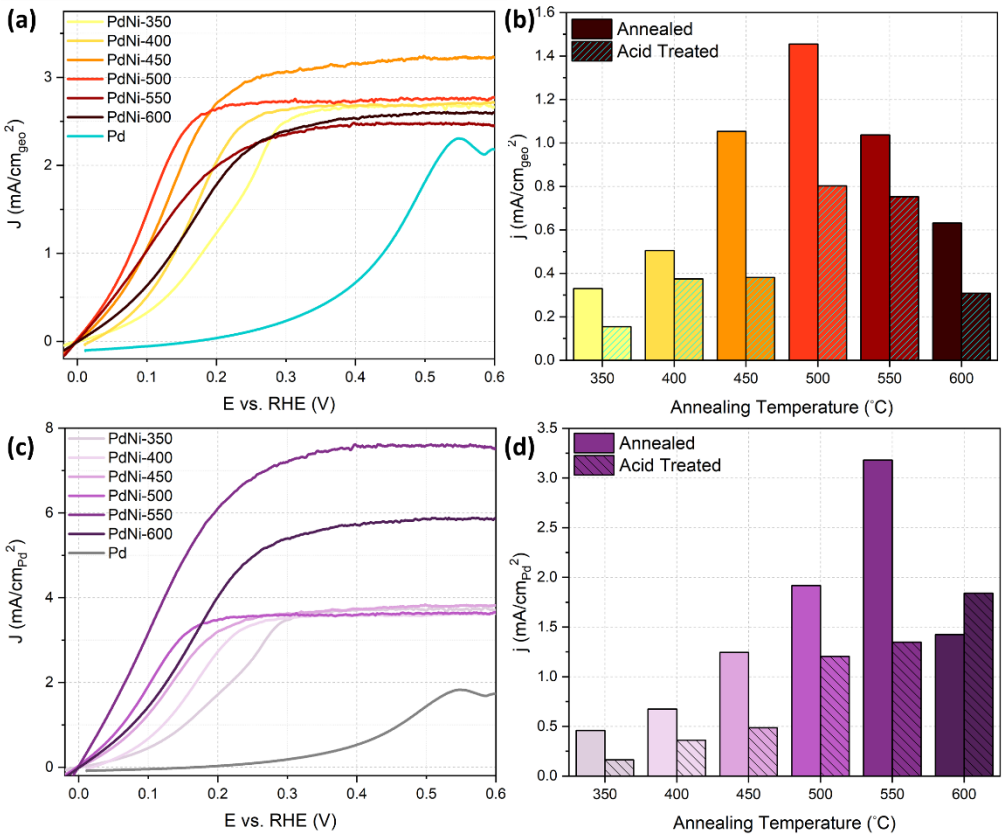

Figure 6 *HOR activity of PdNi samples and a pure Pd thin film in 0.1 M KOH: a) geometric currents of annealed samples at 1600 rpm, 50 mV/s; b) geometric activities of annealed and annealed + acid treated samples at 0.1 V; c) specific currents of annealed samples at 1600 rpm, 50 mV/s; d) specific activities of annealed and annealed + acid treated samples at 0.1 V.*

At 0.1 V, the geometric activities of annealed samples increase with increasing annealing temperature until 500 °C, after which they show a decay (Fig. 6b). Although the surface Pd % in Fig. 5 also follows a volcano-type trend, the rise and decline tendency in activity cannot be justified by the surface Pd. If the activity was dependent on the amount of Pd on the surface, PdNi-400 would have the highest activity since it has the largest Pd ECSA and higher surface roughness than PdNi-500. Instead, this trend at low overpotentials can be explained by both the degree of alloying and crystallite size. The

degree of alloying in PdNi mixtures has been reported to increase up to 500 °C and remain almost constant thereafter[64–66]. Annealed thin film alloys typically exhibit the highest defect-mediated interdiffusion at annealing temperatures around 0.3 of the melting temperatures[67,68]. Thus, for Ni (1455 °C) and Pd (1555 °C)[69], 500 °C falls into the temperature range at which the highest atomic mixing through diffusion takes place, resulting in the largest degree of surface alloying. The HOR activity would then depend on both Pd and Ni atomic surface distribution, which a priori could be an indication of the bifunctional mechanism through which the HOR is believed to be enhanced in alkaline media[27,70]. Similarly, the crystallite size of thin films also increases with increasing annealing temperature[71–73], which might be the reason behind the activity decay after 500 °C. Grain agglomeration at higher annealing temperatures (Fig. 3), which is not favorable for electrochemical reactions[73,74], may also be the underlying reason for the lower HOR activity at higher temperatures. Thus, from the results presented above it is reasonable to infer that the rise and decay of the HOR geometric activity with increasing temperature demonstrates the relationship between Pd and Ni surface atomic distribution and the high HOR activity.

Specific activities (SA) expressed as current density per Pd ECSA (Fig. 6c) show that all PdNi alloys exhibit a higher activity than pure Pd, confirming the role of Ni in the enhancement of the HOR activity in alkaline media. Up to 500 °C, all samples reach the same limiting current density although they have different half-wave potentials, which increase with increasing annealing temperature. The highest SA at 0.1 V vs. RHE (Fig. 6d) corresponds to the PdNi-550 sample, which shows the best utilization of surface Pd. Although XPS revealed a rather high Pd content on the surface at 550 °C, the difference between the Pd ECSA before and after acid treatment shown in Fig. 5 suggests that PdNi-550 most likely has the highest Ni content at the very surface.

Acid treated annealed samples entirely composed of a Pd overlayer over the PdNi alloy were also evaluated in RDE. All annealed samples show a decrease in the geometric activity after acid treatment (Fig. 6b), which provides further evidence on the beneficial effect of the added oxophilicity provided by surface Ni. Similar to annealed samples, the resulting geometric activities reveal a volcano-type dependence on temperature. PdNi-500 shows the highest geometric activity at 0.1 V vs. RHE (0.80 mA/cm^2_{geo}), which is 5 times higher than that of PdNi-350, the sample with the lowest geometric activity at 0.1 V vs. RHE. The activity decrease after PdNi-500 is attributed to the steep decrease of the total surface area due to the effect of temperature on the surface roughness. The effect of decreasing total surface area with increasing temperature is further evidenced by the trend in SAs (Fig. 6d). The trend in activities in acid treated samples shows a better Pd utilization as annealing temperature increases, with PdNi-600 exhibiting the highest activity per Pd atom (1.84 mA/cm^2_{Pd}), most likely due to a much lower Pd ECSA evidenced by its CV (Fig. S1l, Supporting Information). As previously shown

in Fig. 5, smoothening of the surface with increasing temperature also takes place at low annealing temperatures, although it shows a less prominent decrease. Thus, the increase in geometric activity between PdNi-350 and PdNi-500 cannot be explained by the surface smoothening effect. Instead, this increase in activity is ascribed to a ligand effect, which is induced in the Pd overlayer by the Ni underneath. The presence of a Ni in the Pd lattice results in an alteration of the d band structure and electron density of the latter, thereby changing its catalytic properties[75,76]. Thus, the amount of Ni in the underlying alloy establishes how much the electronic properties of the covering Pd differ from that of electronically unaltered Pd. However, the modification of the Pd electronic properties can also be attributed to a lattice strain effect. This effect is also caused by the addition of Ni to the Pd lattice, which results in an alteration of the Pd-Pd bond distance and thus a modification of the electronic properties of the Pd overlayer[75,77]. The extent of both effects relies on the compositions of the underlying alloy, which result in different enhancements of the HOR activity.

Determination of the HBE is a good strategy to determine whether the enhancement of the HOR activity occurs through an electronic effect that modifies the HBE of Pd, or through a bifunctional effect where $Ni(OH)_2$ provides oxophilic sites for the OH^- adsorption. The HBE can be calculated experimentally from the hydrogen desorption peak on a metal surface by using the following equation derived in the literature[78,79]:

$$E_{M-H} = -FE_H - \frac{1}{2}TS^o \quad (4)$$

where E_{M-H} is the hydrogen binding energy, F is the Faraday's constant, E_H the hydrogen desorption peak potential, T is the temperature and S^o the entropy of H_2 at standard conditions. The H desorption peak potential can be obtained from the CV profiles of the annealed samples (Fig. S1, Supporting Information) between 0.25 and 0.35 V vs. RHE to calculate the HBE. All the annealed samples show H desorption peaks at lower potentials than pure Pd (0.48 V). The SA at 0.1 V vs. RHE was plotted against the HBE calculated from the H desorption peak (Fig. 7a, black fitted line). The plot shows a linear relationship between the SA and the HBE, with the activity increasing as the binding energy becomes weaker. This monotonic increase of the SA with decreasing HBE confirms that the latter is a descriptor for the HOR in alkaline electrolytes. Since it has been reported that the reason behind the sluggish HOR for PGMs in alkaline media is the increase of the HBE with increasing pH[17,80], these results confirm that the weakening of the HBEs is crucial to enhance the HOR kinetics on PGMs in alkaline conditions. Moreover, the fact that PdNi-550 shows the highest SA is in good agreement with DFT studies on the electronic structure of Pd-Ni systems, which affirmed that equal amounts of Ni and Pd result in the weakest HBE[81].

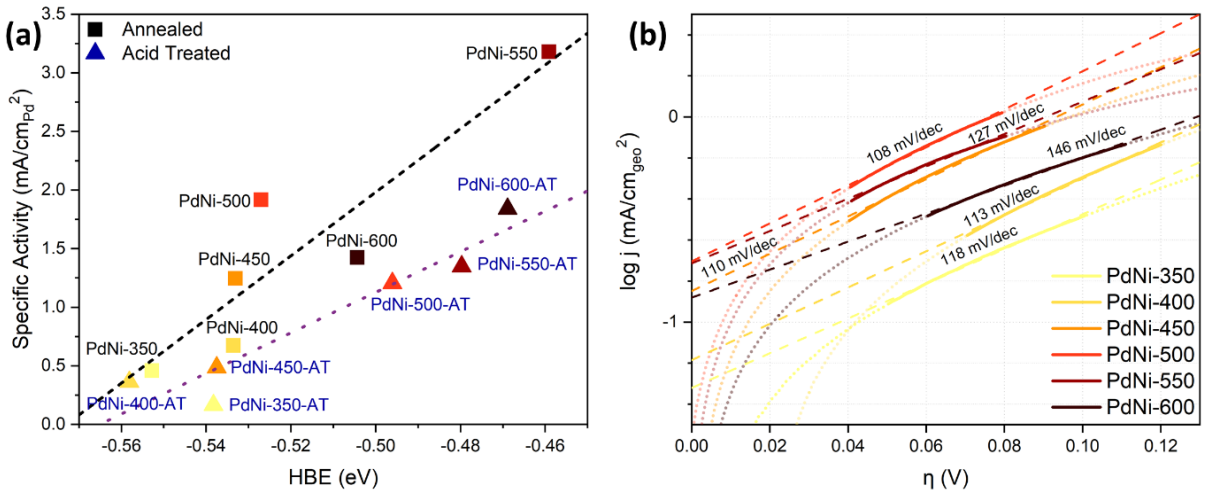

Figure 7 *(a) Specific activities of annealed and annealed + acid treated samples against the hydrogen binding energy and (b) Tafel plots and slopes of PdNi annealed samples.*

Electronic effects on the HOR activity are further evidenced by the linear relation between the SA of acid treated samples and the HBE (blue fitted line in Fig. 7a). Since all surfaces are entirely covered by Pd, the relation between the activity of acid treated samples and their HBE proves once again that the weaker HBE is the main reason behind the improved HOR kinetics in PdNi alloys. However, the lower slope in the fitted curve of acid treated samples shows that the activity increase with the weakening of the HBE is less pronounced in the absence of surface Ni. This proves the favorable role of surface Ni in catalyzing the HOR reaction. As explained above, the weakening of the HBE is ascribed to lattice and electronic effects caused by the addition of Ni to the Pd lattice, which results in an alteration of the electronic properties of Pd and thus its HBE. However, the significant decrease in HOR activities after the removal of surface Ni authenticates that adding oxophilic sites translates into a boosting of the HOR kinetics, although to a much lesser extent than the HBE.

Tafel analysis of the annealed samples revealed Tafel slopes between 108 and 146 mV/dec (Fig. 7b). The slopes follow the same volcano-type dependence with temperature as the geometric activities, with PdNi-500 showing the lowest slope and thus faster HOR kinetics. The intercepts of the Tafel plots were used to calculate the exchange current densities. When normalizing to the Pd ECSA, PdNi-550 showed the highest exchange current density among all annealed samples (0.41 mA/cm$^2_{Pd}$), which agrees with its SA at 0.1 V (Fig. 6d). The high Tafel slopes indicate that the charge transfer step (Heyrovsky or Volmer) is the rate determining step (RDS) on all surfaces[19,76]. This is in good agreement with previous studies claiming that the HOR rate is controlled by the Volmer step on PGMs, where OH^- affects its rate merely through hindering the H adsorption rather than being an active participant[82,83].

The results presented above provide evidence of the extensively discussed role of Ni in improving the HOR kinetics in alkaline media. It has been broadly argued that the reason behind the increased HOR

activity is lowering of the energy barrier of the Volmer step through added oxophilicity from surface $Ni/Ni(OH)_2$ atoms, which provides crucial adsorption sites for the OH^- adsorption[27,37,84]. However, we conclude that the HBE is the dominant descriptor of the HOR activity on Pd-based catalyst, although the so-called bifunctional mechanism is also accountable for the enhanced HOR activity. The HBE is tuned by ligand effects that change the electronic structure of Pd and lattice strain effects caused by the addition of $Ni/Ni(OH)_2$ atoms into the Pd lattice. Thus, the role of Ni in catalyzing the HOR comprises a major electronic effect that modifies the HBE of Pd and, to a lesser extent, a structural effect through added oxophilicity. This is in good agreement with previous studies stating that in PGMs the reason for slower HOR kinetics is attributed to a stronger HBE in base, which affects both H and H_2O adsorption and thus the rate of the Volmer step[17,80,82,83].

3.3. ORR

Fig. 8a shows the cathodic scan of ORR polarization curves of the annealed PdNi thin films together with a pure Ni and pure Pd thin films as a reference. The curves show two different sets of onset potentials, with pure Pd and samples annealed at low temperatures (350 – 450 °C) showing the highest onset potential. Annealing at temperatures above 450 °C results in a significant decrease of the half-way potential, although they all exhibit very similar limiting current densities below 0.6 V vs RHE. PdNi-400 and PdNi-450 present the highest onset and half-wave potentials. The higher activities at low annealing temperatures seem to correlate well with the ratio of Pd surface area to subsurface Pd (Fig. 5), with PdNi-400 and Pd-450 showing the largest amount of surface Pd per subsurface Pd. In other words, high amounts of surface Pd and subsurface Ni result in substantial ORR activities. This correlation is evidenced when comparing PdNi-400 and PdNi-500. As shown in Fig. 5, these samples have very similar Pd surface areas (0.151 cm_{Pd}^2 vs. 0.154 cm_{Pd}^2), although PdNi-400 has 5% more surface Ni derived from XPS measurements. The slightly higher surface Ni content in PdNi-400 is responsible for the 50 mV higher half-wave potential compared to PdNi-500, thereby corroborating the beneficial effect of subsurface Ni on the ORR. Thus, the significant decrease in activities above 450 °C is attributed to the major decrease in Ni beneath the PdNi layer (Fig. 5). Whereas the presence of Ni underneath a Pd layer seems to result in higher activities, surface Ni seems to be disadvantageous for enhancing the ORR kinetics because there is no annealed sample performing remarkably better than Pd at any potential.

ORR specific activities of annealed samples also show a substantial decrease in activities at annealing temperatures above 450 °C (Fig. 8c), most likely also attributed to Ni content in the top layers. However, when normalizing for the Pd surface area, PdNi-350, PdNi-400 and PdNi-450 show a better

Pd utilization than pure Pd at 0.8 V vs. RHE (Fig. 8d). Again, the higher SAs follow the trend of higher surface Pd and higher subsurface Ni. All annealed samples reach much higher limiting current densities than pure Pd, with PdNi-600 showing the largest limiting current due to a much lower Pd surface area.

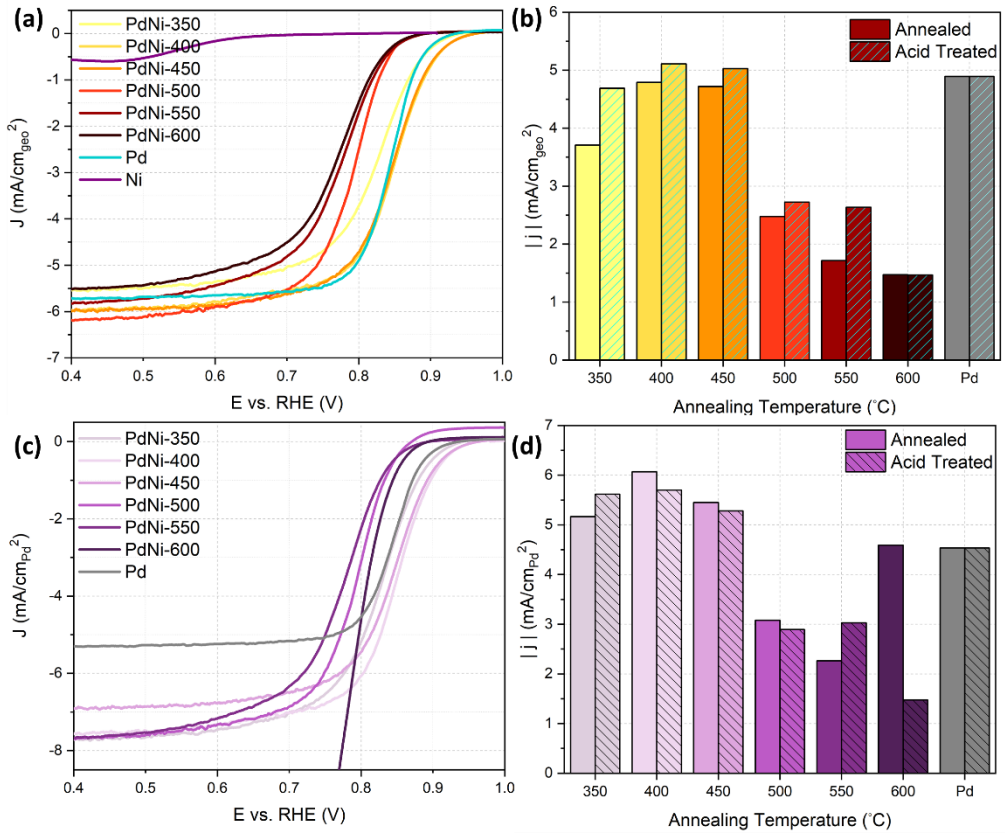

Figure 8 *ORR activity of PdNi samples and a pure Pd thin film in 0.1 M KOH: a) geometric currents of annealed samples at 1600 rpm, 50 mV/s; b) geometric activities of annealed and annealed + acid treated samples at 0.8 V; c) specific currents of annealed samples at 1600 rpm, 50 mV/s; d) specific activities of annealed and annealed + acid treated samples at 0.8 V. This potential has been chosen for comparing activities because at 0.8 V all samples were found at the kinetic and mass transport mixed region.*

The geometric activities of acid treated samples demonstrate a positive effect of a Pd overlayer for the ORR (Fig. 8b). After acid treatment, all samples are composed of a pure Pd layer over the PdNi alloy and they all exhibit higher geometric activities than before the acid treatment. PdNi-350, PdNi-400 and PdNi-450 show higher activities than Pd at 0.8 V. However, acid treated samples annealed at temperatures above 450 °C show ORR activities markedly lower than Pd and the low-temperature annealed samples after acid treatment. Again, this is attributed to the higher subsurface Ni content (Fig. 5). The reason behind the positive effect of subsurface Ni is ascribed to a d-orbital coupling effect between the two transition metals, which has been reported to result beneficial in bimetallic catalysts for the ORR in numerous studies[16,85–87]. By alloying a metal with low occupancy in its d-orbitals such as Ni with a metal with fully occupied d-orbitals such as Pd, the d-band of the resulting alloy is shifted downwards. The d-orbital coupling between the two metals results in a decrease of the Gibbs free energy of the electron transfer steps in the ORR, thereby enhancing the reaction by weakening the

desorption of oxygenated intermediates on Pd[14,15]. Therefore, since Pd already exhibits a good O-O bond breakage, alloying with Ni results in a boosting of the ORR activity through an electronic effect. In the same way, since the kinetics of the O-O breakage on Ni is very slow, addition of Ni into a Pd lattice is beneficial only if the former is not present at the surface. Thus, the remarkable activity of PdNi-350-AT, PdNi-400-AT and PdNi-450-AT is assigned to a higher subsurface Ni content lowering the d-band center of the Pd layer above. The lower activity at higher temperatures could also be attributed to a lower surface area owing to a higher surface smothering at those temperatures. However, their also low SAs (Fig. 8d) confirm that it is not attributable to a smoother surface. SAs provide even stronger evidence of the better Pd utilization in PdNi alloys compared to pure Pd.

The kinetics of the ORR were studied by collecting ORR polarization curves at different rotation speeds (Fig. S2, supporting information). The data was analyzed by extracting the Koutecky-Levich (K-L) plots from the mass-transport region of the corresponding ORR polarization curves (i.e. 0.4 V). The transferred electron number (n) was obtained using the K-L equation[88]:

$$\frac{1}{j} = \frac{1}{j_k} + \frac{1}{j_d} = \frac{1}{j_k} + \frac{1}{B\omega^{1/2}} \tag{5}$$

$$[B = 0.2nF\left(D_{O_2}\right)^{\frac{2}{3}}(v)^{-\frac{1}{6}}C_{O_2}] \tag{6}$$

where j is the measured current density, j_k and j_d are the kinetic and diffusion-limited current densities respectively, n is the number of electrons transfer per O_2 molecule, ω is the electrode rotation rate, F is the Faraday constant (96485 C/mol), D_{O_2} is the diffusion coefficient of O_2 in KOH 0.1 M (1.9×10^{-5} cm^2/s), v the kinetic viscosity (0.01 cm^2/s) and C_{O_2} is the bulk concentration of O_2 (1.2×10^{-6} mol/cm^3)[38,89]. The constant 0.2 is used when the rotation rate is expressed in rpm.

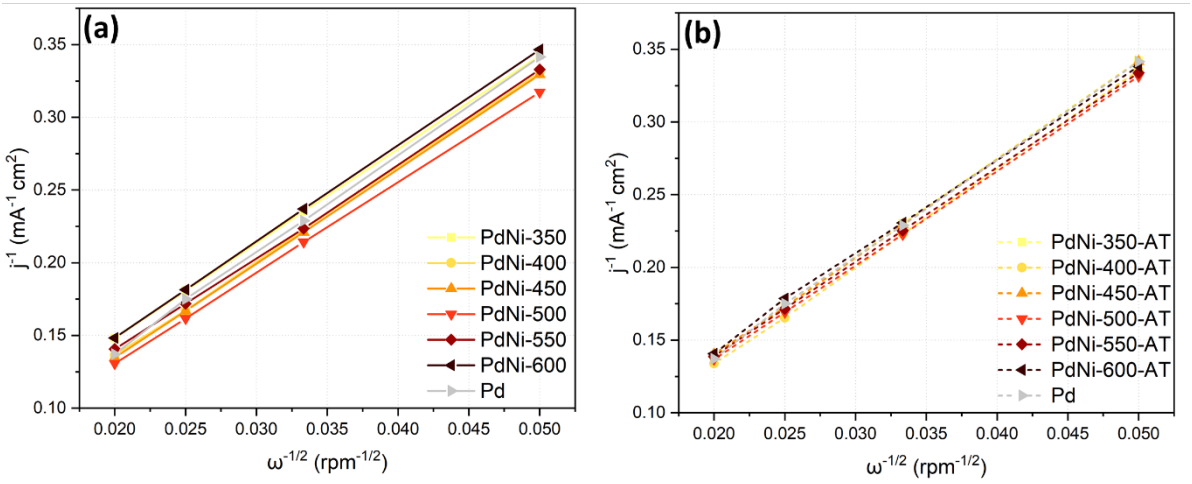

Figure 9 *K-L plots derived from the ORR polarization curves at 0.4 V of (a) annealed samples and (b) acid treated samples.*

Fig. 9a shows the K-L plots for ORR on the annealed samples. All samples studied present linear and parallel K-L plots, which indicate first order kinetics with respect to molecular oxygen[90]. The transferred electron number was calculated from the K-L slopes and it was found to be 4.30-4.50 for all annealed samples (Table S1, Supporting Information). These n values confirm that the ORR is governed by a 4-electron pathway, thereby reducing O_2 to OH^- during the reaction. A dominant 4-electron pathway was also observed in previous studies for Pd-based catalysts in alkaline conditions[38,91]. K-L analysis of acid treated samples (Fig. 9b) also exhibit parallel and linear plots, but much more similar intercepts indicating very similar kinetic current densities (j_k). The n value was also found to be around 4 for all acid treated samples, indicating the same reduction pathway as annealed samples.

The results presented in this section support the picture of a beneficial effect of alloying transition metals with different d-orbital occupancy to enhance the ORR kinetics, which has been discussed in earlier studies. The overall increase in the ORR activity when surface Ni is removed by acid treatment evidences the detrimental effect of Ni as a direct active site in this reaction. However, the activities of acid treated samples surpassing the activity of pure Pd justify the electronic effect induced by the Ni underneath. Hence, we confirm the positive effect of lowering the d-band center of transition metals with excellent O-O breakage and unfavorable desorption of oxygenated species.

3.4 XPS

To further investigate the reasons behind both the overall decrease in HOR activities and the increase in ORR activities after the acid treatment, the surface elemental composition and the chemical state of both Pd and Ni were investigated by XPS on both annealed and acid treated samples, as well as after the electrochemical tests. For the Ni-2p XPS spectra, only the $2p_{3/2}$ splitting was deconvoluted (Fig. 10a) and the sensitivity factor corresponding to only one peak doublet was used for quantification. Three binding energies of three Ni species are distinguished in the core level spectra: Ni ($2p_{3/2}$: 852.6 eV); Ni^{2+} in NiO ($2p_{3/2}$: 853.7 eV); and Ni^{2+} in $Ni(OH)_2$ ($2p_{3/2}$: 855.6 eV)[92–94]. Shake-up satellite peaks at higher binding energies (~857 eV, ~861 eV and ~863 eV)[93–95] were also considered for fitting of Ni-$2p_{3/2}$ spectra, although their relative intensities were not taken into account for quantification of Ni species. Pd-3d spectra (Fig. 10b) was deconvoluted using three d-doublets corresponding to: Pd ($3d_{5/2}$: 335.5 eV); Pd^{2+} in PdO ($3d_{5/2}$: 336.8 eV); and Pd^{4+} in PdO_2 ($3d_{5/2}$: 338.3 eV)[96,97]. Gaussian-Lorentzian peaks were used for the deconvolution of all Ni species and Pd oxides, whereas metallic Pd peaks were fitted using asymmetric peaks. An iterated Shirley background was subtracted from all data and all Ni and Pd deconvoluted peaks were allowed to vary by ±0.3 eV.

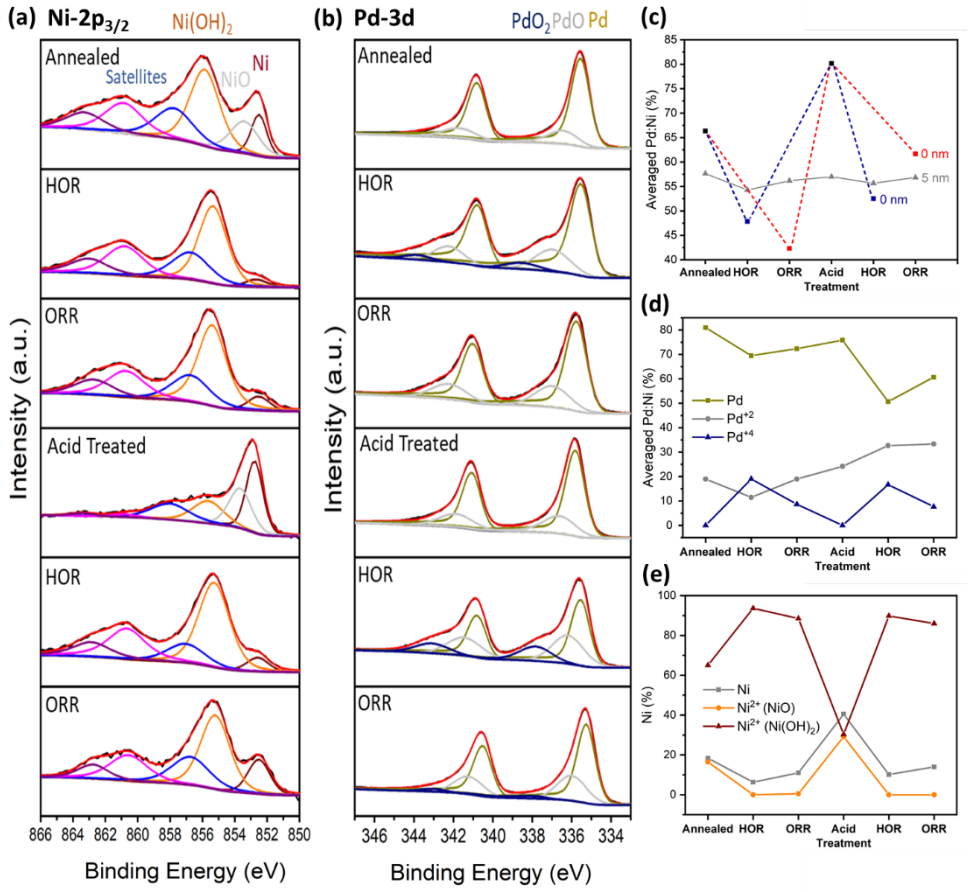

Figure 10 *XPS deconvoluted spectra of (a) Ni-2$p_{3/2}$ and (b) Pd-3d for annealed and annealed + acid treated samples; (c) averaged Pd:Ni composition and content of (d) Ni species and (e) Pd species extracted from XPS before and after annealing, acid treatment and electrochemical tests.*

The relative content of Pd and Ni species was obtained by integrating their respective peak areas in their XPS spectra. Fig. 10c shows the Pd:Ni composition average of all samples after the indicated treatments. The results show that annealed and acid treated samples are composed of a Pd-rich surface, especially after acid treatment due to the effective removal of surface Ni in the form of oxide. HOR and ORR measurements of both annealed and acid treated samples result in a Ni enrichment of the surface. This provides evidence for the Ni diffusion to the surface triggered by its stronger OH-adsorption energy compared to Pd[98]. After HOR measurements the averaged compositions result in almost equal amounts of superficial Pd:Ni. However, after ORR, annealed samples exhibit a much higher increase in surface Ni than ORR-measured acid treated samples, evincing the more hindered diffusion of Ni through a Pd overlayer in the presence of oxygen.

Both Pd and Ni oxidated species were quantified from XPS deconvoluted spectra and averaged after every treatment as shown in Fig. 10d and Fig. 10e respectively. As shown, the higher metallic Pd on surface is observed after both annealing and acid treatment, whereas oxidated Pd species (Pd^{2+} and Pd^{4+}) are formed during electrochemical testing. However, spectra of acid treated samples show the

ineffectiveness of HCl in the removal of Pd oxides. HOR measurements mainly result in the higher valence oxides, indicating the formation of Pd^{4+} species (PdO_2) from the oxidation of both Pd and, partially, PdO. ORR testing also leads to Pd oxidation, although the resulting alloys are primarily composed of a Pd^{2+} oxide. In contrast to Pd, Ni oxidated species are highly present already in the annealed samples due to the ease by which Ni to oxidizes in air. Annealed samples show a major amount of $Ni(OH)_2$, which increases drastically after HOR and ORR measurements due to contact with the alkaline electrolyte. Acid treatment results in a severe decrease of Ni hydroxide, causing a rise of 30% in the relative amounts of both Ni and NiO. Since both Ni and NiO dissolves in acidic media and Ni forms a hydroxide in aqueous solutions[99], the remaining Ni and NiO is attributed to subsurface Ni that is not reachable by neither the electrolyte nor the HCl. This supports the formation of a Pd overlayer due to Ni removal upon contact with acid. The amount of $Ni(OH)_2$ becomes again significant after ORR and HOR testing, suggesting the diffusion of Ni through the Pd layer owing to the higher affinity of Ni for OH^- [97].

4. Conclusions

In this study, we investigated the electronic and structural effects in alloyed PdNi thin films and in a Pd layer over a PdNi alloy influence both HOR and ORR activity in alkaline media. HOR measurements revealed that both electronic and structural effects play a role in accelerating the HOR kinetics. It was found that the main responsible for the activity enhancement observed in PdNi alloys is the weaker HBE of Pd as a result of the Ni addition. Removal of surface Ni by acid treatment resulted in an overall decrease of the HOR activities, thereby providing strong evidence that surface $Ni/Ni(OH)_2$ is also boosting the HOR kinetics by providing oxophilic sites for OH^- adsorption, i.e. a bifunctional mechanism. ORR measurements also displayed a beneficial effect of alloying Pd with Ni. In contrast to the HOR, surface Ni has a detrimental effect on the ORR kinetics in alkaline media, as evinced by the overall activity increase after forming a Pd overlayer by acid treatment. The resulting protective Pd layer turned out to be a more effective ORR catalyst due to electronic effects induced by a modified d-band, which favors the desorption of oxygenated species. Therefore, we confirm that structural effects are crucial if the electronic effects are meant to be observed, which in turn are the main reason for the observed HOR and ORR activity enhancement in alkaline media.

Bibliography

1. Borup, R. *et al.* Scientific aspects of polymer electrolyte fuel cell durability and degradation. *Chem. Rev.* **107**, 3904–3951 (2007).

2. Eberle, U., Müller, B. & Von Helmolt, R. Fuel cell electric vehicles and hydrogen infrastructure: Status 2012. *Energy Environ. Sci.* **5**, 8780–8798 (2012).

3. Kiani, M. *et al.* Recent developments in electrocatalysts and future prospects for oxygen reduction reaction in polymer electrolyte membrane fuel cells. *J. Energy Chem.* **27**, 1124–1139 (2018).

4. Shahgaldi, S. & Hamelin, J. Improved carbon nanostructures as a novel catalyst support in the cathode side of PEMFC: A critical review. *Carbon N. Y.* **94**, 705–728 (2015).

5. Stephens, I. E. L., Bondarenko, A. S., Grønbjerg, U., Rossmeisl, J. & Chorkendorff, I. Understanding the electrocatalysis of oxygen reduction on platinum and its alloys. *Energy Environ. Sci.* **5**, 6744–6762 (2012).

6. Rabis, A., Rodriguez, P. & Schmidt, T. J. Electrocatalysis for polymer electrolyte fuel cells: Recent achievements and future challenges. *ACS Catal.* **2**, 864–890 (2012).

7. Kongkanand, A. & Mathias, M. F. The Priority and Challenge of High-Power Performance of Low-Platinum Proton-Exchange Membrane Fuel Cells. *J. Phys. Chem. Lett.* **7**, 1127–1137 (2016).

8. Debe, M. K. Electrocatalyst approaches and challenges for automotive fuel cells. *Nature* **486**, 43–51 (2012).

9. He, Q. & Cairns, E. J. Review—Recent Progress in Electrocatalysts for Oxygen Reduction Suitable for Alkaline Anion Exchange Membrane Fuel Cells. *J. Electrochem. Soc.* **162**, F1504–F1539 (2015).

10. Pan, Z. F., An, L., Zhao, T. S. & Tang, Z. K. Advances and challenges in alkaline anion exchange membrane fuel cells. *Prog. Energy Combust. Sci.* **66**, 141–175 (2018).

11. Varcoe, J. R., Slade, R. C. T., Wright, G. L. & Chen, Y. Steady-state dc and impedance investigations of H2/O2 alkaline membrane fuel cells with commercial Pt/C, Ag/C, and Au/C cathodes. *J. Phys. Chem. B* **110**, 21041–21049 (2006).

12. G.F. McLean ∗, T. Niet, S. Prince-Richard, N. D. An assessment of AFC technology. *Int. J. Hydrogen Energy* **27**, 507–526 (2002).

13. Stephens, I. E. L. *et al.* Tuning the activity of Pt(111) for oxygen electroreduction by subsurface alloying. *J. Am. Chem. Soc.* **133**, 5485–5491 (2011).

14. Wang, Y. & Balbuena, P. B. Design of oxygen reduction bimetallic catalysts: Ab-initio-derived thermodynamic guidelines. *J. Phys. Chem. B* **109**, 18902–18906 (2005).

15. Lima, F. H. B. *et al.* Catalytic activity - d-band center correlation for the O2 reduction reaction on platinum in alkaline solutions. *J. Phys. Chem. C* **111**, 404–410 (2007).

16. Park, S. A., Lim, H. & Kim, Y. T. Enhanced Oxygen Reduction Reaction Activity Due to Electronic Effects between Ag and Mn3O4 in Alkaline Media. *ACS Catal.* **5**, 3995–4002 (2015).

17. Durst, J. *et al.* New insights into the electrochemical hydrogen oxidation and evolution reaction mechanism. *Energy Environ. Sci.* **7**, 2255–2260 (2014).

18. Jervis, R. *et al.* Hydrogen Oxidation on PdIr/C Catalysts in Alkaline Media. *J. Electrochem. Soc.* **161**, F458–F463 (2014).

19. Cong, Y., Yi, B. & Song, Y. Hydrogen oxidation reaction in alkaline media: From mechanism to recent electrocatalysts. *Nano Energy* **44**, 288–303 (2018).

20. Schmidt, T. J., Stamenkovic, V., Ross, P. N. & Markovic, N. M. Temperature dependent surface

electrochemistry on Pt single crystals in alkaline electrolyte: Part 3. The oxygen reduction reaction. *Phys. Chem. Chem. Phys.* **5**, 400–406 (2003).

21. Wang, Y. *et al.* Pt-Ru catalyzed hydrogen oxidation in alkaline media: Oxophilic effect or electronic effect? *Energy Environ. Sci.* **8**, 177–181 (2015).

22. Sheng, W., Gasteiger, H. A. & Shao-Horn, Y. Hydrogen Oxidation and Evolution Reaction Kinetics on Platinum: Acid vs Alkaline Electrolytes. *J. Electrochem. Soc.* **157**, B1529 (2010).

23. Pattabiraman, R. Electrochemical investigations on carbon supported palladium catalysts. *Appl. Catal. A Gen.* **153**, 9–20 (1997).

24. Erikson, H., Sarapuu, A., Solla-Gullón, J. & Tammeveski, K. Recent progress in oxygen reduction electrocatalysis on Pd-based catalysts. *J. Electroanal. Chem.* **780**, 327–336 (2016).

25. Shao, M. Palladium-based electrocatalysts for hydrogen oxidation and oxygen reduction reactions. *J. Power Sources* **196**, 2433–2444 (2011).

26. Martin, M. H. & Lasia, A. Study of the hydrogen absorption in Pd in alkaline solution. *Electrochim. Acta* **53**, 6317–6322 (2008).

27. Alesker, M. *et al.* Palladium/nickel bifunctional electrocatalyst for hydrogen oxidation reaction in alkaline membrane fuel cell. *J. Power Sources* **304**, 332–339 (2016).

28. Li, B. & Prakash, J. Oxygen reduction reaction on carbon supported Palladium–Nickel alloys in alkaline media. *Electrochem. commun.* **11**, 1162–1165 (2009).

29. Chen, L. *et al.* Nanoporous PdNi bimetallic catalyst with enhanced electrocatalytic performances for electro-oxidation and oxygen reduction reactions. *Adv. Funct. Mater.* **21**, 4364–4370 (2011).

30. Jiang, S., Yi, B., Zhao, Q., Yu, H. & Shao, Z. Palladium-nickel catalysts based on ordered titanium dioxide nanorod arrays with high catalytic peformance for formic acid electro-oxidation. *RSC Adv.* **7**, 11719–11723 (2017).

31. Del Rosario, J. A. D. *et al.* Enhancing role of nickel in the nickel-palladium bilayer for electrocatalytic oxidation of ethanol in alkaline media. *J. Phys. Chem. C* **118**, 22473–22478 (2014).

32. Zhang, L., Chang, Q., Chen, H. & Shao, M. Recent advances in palladium-based electrocatalysts for fuel cell reactions and hydrogen evolution reaction. *Nano Energy* **29**, 198–219 (2016).

33. Ramaswamy, N. *et al.* Hydrogen oxidation reaction in alkaline media: Relationship between electrocatalysis and electrochemical double-layer structure. *Nano Energy* **41**, 765–771 (2017).

34. Zhou, Z., Liu, Y., Zhang, J., Pang, H. & Zhu, G. Non-precious nickel-based catalysts for hydrogen oxidation reaction in alkaline electrolyte. *Electrochem. commun.* **121**, 106871 (2020).

35. Pan, Y., Hu, G., Lu, J., Xiao, L. & Zhuang, L. Ni(OH)2-Ni/C for hydrogen oxidation reaction in alkaline media. *J. Energy Chem.* **29**, 111–115 (2019).

36. Oshchepkov, A. G., Bonnefont, A. & Savinova, E. R. On the Influence of the Extent of Oxidation on the Kinetics of the Hydrogen Electrode Reactions on Polycrystalline Nickel. *Electrocatalysis* **11**, 133–142 (2020).

37. Shviro, M., Polani, S., Dunin-Borkowski, R. E. & Zitoun, D. Bifunctional Electrocatalysis on Pd-Ni Core–Shell Nanoparticles for Hydrogen Oxidation Reaction in Alkaline Medium. *Adv. Mater. Interfaces* **5**, 1–8 (2018).

38. Wang, M. *et al.* PdNi hollow nanoparticles for improved electrocatalytic oxygen reduction in alkaline environments. *ACS Appl. Mater. Interfaces* **5**, 12708–12715 (2013).

39. Rheinländer, P. J., Herranz, J., Durst, J. & Gasteiger, H. A. Kinetics of the Hydrogen Oxidation/Evolution Reaction on Polycrystalline Platinum in Alkaline Electrolyte Reaction Order

with Respect to Hydrogen Pressure. *J. Electrochem. Soc.* **161**, F1448–F1457 (2014).

40. Lu, S. & Zhuang, Z. Investigating the Influences of the Adsorbed Species on Catalytic Activity for Hydrogen Oxidation Reaction in Alkaline Electrolyte. *J. Am. Chem. Soc.* **139**, 5156–5163 (2017).

41. Zhao, L. *et al.* Mechanistic Insights into the Hydrogen Oxidation Reaction on PtNi Alloys in Alkaline Media: A First-Principles Investigation. *ACS Appl. Mater. Interfaces* **12**, 40248–40260 (2020).

42. Ramaswamy, N. & Mukerjee, S. Influence of inner- and outer-sphere electron transfer mechanisms during electrocatalysis of oxygen reduction in alkaline media. *J. Phys. Chem. C* **115**, 18015–18026 (2011).

43. Ge, X. *et al.* Oxygen Reduction in Alkaline Media: From Mechanisms to Recent Advances of Catalysts. *ACS Catal.* **5**, 4643–4667 (2015).

44. Schalenbach, M. *et al.* The Electrochemical Dissolution of Noble Metals in Alkaline Media. *Electrocatalysis* **9**, 153–161 (2018).

45. Zadick, A., Dubau, L., Sergent, N., Berthomé, G. & Chatenet, M. Huge Instability of Pt/C Catalysts in Alkaline Medium. *ACS Catal.* **5**, 4819–4824 (2015).

46. Lafforgue, C., Zadick, A., Dubau, L., Maillard, F. & Chatenet, M. Selected Review of the Degradation of Pt and Pd-based Carbon-supported Electrocatalysts for Alkaline Fuel Cells: Towards Mechanisms of Degradation. *Fuel Cells* **18**, 229–238 (2018).

47. Wei, C. *et al.* Recommended Practices and Benchmark Activity for Hydrogen and Oxygen Electrocatalysis in Water Splitting and Fuel Cells. *Adv. Mater.* **31**, 1–24 (2019).

48. Čolić, V. *et al.* Experimental Aspects in Benchmarking of the Electrocatalytic Activity. *ChemElectroChem* **2**, 143–149 (2015).

49. Myland, J. C. & Oldham, K. B. Uncompensated resistance. 1. The effect of cell geometry. *Anal. Chem.* **72**, 3972–3980 (2000).

50. Smentkowski, V. S. Trends in sputtering. *Prog. Surf. Sci.* **64**, 1–58 (2000).

51. Skriver, H. L. & Rosengaard, N. M. Surface energy and work function of elemental metals. *Phys. Rev. B* **46**, 7157–7168 (1992).

52. Greeley, J. & Mavrikakis, M. Surface and subsurface hydrogen: Adsorption properties on transition metals and near-surface alloys. *J. Phys. Chem. B* **109**, 3460–3471 (2005).

53. Grdeń, M. & Czerwiński, A. EQCM studies on Pd-Ni alloy oxidation in basic solution. *J. Solid State Electrochem.* **12**, 375–385 (2008).

54. Liang, Z. X., Zhao, T. S., Xu, J. B. & Zhu, L. D. Mechanism study of the ethanol oxidation reaction on palladium in alkaline media. *Electrochim. Acta* **54**, 2203–2208 (2009).

55. Liang, R., Hu, A., Persic, J. & Norman Zhou, Y. Palladium nanoparticles loaded on carbon modified TiO2 nanobelts for enhanced methanol electrooxidation. *Nano-Micro Lett.* **5**, 202–212 (2013).

56. Hall, D. S., Bock, C. & MacDougall, B. R. The Electrochemistry of Metallic Nickel: Oxides, Hydroxides, Hydrides and Alkaline Hydrogen Evolution. *J. Electrochem. Soc.* **160**, F235–F243 (2013).

57. Alsabet, M., Grdeń, M. & Jerkiewicz, G. Electrochemical Growth of Surface Oxides on Nickel. Part 3: Formation of β-NiOOH in Relation to the Polarization Potential, Polarization Time, and Temperature. *Electrocatalysis* **6**, 60–71 (2014).

58. Suo, Y., Zhuang, L. & Lu, J. First-principles considerations in the design of Pd-alloy catalysts for oxygen reduction. *Angew. Chemie - Int. Ed.* **46**, 2862–2864 (2007).

59. Henning, S., Herranz, J. & Gasteiger, H. A. Bulk-Palladium and Palladium-on-Gold Electrocatalysts for the Oxidation of Hydrogen in Alkaline Electrolyte. *J. Electrochem. Soc.* **162**, F178–F189 (2015).

60. Rand, D. A. J. & Woods, R. The nature of adsorbed oxygen on rhodium, palladium and gold electrodes. *J. Electroanal. Chem.* **31**, 29–38 (1971).

61. Yang, Z., Ling, Y., Zhang, Y. & Xu, G. High Performance Palladium Supported on Nanoporous Carbon under Anhydrous Condition. *Sci. Rep.* **6**, 1–10 (2016).

62. Johansson, M. *et al.* Hydrogen adsorption on palladium and palladium hydride at 1 bar. *Surf. Sci.* **604**, 718–729 (2010).

63. Griessen, R., Strohfeldt, N. & Giessen, H. Thermodynamics of the hybrid interaction of hydrogen with palladium nanoparticles. *Nat. Mater.* **15**, 311–317 (2016).

64. Wang, W. *et al.* Carbon-supported Pd-Co bimetallic nanoparticles as electrocatalysts for the oxygen reduction reaction. *J. Power Sources* **167**, 243–249 (2007).

65. Liu, H. & Manthiram, A. Tuning the electrocatalytic activity and durability of low cost Pd70Co30 nanoalloy for oxygen reduction reaction in fuel cells. *Electrochem. commun.* **10**, 740–744 (2008).

66. Choi, D. S., Robertson, A. W., Warner, J. H., Kim, S. O. & Kim, H. Low-Temperature Chemical Vapor Deposition Synthesis of Pt–Co Alloyed Nanoparticles with Enhanced Oxygen Reduction Reaction Catalysis. *Adv. Mater.* **28**, 7115–7122 (2016).

67. Gupta, D. Special Aspects of Diffusion in Metallic Thin Films. *Mater. Res. Soc. Symp. Proc.* **47**, 11–26 (1985).

68. Hultman, L. Thermal stability of nitride thin films. *Vacuum* **57**, 1–30 (2000).

69. TRIPP, E. H. *Materials Handbook*. *Nature* **150**, (1942).

70. Bakos, I., Paszternák, A. & Zitoun, D. Pd/Ni Synergestic Activity for Hydrogen Oxidation Reaction in Alkaline Conditions. *Electrochim. Acta* **176**, 1074–1082 (2015).

71. Benramache, S. & Benhaoua, B. Influence of annealing temperature on structural and optical properties of ZnO: In thin films prepared by ultrasonic spray technique. *Superlattices Microstruct.* **52**, 1062–1070 (2012).

72. Metin, H. & Esen, R. Annealing studies on CBD grown CdS thin films. *J. Cryst. Growth* **258**, 141–148 (2003).

73. Sugawara, K., Minamide, Y., Kawamura, M., Abe, Y. & Sasaki, K. Agglomeration behavior of Ag films suppressed by alloying with some elements. *Vacuum* **83**, 610–613 (2008).

74. She, Y., Lu, Z., Fan, W., Jewell, S. & Leung, M. K. H. Facile preparation of PdNi/rGO and its electrocatalytic performance towards formic acid oxidation. *J. Mater. Chem. A* **2**, 3894–3898 (2014).

75. Scofield, M. E. *et al.* Role of chemical composition in the enhanced catalytic activity of Pt-based alloyed ultrathin nanowires for the hydrogen oxidation reaction under alkaline conditions. *ACS Catal.* **6**, 3895–3908 (2016).

76. Hu, J., Kuttiyiel, K. A., Sasaki, K., Zhang, C. & Adzic, R. R. Determination of Hydrogen Oxidation Reaction Mechanism Based on Pt−H ad Energetics in Alkaline Electrolyte . *J. Electrochem. Soc.* **165**, J3355–J3362 (2018).

77. Wang, X. *et al.* Strain Effect in Bimetallic Electrocatalysts on the Hydrogen Evolution Reaction. *ACS Energy Lett.* (2018). doi:10.1021/acsenergylett.8b00454

78. Bhowmik, T., Kundu, M. K. & Barman, S. Palladium Nanoparticle-Graphitic Carbon Nitride Porous Synergistic Catalyst for Hydrogen Evolution/Oxidation Reactions over a Broad Range of

pH and Correlation of Its Catalytic Activity with Measured Hydrogen Binding Energy. *ACS Catal.* **6**, 1929–1941 (2016).

79. Karlberg, G. S. *et al.* Cyclic voltammograms for H on Pt(111) and Pt(100) from first principles. *Phys. Rev. Lett.* **99**, 1–4 (2007).

80. Sheng, W. *et al.* Correlating hydrogen oxidation and evolution activity on platinum at different pH with measured hydrogen binding energy. *Nat. Commun.* **6**, 6–11 (2015).

81. Leppert, L., Kempe, R. & Kümmel, S. Hydrogen binding energies and electronic structure of Ni-Pd particles: a clue to their special catalytic properties. *Phys. Chem. Chem. Phys.* **17**, 26140–26148 (2015).

82. Huang, J., Li, P. & Chen, S. Quantitative Understanding of the Sluggish Kinetics of Hydrogen Reactions in Alkaline Media Based on a Microscopic Hamiltonian Model for the Volmer Step. *J. Phys. Chem. C* **123**, 17325–17334 (2019).

83. Intikhab, S., Snyder, J. D. & Tang, M. H. Adsorbed Hydroxide Does Not Participate in the Volmer Step of Alkaline Hydrogen Electrocatalysis. *ACS Catal.* **7**, 8314–8319 (2017).

84. Shi, G., Yano, H., Tryk, D. A., Iiyama, A. & Uchida, H. Highly Active, CO-Tolerant, and Robust Hydrogen Anode Catalysts: Pt-M (M = Fe, Co, Ni) Alloys with Stabilized Pt-Skin Layers. *ACS Catal.* **7**, 267–274 (2017).

85. Xu, C., Liu, Y., Hao, Q. & Duan, H. Nanoporous PdNi alloys as highly active and methanol-tolerant electrocatalysts towards oxygen reduction reaction. *J. Mater. Chem. A* **1**, 13542–13548 (2013).

86. Aguirre, M. del C., Rivas, B. L., Fabietti, L. M. & Urreta, S. E. Enhanced performance of nano-electrocatalysts of Pd and PdCo in neutral and alkaline media. *J. Appl. Electrochem.* **49**, 1–15 (2019).

87. Kim, J., Park, J. E., Momma, T. & Osaka, T. Synthesis of Pd-Sn nanoparticles by ultrasonic irradiation and their electrocatalytic activity for oxygen reduction. *Electrochim. Acta* **54**, 3412–3418 (2009).

88. Zhou, R., Zheng, Y., Jaroniec, M. & Qiao, S. Z. Determination of the Electron Transfer Number for the Oxygen Reduction Reaction: From Theory to Experiment. *ACS Catal.* **6**, 4720–4728 (2016).

89. Elezović, N. R., Babić, B. M., Vračar, L. J. M. & Krstajić, N. V. Oxygen reduction at platinum nanoparticles supported on carbon cryogel in alkaline solution. *J. Serbian Chem. Soc.* **72**, 699–708 (2007).

90. Mukerjee, S. & Srinivasan, S. Enhanced electrocatalysis of oxygen reduction on platinum alloys in proton exchange membrane fuel cells. *J. Electroanal. Chem.* **357**, 201–224 (1993).

91. Alexeyeva, N. *et al.* Electroreduction of oxygen on Vulcan carbon supported Pd nanoparticles and Pd-M nanoalloys in acid and alkaline solutions. *Electrochim. Acta* **56**, 6702–6708 (2011).

92. He, W. *et al.* 3D β-Ni(OH)2 nanowires/RGO composite prepared by phase transformation method for superior electrochemical performance. *Sci. Rep.* **9**, 1–8 (2019).

93. Biesinger, M. C., Payne, B. P., Lau, L. W. M., Gerson, A. & Smart, R. S. C. X-ray photoelectron spectroscopic chemical state Quantification of mixed nickel metal, oxide and hydroxide systems. *Surf. Interface Anal.* **41**, 324–332 (2009).

94. Yu, X. *et al.* Hydrogen Evolution Reaction in Alkaline Media: Alpha- or Beta-Nickel Hydroxide on the Surface of Platinum? *ACS Energy Lett.* **3**, 237–244 (2018).

95. Marchetti, L., Miserque, F., Perrin, S. & Pijolat, M. XPS study of Ni-base alloys oxide films formed in primary conditions of pressurized water reactor. *Surf. Interface Anal.* **47**, 632–642 (2015).

96. Bhalothia, D., Chen, P.-C., Yan, C., Wang, K.-W. & Chen, T.-Y. Heterogeneous NiO 2 -to-Pd Epitaxial Structure Performs Outstanding Oxygen Reduction Reaction Activity . *J. Phys. Chem. C* **124**, 2295–2306 (2020).

97. Lu, X., Ahmadi, M., Disalvo, F. J. & Abruña, H. D. Enhancing the Electrocatalytic Activity of Pd/M (M = Ni, Mn) Nanoparticles for the Oxygen Reduction Reaction in Alkaline Media through Electrochemical Dealloying. *ACS Catal.* **10**, 5891–5898 (2020).

98. Nørskov, J. K. *et al.* Origin of the overpotential for oxygen reduction at a fuel-cell cathode. *J. Phys. Chem. B* **108**, 17886–17892 (2004).

99. Ziemniak, S. E., Jones, M. E. & Combs, K. E. S. Solubility and phase behavior of Nickel Oxide in aqueous sodium phosphate solutions at elevated temperatures. *J. Solution Chem.* **21**, 1153–1176 (1992).

Supplementary Information

PdNi Thin Films for Hydrogen Oxidation Reaction and Oxygen Reduction Reaction in Alkaline Media

Gerard Montserrat-Sisó, Björn Wickman

Division of Chemical Physics, Department of Physics, Chalmers University of Technology, SE-412 96 Gothenburg, Sweden

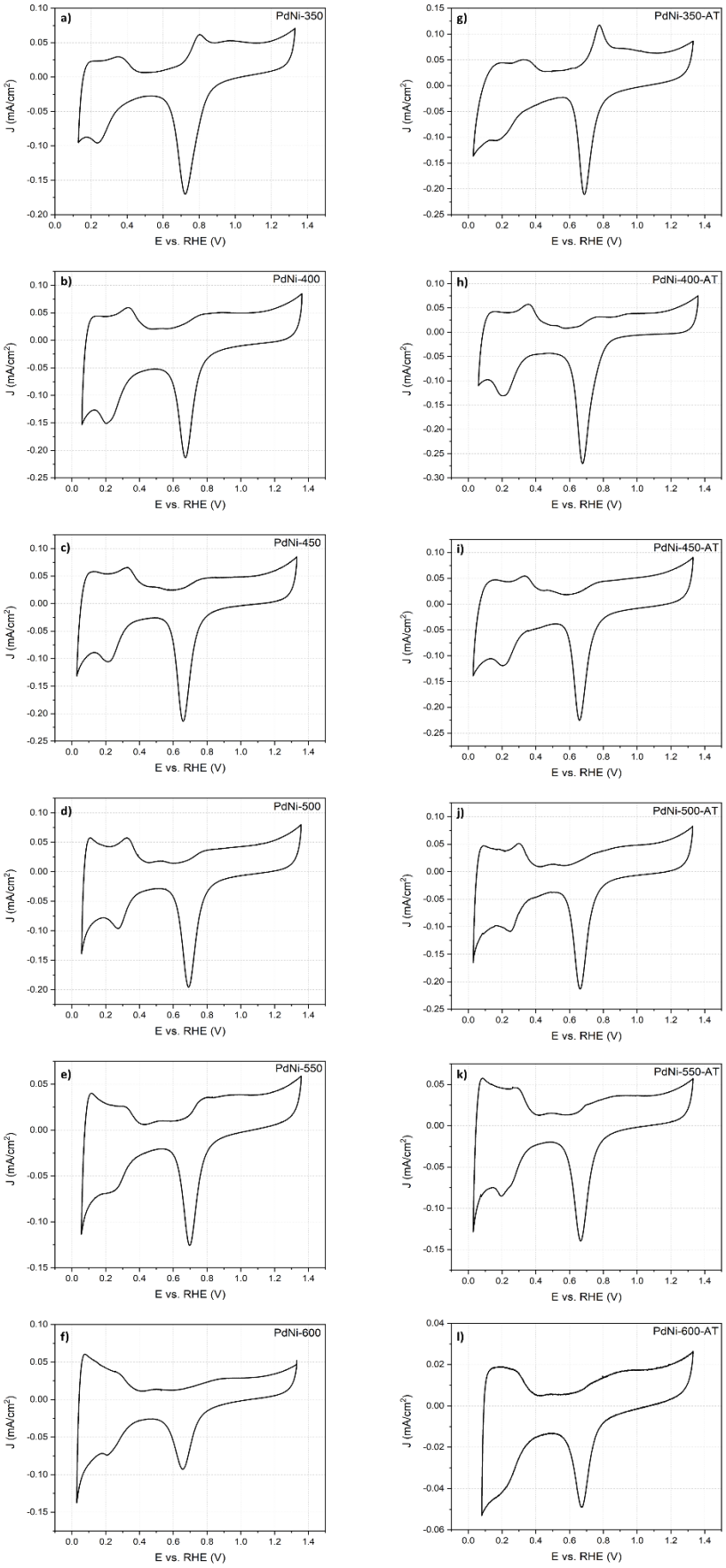

Figure S1 *Cyclic voltammograms in Ar-saturated 0.1 M KOH of a)-f) annealed samples and g)-l) acid treated samples.*

1. Koutecky-Levich plots and electron transfer number

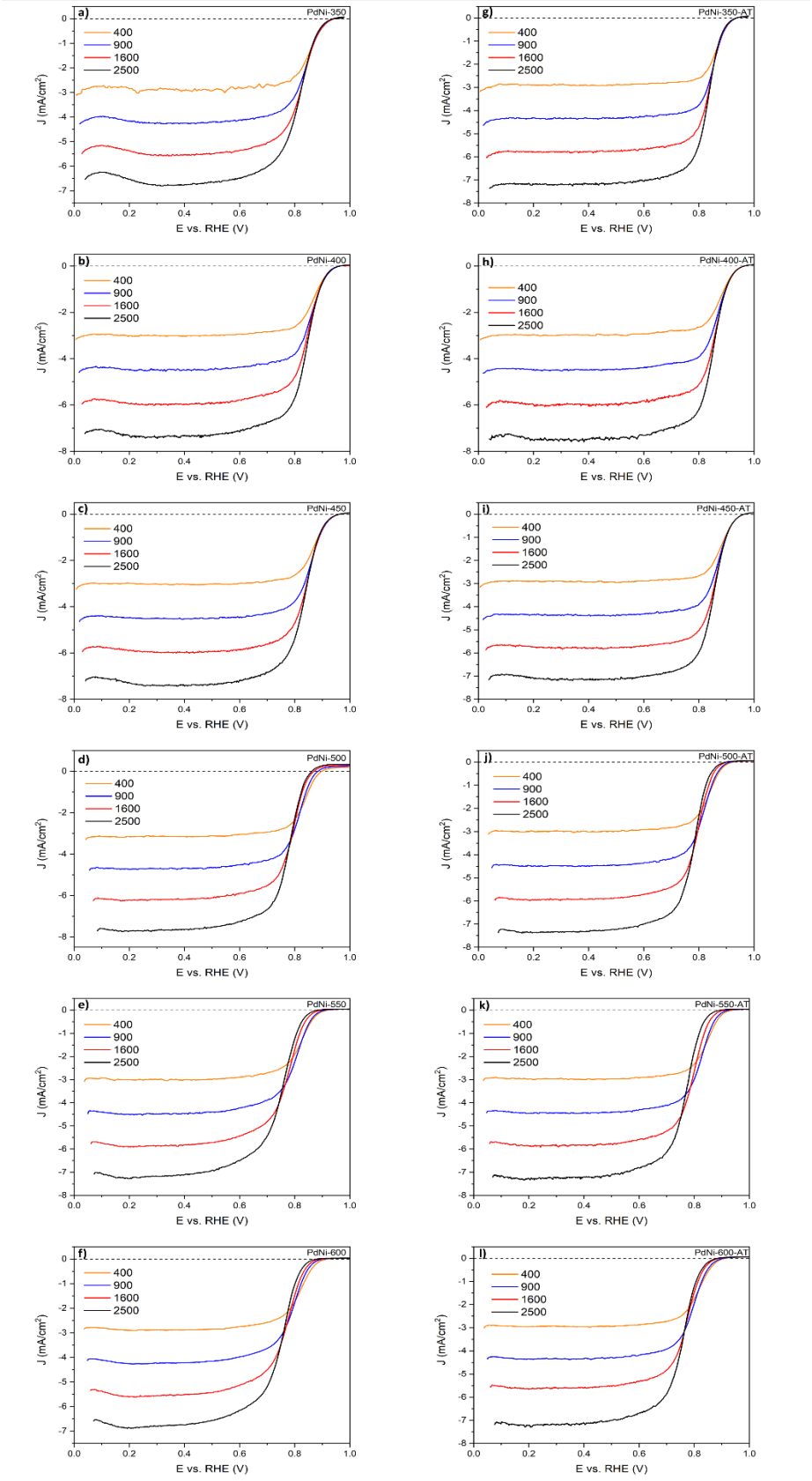

Figure S2 *ORR polarization curves of a)-f) annealed samples and g)-l) acid treated samples at different rotation rates used for Koutecky-Levich plots.*

Table S1 *Electron transfer number (n) extracted from Koutecky-Levich plots for all annealed and acid treated samples.*

	Electron Transfer Number (n)	
Sample	**Annealed**	**Acid Treated**
PdNi-350	4.35	4.16
PdNi-400	4.33	4.17
PdNi-450	4.34	4.18
PdNi-500	4.53	4.34
PdNi-550	4.39	4.33
PdNi-600	4.26	4.31

2. Fitting of XPS Data

X-ray photoelectron spectroscopy (XPS) peak fitting was used to quantify the amount of metallic and oxide Pd and Ni species in annealed samples, acid treated, and after HOR and ORR measurements in the same samples (Table S2). The curve fitting of both Pd-3d and Ni-2p was carried out using the Multipak software, with a standard Shirley background and Gaussian-Lorentzian peak profiles. All peaks emerging from core level photoelectrons were fitted using a doublet with a ratio suitable for the orbital (2:1 for Ni-2p and 2:3 for Ag-3d). The study of the oxidation state of the Ni-2p core level spectrum is known to be compromised by the presence of secondary peaks emerging from multiplet splitting, plasmon loss structures and satellite peaks overlapping with the primary structure of the spectrum. Thus, only the $2p_{3/2}$ was considered for quantification of Ni species because overlapping of the secondary electron peaks with the $2p_{1/2}$ photoelectron lines make the curve fitting by doublets very problematic. For Pd-3d, instead, both d peaks were used for peak area integration and were compared to Ni-$2p_{3/2}$ to obtain the ratio of Pd and Ni species by using sensitivity factors that accounted for the different peak areas considered for quantification. The binding energy values were allowed to shift by ±0.3 eV to account for error associated with referencing to adventitious carbon. Besides metallic Ni (852.7 eV), two Ni species with the same oxidation state (Ni^{2+}) were identified in the Ni-2p spectrum: NiO (853.6 eV) and $Ni(OH)_2$ (855.6 eV)[1–6]. Similarly, besides metallic Pd (335.5 eV), two Pd oxides were found when deconvoluting the Pd-3d peak: PdO (336.6 eV) and PdO_2 (337.9 eV)[7–10].

Table S2 *Quantification of Pd and Ni species from XPS spectra deconvolution for annealed, acid treated samples and after both HOR and ORR.*

Sample	Annealed						HOR						ORR					
	Pd (%)			Ni (%)			Pd (%)			Ni (%)			Pd (%)			Ni (%)		
	Pd	PdO	PdO_2	Ni	NiO	$Ni(OH)_2$	Pd	PdO	PdO_2	Ni	NiO	$Ni(OH)_2$	Pd	PdO	PdO_2	Ni	NiO	$Ni(OH)_2$
PdNi-350	89	11	-	18	8	73	81	19	-	8	-	92	69	31	-	24	-	76
PdNi-400	86	14	-	17	8	74	80	20	-	6	-	94	74	-	26	8	4	88
PdNi-450	82	18	-	16	23	61	73	21	6	6	-	94	75	25	-	10	-	90
PdNi-500	81	19	-	15	20	65	60	-	40	3	-	97	88	12	-	8	-	92
PdNi-550	77	23	-	21	26	53	85	-	15	8	-	92	73	27	-	8	-	92
PdNi-600	70	30	-	22	22	56	41	-	59	10	-	90	55	19	26	7	-	93
Average	**81**	**19**	**-**	**18**	**18**	**64**	**70**	**10**	**20**	**7**	**-**	**93**	**72**	**19**	**9**	**11**	**1**	**89**
	Acid Treated						**HOR**						**ORR**					
	Pd (%)			**Ni (%)**			**Pd (%)**			**Ni (%)**			**Pd (%)**			**Ni (%)**		
	Pd	PdO	PdO_2	Ni	NiO	$Ni(OH)_2$	Pd	PdO	PdO_2	Ni	NiO	$Ni(OH)_2$	Pd	PdO	PdO_2	Ni	NiO	$Ni(OH)_2$
PdNi-350-AT	79	21	-	37	38	25	57	37	6	9	-	91	60	35	5	12	-	88
PdNi-400-AT	78	22	-	30	39	31	47	35	18	11	-	89	46	37	17	12	-	88
PdNi-450-AT	76	24	-	42	25	33	50	32	18	10	-	90	67	28	5	25	-	75
PdNi-500-AT	73	27	-	45	25	30	69	19	12	10	-	90	57	35	8	14	-	86
PdNi-550-AT	73	27	-	48	23	29	38	37	25	13	-	87	65	30	6	9	-	91
PdNi-600-AT	69	31	-	40	20	40	43	36	21	8	-	92	69	35	5	12	-	88
Average	**75**	**25**	**-**	**40**	**28**	**31**	**51**	**33**	**17**	**10**	**-**	**90**	**61**	**33**	**8**	**14**	**-**	**86**

References

1. Payne, B. P., Biesinger, M. C. & McIntyre, N. S. The study of polycrystalline nickel metal oxidation by water vapour. *J. Electron Spectros. Relat. Phenomena* **175**, 55–65 (2009).
2. Biesinger, M. C. *et al.* Resolving surface chemical states in XPS analysis of first row transition metals, oxides and hydroxides: Cr, Mn, Fe, Co and Ni. *Appl. Surf. Sci.* **257**, 2717–2730 (2011).
3. Yu, X. *et al.* Hydrogen Evolution Reaction in Alkaline Media: Alpha- or Beta-Nickel Hydroxide on the Surface of Platinum? *ACS Energy Lett.* **3**, 237–244 (2018).
4. Biesinger, M. C., Payne, B. P., Lau, L. W. M., Gerson, A. & Smart, R. S. C. X-ray photoelectron spectroscopic chemical state Quantification of mixed nickel metal, oxide and hydroxide systems. *Surf. Interface Anal.* **41**, 324–332 (2009).
5. Marchetti, L., Miserque, F., Perrin, S. & Pijolat, M. XPS study of Ni-base alloys oxide films formed in primary conditions of pressurized water reactor. *Surf. Interface Anal.* **47**, 632–642 (2015).
6. Chhetri, M., Sultan, S. & Rao, C. N. R. Electrocatalytic hydrogen evolution reaction activity comparable to platinum exhibited by the Ni/Ni(OH)2/graphite electrode. *Proc. Natl. Acad. Sci. U. S. A.* **114**, 8986–8990 (2017).
7. Toyoshima, R. *et al.* In situ ambient pressure XPS study of CO oxidation reaction on Pd(111) surfaces. *J. Phys. Chem. C* **116**, 18691–18697 (2012).
8. Tura, J. M., Regull, P., Victori, L. & de Castellar, M. D. XPS and IR (ATR) analysis of Pd oxide films obtained by electrochemical methods. *Surf. Interface Anal.* **11**, 447–449 (1988).
9. Brun, M., Berthet, A. & Bertolini, J. C. XPS, AES and Auger parameter of Pd and PdO. *J. Electron Spectros. Relat. Phenomena* **104**, 55–60 (1999).
10. Militello, M. C. & Simko, S. J. Palladium Oxide (PdO) by XPS. *Surf. Sci. Spectra* **3**, 395–401 (1994).